Anisotropy in Molecular Magnetism – Magnetic Exchange Coupling of Octahedral Cobalt(II) Ions

A Thesis submitted to The University of Manchester
for the degree of Doctor of Philosophy
in the Faculty of Engineering and Physical Sciences

2009

Angelika Brigitte Boeer
School of Chemistry
The University of Manchester

(EUTFF)

TH 32594

Contents

Chapter II

Chapter III

Chapter IV

Chapter V

Chapter VI

List of figures

List of tables

List of equations

Abbreviations and physical constants

Abbreviations

a.u.	Arbitrary unit
AOM	Angular overlap model
bta	Benzotriazolate
cit	Citrate
dmp	3,3-Dimethyl-1-butanol
EPR	Electron paramagnetic resonance
Hchp	6-chloro-2-hydroxypyridine
HDvV	Heisenberg-Dirac-van-Vleck
HFEPR	High field electron paramagnetic resonance
Hhmp	2-Hydroxy-methylpyridine
INS	Inelastic neutron scattering
MCD	Magnetic circular dichroism
NMR	Nuclear magnetic resonance
py	Pyridine
SCM	Single chain magnet
SEL	Strong exchang limit
SMM	Single molecule magnet
SOC	Spin-orbit coupling
SQUID	Superconducting quantum interference device
tmen	Tetramethylethylene diamine
ZFS	Zero-field splitting

Variables and physical constants

$\vec{B}, B$	Magnetic field vector, scalar
χ, χ	Magnetic susceptibility tensor, parameter
D	Zero-field splitting matrix
D	Axial zero-field splitting parameter
Δ	Crystal field splitting parameter
Δe_π	Difference between $e_{\pi x}$ and $e_{\pi y}$

Δ_O	Octahedral crystal field splitting
E	Energy
E	Rhombic zero-field splitting parameter
$E^{(0)}$	Zero-field energy
$E^{(1)}$	First order Zeeman coefficient
$E^{(2)}$	Second order Zeeman coefficient
e_σ, e_π	AOM parameters, defining covalent σ- and π-bonding, respectively
g, g	g-matrix, g-parameter
g_e	Free electron g-value (2.0023)
$\hat{H}$	Hamiltonian
$\vec{H}$, H	Magnetic field vector, scalar
j	Total angular momentum quantum number
$\hat{j}$	Total angular momentum operator
J, J	Exchange coupling matrix, exchange parameter
k	Orbital reduction parameter
$\vec{k}$, k	Wave vector (INS), scalar
k_B	Boltzmann constant (0.69501cm^{-1} K^{-1})
l	Orbital angular momentum quantum number
$\hat{l}$	Orbital angular momentum operator
λ	Spin-orbit coupling parameter (within term)
M	Magnetisation
m_s, m_S, m_l	Magnetic quantum number
μ_B	Bohr magneton (4.66858 10^{-5} G^{-1}mol^{-1})
N	Avogadro number (6.022 10^{23} mol^{-1})
$\vec{Q}$, Q	Scattering vector (INS), scalar
S, s	Spin quantum number
$\hat{S}$, $\hat{s}$	Spin operator
T	Temperature
τ	Torque
θ, ϕ	Azimuthal angles defining the ligand positions (AOM)
ϕ	Angle between crystal axis a and χ_1 in monoclinic crystals
ψ	Angle defining the orientation of π-orbitals (AOM)
ζ	Spin-orbit coupling parameter (free ion)

Abstract

Molecular magnets are of growing interest towards the development of molecular magnetic storage devices, magnetic refrigeration and quantum information processing. A particularly important property to achieve a magnetic memory effect is magnetic anisotropy. One possibility to increase such anisotropy is the use of magnetic ions with an unquenched orbital angular momentum *e.g.* octahedral Co(II). Spin-orbit coupling leads to a large effective splitting in zero-field, but a simplistic spin-only interpretation of magnetic exchange interactions is no longer sufficient. Very little is understood about the exchange coupling of Co(II) ions to date.

In this Ph.D. research a series of carboxylate and water bridged dimetallic octahedral Co(II) compounds, both ferro- and antiferromagnetically coupled, has been studied on powder and single crystal samples. Single crystal rotational studies with both SQUID magnetometry and EPR spectroscopy have provided the orientation of the molecular principal magnetic axes with respect to the molecular structure. Strong anisotropy has been observed in all cases, which manifests in particular in the Zeeman splitting or "*g*"-anisotropy ("g_{eff}" = 2.3 – 6.2), but also in the magnetic exchange interactions. To our knowledge, the first multifrequency powder spectra and single crystal rotational studies on exchange coupled Co(II) systems with EPR spectroscopy have allowed for anisotropic principal effective "*g*"-values to be assigned to different orientations of the molecule. The direct cobalt-cobalt vector was found particularly important in the magnetic exchange: along this vector the smallest Zeeman splittings and smallest exchange interactions were found in the dimetallics, but more importantly, along the Co-Co vector weak antiferromagnetic coupling was observed on a compound with overall ferromagnetic behaviour. A new semi-quantitative model, which has proved transferable between ferro- and anti-ferromagnetically coupled dimetallics, has been proposed for the magnetic exchange coupling between spin-orbit ions, and complementing calculations with the angular overlap model have enhance the understanding of octahedral Co(II). Based on the interaction of two pseudo spins "*s*" = $^1/_2$ to an effective "singlet" and "triplet", where all degeneracy is lifted, magnetic properties, EPR transitions and INS data have been reproduced simultaneously with calculations using solely experimental observables.

In addition, heterometallic rings (Cr_7M, Cr_6M_2, Cr_7M_2 with M = Co(II), Ni(II)) have been studied with SQUID magnetometry, EPR and NMR spectroscopy towards the influence of anisotropic Co(II) ions on the magnetic properties of the rings, and the isomeric compositions of rings with more than one heteroatom. Prior to Cr-Co rings, a method for the determination of the position of heteroions has been devised on spin-only Cr-Ni rings, which have shown 2:1 mixtures of positional isomers with magnetically different properties. To our knowledge, odd-numbered heterometallic rings with two hetero-atoms have been studied for the first time, and spin frustration has been observed in Cr_7Ni_2 and Cr_7Co_2. The anisotropy of the Co(II) ion within the rings has been studied on a Ga_7Co ring. Overall, the influence of Co(II) on the magnetic exchange within the rings is masked by the dominating Cr-Cr exchange, at least for powder samples.

Declaration

No portion of the work referred to in the thesis has been submitted in support of an application for another degree or qualification of this or any other university or other institute of learning.

Copyright

1. The author of this thesis (including any appendices and/or schedules to this thesis) owns any copyright in it (the "Copyright") and she has given The University of Manchester the right to use such Copyright for any administrative, promotional, educational and/or teaching purposes.
2. Copies of this thesis, either in full or in extracts, may be made only in accordance with the regulations of the John Rylands University Library of Manchester. Details of these regulations may be obtained from the Librarian. This page must form part of any such copies made.
3. The ownership of any patents, designs, trade marks and any and all other intellectual property rights except for the Copyright (the "Intellectual Property Rights") and any reproductions of copyright works, for example graphs and tables ("Reproductions"), which may be described in this thesis, may not be owned by the author and may be owned by third parties. Such Intellectual Property Rights and Reproductions cannot and must not be made available for use without the prior written permission of the owner(s) of the relevant Intellectual Property Rights and/or Reproductions.
4. Further information on the conditions under which disclosure, publication and exploitation of this thesis, the Copyright and any Intellectual Property Rights and/or Reproductions described in it may take place is available from the Head of School of Chemistry (or the Vice-President) and the Dean of the Faculty of Life Sciences, for Faculty of Life Sciences' candidates.

Acknowledgement

I was fortunate to work and collaborate with many excellent scientists and wonderful friends during my Ph.D. I would like to acknowledge and thank the following people in particular:

Prof. David Collison, my supervisor, for his enthusiasm, guidance and encouragement, many stimulating suggestions on theory along with his sense of humour if theory got a little intense, and for always having time for discussions.

Prof. Richard Winpenny, my supervisor, again for enthusiasm, guidance, and encouragement. Furthermore I would like to thank him for allowing me to have scientific freedom, and for the support of numerous international collaborations.

Prof. Eric McInnes for his enthusiasm, help and advice during this project.

Everybody past and present in the EPR department, in particular Dr. Joanna Wolowska, Dr. Ruth Edge and Dr. Floriana Tuna for their help with EPR spectroscopy and for lighting up many hours in the basement. In addition I would like to thank Dr. Floriana Tuna for all her help, training, and discussions regarding magnetic measurements, and for her trust in me guarding the SQUID.

Dr. Grigore Timco for the synthesis of all ring compounds in the requested space group, and for the synthesis of the deuterated dimetallics at short notice.

Dr. Rebecca Laye and Dr. Victoria Milway for all their hard work, patience, charm, and organizing talent to keep the magnetism lab running.

All members of the magnetism group past and present for forming a fantastic team, where I found wonderful friends and thoroughly enjoyed working on a daily basis.

Dr. Christopher Muryn for all his help and training regarding X-ray crystallography.

Prof. Talal Mallah and Dr. Gaëlle Charron for an intensive training on AOM.

Dr. Anne-Laure Barra for high field electron paramagnetic resonance spectroscopy.

Dr. Richard Mole and Dr. Tobias Unruh for inelastic neutron scattering experiments.

Dr. Carolina Sañudo for help with paramagnetic NMR spectroscopy.

Prof. Marco Affronte, Dr. Alberto Ghirri and Giulia Lorusso for torque experiments.

Prof. Andrew Thompson and Dr. Justin Bradley for MCD spectroscopy.

The technicians in the electronic and mechanical workshop for immediate assistance.

I would like to thank all my friends for fabulous non-scientific distraction, and reminding me that even a Ph.D. student is a human being.

Finally I would like to the thank James and my family for all the support, love and happiness they gave me, without which this work would have not been possible.

„Phantasie ist wichtiger als Wissen,
denn Wissen ist begrenzt"

Albert Einstein

Chapter I

Introduction

Magnetism has always been a keystone in technical applications, especially in the broad field of data storage. Traditionally, magnetism is known as a bulk phenomenon, where magnetic properties are related to cooperative effects between magnetic moments of atoms, molecules or particles. More recently, *molecular magnetism* has become a subject of growing interest. In contrast to conventional bulk magnetism, magnetic properties are based on *intra*molecular exchange interactions between spins of isolated molecular cluster arrangements. A special group of molecules within exchange coupled oligomers are the so-called "single molecule magnets" (SMMs). Those molecules contain a number of parallel or antiparallel aligned spin centres, and can be magnetised as single molecules at very low temperature. Not only are SMMs of importance for future applications, many different kinds of molecular nano-magnets have been studied intensively during the past twenty years, and are still of growing interest towards the development of molecular magnetic storage devices, magnetic refrigeration and quantum information processing.

A particularly important property to achieve a magnetic memory effect, but also in related areas such as quantum computing, is *magnetic anisotropy*. One obvious, but widely neglected, possibility to increase magnetic anisotropy is the use of magnetic ions that contain an unquenched angular momentum, for example vanadium(III), high spin iron(II) or cobalt(II) in octahedral complexes. Many such compounds are known, but very little is understood about their magnetic exchange coupling because of the theoretical complication arising from first order spin-orbit coupling. Work reported within this Ph.D. Thesis concentrates on the magnetic and spectroscopic properties of single ion and exchange coupled octahedral cobalt(II) coordination compounds. The key towards a better understanding of magnetic anisotropy lies in the use of complementary measurement techniques, and in particular in single crystal measurements, which provide direct access to crystal and/or molecular anisotropy.

I.1 Setting the scene: Magnetism, anisotropy and spin-orbit coupling

I.1.1. Molecular magnetism

A coordination compound containing a certain number of paramagnetic metal centres experiences three different magnetic interactions: (i) Spin-orbit coupling can lead to mixed energy states and cancels the degeneracy between different $|m_S|$ states for systems with a spin $s > {}^1/_2$. (ii) Magnetic exchange coupling of the spins can lead to an intramolecular magnetic ordering. Finally, (iii) the Zeeman effect in a magnetic field leads to a splitting of degenerate m_S levels into + m_S and - m_S.[1]

For metal ions, which exhibit a quenched orbital angular momentum (so called "spin-only ions") through the surrounding ligand field, the magnetic properties are well understood. The major part of magnetic exchange energy is generated by electrostatic interactions, a quantum mechanical phenomenon that can be related to the overlap of two paramagnetic orbitals. The difference in the two resulting energies E_1 and E_2 is quantified by the exchange parameter J in Equation I.1.[2]

$$J = \frac{E_2 - E_1}{2} \tag{I.1}$$

Exchange interactions can occur directly between the metal centres (direct exchange) or mediated by bridging ligands (super-exchange), which provide delocalised electrons for the interaction between the spin-centres. Often direct exchange is weak, and the most common exchange interaction in molecular magnetic compounds is super-exchange.

Quantum mechanically, the empirical Heisenberg-Dirac-van-Vleck Hamiltonian $\hat{H}_{\mathrm{HDvV}}$ can be derived (Equation I.2).[2]

$$\hat{H}_{\mathrm{HDvV}} = -2\sum_{i,j} \hat{s}_i \mathbf{J} \hat{s}_j \quad \text{where } \hat{s}_i, \hat{s}_j = \text{spin operators, } \mathbf{J} = \text{exchange matrix} \tag{I.2}$$

Equation (I.3) shows a more general Hamiltonian including the isotropic exchange coupling ($\hat{H}_{\mathrm{HDvV}}$), the zero-field splitting ($\hat{H}_{\mathrm{ZFS}}$) arising from second order spin-orbit coupling, and the Zeeman contribution in the presence of a magnetic field ($\hat{H}_{\mathrm{Zeeman}}$).[3]

$$\hat{H} = \hat{H}_{\mathrm{HDvV}} + \hat{H}_{\mathrm{ZFS}} + \hat{H}_{\mathrm{Zeeman}} = -2\sum_{i,j} \hat{s}_i \mathbf{J} \hat{s}_j + \sum_i \hat{s}_i \mathbf{D} \hat{s}_i + \sum_i \mu_{\mathrm{B}} \vec{B} \mathbf{g}_i \hat{s}_i \qquad \text{(I.3)}$$

Within the strong exchange limit (SEL), zero-field splitting and Zeeman contributions can be treated as small perturbations on the strongly exchange coupled system (Equation I.4) for each total molecular spin-state.

$$\hat{H}_{\mathrm{SEL}} = \hat{S}_{\mathrm{eff}} \mathbf{D}_{\mathrm{eff}} \hat{S}_{\mathrm{eff}} + \mu_{\mathrm{B}} \vec{B} \mathbf{g}_{\mathrm{eff}} \hat{S}_{\mathrm{eff}} \qquad \text{(I.4)}$$

Here the zero-field splitting matrix **D** and the gyromagnetic **g**-matrix corresponds to the total spin state S_{eff}, which can be derived by pair wise coupling of the single spins s_i (Equation I.5).[2]

$$S_{\mathrm{eff}} = s_1 + s_2, s_1 + s_2 - 1, \ldots, |s_1 - s_2| \qquad \text{(I.5)}$$

The zero-field splitting parameters D and E are related to the principal zero-field splitting tensor values through Equations I.6.

$$D_{\mathrm{eff}} = \frac{3D_{\mathrm{eff},zz}}{2} \quad \text{and} \quad E_{\mathrm{eff}} = \frac{\left|D_{\mathrm{eff},xx} - D_{\mathrm{eff},yy}\right|}{2}. \qquad \text{(I.6)}$$

The energy levels of the system in a magnetic field can be expanded in a power series (Equation I.7) [2]

$$E_n = E_n^{(0)} + E_n^{(1)} H + E_n^{(2)} H^2 + \ldots \quad \text{with} \quad \begin{array}{l} E_n^{(0)} = \text{energy of level } n \text{ in zero - field} \\ E_n^{(1)} = \text{first order Zeeman coefficient} \\ E_n^{(2)} = \text{second order Zeeman coefficient} \end{array} \qquad \text{(I.7)}$$

The first order Zeeman coefficient splits the energy level, n, into equally spaced components separated by $g\mu_{\mathrm{B}}H$, while the second order Zeeman coefficient mixes

wavefunctions of excited states into the ground state. A relation between Zeeman coefficients based on exchange coupling, zero-field splitting and the magnetic susceptibility has been derived by van Vleck (Equation I.8).[2]

$$\chi = \frac{N\sum_{n}\left(-\frac{E_n^{(1)^2}}{k_B T} - 2E_n^{(2)}\right)\cdot \exp\left(-\frac{E_n^{(0)}}{k_B T}\right)}{\sum_{n}\exp\left(-\frac{E_n^{(0)}}{k_B T}\right)} \qquad \text{(I.8)}$$

In the SEL, and restricted to a quenched orbital angular momentum, this equation can be applied directly to fit magnetic properties observed for magnetically coupled transition metal clusters, and values for J, g_{eff} and D_{eff} are determined. Most conventional software packages available for magnetic models are based on the van Vleck equation. For systems that exhibit weak exchange interactions, magnetic exchange is of a similar order to zero-field splitting and Zeeman effect, and the three different parts of the Hamiltonian I.3 have to be solved simultaneously.

Significantly more complicated are magnetic exchange interactions between metal ions with an *unquenched* orbital angular momentum. Spin-orbit coupling between spin and orbital angular momentum leads to strong single ion anisotropy, which significantly influences the magnetic exchange interactions. Furthermore, the wavefunctions involved in magnetic exchange coupling are no longer pure spin-functions, but include both spin and orbital angular momentum contributions. In Section I.1.2 different theoretical approaches will be introduced, which address the problem of exchange coupling between spin-orbit ions using the example of cobalt(II).

I.1.2. Magnetic anisotropy

Magnetic anisotropy plays an important role for different magnetic properties achieved with different exchange coupled oligomers.

Single molecule magnets (SMMs), first discovered in 1993 with $[Mn_{12}(O_2CCH_3)_{16}(H_2O)_4O_{12}]\cdot 2CH_3COOH\cdot 4H_2O$ (Mn12),[4] are based on the combination of a large molecular spin ground state S_{eff} with a strong negative axial anisotropy. Along the easy axis of the crystal this leads to a significant zero-field splitting between the $\pm m_{S,eff}$ levels within the total spin ground state of the molecule, which allows for magnetisation of the crystal, followed by a retention of the magnetisation after removal of the magnetic field, if the crystal was magnetized along the easy axis. In addition to a magnetic memory effect, new anisotropy-related quantum-physical phenomena, such as quantum tunnelling of the magnetisation, have been observed in SMMs.[5]

Single chain magnets (SCMs) are composed of magnetically isolated molecular chains that can be individually magnetised. Similar to SMMs, these materials can retain their magnetisation after the removal of the external magnetic field, related to a large uni-axial anisotropy and strong magnetic interactions between magnetic units of the chain. SCMs can exhibit different anisotropic behaviour, for example classical spin-Heisenberg chains, or Ising chains, in which spins are aligned along a given *z*-axis that introduces an infinite uni-axial anisotropy with an easy *z* axis, have been reported.[6] The first molecular SCM reported in 2002 by Gatteschi *et al.* is based on cobalt(II).[7]

A magnetocaloric effect has been observed on compounds with no or very little anisotropy *e.g.* $[Fe_{14}O_6(bta)_6(\mu_2\text{-}OC(CH_3)_{18})Cl_6]$ and derivatives.[8,9] The degeneracy of the molecular m_{Seff} states at zero-field (in the absence of anisotropy) is lifted in a magnetic field leading to a drop in entropy if the temperature of the sample is kept constant. Subsequent adiabatic demagnetisation requires a constant entropy if the system is isolated from its surroundings. This results in a cooling effect, which is proposed in applications for molecule-based magnetic refrigeration.[10]

For a family of decametallic nickel and cobalt clusters a magnetic memory effect has been observed in the absence of any anisotropy.[11,12] Super-tetrahedral arrangement of ten oxygen bridged nickel(II) or cobalt(II) ions leads to a high band-like density of energy levels arising from the coupling of the spin states. Phonon trapping (essentially the re-absorption of emitted phonons because of the high density of states) prevents conventional relaxation mechanisms in a magnetised sample through phonon emission and the sample retains its magnetisation.[13] This phenomenon is in

contrast with the basis of SMM behaviour, because the effect can be observed for a powder as well as any orientations of a single crystal in a magnetic field.

A significant orbital contribution to magnetic properties, and hence a strong anisotropy is expected from lanthanide containing coordination compounds. Powell *et al.* have reported a triangular tridysprosium complex, which not only shows SMM behaviour, but also exhibits a non-magnetic ground state, despite an *odd* number of electrons. Furthermore, orientation-dependent steps in the field-dependent magnetisation are reported.[14] Single crystal studies have revealed non *co*-linearity of the dysprosium single ion axes, which results in a spin-chirality within the non-magnetic ground doublet and results in the slow relaxation of the ground state.[15] These studies show that anisotropy, rather than a large spin-ground state, appears to be the key towards a better understanding of SMM behaviour.

Recently Loss *et al.* have proposed advantages for quantum computing in the presence of spin-orbit interactions.[16] The authors report studies on a triangular copper(II) cluster encapsulated between polyoxometalates and identify a spin-electric coupling caused by an interplay between spin-exchange, spin-orbit interaction, and the chirality of the underlying spin structure of the molecular magnet. The coupling allows for the electric control of the spin (qubit) states.

Of course the above examples are only a small selection out of many different phenomena observed on molecular magnets. Nevertheless, they show how important understanding of magnetic anisotropy is, because presence or absence of different kinds of anisotropic features can lead to very different magnetic properties.

One way of increasing anisotropy is the introduction of transition metal ions with an unquenched orbital angular momentum. For single ions, spin-orbit coupling is theoretically well understood, and Section I.1.3 will provide a brief introduction into the ligand field theory of cobalt(II) and the effect of spin-orbit coupling. However, despite many theoretical approaches (see Section I.2) very little is *understood* about the exchange coupling of cobalt(II), and how the large single ion anisotropy affects magnetic interactions.

Figure I.1 shows two examples of cobalt(II) compounds characterized by a "butterfly"-shaped hysteresis loop: the octametallic $[Et_3NH][Co_8(chp)_{10}(O_3PPh)_2(NO_3)_3(Hchp)_2]$ and the tetrametallic $[C(NH_2)_3]_8[Co_4(cit)_4]\cdot 4H_2O$.[17,18] Similar to conventional SMM behaviour a hysteresis opening is observed after the sample has

been magnetised, however the hysteresis collapses at zero-field. The unusual behaviour is attributed to some fast quantum tunnelling; however the origin of the phenomenon remains unclear. Studies on other (spin-only) systems have shown that enhanced quantum tunnelling of the magnetisation is often related to mixing of spin-states,[19-21] showing that a better understanding of the electronic structure in exchange coupled cobalt(II) systems is required to explain the observed magnetic properties.

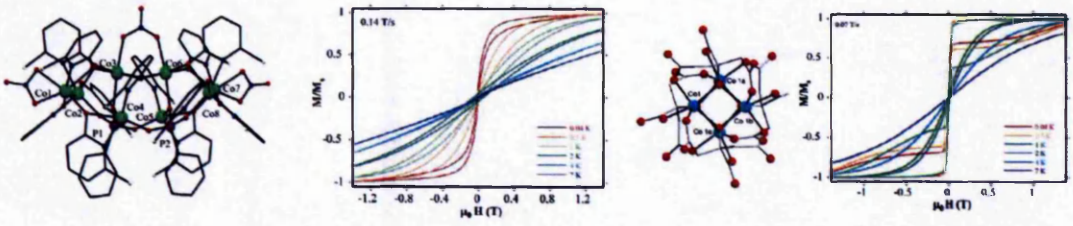

Figure I.1: Octametallic ($[Et_3NH][Co_8(chp)_{10}(O_3PPh)_2(NO_3)_3(Hchp)_2]$)[17] and tetrametallic ($[C(NH_2)_3]_8[Co_4(cit)_4]\cdot 4H_2O$)[18] exchange coupled cobalt(II) systems showing a "butterfly"-shaped hysteresis loop.

I.1.3. Ligand field theory and spin-orbit coupling of cobalt(II)

A weak octahedral ligand field splits the free ion ^4F and ^4P terms of cobalt(II) (derived from the electronic configuration d^7) into a 12-fold degenerate $^4T_{1g}$ ground state and well separated excited states ($^4T_{2g}$, $^4A_{2g}$, $^4T_{1g}$) with respect to the thermal energy at room temperature.[22-24] The matrix elements of the orbital angular momentum operator $\hat{l}$ within the $^4T_{1g}$ ground state are exactly the same as the matrix elements of $-^3/_2\ \hat{l}$ within the $^4T_{1g}$ excited state derived from the ^4P-term. Despite the energy gap of approximately 10000 cm^{-1} the symmetry equivalence of the states leads to a significant mixture of the excited ^4P term into the ^4F ground term. This effect is present even for the free ion and reduces the matrix elements of the pure $^4T_{1g}$ (^4F) term by about 6-7 %.[25] A second contribution that results in spin-orbit reduction arises from the physical distortion of the metal orbitals through partial covalent bonding with the ligands. This effect is dependent on the character of the ligand. The total reduction arising from both contributions is represented by the orbital reduction parameter k.

In the presence of an orbital angular momentum larger than $^1/_2$, spin-orbit coupling splits a given term by mixing spin and orbital parts of the wavefunctions.

The free ion spin-orbit coupling can be expressed by the spin-orbit operator (I.9) including a combination of the spin and the orbital angular momentum operators, and the spin-orbital coupling constant λ.[24]

$$\lambda \hat{l} \cdot \hat{s}, \text{ where } \lambda = -\frac{\zeta}{2s} \text{ and } \zeta \approx 515 \text{ cm}^{-1} \text{ (free ion spin-orbit coupling parameter)} \quad \text{(I.9)}$$

Taking the orbital reduction into account, the influence of spin-orbit coupling on the $^4T_{1g}$ term can be evaluated by diagonalizing the spin-orbit operator within the representations of the wavefunctions $|m_l, m_s\rangle$ where $m_l = 0, \pm 1$, $m_s = \pm^3/_2, \pm^1/_2$:

$$E = \langle m_l, m_s | -\frac{3}{2} k\lambda \hat{l} \cdot \hat{s} | m_l, m_s \rangle \quad \text{(I.10)}$$

The resulting energies are a ground doublet, a quartet and a sextet, with energies and wavefunctions as listed in Table I.1.[25]

$E = \frac{9}{4}k\lambda$	$\Psi_{\pm 6} = \left\|\pm 1, \pm\frac{3}{2}\right\rangle$
$E = \frac{9}{4}k\lambda$	$\Psi_{\pm 5} = \frac{1}{\sqrt{5}}\left[\sqrt{2}\left\|0, \pm\frac{3}{2}\right\rangle + \sqrt{3}\left\|\pm 1, \pm\frac{1}{2}\right\rangle\right]$
$E = \frac{9}{4}k\lambda$	$\Psi_{\pm 4} = \frac{1}{\sqrt{10}}\left[\left\|\mp 1, \pm\frac{3}{2}\right\rangle + \sqrt{6}\left\|0, \pm\frac{1}{2}\right\rangle + \sqrt{3}\left\|\pm 1, \mp\frac{1}{2}\right\rangle\right]$
$E = \frac{3}{2}k\lambda$	$\Psi_{\pm 3} = \frac{1}{\sqrt{5}}\left[-\sqrt{3}\left\|0, \pm\frac{3}{2}\right\rangle + \sqrt{2}\left\|\pm 1, \pm\frac{1}{2}\right\rangle\right]$
$E = \frac{3}{2}k\lambda$	$\Psi_{\pm 2} = \frac{1}{\sqrt{15}}\left[\sqrt{6}\left\|\mp 1, \pm\frac{3}{2}\right\rangle + \left\|0, \pm\frac{1}{2}\right\rangle - 2\sqrt{2}\left\|\pm 1, \mp\frac{1}{2}\right\rangle\right]$
$E = \frac{15}{4}k\lambda$	$\Psi_{\pm 1} = \frac{1}{\sqrt{6}}\left[-\sqrt{3}\left\|\mp 1, \pm\frac{3}{2}\right\rangle + \sqrt{2}\left\|0, \pm\frac{1}{2}\right\rangle - \left\|\pm 1, \mp\frac{1}{2}\right\rangle\right]$

Table I.1: Energy levels and wavefunctions of cobalt(II) in a pure octahedral ligand field derived from spin-orbit coupling.[25]

Figure I.2 shows the corresponding energy level diagram. The energy difference between the ground doublet and the first excited state is $^9/_4 k\lambda$ (*ca.* 300 cm^{-1}), and

hence far from large with respect to the thermal energy of about 210 cm^{-1} at room temperature.

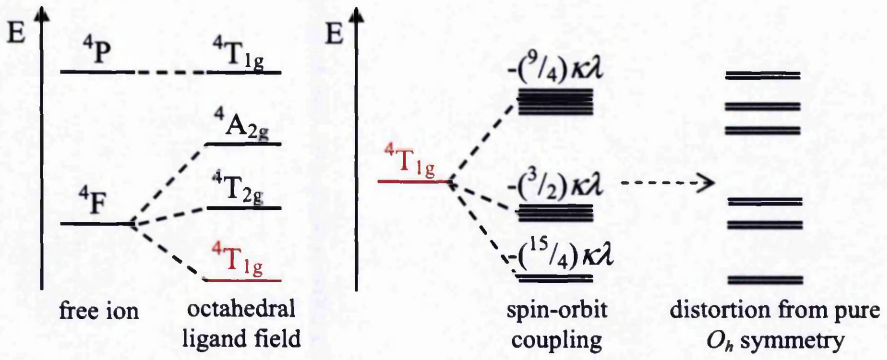

Figure I.2: Qualitative energy diagrams illustrating the effect of spin-orbit coupling and ligand field distortions on the ground $^4T_{1g}$ term in octahedral cobalt(II) ions.

However, very few compounds contain a pure octahedrally coordinated cobalt(II) centre. More common is a distortion of the ligand field, which results in a further splitting of the energy levels into six Kramers doublets.

At very low temperatures only the ground Kramers doublet is thermally populated, and for low temperature experiments cobalt(II) ions are often approximated as an "effective" or "pseudo" spin "s" = $^1/_2$ (see also Section I.2). It is important to note that the ground doublet is not a spin-function (despite the treatment as a spin), but comprises both orbital and spin parts in the wavefunction. A simple analogy to the spin-only system is therefore not physically correct, nevertheless results in this Thesis will show how a very useful qualitative picture and a semi-quantitative interpretation can be gained from this simple model. Ligand field theory predicts a Zeeman splitting constant (g-value in spin-only terms) of "g" = 4 – 4.3 for the ground Kramers doublet with a magnetic moment of $^1/_2$ arising from a d^7 electron configuration.[23]

A comment on convention of nomenclature used in this Ph.D. Thesis may be useful at this point:

- Single ion spin-only functions and operators are labelled with lower case letters *e.g.*: $\hat{s}$, s, m_s, the related spin-only Hamiltonian parameters are labelled with conventional variables *e.g.*: g, D, E.

- Spin functions and operators arising from coupling of spin-only functions within the SEL are labelled as effective spins and capital letters *e.g.*: $\hat{S}_{eff}$, S_{eff}, m_{Seff}, the related Hamiltonian parameters are labelled with effective variables *e.g.*: g_{eff}, D_{eff}, E_{eff}.
- Single ion spin-orbit functions treated like pseudo spin-functions and related parameters are labelled with conventional variables in inverted commas *e.g.*: "*s*", "m_s", "*g*", "*D*", "*E*"
- Parameters related to spin-orbit functions arising from the coupling of single ion spin-orbit functions within the SEL are labelled as "S_{eff}", "m_{Seff}", "g_{eff}", "D_{eff}", "E_{eff}".

I.1.4. The angular overlap model

The angular overlap model (AOM) was developed in the 1960s by Jørgensen and Schäffer[26] as an extended ligand field theory to describe metal-ligand bond interactions in coordination compounds.[22,27] In contrast to the conventional ligand field theory based on electrostatic interactions, the AOM adapts the molecular orbital theory, describing the covalent σ- and π-bonding character of the metal-ligand bonds. It is important to note that the AOM does not aim for the calculation of physically real values of energy levels in a transition metal complex, but parameterizes the metal-ligand interactions with σ- and π-bonding parameters. Those parameters, conventionally expressed as e_σ, $e_{\pi,x}$ and $e_{\pi,y}$, are always derived from experiments and refer to a particular metal-ligand interaction, not to the complex as a whole. Within limits, this leads to a transferability of parameters from one compound to another, a major advantage of the AOM because several review articles provide a large number of AOM parameters for various transitions metal complexes.[28-30]

To compute the energies of the *d*-electrons within a transition metal complex, a Hamiltonian (Equation I.11), composed of a ligand field operator in the AOM parameterization $\hat{H}_{AOM}$, an electron-electron repulsion operator $\hat{H}_{ER}$, a spin-orbit coupling operator $\hat{H}_{SOC}$, and a Zeeman operator $\hat{H}_Z$, operates on a basis function set given by the five outer-shell *d*-orbitals of the metal.[31]

$$\hat{H} = \hat{H}_{\mathrm{AOM}} + \hat{H}_{\mathrm{ER}} + \hat{H}_{\mathrm{SOC}} + \hat{H}_{\mathrm{Z}} \quad \text{operating on} \quad \psi = \left| \hat{\alpha}, \hat{l}, \hat{s}, \hat{j}, \hat{m}_j \right\rangle \qquad \text{(I.11)}$$

The wavefunctions are determined by the quantum numbers j and m_j following the Russell-Saunders coupling scheme for eigenstates of a total angular momentum $\hat{j} = \hat{l} + \hat{s}$. The additional quantum number α is required to define completely the state vector.

The ligand field operator $\hat{H}_{\mathrm{AOM}}$ is parameterized according to Equation I.12.

$$\Delta_O = 10Dq = 3e_\sigma - 2\left(e_{\pi x} + e_{\pi y}\right) \qquad \text{(I.12)}$$

$\Delta_O = 10Dq$ refers to the octahedral crystal field splitting, which can be experimentally observed from optical spectroscopy (*e.g.* UV-Vis or MCD spectroscopy) to reduce the number of free parameters in the calculation. For anisotropic π-interactions the π-anisotropy is expressed as cosine- $e_{\pi,\cos}$ (= $e_{\pi,x}$) and sine- functions $e_{\pi,\sin}$ (= $e_{\pi,y}$) of the anisotropy interaction parameter e_π. In comparison to other ligand field models, the AOM accounts for the exact geometry of the complex by parameterizing the exact position of each ligand through polar coordinates as depicted in Figure I.3[22]

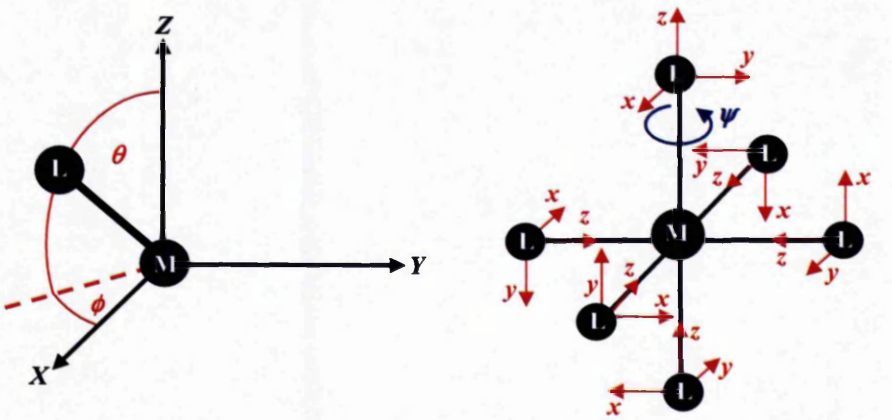

Figure I.3: Global (left) and ligand based (right) coordinate system to define position and anisotropy of the ligand atoms for AOM calculations.

The azimuthal angles θ and ϕ define the position of the ligand within a chosen *XYZ* axis frame centred on the metal ion. A third angle ψ defines the orientation of an axis

frame on each ligand atom in order to account for anisotropic π-interactions. The metal ligand bond is defined as z, while rotation around z by ψ defines the direction of x and y, corresponding to the parameters $e_{\pi x}$ and $e_{\pi y}$.

The electron-electron repulsion operator $\hat{H}_{ER}$ is parameterized through the Racah parameters B and C.[22]

Spin-orbit coupling has been discussed in the previous section, and the spin-orbit coupling operator $\hat{H}_{SOC}$ (Equation I.13) is used to introduce spin-orbit mixing exactly into the AOM calculations.

$$\hat{H}_{SOC} = k\zeta \sum_i \hat{l}_i \hat{s}_i \tag{I.13}$$

The electron Zeeman operator (Equation I.14) contains the influence of the magnetic field on both the orbital and the spin part of the wavefunctions, and allows for the computation of the eigenvalues in both zero- and applied magnetic field.

$$\hat{H}_Z = \left(k\hat{l} + g\hat{s}\right)\mu_B \vec{B} \tag{I.14}$$

It has been shown that magnitude and orientation of single ion anisotropy, and corresponding spin-Hamiltonian parameters on many different (spin-only) systems, can be explained with calculations using the AOM.[31-33]

In this Ph.D. Thesis the AOM is used to provide a better understanding of the anisotropy of single cobalt(II) ions. Results from calculations are used to complement the effective model of cobalt(II) as an "s" = $^1/_2$ at low temperatures and to explain deviations of the real system from the over-simplified model.

I.2 Magnetic properties of exchange coupled cobalt(II) compounds

In the previous sections the problem of spin-orbit coupling in cobalt(II) ions in an octahedral ligand field was introduced. The orbital contribution and large magnetic anisotropy induced by spin-orbit coupling does not allow for a simplistic spin-only

treatment. In this section an overview of magnetic measurements reported in the past, and of different theoretical approaches towards a better understanding of the magnetic properties, is given.

Investigations in this Ph.D. Thesis are focused on dimetallic octahedral cobalt(II) compounds, the smallest, and therefore most simple exchange coupled unit. Different authors report the powder magnetic susceptibility on different octahedral cobalt(II) dimetallics.[34-48] Most of those dimetallics exhibit antiferromagnetic exchange interactions, but ferromagnetically coupled examples are also known. At room temperature the magnitude of various effects contributing to the observed magnetic susceptibility allows for an uncoupled, additive treatment of the spin and orbital angular momentum. Decrease in temperature leads to a thermal depopulation of spin-orbit states, leaving only less magnetic lower energy states to contribute to the magnetic susceptibility, and a characteristic decrease in χT is observed.

In all above cases the magnetic properties have been measured and discussed on powder samples. Aside from micro-SQUID analysis of cobalt(II) clusters, which show a slow relaxation of magnetisation,[17,18,49,50] we are only aware of two magnetic measurements reported on single crystals of molecular exchange coupled octahedral cobalt(II) systems (see below).[51,52] This seems surprising, because many groups have developed theoretical models to interpret anisotropic effects in exchange coupled cobalt(II) systems, and single crystal experiments are the only *direct* probe of anisotropy.

In a brief overview different models, which have been proposed for the simulation of the magnetic properties of exchange coupled octahedral cobalt(II) compounds, are summarized.

In the early 1970s Lines developed a theoretical approach, in which the assumption of an "s" = $^1/_2$ effective ground state is taken as a starting point and extended to a fictitious "temperature dependent" ground doublet per cobalt(II) ion.[25] Effectively this was incorporated in a temperature dependent "g"-factor and temperature dependent eigenfunctions, which accounted for the different single ion spin-orbit energy levels. A hybrid theory was proposed, in which exchange interactions for example, were included as a molecular field in the excited single-ion levels, but treated exactly within the ground single-ion doublets of the cluster. Variables in the model were the spin-orbit coupling parameter λ, (which can usually be fixed to the

free ion value), the orbital reduction parameter k, the isotropic Heisenberg magnetic exchange parameter J and an additional inter-cluster exchange parameter J'.

More recent work by Julve and *co*-workers is based on Lines' theory.[42,44,53,54] For dimetallic compounds in an axially distorted ligand field, the diagonalization of the spin-orbit Hamiltonian I.15 is proposed, however for a larger number of metal centres the above hybrid theory has been applied.

$$\hat{H} = \sum_{i=1}^{n} -J_i \hat{s}_i \hat{s}_{i+1} - \sum_{i=1}^{n} k_i \lambda_i \hat{l}_i \hat{s}_i + \sum_{i=1}^{i} \Delta_i \left[\hat{l}_{z,i}^2 - \frac{2}{3} \right] + \mu_B \vec{B} \sum_{i=1}^{n} \left(-k_i \hat{l}_i + g_e \hat{s}_i \right) \qquad \text{(I.15)}$$

The first section of Equation I.15 describes isotropic Heisenberg spin-spin exchange interactions between the cobalt(II) spins $s = {}^3/_2$ and the second term accounts for spin-orbit coupling. An axial distortion is introduced in the third term with Δ being the energy difference between the ^{4}A and ^{4}E term, arising from an axial distortion in the ^{4}T ground term. Finally the last term calculates the Zeeman splitting for both spin and orbital components. Fitting variables are the magnetic exchange coupling parameter J, the spin-orbit coupling constant λ with the orbital reduction factor k, and the axial spitting parameter Δ.

A similar approach has also been followed by Sakiyama *et al.*[55-57] Again an axially distorted ligand field with the above Hamiltonian terms is considered to simulate high temperature magnetic properties. Magnetic exchange interactions are introduced between effective spins "s" = $^1/_2$. Fitting parameters are once again J, λ, k, and a variable $\nu = \Delta / k\lambda$. Furthermore, the authors report how the introduction of a tilt between the single ion axial distortion axes, has allowed for an increase of χT at low temperature to be modelled, despite overall antiferromagnetic exchange interactions.[58] However, introduction of such further anisotropy *via* two torsion angles also increases the number of free variables from four to six for a fitting procedure to the powder susceptibility.

Ostrovsky, Brown and *co*-workers have simulated a number of cobalt(II) dimetallics based on the spin-Hamiltonian I.16 with $s = {}^3/_2$.[39,40,46]

$$\hat{H} = -2J_i \hat{s}_1 \hat{s}_2 + \sum_{i=1}^{2} \hat{s}_i \mathbf{D} \hat{s}_i + \sum_{i=1}^{2} \mu_B \vec{B} \mathbf{g} \hat{s}_i \qquad \text{(I.16)}$$

The low symmetry crystal field is assumed to be strong enough to allow neglecting of the orbital contribution to the magnetic exchange interaction. The splitting of the ground term in zero-field is due to distortion, and spin-orbit coupling is incorporated in the "zero-field splitting" tensor **D** and the influence of the orbital angular momentum into the Zeeman splitting *via* the local **g**-tensors. Variables in the calculation are J, D (values of 30 – 46 cm^{-1} are reported), $g_{||}$ and $g_{\perp}$. In more recent work, the authors follow an approach similar to Julve *et al.* with a Hamiltonian comparable to I.15.[45]

Probably the largest number of exchange coupled cobalt(II) systems have been reported and modelled by the groups of Coronado and Tsukerblat. The authors have proposed different approaches varying from "pseudo spin" $^1/_2$ models to more general treatments. The "pseudo spin" Hamiltonian is given in Equation I.17[59] and has been applied to many exchange coupled cobalt(II) clusters even without the second order term.[60-65] For larger clusters more than one exchange pathway has been considered.

$$\hat{H} = \sum_{\alpha=X,Y,Z} \left[-2 J_\alpha \hat{s}_{\alpha,1} \hat{s}_{\alpha,2} + g_\alpha \mu_B \left(\hat{s}_{\alpha,1} + \hat{s}_{\alpha,2} \right) \vec{B}_\alpha - \Lambda_\alpha \mu_B^2 \vec{B}_\alpha^2 \right] \qquad \text{(I.17)}$$

In a series of reports the authors have derived a model, in which irreducible tensor operators are used to add low-symmetry crystal field terms, Coulomb interaction, spin-orbit coupling and Zeeman interaction within a unified computational scheme to the effective exchange Hamiltonian.[66-69] These authors include spin-orbit coupling in the simulation of exchange interactions, in contrast to the Lines theory, where exchange interactions are treated isotropically.

Recently Chibotaru *et al.* have proposed a new application of the principle suggested in the Lines model.[43,70] *Ab-inito* calculations of the single ion ligand field provide the spin-orbit multiplets of each cobalt(II) ion, and hence account for anisotropy. Exchange interactions have been taken into account within the Lines model. Compared to all models described so far, this is the first example, where the isotropic exchange parameter(s) is (are) the *only* fitting parameter(s) implemented in the calculation. Unfortunately, so far the theoretical calculations have only been compared to experimental magnetic data observed on powder samples.

In the last two examples single crystal magnetic properties have been analysed by two very different approaches.

Waldmann *et al.* have performed single crystal magnetic measurements on the cobalt(II) [2 x 2] grid compound $[Co_4L_4](PF_6)_8$ (L = bis(bipyridyl)-pyrimidine derivative), which shows metamagnetic-like behaviour.[51] In a first step, the single ion properties have been determined on the monomer in a comparable ligand field, using a ligand field Hamiltonian, which includes spin-orbit coupling. In the following cobalt(II) is treated as an $s = {}^3/_2$ system with a large negative D describing the splitting between the Kramers doublets. At low temperature exchange interactions are then treated as a perturbation on the single ion wavefunctions, justified by a splitting in zero-field $|D| >> k_BT$ using an effective Ising Hamiltonian for "s" = ${}^1/_2$ ions. The authors simulate qualitatively the experimental single crystal anisotropy and to a high accuracy the level crossings observed in the field dependent magnetisation curve.

A semi-empirical approach has been followed by Gerloch *et al.* in the late 1970s.[52,71,72] In a first step the single ion properties are determined, this time based on the angular overlap model (see Section I.1.4). To introduce the influence of the orbital angular momentum into the magnetic exchange interactions, the authors define exchange parameters based on distinct orbital pairs. For five *d*-orbitals this leads theoretically to fifteen independent exchange parameters per cobalt(II) centre. Constraints are introduced by close inspection of the molecular geometry, allowing for "exchange active" orbitals to be determined. By restricting exchange to the contribution from these orbitals, magnetic exchange is no longer isotropic, but depends greatly on the orbital contribution to those particular wavefunctions. The model has been applied to a single crystal study of the strongly antiferromagnetically coupled cobalt(II) dimetallic $[Co_2(O_2CC_6H_5)_4(L)_2]$ (L = 4-methylquinoline) in triclinic crystal symmetry, where molecular magnetic contributions can be derived directly from the crystal response (Section I.4.4). Overall the magnetic anisotropy is reproduced reasonably well over a wide temperature range, with three "exchange active" orbital pairs. However, a complete quantitative reproduction has not been achieved. Interestingly the mean (or powder) susceptibility is reproduced remarkably well by the model calculations, deviations are only observed in the principal magnetic directions. This emphasises again the need for single crystal data against which to test anisotropic models. A successful fit of the powder susceptibility with

anisotropic parameters does *not* necessarily mean that the real anisotropy in the system is reproduced.

I.3 Heterometallic antiferromagnetically coupled molecular rings

Heterometallic antiferromagnetically coupled molecular ring structures of the composition $[R_2NH_2][M(III)_7M'(II)F_8(O_2CR')_{16}]$ (generally abbreviated to M_7M') were first reported by Winpenny *et al.* in 2003.[73] Synthetic access to numerous derivatives, by changing both the trivalent as well as the bivalent metal, organic groups on the secondary amine and the carboxylic acids, has lead to a huge family of compounds mainly based on chromium(III).[74,75] Studies on "open" or "horseshoe"-shaped derivatives[76-78] have allowed insight into the mechanism of the ring formation and have provided understanding for controlled synthesis.

Depending on the bivalent metal in the heterometallic chromium rings, different molecular ground states are achieved through antiferromagnetic coupling, which have been studied towards different potential applications. Cr_7Cd for example exhibits a molecular ground state of $S_{eff} = {}^3/_2$ and has been studied for applications in magnetic refrigeration.[79] Perhaps most interesting are derivatives of Cr_7Ni with a ground state of $S_{eff} = {}^1/_2$. Large spin clusters with an overall ground state of ${}^1/_2$ have been proposed for applications in quantum computing, allowing a two quantum gate to be achieved.[80-83] Intense research has been devoted to three major challenges, namely addressing molecules, and hence attachment of molecular rings to surfaces,[84] decoherence times,[85] and the linking of heterometallic rings to induce controlled communication between two molecular "qubit"-units.[86-88]

Not only Cr_7Ni has been intensely studied in the past. The family of Cr_7M' rings with M' being cadmium(II), zinc(II), nickel(II), manganese(II), iron(II) and cobalt(II) provides a system where tuning of the magnetic properties *via* different spin ground and excited states is possible within a constant geometric and chemical environment. This makes Cr_7M' rings excellent candidates for model studies on unidimensional exchange coupled systems, as well as for the study of interesting quantum phenomena. Aside from cobalt(II)-containing heterometallic rings, all systems can be

treated in a "spin-only" fashion, and extensive magnetic and spectroscopic studies have provided detailed information and understanding of the physical properties associated with spin-only molecular Cr_7M' rings.[73,78,89-94]

In this Ph.D. Thesis, the focus lies on magnetic properties arising from systems that exhibit an unquenched orbital angular momentum, and investigations on antiferromagnetically coupled rings have been extended to cobalt(II)-containing heterometallic rings, in direct comparison to the more readily analyzed spin-only nickel analogues.

I.4 Measurement techniques

The quantitative description of the physical backgrounds regarding the different measurements techniques reported in this Ph.D. Thesis can be found in numerous textbooks (for selected references see below), and here only a very brief introduction into the principle concepts is given.

I.4.1. Magnetic measurements

The most sensitive commercially available technique to measure magnetic properties today is a Superconducting Quantum Interference Device (SQUID) magnetometer.[27,95] SQUID magnetometers are equipped with a superconducting magnet providing magnetic fields up to several Tesla, a superconducting detection coil, which is coupled inductively to the sample, and a SQUID device connected to the detection coil. The superconducting magnet produces a longitudinal uniform magnetic field, which leads to a magnetization of the sample. A superconducting detection coil (or pick-up) coil is located within the uniform region of the magnetic field. The sample is moved through the pick-up coils, thus the magnetic moment of the sample induces a current in the pick-up coil system. The SQUID device functions as an extremely sensitive current-to-volt-converter, and a change of the magnetic flux in the pick-up coils produces a variation in the SQUID output voltage proportional to the magnetic moment of the sample. In direct current (DC) mode the

magnetic moment can be detected as a function of temperature, DC magnetic field and time. In alternating current (AC) mode the real and imaginary components of the susceptibility are detected as a function of frequency, temperature, AC magnetic field amplitude and DC magnetic field value. This mode is particularly useful to detect a weak magnetic memory effect.

A torque magnetometer allows for the analysis of the magnetic anisotropy. In this research a cantilever torque was used, which consists of a silicon device with a thin lever suspended by two arms that is free to twist in the direction of the projection of the torque moment.[96,97] A crystal is mounted onto the cantilever device and placed into a superconducting magnet that produces a uniform longitudinal magnetic field. A magnetic moment is induced into the sample by the magnetic field, and the crystal experiences a torque moment $\tau = M \times H$. Torque magnetometry allows for the measurement of the projection τ_y, which is related to the difference between the magnetic susceptibilities χ_x and χ_y. 360° rotation of the crystal leads to a sinusoidal angular dependence, describing amplitude and sign of the magnetic anisotropy.

I.4.2. Electron paramagnetic resonance spectroscopy

Electron paramagnetic resonance (EPR) spectroscopy[3] is a powerful technique to gain detailed insight into the electronic structure of transition metal ions or clusters. In continuous wave EPR spectroscopy, the sample is irradiated with a continuous supply of microwaves in a limited frequency range, while the magnetic field $\vec{B}_0$ (typically generated by an electromagnet or superconducting magnet) is swept to induce Zeeman splitting in the energy manifold of the studied system. Once the Zeeman splitting matches the microwave energy, resonance occurs, and a transition is observed. In addition, a small oscillating magnetic field $\vec{B}_1$ is superimposed on the cavity *via* modulation coils. Amongst other effects, this modulation of the cavity signal influences the signal amplitude and allows for different harmonics of the Zeeman modulation to be recorded. Conventionally the first harmonic, which approximates to the first derivative of the absorption spectrum, is recorded in EPR spectroscopy.

Most commonly EPR spectra are recorded in perpendicular mode, where the excitation field $\vec{B}_1$ is oriented perpendicular to $\vec{B}_0$. For this set-up, the EPR selection rules can be derived from the transition probabilities to $\Delta S = 0$, $\Delta M_S = \pm 1$.

EPR spectroscopy is an additive technique and consequently detects the *sum* over all occurring signals. In the case of anisotropic systems this leads to spectral responses, which, to a certain extent, allow for anisotropy parameters to be determined even on powder samples. In Section I.4.4 single crystal experiments are introduced. On a simple, well studied example of an axial spin-triplet, the relation between different orientations (studied on a single crystal) and the powder spectrum is illustrated.

In work reported in this Ph.D. Thesis, the advantage of an additive technique is also used to identify different magnetic isomers within compounds of antiferromagnetically coupled heterometallic ring systems.

I.4.3. Inelastic neutron scattering

To measure the inelastic neutron scattering (INS) of a compound, a monochromatic neutron beam is targeted to the sample, leading to scattering and absorption of the neutrons by the nuclei, and scattering through magnetic interactions between the intrinsic magnetic moment of the neutrons and the magnetic field generated by the unpaired electrons in the sample.[98-102]

For this Ph.D. Thesis a time-of-flight neutron scattering spectrometer was used.[103] A polychromatic neutron beam, generated in a nuclear reactor, is guided through several choppers, leading to a highly monochromatic beam with defined initial energy E_i and defined wave-vector $\vec{k}_i$. After the sample target, scattered neutrons are collected in an array of time-resolved detectors. The final neutron energy E_f (characterised by energy loss or gain from transitions within the sample) can be determined from the time of arrival, while the final wave-vector $\vec{k}_f$ is deduced from the scattering angle. The scattering vector $\vec{Q}$ is defined by $\vec{k}_i - \vec{k}_f$ and the Q-dependence of the transition intensity allows for detailed analysis of the magnetic properties related to the excitation.

One important characteristic of INS is the possibility of measuring at zero- and applied magnetic fields. In contrast to other magnetic measurement techniques, INS

allows for the zero-field energy manifold to be detected directly, whilst still providing information about the magnetic character of the associated wavefunctions. Furthermore, INS exhibits a second complementary aspect compared to EPR spectroscopy. Transition probabilities lead to a different set of selection rules with $\Delta S = 0, \pm 1$ and $\Delta M_S = 0, \pm 1$, hence transitions that are formally forbidden in EPR spectroscopy (*e.g.* inter-multiplet transitions) become fully allowed in INS.

I.4.4. Single crystal experiments

In Section I.1 the electronic structure of cobalt(II) and its large magnetic anisotropy has been discussed. Anisotropic effects can only be fully investigated by studying the magnetic properties on single crystals.

In isotropic systems the magnetisation $\vec{M}$ of a compound and the applied magnetic field $\vec{H}$ are linearly proportional, and the magnetic susceptibility χ is a scalar (Equation I.18).

$$\vec{M} = \chi \vec{H} \tag{I.18}$$

For anisotropic systems, the field direction and the magnetisation are only co-parallel in special orientations. χ is no longer a scalar multiplier, but a second rank tensor that relates the two vectors, which do not necessarily point in the same direction and Equation I.18 changes to Equation I.19

$$\begin{pmatrix} M_1 \\ M_2 \\ M_3 \end{pmatrix} = \begin{bmatrix} \chi_{11} & \chi_{12} & \chi_{13} \\ \chi_{12} & \chi_{22} & \chi_{23} \\ \chi_{13} & \chi_{23} & \chi_{33} \end{bmatrix} \begin{pmatrix} H_1 \\ H_2 \\ H_3 \end{pmatrix} \quad \text{and} \quad \vec{M}_i = \sum_j^3 \chi_{ij} \vec{H}_j \tag{I.19}$$

The thermodynamic reversibility of susceptibility and magnetic polarisation causes the tensor to be symmetric and hence three mutually perpendicular directions exist in space, parallel to which an applied field induces a real co-parallel moment. If these axes are taken to be the reference frame, only the diagonal (principal) values χ_1, χ_2 and χ_3 remain non-zero. Diagonalization of the tensor in I.19 yields Expression I.20.

Neumann's principle proposes that "*the symmetry elements of any physical property of a crystal must include the symmetry elements of the point group of the crystal.*"[27]

$$\begin{bmatrix} \chi_1 & 0 & 0 \\ 0 & \chi_2 & 0 \\ 0 & 0 & \chi_3 \end{bmatrix} \quad \text{with} \quad \begin{aligned} M_1 &= \chi_1 H_1 \\ M_2 &= \chi_2 H_2 \\ M_3 &= \chi_3 H_3 \end{aligned} \tag{I.20}$$

Table I.2 shows the different forms of the susceptibility tensor expressed in the crystal axes frame of different crystal systems.

crystal system	characteristic symmetry	number of independent tensor coefficients	susceptibility tensor
triclinic	P1 or P$\bar{1}$	6	$\begin{bmatrix} \chi_{11} & \chi_{21} & \chi_{31} \\ \chi_{21} & \chi_{22} & \chi_{32} \\ \chi_{31} & \chi_{32} & \chi_{33} \end{bmatrix}$
monoclinic	one 2-fold axis	4	$\begin{bmatrix} \chi_{11} & \chi_{12} & 0 \\ \chi_{12} & \chi_{22} & 0 \\ 0 & 0 & \chi_{33} \end{bmatrix}$
orthorhombic	three mutually orthogonal 2-fold axes	3	$\begin{bmatrix} \chi_a & 0 & 0 \\ 0 & \chi_b & 0 \\ 0 & 0 & \chi_c \end{bmatrix}$
uniaxial *trigonal* *tetragonal* *hexagonal*	one 3-fold axis one 4-fold axis one 6-fold axis	2	$\begin{bmatrix} \chi_\perp & 0 & 0 \\ 0 & \chi_\perp & 0 \\ 0 & 0 & \chi_\parallel \end{bmatrix}$
cubic (isotropic)	four 3-fold axes	1	$\begin{bmatrix} \chi & 0 & 0 \\ 0 & \chi & 0 \\ 0 & 0 & \chi \end{bmatrix}$

Table I.2: Relationship between the crystal system and the susceptibility tensor.[27]

In a triclinic system, no direction is made special by symmetry and the susceptibility tensor contains the maximum number of 6 different χ_{ij}. In a monoclinic system, the *b* axis is unique in symmetry, and one principal magnetic axis (χ_3 by conventions) runs parallel to the crystal axis *b*. The next highest crystal symmetry is orthorhombic, where the three mutually perpendicular symmetry axes of the susceptibility coincide with the three perpendicular crystal axes to $\chi_1 = \chi_a$, $\chi_2 = \chi_b$, $\chi_3 = \chi_c$. In uniaxial (trigonal, hexagonal and tetragonal) systems, a unique direction is defined by the three-, four-, or six-fold rotational symmetry, respectively. By convention, the susceptibility parallel to the rotation axis *c* is labelled $\chi_\parallel = \chi_c$, while the susceptibility

in the *ab*-plane is isotropic and defined as $\chi_{\perp} = \chi_{ab}$. Finally, in the cubic crystal system all three Cartesian axes are equivalent and the isotropic susceptibility tensor reduces to a scalar.

For isolated molecules with no inter-molecular interactions the total crystal susceptibility represents the sum of the molecular properties, each of which refers to all molecules with the same orientation (normalized to 1 mole). A centrosymmetric molecular susceptibility tensor with three principal axes can be defined.

Powder and single crystal susceptibility are linked by Equation I.21. Comparison between the principal average and the powder experiment provides control over the quality of the experiment.

$$\chi_{\text{powder}} = \frac{(\chi_1 + \chi_2 + \chi_3)}{3} \tag{I.21}$$

Similar constraints can be derived for the **g**-matrix in single crystal EPR experiments. In isotropic systems the matrix reduces to a scalar *g*-value, for all other systems principal *g*-values can be assigned to the three principal directions of the **g**-matrix after diagonalization. Table I.3 shows the different symmetry groups, the relation of the corresponding principal *g*-values and the orientation of the **g**-matrix with respect to the crystal unit cell axes.[3]

symmetry (crystal system)	principal *g*-values	relation of principal and crystal axes	Number of magnetically inequivalent sites						
			$\vec{B}$ in plane			$\vec{B}$ in plane			$\vec{B}$ general
			a	*b*	*c*	*ab*	*bc*	*ac*	
triclinic	$g_{xx} \neq g_{yy} \neq g_{zz}$	no constraints	1	1	1	1	1	1	1
monoclinic	$g_{xx} \neq g_{yy} \neq g_{zz}$	one principal axis ‖ *b*	1	1	1	2	1	2	2
rhombic (orthorhombic)	$g_{xx} \neq g_{yy} \neq g_{zz}$	all principal axes ‖ *abc*	1	1	1	2	2	2	4
axial (trigonal, tetragonal, hexagonal)	$g_{xx} = g_{yy} = g_{\perp}$ $g_{zz} = g_{\parallel}$	parallel component ‖ *c*, perpendicular component in the *ac*-plane	1 2 3	1 2 3	1 1 1	3 2 2	3 4 6	3 4 6	3 4 6
isotropic (cubic)	$g_{xx} = g_{yy} = g_{zz} = g$	all principal axes ‖ *abc*	3	3	3	6	6	6	12

Table I.3: Relation of the **g**-matrix to the crystal symmetry.[3]

Furthermore, Table I.3 shows the number of magnetically inequivalent sites (molecules) for the different crystal systems in special positions (*e.g.* along the crystallographic axes *abc* or in specific crystal planes) and in a general orientation. The higher the symmetry in the system, often the easier is the performance of single crystal experiments, because the crystal can readily be mounted in specific directions with respect to the magnetic field. Unfortunately the increase in symmetry also increases the number of magnetically inequivalent sites in the crystal. While for EPR, an averaging technique, an addition of the different signals is observed, this increase is problematic for single crystal SQUID experiments, which only detect the average of the different sites. In most cases the relationship between the principal magnetic axes and the molecular geometry is unknown, and the molecular susceptibility cannot necessarily be back-calculated from the principal crystal values. Rather, experimental values have to be fitted against model systems, which allows for the principal molecular susceptibilities to be determined. Only in some special cases (for example triclinic systems), can the molecular susceptibility be directly observed from the crystal response.

In Chapter III single crystal EPR transitions will be related to multi-frequency powder spectra. In the following, a simple, well studied example of a spin-triplet illustrates the relation between powder and single crystal EPR spectra, and how spin-Hamiltonian parameters, related to the anisotropy of the system, can be determined, even from powder spectra.

Figure I.4 shows the Zeeman splitting for an axial triplet with an isotropic g-value and a zero-field splitting D in z and xy direction. On the right, a "road-map" of the transitions occurring during a 90° rotation moving from z to xy is shown. In a powder spectrum, all possible orientations are observed at the same time. Cancellation effects of the derivative intensities lead to the depicted powder spectrum, where only the four extrema along the principal magnetic axes are observed as transitions. The distance between the signals can be related to the zero-field splitting, however, equations in Figure I.4 only account exactly for isotropic g-values.

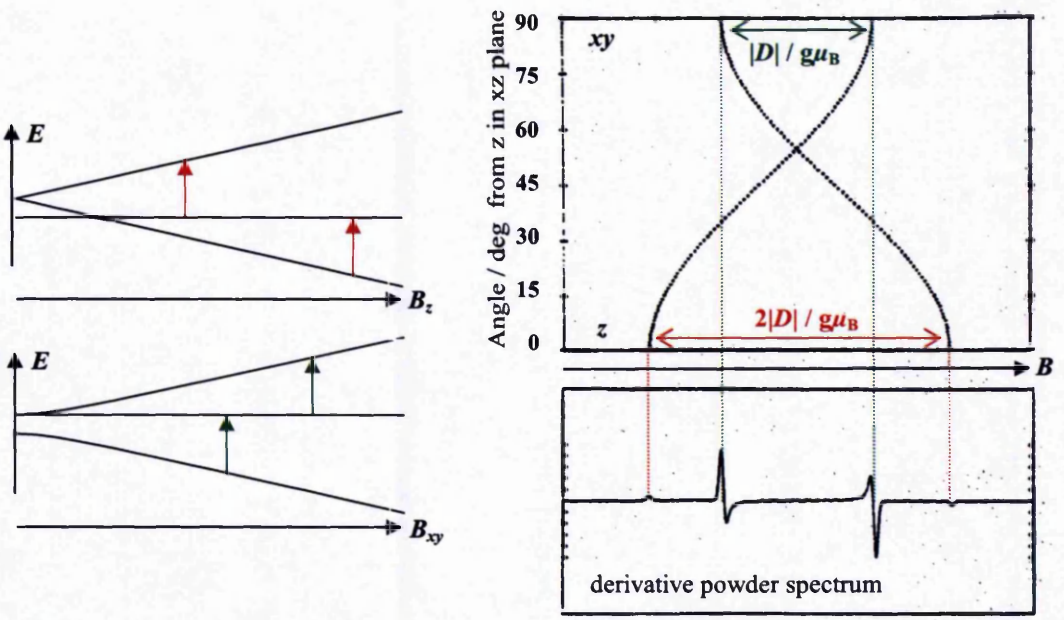

Figure I.4: Left: Zeeman splitting of an axial triplet with isotropic *g* and zero-field splitting *D* along *z* and *xy*. Right: "Road-map" of single crystal transitions moving from *z* to *xy* and corresponding powder spectrum (picture copied and modified from reference[3])

I.5 Project proposal

Intense studies on the magnetic properties of cobalt(II) have been generally avoided in the past, due to its complex electronic structure compared to other transition metals.

Different theoretical models addressing the problem of exchange coupling between octahedral cobalt(II) ions have been introduced in Section I.1.2, but in most cases theoretical calculations have only been compared to the temperature dependent susceptibility of powder experiments, which exhibits very limited sensitivity to the magnetic anisotropy.

The aim of this research project was the investigation of magnetic and electronic properties of exchange coupled octahedral cobalt(II) coordination compounds with a combination of various techniques such as SQUID magnetometry, EPR spectroscopy and INS on both powder and single crystal samples. Availability of such complementary experimental data allows for a critical comparison of calculated properties, in particular the calculated anisotropy, to experimental observations;

hence provides a major contribution towards a better understanding of magnetic properties in cobalt(II) coordination compounds.

The smallest exchange coupled units are dimetallic complexes, which, due to their relative simplicity, provide a useful starting point for detailed investigations into the understanding of exchange coupling between metal ions with an unquenched orbital angular momentum.

Investigations of spin-orbit effects were also to be extended to more complex systems. Synthesis and investigations into heterometallic molecular ring systems have a great tradition in the "Molecular Nanomagnetism Group" at The University of Manchester, but so far analyses have concentrated on spin-only systems. The aim of this project was to extend such investigations to heterometallic chromium-cobalt rings with one or more heteroatoms. The study of the isostructural spin-only nickel analogues can provide a helpful step, prior to the investigation of the theoretically more challenging cobalt(II) compounds.

Chapter II

Hexakis(pyridine-N-oxide)cobalt(II) dinitrate - a test compound for magnetic modelling

In order to simulate exchange coupling between two or more metal ions, it is important to have a good understanding of the single ion itself. Octahedral cobalt(II) ions are known to have a high single ion anisotropy arising from spin-orbit coupling within the ground $^4T_{1g}$ term.[25] Below 30 K the magnetic properties of monometallic octahedral cobalt(II) compounds are often interpreted as effective "*s*" = $^1/_2$ systems, taking only the lowest Kramers doublet into account (See Section I.1) However, this model is very limited, and restricted to very low temperatures, because effects such as for example mixing from higher energy levels into the ground state are neglected. A more valid approach is the calculation of the energy levels produced by ligand field interactions with the metal *d*-orbitals and spin-orbit coupling to understand the magnetic properties of cobalt(II) ions. Mackey *et al.* have successfully applied the angular overlap model (AOM) to simulate the temperature dependent single crystal magnetic susceptibility of the monometallic hexakis(pyridine-N-oxide)cobalt(II) dinitrate, $[Co(C_5H_5NO)_6](NO_3)_2$ (**1**).[104] Their detailed study provides a useful starting point to test the software packages used for AOM calculations against single crystal magnetic properties measured on our own SQUID magnetometer. Measurements on **1** have been extended to EPR spectroscopy, to probe the application of the derived AOM parameters to the calculation of EPR spectra.

II.1 Brief synthetic and structural description of hexakis-(pyridine-N-oxide)cobalt(II) dinitrate

Hexakis(pyridine-N-oxide)cobalt(II) dinitrate (**1**) is readily synthesised from a solution of cobalt(II) nitrate and pyridine-N-oxide in methanol, giving large red diamond shaped crystals upon cooling or slow evaporation.[105]

The compound crystallizes in the hexagonal space group *R3* (a = 12.4142(21) Å, c = 18.0012(2) Å, V = 2402.53 Å^3, Z = 3) with a molecular asymmetric unit of only one cobalt-pyridine-N-oxide fragment. O'Connor *et al.* have published the identical structure in the rhombohedral space group $R\bar{3}$ (a = 9.487 Å, α = 83.35, V = 837.86 Å^3, Z = 1),[106] which is easily transformed into the above hexagonal space group; there are two possibilities to index crystals in the rhombohedral space groups, either as a primitive squashed cube with equal sides, identical angles and three fold symmetry down the body diagonal, or as a hexagonal cell with three times the volume and a c-axis equivalent to the body diagonal of the primitive cell.

The molecule is highly symmetric approaching a perfect octahedral ligand arrangement with only a very small trigonal distortion. All molecules are aligned parallel within the crystal unit cell as shown in Figure II.1 and hence magnetically equivalent.

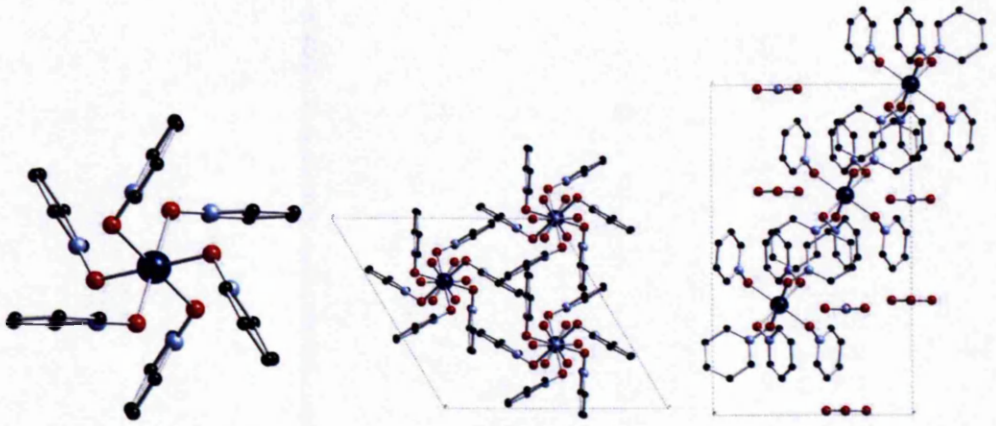

Figure II.1: Left: $[Co(C_5H_5NO)_6]^{2+}$ cation, middle/right: crystal packing of $[Co(C_5H_5NO)_6](NO_3)_2$ (**1**) down c and a, respectively; hydrogen atoms are omitted for clarity, *R3*, a = 12.4142(21) Å, c = 18.0012(2) Å, V = 2402.53 Å^3, Z = 3

II.2 Magnetic and spectroscopic properties of hexakis-(pyridine-N-oxide)cobalt(II) dinitrate

II.2.1. Powder and single crystal magnetic properties of 1

The temperature dependent powder susceptibility of **1** in a field of 0.1 and 1 T is shown in Figure II.2. Consistent with Carling *et al.* who have reported the magnetic properties of $[Co(C_5H_5NO)_6](X)_2$ (X = BF_4^-, ClO_4^-, NO_3^-),[106,107] a paramagnetic behaviour with a very weak antiferromagnetic intermolecular ordering at temperatures below 2 K has been observed. The room temperature susceptibility of χT = 3.38 cm^3 K mol^{-1} agrees well with the expectations of 3.375 cm^3 K mol^{-1} for a single cobalt(II) ion composed of a spin angular momentum s = $^3/_2$ and an orbital angular momentum of l = 3 (Equation II.1).[1]

$$300\ \text{K:}\ \chi T = n\frac{l(l+1)+g^2 s(s+1)}{8}\ \text{with } n = \text{number of spin centres } s \qquad \text{(II.1)}$$

$$\text{low temperature:}\ \chi T = \frac{"g"^2\ "S_{eff}"("S_{eff}"+1)}{8}\ \text{with } S_{eff} = \text{total spin ground state} \qquad \text{(II.2)}$$

A decrease in χT upon lowering the temperature and for an effective ground angular momentum of $^1/_2$ arises from spin-orbit coupling within the ground $^4T_{1g}$ term. χT can be estimated as 1.5 cm^3 K mol^{-1} for an effective moment or pseudo spin of "s" = $^1/_2$ and an effective "g-value" "g" = 4 from Equation II.2.[1, 23]

Experimentally χT is 1.33 cm^3 K mol^{-1} at 2 K, and the value is slightly below the expectation value for an effective "s" = $^1/_2$ and confirms the weak antiferromagnetic ordering of the molecules. A clear saturation of the magnetisation has been observed at 2 K indicating a well separated magnetic ground state at low temperatures (Figure II.2). The value of 2.33 $N\mu_B$ is slightly higher than expected for an approximate interpretation with an effective magnetic moment "s" = $^1/_2$ and an effective "g-value" "g" = 4.

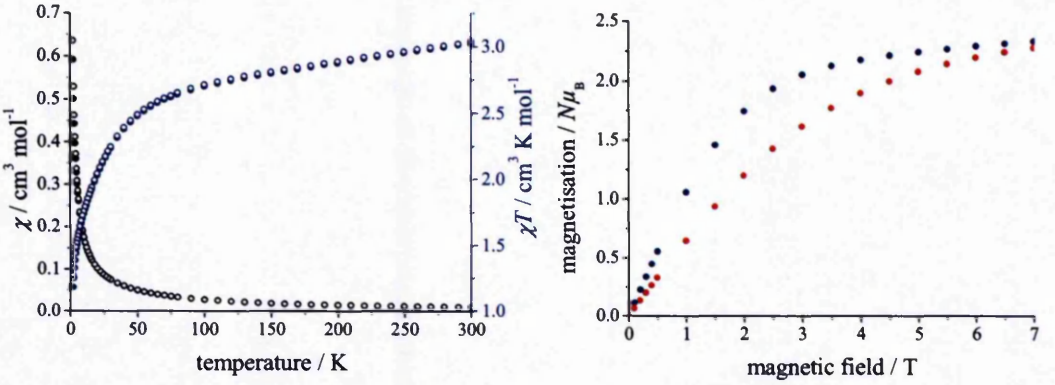

Figure II.2: Magnetic properties of **1** measured on a powder sample fixed in eicosane. Left: temperature dependent susceptibility at 1 T (dot) and 0.1 T (ring), right: field dependent magnetisation at 2 K (blue) and 4 K (red).

To confirm the magnetic anisotropy of the cobalt(II) ion reported by Mackey *et al.*,[104] magnetic measurements have been performed on single crystals. In uniaxial crystal systems (here *R3*), magnetic anisotropy is constrained by symmetry and can be fully described by only two independent diagonal elements $\chi_c = \chi_{\parallel}$ and $\chi_{ab} = \chi_{\perp}$ in the susceptibility tensor $\boldsymbol{\chi}$. Crystallographically the unit cell axes can be determined with respect to the crystal morphology, allowing the measurement of magnetic properties along the principal magnetic axis $\chi_{\parallel}$ and $\chi_{\perp}$. Details on the indexing of the crystal faces and the experimental set-up are described in Chapter VI.3.

Figure II.3 shows the single crystal temperature dependent susceptibility and field dependent magnetisation of **1** along the principal magnetic axis. As expected for an octahedral cobalt(II) ion in *R3* symmetry, a strong axial anisotropy has been observed.

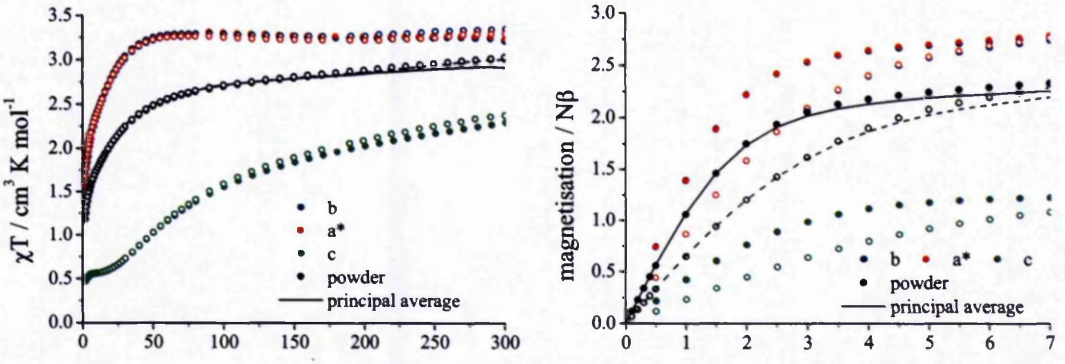

Figure II.3: Single crystal magnetic properties of **1**. Left: temperature dependent susceptibility at 1 T (dot) and 0.1 T (ring), right: field dependent magnetisation at 2 (dot) and 4 K (ring).

$\chi_\perp$ has been measured in two independent set-ups (b, a^*) and the excellent agreement allows high confidence in the absolute values for single crystal susceptibility and magnetisation data. Powder magnetic measurements represent an average over all possible orientations and in this case a weighted average of $\chi_{powder} = 2\,\chi_\perp + \chi_\parallel$ is expected. Very good agreement between the powder experiment and the calculated average of the principal magnetic properties has been observed.

II.2.2. Electron paramagnetic resonance spectroscopy of 1

A second method to probe the single ion anisotropy in a monometallic cobalt(II) compound is electron paramagnetic resonance (EPR) spectroscopy. In contrast to the averaging of magnetic properties found from SQUID magnetometry, EPR spectroscopy detects the *sum* of all molecular orientations and therefore allows the detection of anisotropy even on powder or frozen solution samples.

Makinen *et al.* report EPR spectroscopy on a frozen solution sample of aqueous $[Co(C_5H_5NO)_6](ClO_4)_2$ (**2**) at 9.4 GHz and 5 K (Figure II.4).[108] The cation of **2** is identical with the cation of **1** and a very similar, if not identical, frozen solution spectrum is expected for the two compounds. Even at this low frequency the anisotropy is visible and the two signals can be assigned to the parallel (~ 3000 G, ("g" ~ 2.2) and perpendicular (~ 1500 G, "g" ~ 4.5) component.

For any model that parameterizes spectral properties it is useful to interpret data from at least two different frequencies to increase the confidence in derived parameters. Therefore, a powder spectrum of **1** at 5 K has been collected at Q-band frequency (34 GHz) for comparison; the spectrum is shown in Figure II.4. Again two broad transitions have been observed: A strong transition from the perpendicular component at ~ 5300 G ("g" ~ 4.6) and a broad weak shoulder at ~ 9000 G ("g" ~ 2.7) from the parallel component. Both frequencies show a similar effective "g-value" of the perpendicular component, but some frequency dependence is observed in the signal of the parallel component, which resonates at a higher "g-value" at Q-band frequency.

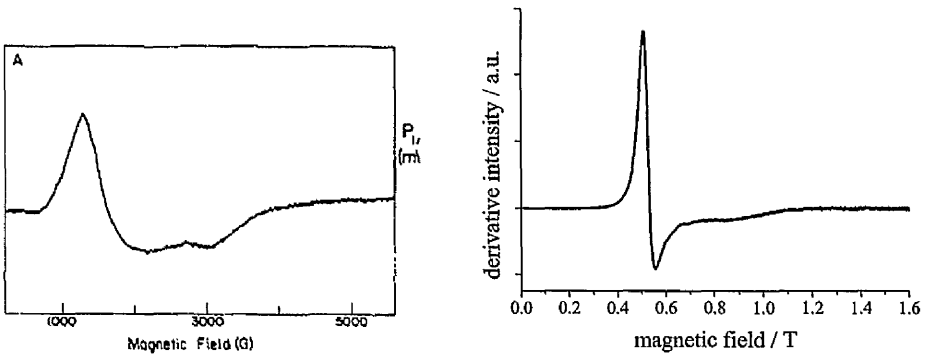

Figure II.4: Left: 5 K aqueous frozen solution X-band EPR spectrum of **2** reported by Makinen *et al.*,[108] right: 5 K Q-band EPR spectrum on a powder sample of **1** fixed in eicosane.

II.3 Modelling of the physical properties of hexakis(pyridine-N-oxide)cobalt(II) dinitrate

In a monometallic compound the strong magnetic anisotropy can only originate from an anisotropic Zeeman-splitting of the energy levels in different directions of the magnetic field. In spin-only systems, such behaviour is introduced by second order spin-orbit coupling and/or ligand field distortions and is conventionally parameterized with an anisotropic **g**-matrix allowing for small deviations from the isotropic free electron *g*-value of 2.0023 and, for $s > {}^1/_2$, a zero-field splitting **D**-matrix. First order spin-orbit coupling has a much stronger effect on the Zeeman splitting, usually resulting in larger splitting and stronger anisotropy. For spin-orbit eigenfunctions, the development in a magnetic field can no longer be described with an electron *g*-value, but the orbital angular momentum has to be included into the Zeeman operator.

Subsequently two different theoretical approaches are discussed: in the first and simpler model the lowest Kramers doublet arising from spin-orbit coupling is treated as an effective or pseudo "s" = $^1/_2$. In the second approach, the angular overlap model (AOM) is used to parameterize the ligand field and allow a complete calculation of the spin-orbit coupling effect on the Zeeman splitting.

II.3.1. Effective model

At low temperatures, cobalt(II) ions are often interpreted as effective doublets with "s" = $^1/_2$. It is very important to keep in mind that those effective eigenfunctions are not real spin-functions, but functions of the total angular momentum $^1/_2$ arising from spin-orbit coupling between the orbital angular momentum of 1 and the spin $s = {}^3/_2$ within the $^4T_{1g}$ ground term. In a simple effective model, only the effective "**g**-matrix", which in principle is no more than a parameterization of the Zeeman effect, can account for the influence of the orbital angular momentum. Effective "*g*-values" used to describe the Zeeman splitting of spin-orbit states treated as pseudo spins are therefore *not* electron *g*-values, but simply values associated with the slope of the Zeeman splitting in the applied magnetic field. An effective treatment of the lowest Kramers doublet may be the simplest model to describe the magnetic properties of cobalt(II) ions, however the physical meaningfulness of the treatment of spin-orbit functions as effective spins may be questionable. Furthermore, the model is very limited. The energy separation from the ground to the first excited Kramers doublet is usually < 300 cm^{-1} and can be as small as ~ 50 cm^{-1} depending on the ligand field. Therefore, the model can only be applied if the temperature is small enough to ensure a good isolation of the ground Kramers doublet, *e.g.* low temperature spectroscopy or field dependent magnetisation. Secondly, mixing from excited states such as the $^4T_{1g}$(P) term into the ground $^4T_{1g}$(F) term is totally neglected in the effective model, even though this admixture can lead to a non-linearity in the Zeeman splitting and significantly influence the magnetic properties of the cobalt(II) ions. Nevertheless, often a good qualitative understanding can be drawn from the effective model. Figures II.5 and II.6 show some calculations of the field dependent magnetisation and the Q-band EPR spectrum based on the conventional spin-only Zeeman operator II.3.[3]

$$\hat{H}_{\text{Zeeman}} = \sum_i \mu_B \, \mathbf{g}_i \, \hat{s}_i \, \vec{B} \qquad \text{(II.3)}$$

Two sets of parameters have been used to gain a qualitative understanding of the field dependent magnetisation and the resulting calculations are shown in Figure II.5. With "g_{xx}" = "g_{yy}" = 5.58, "g_{zz}" = 2.50 the saturation of the magnetisation at

magnetic fields > 6 T is reproduced well, however only the calculated *z* magnetisation also fits the experimental data at lower magnetic fields. To reproduce the magnetic properties at magnetic fields < 2 T a different value for "g_{xx}" = "g_{yy}" is required.

The Q-band EPR spectrum of **1** has been recorded between 0 and 1.6 T and should consequently be simulated with the same parameters as the magnetisation < 2 T. For "g_{xx}" = "g_{yy}" = 4.68 it is indeed possible to simulate the contribution of the *xy*-component to both the EPR spectrum and the field dependent magnetisation. However, the *z*-component is not very well resolved in the EPR spectrum, but seems to require a higher effective "*g*-value" of ~ 2.75 (Figure II.6).

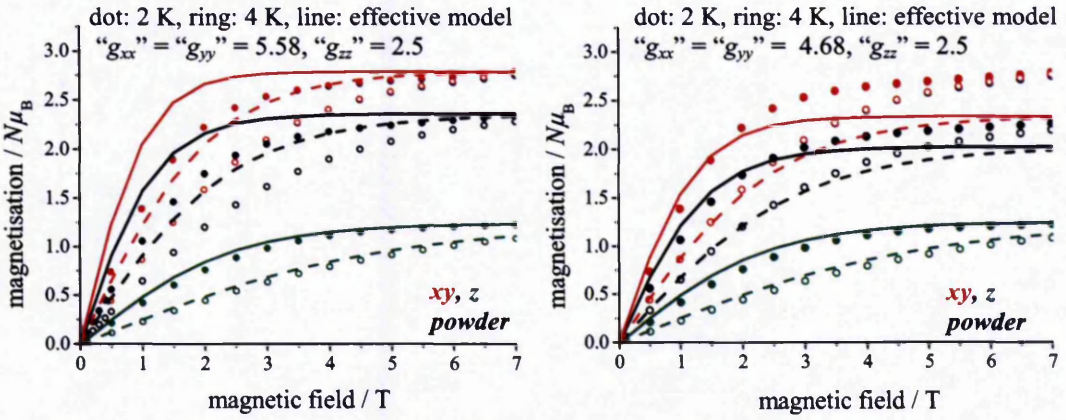

Figure II.5: Two different sets of parameters to calculate the field dependent magnetisation of **1**. Left: parameters are chosen to fit high field data, right: parameters chosen to fit low field data.

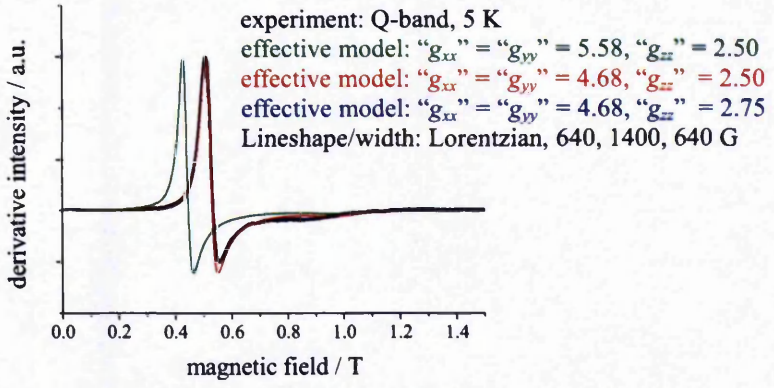

Figure II.6: Three different sets of parameters to calculate the EPR spectrum of **1**. Green and red: parameters from field dependent magnetisation, blue: best parameters to fit the EPR.

In summary these calculations show that even at low temperatures ($T \leq 5$ K) this simple effective model is not sufficient to fully describe the magnetic properties of the single ion cobalt(II) centre. The apparent field dependence of the effective "*g*-value" clearly indicates mixing from higher energy levels into the magnetic ground term, which leads to a non-linearity of the Zeeman splitting particularly in the *xy*-direction. Such behaviour can only be reproduced by a more general ligand field approach including the full *d*-orbital function basis set and spin-orbit coupling effects. Nevertheless, a good estimate of the anisotropic Zeeman splitting associated with different orientations is possible within the effective model and provides a first qualitative understanding of the system.

II.3.2. Angular overlap model

The angular overlap model (AOM) is based on an extended ligand field approach in which the metal-ligand bond interactions are parameterized and has been introduced in Section I.1.4. All calculations have been performed on a complete set of *d*-orbital basis functions; this accounts for both the influence of spin-orbit coupling as well as mixing from higher energy levels into the ground term (see also Section I.1.3). Two software packages (*AOMX*[109] and *LIGFIELD*[110]) and a self-written routine in *Mathematica*[111] have been used to calculate energetic, magnetic and spectroscopic properties of compound **1**. The AOM allows for the calculation of the 120 eigenvalues and eigenfunctions arising from the d^7 orbital configuration of cobalt(II). All magnetic properties can be calculated from the observed eigenvalues; the *LIGFIELD* software also implements the calculation of the resulting EPR spectrum.
Single crystal measurements have confirmed the single ion anisotropy for the $[Co(C_5H_5NO)_6]^{2+}$ cation reported by Mackey *et al.*[104] Only a minor deviation from the absolute reported values has been observed, which can be explained by experimental errors due to the use of different magnetic measurement techniques (here: SQUID, reported: Faraday and Krishnan critical-torque). A reproduction of the simulation with the parameters derived by the authors will give high confidence in the applied software packages and routines.

For a compound with a perfect O_h symmetry in the ligand positions the AOM parameters are related to the crystal field splitting Dq by Equation I.12.[104] Crystal field parameters can be obtained by optical techniques, such as UV-Vis spectroscopy or, often more precisely, magnetic circular dichroism (MCD) spectroscopy. Typically such electronic spectra are fitted against Tanabe Sugano diagrams,[22] which provide the crystal field splitting parameter $\Delta_O = 10\ Dq$, and the electronic repulsion Racah parameters B and C. Crystal field parameters should be fixed to experimental observations to reduce the number of fitting parameters in the AOM calculations. The trigonal component of the ligand field and the magnetic anisotropy are determined by the anisotropy in the π-bonding between the cobalt(II) ion and the oxygen atoms. Only the difference $\Delta e_\pi = e_{\pi x} - e_{\pi y}$ influences the trigonal field, which is completely independent of the individual values of e_σ, $e_{\pi x}$ and $e_{\pi y}$. The pyridine-N-oxide ligand provides two lone pairs on the oxygen atom, which can interact with the cobalt(II) ion. In the cobalt(II)-pyridine-N-oxide cation, the cobalt-oxygen-nitrogen angle is close to 120° (118.10°) and the geometry at the pyridine nitrogen is planar. Both geometries indicate an sp^2 hybridized oxygen with a partial conjugation into the pyridine ring. The orientation of the orbitals has been defined as π_x in conjugation with the pyridine ring and π_y perpendicular to the cobalt-oxygen-nitrogen plane. Details of the determination of the ligand field matrix are given in Section VI.4.1.

All crystal field parameters have been taken from Mackey *et al.* and kept constant: Dq = 890 cm^{-1}, Racah A = 0, Racah B = 780 cm^{-1}, Racah C = 3030 cm^{-1}. The spin-orbit coupling parameter ζ has been fixed as the conventionally excepted single ion value of 515 cm^{-1}[24] even though Mackey *et al.* report a value of 525 cm^{-1}. A slight reduction of the spin-orbit coupling can be induced by admixture of the ^{4}P state into the ground ^{4}F term and/or physical distortion of the magnetic-electron orbitals by partial covalent bonding with the ligands. Often this reductions is expressed by a reduction parameter $k \leq 1$ with $k = 1$ for no reduction of the spin-orbit coupling.[25] If k is fixed, the only remaining variable to influence the magnetic properties is Δe_π. All parameters are listed in Table II.1.

Calculations have been performed on a complete set of d-orbital basis functions for a d^7 orbital configuration in both zero-field and a magnetic field oriented along the principal magnetic axes of the molecule. Therefore the AOM ligand field matrix has been set up within the crystallographic and principal magnetic axes $XYZ \equiv abc^*$,

where $c^* = a \times b$ (for details see also Section VI.4.1). Table II.2 shows the lowest twelve out of 120 eigenvalues in zero magnetic field resulting from AOM calculations with parameter sets **A** - **E**.

parameter set	e_σ	Δe_π	ζ	Racah *A*	Racah *B*	Racah *C*	*k*
A	2967	0	515	0	780	3030	1
B[104]	2967	-666	525	0	780	3030	1
C	2967	-666	515	0	780	3030	1
D	2967	666	515	0	780	3030	1
E	2967	-670	515	0	780	3030	1

Table II.1: AOM parameters (energies in cm^{-1}) used to calculate the magnetic anisotropy of **1**.

Energy level no.	parameter set A	parameter set B	parameter set C	parameter set D	parameter set E
11, 12	981	1873	1862	1944	1869
9, 10	861	1657	1650	1826	1658
7, 8	860	1495	1489	759	1496
5, 6	338	1249	1249	450	1256
3, 4	331	60	57	212	57
1, 2	0	0	0	0	0

Table II.2: Calculated eigenvalues (energies in cm^{-1}) for the lowest six Kramers doublets of **1**.

All further 108 states have eigenvalues > 10000 cm^{-1} (relative to energy levels 1,2) and are thermally irrelevant for the magnetic properties of the molecule. Nevertheless it is important to include the full set of basis functions into the calculation to account for all influences of higher states mixing into the ground term. The twelve lowest eigenvalues and eigenfunctions contain all important electronic contributions such as first and second order spin-orbit coupling, geometrical distortions of the ligand field, mixing from higher energy levels, and anisotropic π-bonding. Together, all of those contributions lead to a splitting of the energy levels corresponding to the ground $^4T_{1g}$ term in an octahedral ligand field into six Kramers doublets. Therefore, for the determination of magnetic properties it is sufficient to consider only the Boltzmann population of the energy levels ($3kT$ = 624 cm^{-1} at 300 K) when selecting the necessary number of states to include in the calculations. In comparison with the calculated energies listed in Table II.2 it is clear, that even for the calculation of the temperature dependent susceptibility only the lowest 4 - 6 energy levels are necessary in most cases. Nevertheless all twelve energy levels have

been included in the calculation of the magnetic properties with Equations II.4 and II.5. For computational details see also Section VI.4.2.

$$M = \frac{\sum_{n=1}^{12}\left(-\frac{\partial E_n}{\partial H}\right)exp\left(-\frac{E_n}{kT}\right)}{\sum_{n=1}^{12}exp\left(-\frac{E_n}{kT}\right)\mu_B} \qquad \text{(II.4)}$$

$$\chi = \frac{\partial M}{\partial H} \cong \frac{M}{H} = \frac{\sum_{n=1}^{12}\left(-\frac{\partial E_n}{\partial H}\right)exp\left(-\frac{E_n}{kT}\right)}{\sum_{n=1}^{12}exp\left(-\frac{E_n}{kT}\right)\mu_B H} \qquad \text{(II.5)}$$

The resulting magnetic properties from the calculations with Mackey's parameters[104] and slight variation to optimise the fit to the experimental data obtained from SQUID magnetometry are shown in Figure II.7.

Figures II.7 a) and c) show clearly how sensitive the magnetic anisotropy is to the size and in particular to the sign of Δe_π. As expected for $\Delta e_\pi = 0$ (**A**) the magnetic properties are almost isotropic with only a very small axial anisotropy arising from the small tetragonal distortion of the octahedral ligand field. In agreement with Mackey *et al.*'s results,[2] $\Delta e_\pi = e_{\pi x} - e_{\pi y}$ has to be of negative sign to reproduce the correct magnitude and sense of anisotropy ($\chi_\parallel < \chi_\perp$) (**C**, **D**). In Figures II.7 b) and d) the optimisation of Δe_π is shown starting from the best set of parameters by Mackey *et al.* (**B**).[2] A reasonably good agreement with our experimental data is obtained. In the next step the spin-orbit coupling parameter has been lowered from 525 to 515 cm^{-1} (**C**). The best reproduction of the experimental data has been obtained with parameter set **E** where Δe_π has been slightly adjusted from -666 to -670 cm^{-1}. While small adjustments in ζ and Δe_π influence the high temperature magnetic susceptibility, the low temperature magnetic properties are insensitive to these changes as long as the sign and magnitude are correct.

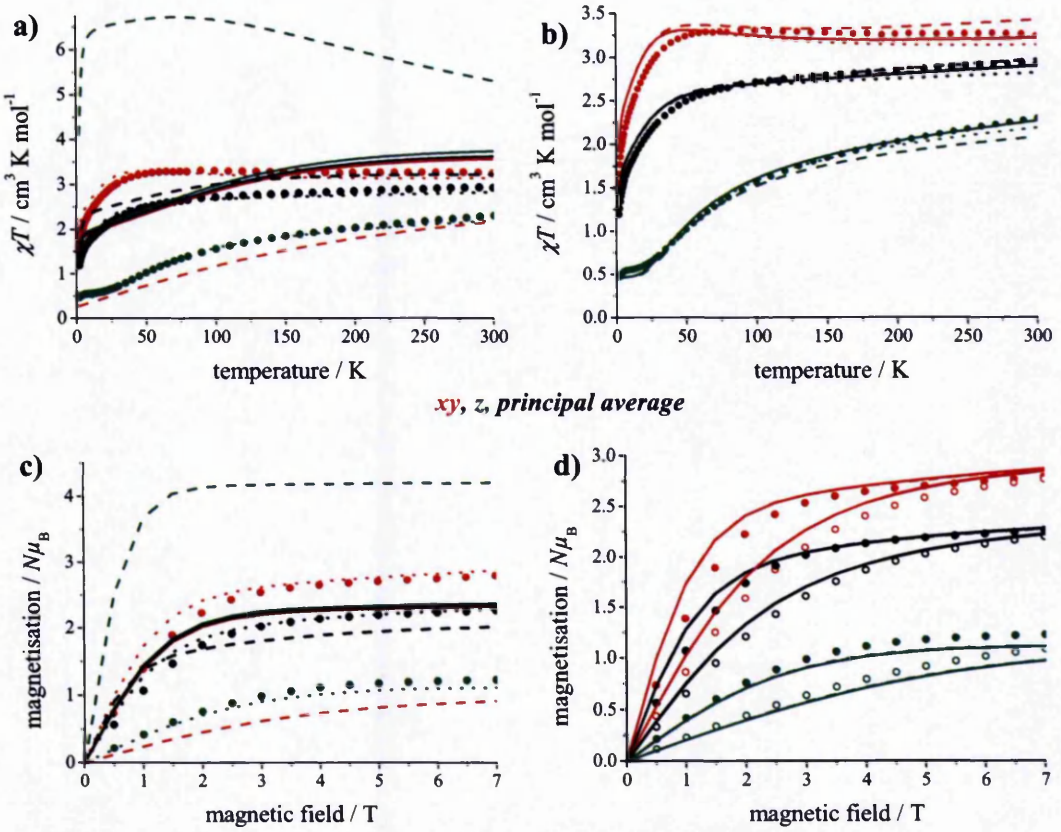

Figure II.7: a) and c): temperature dependent susceptibility (1 T) and field dependent magnetisation (2 K) of **1**, calculation for parameter sets **A** (solid), **C** (dot), and **D** (dash); b) and d): temperature dependent susceptibility (1 T) and field dependent magnetisation (2 K, 4 K) of **1**, calculation for parameter sets **B** (dash), **C** (dot), and **E** (solid)

For the effective model, a field dependence of the "**g**-matrix" arising from a non-linear Zeeman spitting has been observed (Section II.3.1). The angular overlap model allows the calculation of the magnetic properties at each applied magnetic field and therefore should account for such non-linearity. Nevertheless, a small deviation at low magnetic fields is still present, particularly for the perpendicular component, but compared to the effective model a much better agreement between calculated and experimental field dependent magnetisation has been achieved.

Overall the magnetic properties of **1**, especially the large anisotropy, have been reproduced successfully over the whole temperature and field range with the angular overlap model using only one variable parameter Δe_π. Comparison with the results of Mackey *et al.*[2] gives high confidence in the single crystal magnetic data collected

on the SQUID magnetometer used in this work, as well as in the computational routines.

To test the derived parameters further, the *LIGFIELD* software has been used to calculate the X- and Q-band EPR spectra of compound **1** with the parameter sets **B**, **C** and **E**. As expected from the calculation of the low temperature magnetic properties, no significant differences have been detected between the three calculations. The results for parameter set **E** are shown in Figure II.8. Both the X-band and Q-band spectra are reproduced reasonably well with the AOM calculation. The X-band EPR spectrum has been calculated with both a 100% Gaussian and a 100% Lorentzian line-shape and a line-width of 300 G. While the reported experimental line-shape of the frozen solution spectrum seems closer to a Gaussian, the signal position is slightly more accurate for a calculation with a Lorentzian.

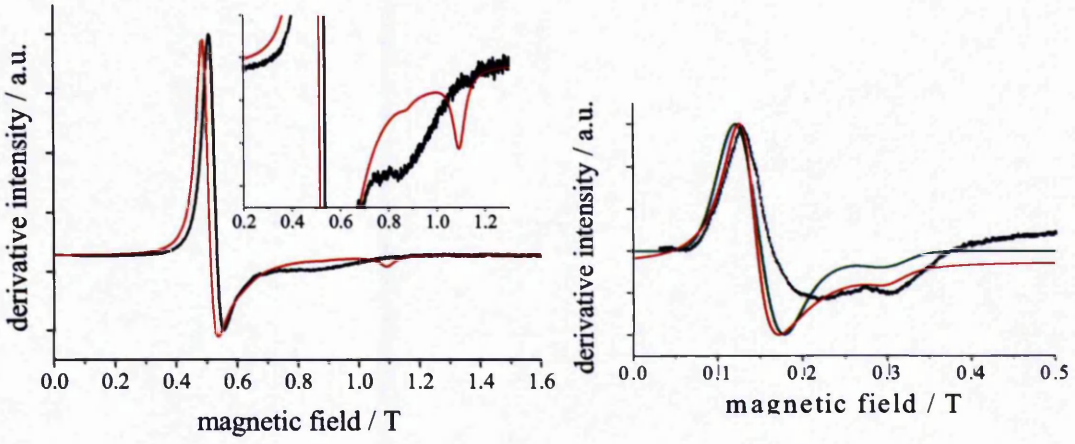

Figure II.8: Left: Q-band EPR spectrum of **1**: black: experiment, red: calculation with parameter set **E**, 300 G Lorentzian line-shape; Right: the X-band EPR spectrum of **2** from[108] has been overlaid with two calculations from parameter set **E**, red: 300 G Lorentzian line-shape, green: 300 G Gaussian line-shape

Positions of both the *xy*- and *z*-components are reproduced well, however the calculated anisotropic intensity does not match the reported experimental spectrum very well. Mackey *et al.* report a good agreement between the calculation and the experimental 9.4 GHz EPR data, however only the calculated and experimentally derived numerical effective "*g*-values" are reported, whilst no comments were made about the shape of the spectrum. A similar observation can be drawn from the simulation of the powder Q-band spectrum. Apart from a very minor field shift, the intense low field component of the spectrum is reproduced very well with the

parameters derived from the single crystal magnetic measurements. Magnification of the weaker features shows that both calculated features at 0.865 and 1.095 T are indeed present in the experimental spectrum even though slightly shifted; however the intensities of the two features with respect to the major peak are not reproduced well. Furthermore, the *EPR tool* within the *LIGFIELD* software does not allow the input of anisotropic line-width parameters, which restricts the simulation of the line broadening observed in the experimental spectrum.

II.4 Conclusions

The monometallic compound hexakis(pyridine-N-oxide)cobalt(II) dinitrate (**1**) has been used as a test compound for experimental and modelling studies on exchange coupled cobalt(II) dimetallics, but also to get an insight into the electronic properties of an isolated octahedral cobalt(II) ion.

Single crystal experiments were performed on the monometallic **1**, and the anisotropic principal temperature dependent susceptibilities agree well with experimental observations reported in the past.[104] In addition, the experiment has proved fully consistent in the reproduction of the perpendicular component of the axial system in two individual crystal mountings, and in the good agreement of the powder magnetic properties with the principal average. These results are very encouraging for single crystal experiments on exchange coupled cobalt(II) systems, because experimental results can be analysed with high confidence in the accuracy and absolute intensity of the experimental observations.

Two models have been tested against the experimental results: an effective model treating cobalt(II) as a pseudo spin "*s*" $=^1/_2$ and a ligand field approach based on the angular overlap model (AOM). Mackey *et al.* have reported AOM calculations to simulate the magnetic properties of **1**.[104] Using the AOM parameters reported by the authors, those calculations have been reproduced successfully for the single crystal experiment. Calculations with the AOM have been extended to applications for EPR spectroscopy. In addition to the X-band EPR spectrum reported by Makinen *et al.*,[108] a powder EPR spectrum was recorded at Q-band. For both frequencies the EPR transitions have been reproduced with calculations based on the derived AOM

parameters, although the intensity of the parallel component is not reproduced well at the higher frequency.

Only at high temperatures the magnetic properties have proved sensitive to small changes in the AOM bonding parameters e_σ, $\Delta e_\pi = e_{\pi x} - e_{\pi y}$ and the spin-orbit coupling parameters ζ, while low temperature properties only respond to the magnitude and sign of the parameters. It appears that the anisotropy of the Zeeman splitting in the ground doublet, which is responsible for low temperature magnetic properties, where no further excited states are populated, is little effected by changes in the strength of the metal-ligand bonds, providing the sign and magnitude of Δe_π, and hence the assignment of the involved π-orbitals, is correct. The energy difference between the ground doublet and further excited states does depend on the strength of metal-ligand bonds, hence the absolute value of the bonding parameters becomes more significant. Most important for the anisotropy of the system at all temperatures is the anisotropy parameter Δe_π. This parameter, and in particular its sign, significantly influences the magnitude and the direction of the anisotropy of the Zeeman splitting and *cannot* be obtained from powder experimental data.

From AOM calculations, the energy difference between the ground and first excited doublet has been calculated as *ca.* 60 cm^{-1} in the axial compound **1**. Consequently only the ground doublet is relevant for the analysis of low temperature magnetic and spectroscopic properties. This explains the correct overall reproduction of the magnitude of the anisotropy with the simple effective model: The use of very anisotropic effective "*g*"-values (2.5 – 4.7), which account for the orbital contribution to the Zeeman splitting, has reproduced roughly the anisotropy of $[Co(C_5H_5NO)_6](NO_3)_2$ (**1**) in both EPR spectra and magnetic properties. At low temperature the cobalt(II) complex does behave as a doublet magnetic moment, despite the real cobalt(II) spin $s = {}^3/_2$, however the wavefunctions are spin-orbit functions and hence a quantitative reproduction with a pseudo-spin model is not possible. Nevertheless, a first interpretation of the magnetic properties associated with cobalt(II) can be obtained from the simple effective model with very little theoretical and mathematical requirements. Deviations from the real system are expected, and can be explained with the AOM, which has led to a much more quantitative simulation of the experimental observations.

Chapter III

Magnetic exchange coupling of cobalt(II) dimetallics

The advantages of the large anisotropy for the rational design of molecular magnetic compounds have been introduced in Section I.1. First order spin-orbit coupling in octahedral cobalt(II) leads to a very large single ion anisotropy, which makes cobalt ions very interesting to study for magnetic properties in clusters. However, the spin-orbit character of the single ion wavefunctions does not allow for a simplistic spin-only treatment of magnetic data, and very little is understood about the magnetic exchange coupling in polymetallic octahedral cobalt(II) compounds. Dimetallic systems provide a useful starting point for such investigations, and in this Ph.D. Thesis a number of both ferro- and antiferromagnetically coupled cobalt(II) dimetallics have been reported with various complementary magnetic and spectroscopic techniques. The key to anisotropy is the performance of experiments on single crystals, which give direct insight into the magnetic properties of the molecules in different directions of the applied magnetic field. Such measurements are not always trivial, and many different crystallographic and symmetry related aspects are of theoretical and practical challenge. Nevertheless, synthetic access to a variety of different examples with different advantages and drawbacks has allowed for detailed analysis of the magnetic properties of cobalt(II) dimetallics with SQUID and torque magnetometry, electron paramagnetic resonance (EPR) and magnetic circular dichroism (MCD) spectroscopy, and inelastic neutron scattering (INS) on powder and in some cases single crystal samples. Such high resolution data provide the necessary experimental evidence to develop and test new theoretical models.

Here, the complementary experimental results are presented and discussed in a semi-quantitative fashion. Analyses in Chapter II have shown, that the treatment of cobalt(II) as an effective moment "s" = $^1/_2$ is not sufficient for quantitative interpretations, but offers a simple intuitive picture to gain a first qualitative access to the interpretation of the magnetic properties. Throughout this chapter the picture of two interacting Kramers doublets with a magnetic moment of $^1/_2$, which give rise to an effective "singlet" and an effective "triplet", is followed through. In Section III.5,

a semi-quantitative model is presented, which cross links experimental results from the different measurements and can explain magnetic and spectroscopic properties of different dimetallics simultaneously.

III.1 Brief structural description of seven dimetallics

The synthesis and molecular structure of most of the seven cobalt(II) dimetallics described in this Ph.D. Thesis have been reported elsewhere.[40,41,112-114] Details on the synthetic procedures and crystal structures can also be found in Section VI.2.2 and Appendix 3.1. Here a brief structural description will summarize the most relevant aspects necessary for the study of the magnetic properties with powder and single crystal techniques.

All seven dimetallics are based on the common core depicted in Figure III.1. The two cobalt(II) ions are bridged by a water molecule and two deprotonated carboxylic acids. An additional carboxylate is coordinated to each cobalt centre and the free oxygen forms a hydrogen bond to the water molecule. The octahedral coordination spheres of the cobalt(II) ions are completed by terminal carboxylic acids and/or nitrogen donor ligands.

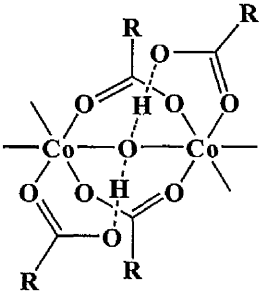

$[Co_2(H_2O)(O_2CC(CH_3)_3)_4(HO_2CC(CH_3)_3)_4]$ (**3**)[113]
$[Co_2(H_2O)(O_2CC(CH_3)_3)_4(HO_2CC(CH_3)_3)_2(py)_2]$ (**4**)[113]
$[Co_2(H_2O)(O_2CCH_3)_4(tmen)_2]$ (**5**)[112]
$[Co_2(H_2O)(O_2CCH_2Cl)_4(tmen)_2]$ (**6**)[112]
$[Co_2(H_2O)(O_2CCHCl_2)_4(tmen)_2]$ (**7**)[114]
$[Co_2(H_2O)(O_2CC(CH_3)_3)_4(tmen)_2]$ (**8**)[40,41]
$[Co_2(H_2O)(O_2C(C_6H_5))_4(tmen)_2]$ (**9**)
tmen = tetramethyl-ethylene-diamine

Figure III.1: Core of the seven cobalt(II) dimetallics **3** – **9**.

Additionally to **3** and **4** the fully deuterated derivatives $\mathbf{3}^{D}$ and $\mathbf{4}^{D}$ for INS experiments have been synthesised and kindly provided for measurements by Dr. Grigore Timco at The University of Manchester. Both compounds have been found

to crystallize isostructurally to their hydrogenated analogues (Appendix 3.1). Figures III.2 – III.5 show the molecular structure and crystal packing for **3** – **6**, respectively.

3 is the most simple of the cobalt(II) dimetallics and the cobalt(II) ions are solely surrounded by protonated and deprotonated pivalic acid molecules and the central water molecule.[113] The cobalt(II) ions are not related by symmetry, but the crystal packing allows for some constraints on the principal molecular magnetic axes: In a monoclinic crystal system, one of the principal molecular magnetic axes has to be parallel to the crystal axis *b* (χ_3 by convention), while the remaining principal axes are located anywhere in the crystal *ac* plane.[27] The packing diagram in Figure III.2 shows that two out of the four molecules are created by an inversion centre, leaving only two magnetically inequivalent molecules. Through symmetry requirements the two molecules give the same magnetic response within the *ac*-plane and for *b* parallel the magnetic field. In any other orientation addition or average of the responses is expected for additive or averaging techniques such as EPR spectroscopy or SQUID magnetometry, respectively.[3]

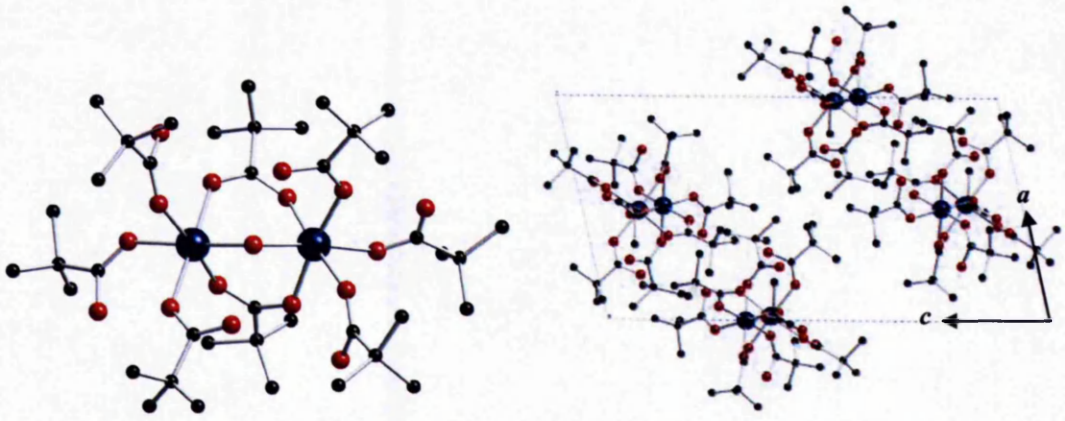

Figure III.2: Molecular structure and packing of $[Co_2(H_2O)(O_2CC(CH_3)_3)_4(HO_2CC(CH_3)_3)_4]$ (**3** and $\mathbf{3}^{D}$, hydrogen / deuterium atoms are omitted for clarity.) $P2_1/n$, a = 12.149(4) Å, b = 20.027(7) Å, c = 23.097(8) Å, β = 103.410(7)°, V = 5466.47 Å^3, Z = 4.[113]

More symmetry can be found in **4**[113] even though structurally **4** only differs from **3** in the replacement of one pivalic acid with one pyridine ligand on each cobalt(II) centre. **4** is the only dimetallic out of the seven examples with crystallographically imposed symmetry equivalent cobalt(II) ions. For single crystal magnetic properties it is also important to note that all cobalt-cobalt vectors are packed in a parallel

fashion within the *ac*-plane. Again the crystal system is monoclinic and one molecular principal magnetic axis aligns with the crystal axis *b* (χ_3 by convention), while the remaining principal axes are located anywhere in the crystal *ac* plane ($\chi_2 > \chi_1$). The special location of the water molecule on the C_2 symmetry axis *b* leads to magnetic equivalence of all molecules in the unit cell.

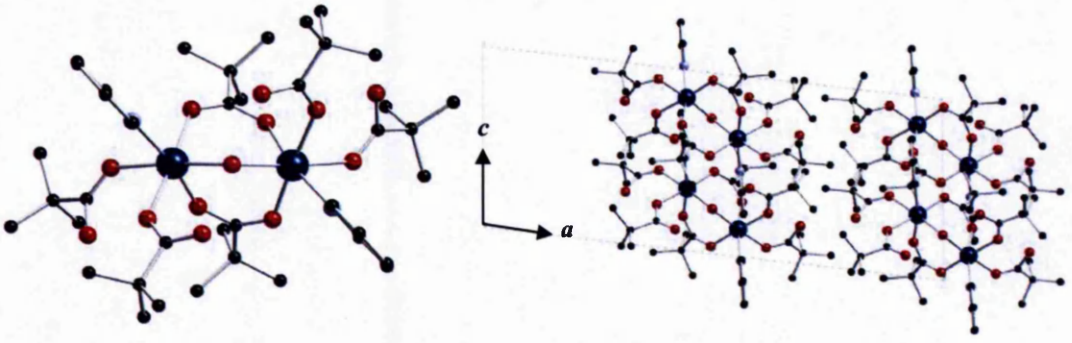

Figure III.3: Molecular structure and packing of $[Co_2(H_2O)(O_2CC(CH_3)_3)_4(HO_2CC(CH_3)_3)_2(py)_2]$ (**4** and $\mathbf{4}^{D}$, hydrogen / deuterium atoms are omitted for clarity.) *C2/c*, $a = 24.715(2)$ Å, $b = 19.5088(19)$ Å, $c = 9.8201(10)$ Å, $\beta = 96.725(2)°$, $V = 4702.2(8)$ Å^3, $Z = 4$.[113]

In the orthorhombic crystal systems **5**[112] the three principal magnetic axes align with the three crystallographic unit cell axes. There is no molecular symmetry relating the two cobalt centres per dimetallic unit. Analysis of the crystal packing diagram shows that four out of the eight molecules are created by an inversion centre which leads to magnetical equivalence of the corresponding pairs. Furthermore, pairs are related by a two fold axis, leaving two magnetically independent molecules. Along the principal magnetic directions all molecules are magnetically equivalent, but in a general orientation the average of sum of two molecules is expected.

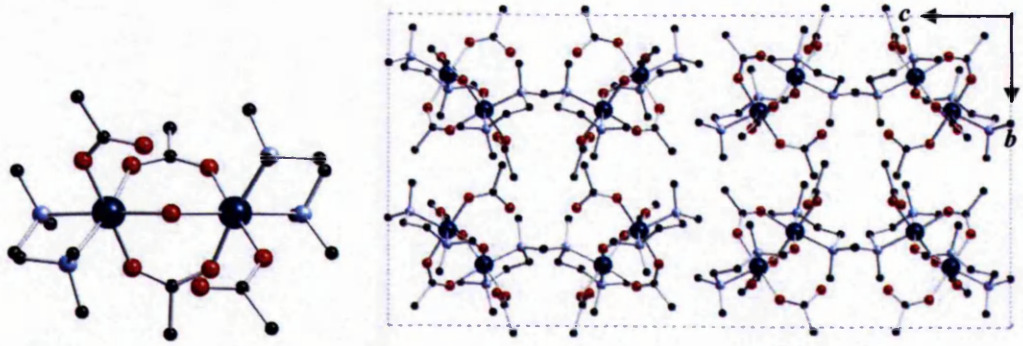

Figure III.4: Molecular structure and packing of $[Co_2(H_2O)(O_2CCH_3)_4(tmen)_2]$ (**5**) (hydrogen atoms are omitted for clarity.) *Pbca*, $a = 12.056(3)$ Å, $b = 15.917(5)°$ Å, $c = 31.33(1)$ Å, $V = 6012.08$ Å^3, $Z = 8$[112]

$[Co_2(H_2O)(O_2CCH_2Cl)_4(tmen)_2]$ has been reported previously in a different space group.[112] While Turpeinen *et al.* report a dimetallic composed of two symmetry related cobalt(II) ions in the space group *P2/n* (see also Appendix 3.2), **6** was found to crystallize reproducibly in the monoclinic space group $P2_1/c$, with non-symmetry related cobalt(II) ions. A cif file including all structure related information can be found on the accompanying disc. Two out of the four molecules are related by an inversion centre, leading to only two magnetically different orientations of the dimetallics in the crystal (Figure III.5). Again, the principal molecular magnetic axis χ_3 is defined by *b*, while the remaining axes are located in the *ac*-plane ($\chi_2 > \chi_1$). Symmetry of the susceptibility tensor leads to magnetic equivalence of all molecules in the *ac* plane and along the unique axis *b*, but leaves two magnetically independent molecules in any other orientation.

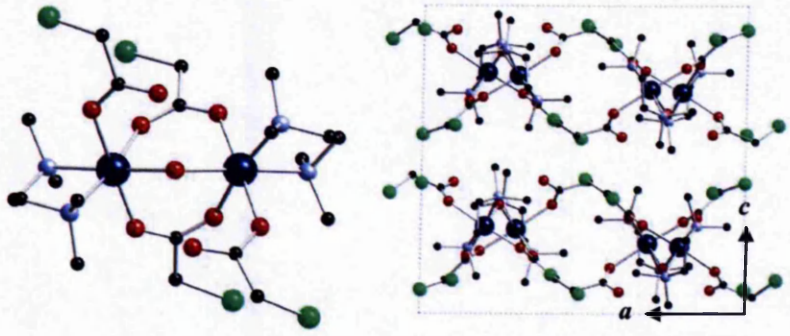

Figure III.5: Molecular structure and packing o $[Co_2(H_2O)(O_2CCH_2Cl)_4(tmen)_2]$ (**6**) (hydrogen atoms are omitted for clarity.) $P2_1/c$, a = 15.7872(3) Å, b = 12.8814(2) Å, c = 15.2748(3) Å, β = 91.126(2)°, V = 3105.7 Å^3, Z = 4

Analogous molecular structures are found for **7**, **8** and **9**, for which molecular structures, unit cells and packing diagrams are depicted in Appendix 3.2. The structure of **9** has not been reported previously; a cif file including all structure related information can be found on the accompanying disc.

Relevant distances, angles and bond valence parameters influencing the magnetic exchange pathway of the seven dimetallics are listed in Table III.1. O-O is the distance between the central water oxygen and the carboxylate oxygen hydrogen bonded to the water molecule (see Figure III.1). In some crystal structures one or both hydrogen atoms have been found on the central oxygen, however the distances

between the central oxygen and the oxygen of the deprotonated pivalic acids are short, and hydrogen bonds have been found.

Structure	Co-Co distance / Å	Co-O-Co angle / deg	O-O distance / Å	*BV* carbox.	*BV* water
$[Co_2(H_2O)(O_2CC(CH_3)_3)_4$-$(HO_2CC(CH_3)_3)_4]$ (**3**)[113]	3.4275(11)	110.235(66)	2.5439(24) 2.5516(22)	1.58 1.60	0.69
$[Co_2(H_2O)(O_2CC(CH_3)_3)_4$-$(O_2CC(CH_3)_3)_2(py)_2]$ (**4**)[113]	3.5042(4)	108.445(9)	2.6182(12)	1.51	0.57
$[Co_2(H_2O)(O_2CCH_3)_4(tmen)_2]$ (**5**)[112]	3.5963(6)	115.024(11)	2.5472(6) 2.5643(6)	1.51 1.56	0.62
$[Co_2(H_2O)(O_2CCH_2Cl)_4(tmen)_2]$ (**6**)	3.5963(5)	116.479(8)	2.5417(28) 2.5293(28)	1.48 1.47	0.65
$[Co_2(H_2O)(O_2CCHCl_2)_4(tmen)_2]$ (**7**)[114]	3.6751(6)	116.386(9)	2.5661(3) 2.6079(4)	1.59 1.59	0.57
$[Co_2(H_2O)(O_2CC(CH_3)_3)_4(tmen)_2]$ (**8**)[40, 41]	3.5353(1)	114.475(3)	2.5840(1) 2.4885(1)	1.63 1.33	0.67
(two molecules in the asymmetric unit)	3.5334(1)	113.104(3)	2.5179(1) 2.5644(1)	1.98 1.50	0.64
$[Co_2(H_2O)(O_2C(C_6H_5))_4(tmen)_5]$ (**9**)	3.5853(1)	115.111(12)	2.53659(1) 2.5592(1)	1.46 1.48	0.63

Table III.1: Selected bond distances and angles of the dimetallics **3** – **9**. O-O is the distance between the central water oxygen and the carboxylate oxygen hydrogen bonded to the water molecule (see Figure III.1). Bond valence calculations estimate the water character of the bridging oxygen.

Bond valence (*BV*) calculations have been carried out using Equation III.1[115] to estimate if the hydrogen is best described by a water / carboxylate system, an oxide / carboxylic acid system, or an intermediate between the two. In all cases the two protons seem equally shared between the bridging oxygen and the hydrogen bonded carboxylates.

$$BV = \sum_i \left(R / R_{1,i}\right)^{-Ni} \text{ with: } BV = 2 \text{ for oxides and } BV = 0 \text{ for water} \qquad \text{(III.1)}$$

R = distance between O and neighbour *i*

$R_{1,i}$ = expected length for a bond unit valence, N_i = empirical constant related to the slope of *BV* ($R_{1,C} = 1.378$, $R_{1,Co(II)} = 1.727$, $R_{1,Ni(II)} = 1.608$, $N_C = 4.065$, $N_{Co(II)} = 5.6$, $N_{Ni(II)} = 5.4$).

III.2 Magnetic properties of cobalt(II) dimetallics

The magnetic properties of all seven compounds have been studied on powder samples. For some of the molecules the temperature dependent susceptibility has already been reported;[34,39,46] however, further measurements have shown, that in the case of weakly antiferromagnetic cobalt(II) dimetallics, the field dependent magnetisation contains more information than the susceptibility.

For a direct measurement of the magnetic anisotropy and the direction of the principal magnetic axes within the dimetallic compounds, magnetic measurements have also been performed on single crystal samples of **4**, **5** and **6**.

III.2.1. Powder magnetic properties of the dimetallics 3 – 9

In all seven dimetallics, the cobalt(II) ions are bridged by two carboxylates, which are expected to induce antiferromagnetic super-exchange, and one water/oxide molecule in which the magnetic exchange interaction depends greatly on the Co-O-Co bond angle. In Table III.1 the Co-O-Co bond angles of all seven dimetallics have been listed. All angles lay between 108° and 117° and antiferromagnetic exchange is expected for the seven compounds. Indeed this is the case for *six* out of the seven dimetallics which behave very similarly and show weak antiferromagnetic exchange interactions between the cobalt(II) ions. Interestingly, weak *ferromagnetic* exchange has been observed between the two cobalt(II) ions in **3**. Although the Co-O-Co bond angle of **3** (108.44°) is the smallest out of the seven and ferromagnetic exchange is expected for small angles close to 90°,[116] it seems surprising that, despite the structural similarity of **3** and **4**, the magnetic properties are inverted. However, a similar effect has been observed for the isostructural nickel analogues $[Ni_2(H_2O)(O_2CC(CH_3)_3)_4(HO_2CC(CH_3)_3)_4]$ and $[Ni_2(H_2O)(O_2CC(CH_3)_3)_4$-$(HO_2CC(CH_3)_3)_2(py)_2]$ by Mikhailova *et al.*[34] The authors report ferromagnetic interactions for the nickel pivalate complex, and antiferromagnetic interactions if pyridine is introduced. Table III.2 shows Co-Co / Ni-Ni bond length and Co-O-Co / Ni-O-Ni bridging angles for the pairs of compounds in comparison. For both

structures, the nickel ions exhibit a slightly larger bond angle with the water molecules than the cobalt ions. An explanation for the inversed magnetic properties cannot be drawn from the geometry. While for cobalt the smaller angle occurs in the ferromagnetic example, the ferromagnetic nickel pivalate complex exhibits a *larger* Ni-O-Ni angle than the antiferromagnetic complex. Significant could also be the contribution of the "lone pairs" on the bridging water molecule to the water-ligand bonds, which depend significantly on the water character of this oxygen, and hence the strength of the hydrogen bonding with the deprotonated pivalic acid ligand. In all four compounds the oxygen-oxygen distance between the deprotonated pivalic acid and the water is short, and hydrogen bonding occurs. Bond valence calculations have estimated the water character of the bridging oxygen molecule, and the results in Table III.2 show that the hydrogen is shared equally between the two oxygen atoms in all cases. However, no trend can be found in the small variations of the *BV*. In all dimetallic compounds the magnetic exchange interactions are weak and the inversion of the magnetic properties may be explained by small changes in the ligand field leading to different single ion properties. This effect is particularly pronounced for ions with a strong single ion anisotropy, which is present in both octahedral nickel(II) and octahedral cobalt(II) ions. For weak interactions, such changes in the ligand field may have a significant influence on the magnetic exchange coupling, and appear to allow for both ferro- and antiferromagnetic exchange interactions.

Structure / magnetic exchange	**M-M distance / Å**	**M-O-M angle / deg**	**O-O distance / Å**	***BV* carbox.**	***BV* water**
$[Co_2(H_2O)(O_2CC(CH_3)_3)_4$-$(HO_2CC(CH_3)_3)_4]$ **(3) antiferromagn.**	3.4275(11)	110.235(66)	2.5439(24) 2.5516(22)	1.58 1.60	0.69
$[Co_2(H_2O)(O_2CC(CH_3)_3)_4$-$(O_2CC(CH_3)_3)_2(py)_2]$ **(4) ferromagn.**	3.5042(4)	108.445(9)	2.6182(12)	1.51	0.57
$[Ni_2(H_2O)(O_2CC(CH_3)_3)_4$-$(HO_2CC(CH_3)_3)_4]$ **ferromagn.**	3.3829(19)	112.22(194)	2.5932(215)	1.53	0.47
$[Ni_2(H_2O)(O_2CC(CH_3)_3)_4$-$(O_2CC(CH_3)_3)_2(py)_2]$ **antiferromagn.**	3.4650(15)	110.720(33)	2.5281(144) 2.5470(104)	1.58	0.57

Table III.2: Selected bond distances and angles of the dimetallics **3** and **4** and the isostructural nickel analogues.[34] O-O is the distance between the central water oxygen and the carboxylate oxygen hydrogen bonded to the water molecule (see Figure III.1). Bond valence calculations estimate the water character of the bridging oxygen.

The magnetic properties of **3** are shown in Figure III.6. The room temperature value of $\chi T = 6.85$ cm^3 K mol^{-1} agrees well with the expectation value of 6.75 cm^3 K mol^{-1} for two non interacting cobalt(II) ions from Equation II.1.

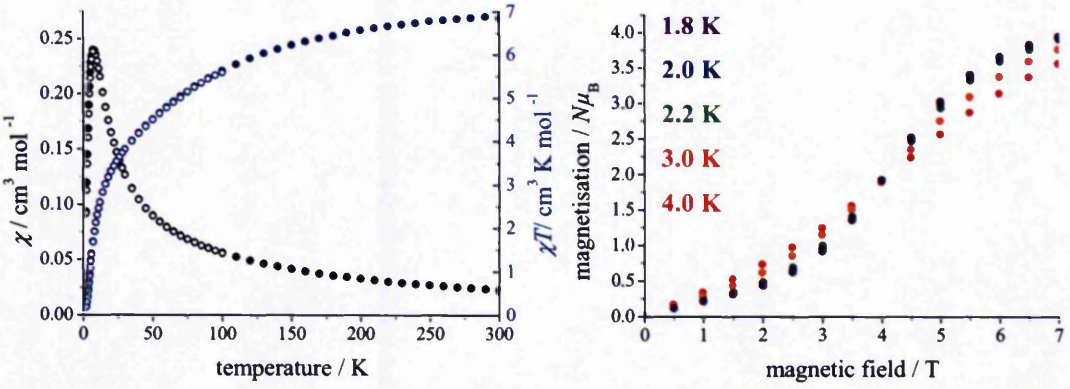

Figure III.6: Magnetic properties of **3** measured on a powder sample (no eicosane). Left: Temperature dependent susceptibility at 1 T (dot) and 0.1 T (ring), right: Field dependent magnetisation between 1.8 and 4 K.

Upon lowering the temperature χT of **3** decreases, initially because of first order spin-orbit coupling (see also Sections I.1.3 and II.2) and subsequently because of antiferromagnetic exchange interactions between the two cobalt(II) ions, resulting in a non-magnetic ground state. The χ *vs.* T plot shows a peak at 7 K. More detailed information can be drawn from the field dependent magnetisation. The magnetisation *vs.* field plot appears to show a level crossing between the non-magnetic ground state and an excited state at 4 T. At 7 T the magnetisation starts to saturate towards a value of *ca.* 4 $N\mu_B$. In Chapter II the origin of the single ion low temperature properties of octahedral cobalt(II) from a reasonably well isolated ground Kramers doublet has been discussed. A similar qualitative picture can be drawn here. Antiferromagnetic coupling between two effective moments "s" = $^1/_2$ with an effective "g"-value of "g" ~ 4 will lead to an effective diamagnetic ground "singlet" and an effective excited "triplet" state, which is also characterised by "g" ~ 4. The sigmoidal shape of the magnetisation *vs.* field plot represents exactly this: At small fields and 1.8 K the non-magnetic ground state is populated almost exclusively, and hence the magnetisation is close to 0. Zeeman splitting in an increasing magnetic field lowers the energy of the effective "m_{Seff}" = -1 state, which leads to a growing thermal population of this energy level. At *ca.* 4 T and the inflection point of the

sigmoidal magnetisation curve, a level crossing between the diamagnetic ground state and the "m_{Seff}" = -1 energy level occurs, which subsequently becomes the most populated level, and hence undergoes saturation of the magnetisation at "S_{eff}" · "g_{eff}" = 4 $N\mu_B$.

Structure	$T_{\chi max}$ / K	χT_{RT}/cm^3 K mol^{-1}	inflection field / T	M_{7T} / $N\mu_B$
$[Co_2(H_2O)(O_2CC(CH_3)_3)_4)(HO_2CC(CH_3)_3)_4]$ (**3**)	7	6.85	4.0	3.94
$[Co_2(H_2O)(O_2CCH_3)_4(tmen)_2]$ (**5**)	3.5	6.41	1.5	4.43
$[Co_2(H_2O)(O_2CCH_2Cl)_4(tmen)_2]$ (**6**)	5.5	6.49	3.0	4.39
$[Co_2(H_2O)(O_2CCHCl_2)_4(tmen)_2]$ (**7**)	4.0	6.54	2.0	4.60
$[Co_2(H_2O)(O_2CC(CH_3)_3)_4(tmen)_2]$ (**8**)	3.5	6.51	2.0	4.48
$[Co_2(H_2O)(O_2C(C_6H_5))_4(tmen)_2]$ (**9**)	5.0	6.41	~2.8	4.39
$[Co_2(H_2O)(O_2CC(CH_3)_3)_4)(HO_2CC(CH_3)_3)_2(py)_2]$ (**4**)	-	6.79	-	3.75

Table III.3: Comparison of room temperature χT, peak temperature of χ, saturation of the magnetisation and inflection point in the field dependent magnetisation of **3** – **9**.

A very similar behaviour has been observed for all other antiferromagnetically coupled dimetallics **5** – **9**. The most important results are summarised in Table III.3 and Figure III.7, which shows the field dependent magnetisation of **5** – **9** at 1.8 K. For completeness all other magnetic measurements on these compounds are plotted in Appendix 3.3.

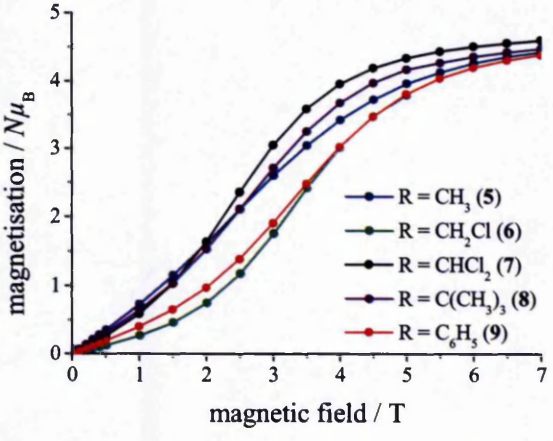

Figure III.7: Field dependent magnetisation of $[Co_2(H_2O)(O_2CR)_4(tmen)_2]$ (**5** – **9**) at 1.8 K.

All five examples show saturation of the magnetisation between 4.3 and 4.6 $N\mu_B$ indicating a similar slope of the Zeeman splitting. The inflection point, hence the level crossing, is a direct measure of the exchange interaction: The stronger the exchange, the higher the magnetic field required to achieve a level crossing. The

following order has been observed: **5** < **8** ≈ **7** < **9** < **6** (< **3**). This order corresponds to the peak of the temperature dependent susceptibility, which is also a direct measure of the strength of antiferromagnetic exchange coupling. Here an order of **5** ≈ **8** < **7** < **9** < **6** (< **3**) is observed. Comparison with Co-Co bond length, Co-O-Co bond angle, *pKa* of the acids, or the water character of the central oxide (hence the extend of the contribution of the oxygen lone pairs towards a metal-ligand bond) does not lead to an obvious trend that can explain the strength of the magnetic exchange. The strong anisotropy of cobalt(II) leads to a high sensitivity to small structural changes in the ligand field, which may be the origin of different magnetic exchange contributions.

The magnetic properties of the ferromagnetically coupled dimetallic **4** are plotted in Figure III.8. Again the room temperature value of χT = 6.83 cm^3 K mol^{-1} agrees well with the expectation value for two non-interacting cobalt(II) ions. First order spin-orbit coupling (see also Sections I.1.3 and II.2) leads to a decrease of χT upon lowering the temperature, but this time a plateau is reached below *ca.* 10 K with χT = 4.23 cm^3 K mol^{-1}. Below 5 K a field dependence of the magnetic susceptibility has been observed: A small increase of χT at low fields (0.01, 0.05 and 0.1 T) indicates weak ferromagnetic interactions between the cobalt(II) ions. At higher magnetic fields of 0.5 or 1 T a decrease in χT is observed, indicative of splitting of the ground multiplet in zero-field.

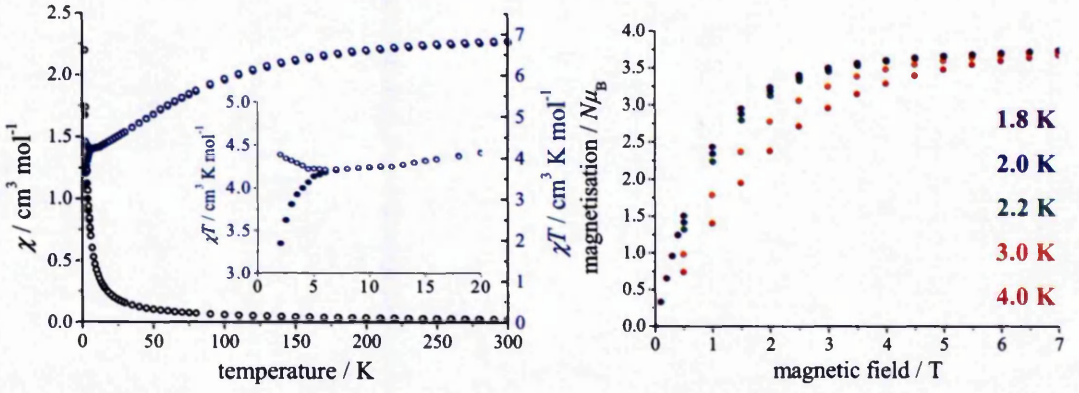

Figure III.8: Magnetic properties of **4** measured on a powder sample. Left: Temperature dependent susceptibility at 1 T (dot) and 0.1 T (ring), right: field dependent magnetisation between 1.8 and 4 K.

A clear saturation of the magnetisation has been observed at low temperatures above 3 T with $M = 3.75\ N\mu_B$. Again the magnetic properties appear to arise from magnetic exchange coupling between the ground Kramers doublets of the two cobalt(II) ions, but this time ferromagnetic, leading to an effective ground "triplet" with "g" = 3.75 and an excited "singlet" state.

A direct comparison between **3** and **4** is shown in Figure III.9, where the similarities between the compounds are even more clear. Both compounds show a saturation of the magnetisation at similar values indicating the presence of an effective "triplet state" with "g" ~ 4, either as ground state or first excited state. The saturation of the magnetisation also indicates a very good isolation of the ground energy manifold from further excited states at low temperatures.

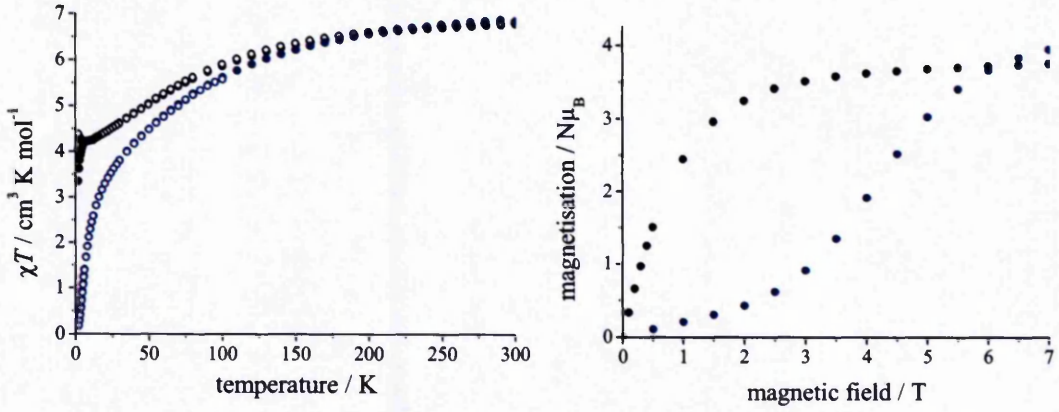

Figure III.9: Comparison of the magnetic properties of **3** (blue) and **4** (black) shows that both compounds behave very similarly at high temperature. The low temperature properties are very reminiscent of the coupling of two effective moments of $^1/_2$, either ferro- or antiferromagnetically.

Above 150 K the two compounds show identical behaviour in χT, which is purely dependent on spin-orbit contributions. At this temperature energy levels arising from the first excited single ion doublets appear to be sufficiently populated to mask any exchange interaction between the bottom Kramers doublets. Below 150 K the influence of the ground multiplets becomes increasingly more important leading to the two different ground states in **3** and **4**. Calculations with the angular overlap model (AOM) on **5** (Appendix 3.4) have shown, that the second Kramers doublet of the cobalt(II) ions within the dimetallics occurs at *ca.* 160 cm^{-1}, which is in good agreement with the observations from the temperature dependent susceptibility.

Calculation of the single ion ligand field performed by Prof. Liviu Chibotaru and *co*-workers at the University of Leuven/Belgium with *ab-initio* methods confirms these observations with a ground to first excited state energy difference of > 150 cm^{-1} (Appendix 3.5).

III.2.2. Magnetic studies on single crystals of 4, 5 and 6

Compound **4** crystallizes in the monoclinic space group *C2/c* and by symmetry only the crystal axis *b* is required to be coincident with a principal magnetic direction, by convention defined as χ_3. χ_1 and $\chi_2 > \chi_1$ can be located anywhere in the crystal *ac*-plane. Their location is defined by the angle ϕ between *a* and χ_1 going from positive *a* towards or beyond positive *c* as depicted in Figure III.10.[27]

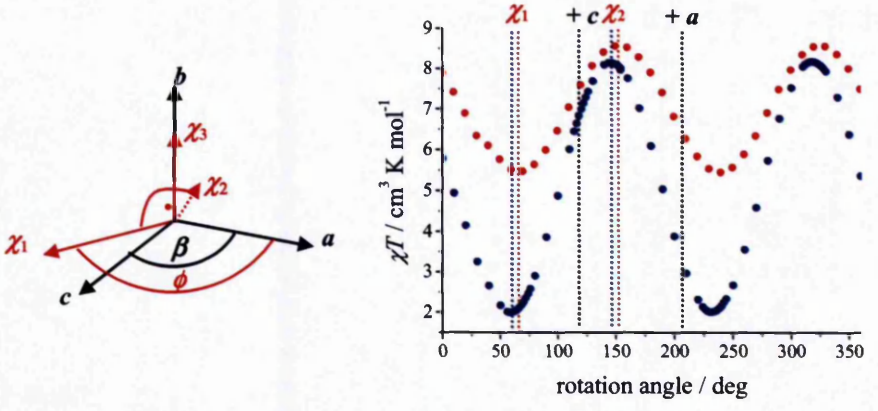

Figure III.10: Left: Definition of the principal magnetic axes in monoclinic crystal systems. Right: Angular dependence of **4** in the *ac*-plane at 1 T and 300 K (red) or 10 K (blue).

Figure III.10 also shows the anisotropy in the *ac*-plane from rotation around the unique *b* axis. The crystal used in this experiment was too small to determine absolute values for the susceptibility. Nevertheless it is possible to determine the principal magnetic axes from the rotational study, where only relative intensities are relevant. Precise mounting with good knowledge of the crystal axes and rotation around the unique *b* axis allows for the determination of the minimum susceptibility χ_1 as *ca.* 150° (ϕ) away from the crystal axis *a*. The error on the angle due to manual mounting, a slight backlash of the goniometer and the number of measurement points

is estimated as ± 5°. Details about the performance of the single crystal experiments and the determination of the principal magnetic axes are discussed in Section VI.3.3. Comparison with the crystal structure shows that the derived angle compares well to the angle of 147.58° between the cobalt-cobalt vector and the crystal axis *a*. It seems reasonable to place a principal magnetic axis along the cobalt-cobalt vector, which allows confidence in the assignment of χ_1 as shown in Figure III.11, despite the relatively large experimental error. χ_2 is given by the cross product of χ_1 and χ_3. The angle ϕ is not necessarily temperature independent,[27] and a shift of *ca.* 8° in the position of minimum and maximum susceptibility between 300 and 10 K has been observed, which may indicate temperature dependence of ϕ in **4**.

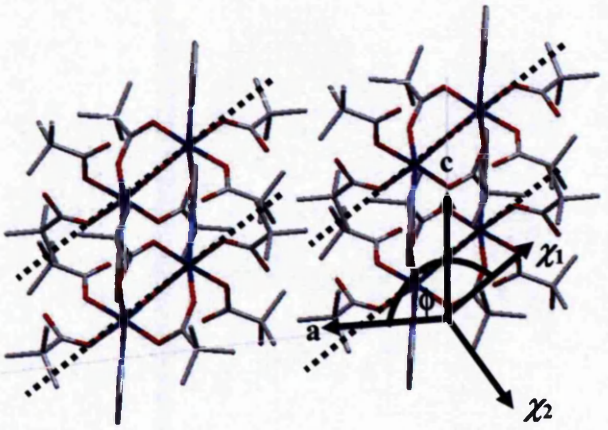

Figure III.11: Location of the magnetic axes in a crystal of **4** determined by single crystal SQUID magnetometry.

Large crystals of **4** do not survive the stress of low temperature measurements. Even though it was possible to perform a rotational study at 10 K, the crystal fractured during further low temperature experiments. Small crystals have shown a higher temperature stability allowing for single crystal torque experiments.

The angular dependences detected on a torque magnetometer at 2 K in the a*/*ac* and the *a***b* planes are plotted in Figure III.12. Mounting of the crystal with a microscope and measurement in 5° steps allows for at least ± 3° accuracy in angle. In both setups the starting points (0°) correspond to a parallel alignment of the cross product of $b \times c = a^*$ with the magnetic field. The torque signal is expected to vanish along the principal magnetic directions. In the *ac*-plane, the torque becomes 0 at 90° intervals as expected, which allows for the principal directions to be determined with respect

to the starting point a^*. The first (and third) inflection point is observed 40° away from $|a^*|$ in the direction of rotation. This corresponds well to the direction of the cobalt-cobalt vector and hence χ_1, which lies 39.15° (or 140.86°) away from $|a^*|$. Therefore, the four inflection points can be assigned to the principal axes as shown in Figure III.12. Surprisingly, the torque experiment does not support a temperature dependence of ϕ in the *ac*-plane. Even though the torque signal has been recorded at 2 K, the position of the principal axes is in agreement with SQUID experiment at room temperature. Despite a small backlash in the SQUID goniometer, no errors as large as ± 8° have been observed in other experiments when cooling from 300 to 10 K. Rather, high precision in the reproduction of maxima and minima at different temperatures has been shown for setups where symmetry constraints define the principal magnetic axes at all temperatures (*e.g.* in **6**, Figure III.15). The origin of the shift observed in the SQUID experiment on **4** remains unclear; however, within the experimental error the shift is small and does not have a significant influence on the overall anisotropy of the susceptibility.

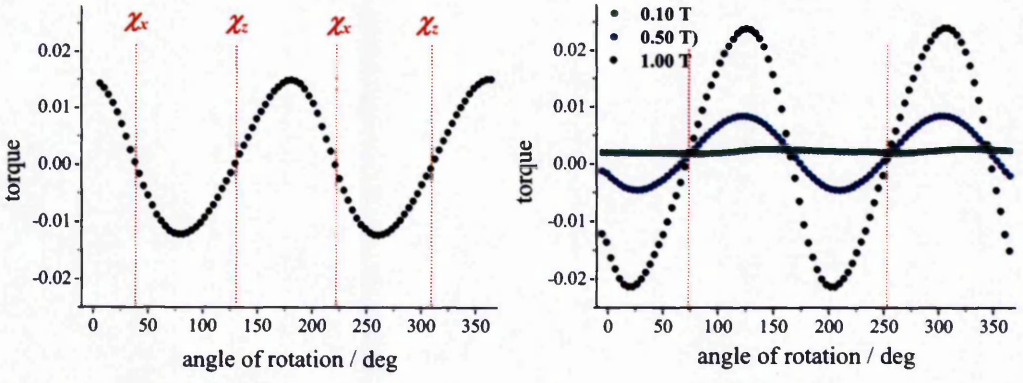

Figure III.12: Angular dependence of **4** measured with a torque magnetometer at 2 K in the *ac*-plane (left, 1 T) and *ba**-plane (right, 0.1, 0.5 and 1 T). The red lines mark the positions of the principal axes.

An unusually asymmetric sinusoidal has been observed for the torque in the *ac*-plane. When moving from maximum to minimum a +80° step is observed, and subsequently a +100° step from minimum to maximum although in both cases 90° steps are expected. In the a^*b-plane the situation is further complicated. Here only one principal magnetic axis is present and a deviation from a regular sinusoidal is not only observed in the extrema, but also in the appearance of the inflection points.

$b \parallel$ B is expected 90° and 270° away from a^* at 0°, however the inflection points occur at 70° and 250° instead. Both the unexpected location of the inflection points as well as the irregular oscillation indicate that a meaningful torque experiment is not possible in this set-up. The experiment only leads to a symmetrical sinusoidal if the rotation is performed around a principal magnetic axis, which is not the case for rotation around c. Rotation should be performed either around the cobalt-cobalt vector (χ_1) or its cross product with b (χ_2). However, the crystal morphology with respect to the principal magnetic axes does not allow for such a setup.

Measurements at different fields are shown for the a^*b-plane in Figure III.12 and show a decrease in the amplitude of anisotropy for smaller magnetic fields. At magnetic fields $\leq$ 0.1 T, where a field dependence has been observed in the low temperature powder susceptibility, the signal is too weak to measure the torque response.

Although it has not been possible to obtain quantitative information from single crystal SQUID or torque experiments regarding the anisotropy of **4**, important qualitative information can be drawn from the comparison of relative intensities:

a) The three principal magnetic axes have been assigned consistently in the two different experiments.

b) The response of the SQUID on the small crystal of **4** is significantly stronger along χ_2 than for the powder sample, especially at 10 K, where the absolute intensity of the susceptibility for a small sample volume is more reliable than at room temperature. Consequently a principal average corresponding to the powder response can only be achieved if χ_2 is larger than χ_1 and χ_3.

c) In the powder experiment (Figure III.8) a decrease in χT due to spin-orbit coupling from $\chi T_{300\ K}$ = 6.83 cm^3 K mol^{-1} to a plateau of $\chi T_{10\ K}$ = 4.23 cm^3 K mol^{-1} is observed. In contrast, $\chi_2 T$ decreases only slightly from $\chi_2 T_{300\ K}$ = 8.56 cm^3 K mol^{-1} to $\chi_2 T_{10\ K}$ = 8.15 cm^3 K mol^{-1}. Spin-orbit coupling is expected to induce a much stronger decrease (compare also the monometallic **1** in Section II.2), indicating that ferromagnetic exchange in the direction of χ_2 must be significantly stronger than the average observed in the powder. Absolute single crystal intensities, especially at room temperature, may not be reliable because of insufficient sample mass; however, such inaccuracy typically leads to values above the true paramagnetic signal at room

temperature. Consequently, for sufficient sample quantities, the effect along χ_2 is more likely to have been enhanced than weakened.

Compound **5** crystallizes in the orthorhombic space group *Pbca*, and by symmetry requirements the three principal magnetic axes describing the magnetic properties of the compound align with the three crystallographic unit cell axes. Figure III.13 shows the magnetic susceptibility of **5** measured along the three principal magnetic axes between 50 and 300 K. The crystal average agrees extremely well with the powder experiment, which allows for a high confidence in the absolute single crystal response. Below 40 K crystals of **5** fracture, hence no data points have been collected below 50 K to ensure stability of the sample.

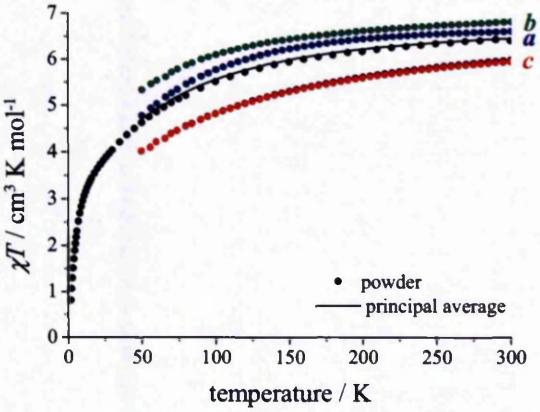

Figure III.13: Principal single crystal susceptibilities of **5** plotted as χT between 50 and 300 K at 1 T (green, blue and red dots), compared to the powder experiment at 1 T (black dots, no eicosane). Line: Principal crystal average.

At high temperature the cobalt-cobalt interaction is masked due to the thermal population of excited states, and the magnetic response can be treated as two non-interacting cobalt(II) ions. Compared to the monometallic compound **1** (Section II.2.1) the anisotropy observed for **5** is smaller than expected for the addition of two non-interacting cobalt(II) centres. In the axially symmetric **1** the principal room temperature values of χT are 2.30 cm^3 K mol^{-1} and 3.24 cm^3 K mol^{-1} (hence 4.60 cm^3 K mol^{-1} and 6.48 cm^3 K mol^{-1} for two cobalt centres). In contrast, values between χT = 5.88 cm^3 K mol^{-1} and χT = 6.81 cm^3 K mol^{-1} have been observed in **5**. The origin for the apparent smaller anisotropy lays in the relative orientation of the single ion

fragments with respect to the crystal axes, and small geometrical differences in the ligand field.

Even though it was not possible to obtain low temperature single crystal measurements on **5**, the information at high temperature allows for AOM parameters to be adjusted and to estimate the crystal field influence on two non-interacting cobalt(II) single ions. Although all molecules are magnetically equivalent along the principal magnetic directions, calculations using the AOM have shown that for the two cobalt(II) centres, very different single ion responses are expected along the principal molecular orientations (Appendix 3.4, Section VI.4.1). SQUID magnetometry is an averaging technique, which does not allow for a distinction between the different contributions, hence the observed anisotropy represents the sum of the two cobalt(II) centres.

Compound **6** crystallizes in the monoclinic space group $P2_1/c$ and consequently the only magnetically unique crystal axis is again b with $\chi_3 = \chi_b$ according to the definitions in Figure III.10. With rotational studies in the *ac*-plane the remaining principal magnetic axes have been determined. An angle of *ca.* 6° has been observed experimentally between a and χ_1, which strongly indicates that the principal magnetic axis χ_1 corresponds to the projection of the molecular cobalt-cobalt vector into the *ac*-plane as shown in Figure III.14. From the crystal structure ϕ can be defined more precisely as 5.7°.

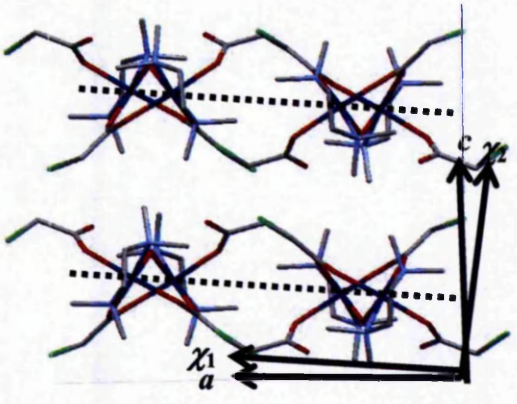

Figure III.14: Location of the principal magnetic axes χ_1 and χ_2 in the *ac*-plane of **6**.

At least two orthogonal planes have to be investigated, and here an orthogonal *abc** system has been chosen with c^* being the cross product of a and b. The rotational

plots in the *ac*- and *bc**-plane are shown in Figure III.15. Again, temperature dependence in the position of the principal magnetic axis has been observed in the *ac*-plane, but this time significantly stronger than in **3**. In the *bc**-plane such a shift is prohibited by the symmetry restrictions of $\chi_b = \chi_3$ at all temperatures, and as expected minimum and maximum susceptibility are observed in exactly the same positions at 300 and 10 K.

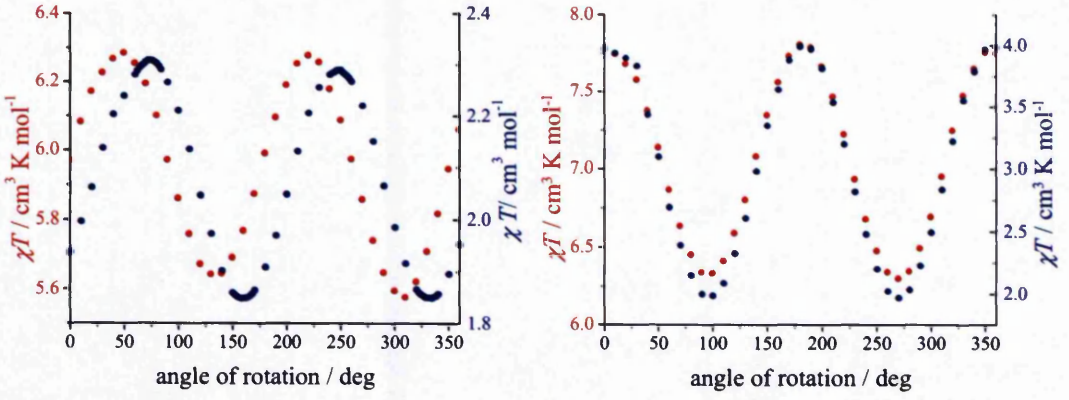

Figure III.15: Rotational studies in the *ac*-plane (left) and the *bc**-plane (right) of **6** at 300 K (red) and 10 K (blue).

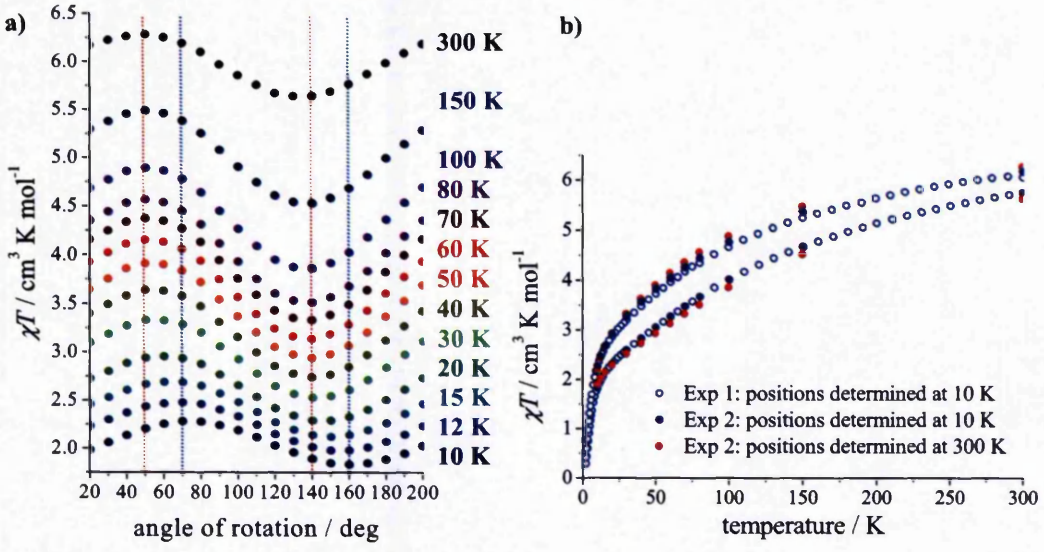

Figure III.16: a) Gradual shift in the minimum and maximum susceptibility observed in the *ac*-plane of **6**. b) Estimation of the influence of the 20° shift on the overall anisotropy of **6** with respect to the experimental error.

To follow the temperature dependence in the *ac*-plane rotational studies have been carried out at various temperatures. The result, a fully reversible change in the

positions of minima and maxima, is plotted in Figure III.16. A structural phase transition is expected to induce a sudden change in the magnetic properties. In contrast a very gradual shift is observed here. Furthermore, the temperature independence in the *bc**-plane does not imply a structural change, and both observations favour the explanation of a change in ϕ rather than in the crystal structure. However, only a low temperature X-ray study, preferably below 20 K, where the strongest shift is observed, could confidently support or exclude a crystallographic phase transition. Figure III.16 b) shows the temperature dependent susceptibility measured in two individual experiments to determine the influence of the 20° shift on the overall anisotropy. The blue rings show the susceptibility between 2 and 300 K in the maximum and minimum positions determined at 10 K. The solid dots are experimental data taken from the rotational plot in Figure III.16 a) in the low temperature extrema (blue) and the high temperature extrema (red) positions. The different positions are indicated as dotted lines in Figure III.16 a). Compared to the anisotropy within the *ac*-plane and the experimental error between different measurements (blue ring and blue dot), the influence of the shift is rather small. At low temperatures the three curves overlay, hence the system is not sensitive to the 20° angle shift.

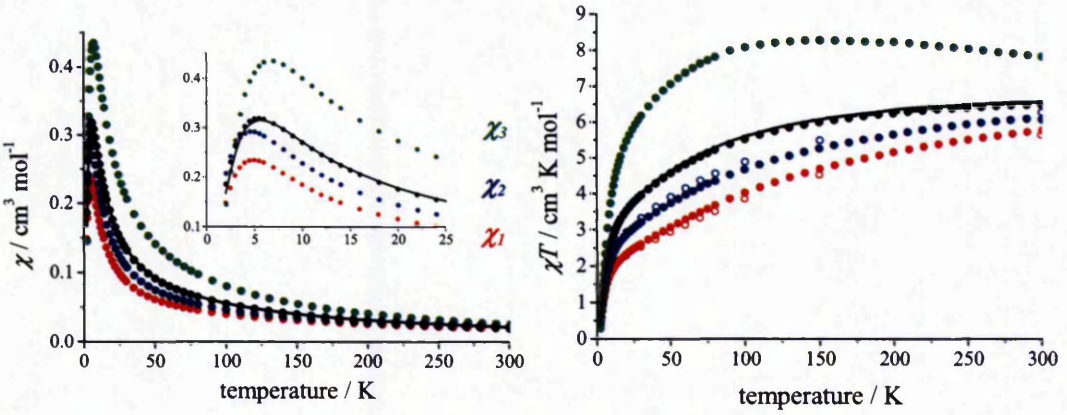

Figure III.17: Temperature dependent susceptibility of **6** along the three principal magnetic axes. χT and the maximum of χ show strong anisotropy. The principal average (line) overlays with the powder experiment (black, no eicosane). Solid dots: position defined at 10 K, rings: position defined at 300 K.

The magnetic properties of **6** were measured along the three principal magnetic directions. Strong anisotropy has been observed in the temperature dependent

susceptibility, the temperature of the maximum of χ, the saturation of the magnetisation, and the inflection point of the sigmoidal magnetisation *vs.* magnetic field curve. In all measurements the principal average agrees very well with the magnetic properties of the powder. Figure III.17 shows χ and χT of **6** along the three principal magnetic axes. Significant experimental values for the different orientations are listed in Table III.4.

orientation	χT at 300 K	Temperature at χ_{peak} / K	Magnetic field at inflection / T	Magnetisation at 7 T / $N\mu_B$
M_1	5.77 / 5.64	5.0	3.65	3.30
M_3	7.83	7.0	2.75	6.22
M_2	6.07 / 6.28	4.5	3.35	3.78
powder / average	6.5	5.5	3.05 / 3.25	4.39

Table III.4: Anisotropic magnetic properties obtained from the single crystal SQUID experiment in the different principal directions (see also Figures III.17 and III.18).

The strongest signal is observed for χ_3 along crystal *b*, the weakest signal χ_1 along the projection of the cobalt-cobalt vector into the *ac*-plane. Overall at room temperature a stronger anisotropy (*ca.* 5.6 cm^3 K mol^{-1} – *ca.* 7.8 cm^3 K mol^{-1}) than in **5** is observed, indicating that crystal packing induces less cancellation effects of the single ion anisotropy. The anisotropy within the *ac*-plane is significantly smaller than the anisotropy between this plane and the unique axis *b*, reminiscent of an almost axial system. Furthermore, the shape of the two χT curves in the *ac*-plane is very similar indicating a very similar exchange interaction. The difference lays in the absolute intensity of χT, which is related to the slope of the Zeeman splitting of the individual components or, in conventional spin-only terminology, the "*g*"-value. In addition, a shift in the temperature of the maximum χ with $T_3 > T_1 > T_2$ has been observed. Again the peak in the powder measurement is reproduced well by the principal average. The peak position in the temperature dependent susceptibility is a direct measure for the strength of the antiferromagnetic exchange interaction. The strongest antiferromagnetic exchange has been observed along *b* with a peak at 7 K. Within the *ac*-plane the exchange interactions are smaller and very similar with a peak at 5 K for χ_1 and a peak at 4.5 K for χ_2. Here it is important to note that measurements have been performed in 0.5 K steps and an error of ± 0.25 K in the determination of the maximum should be taken into account, which leads to an even stronger similarity of χ_1 and χ_2. The above interpretations are supported by the field

dependent magnetisation, which is shown in Figure III.18 for 1.8 and 4 K. Intermediate temperatures are plotted for completeness in Appendix 3.6.

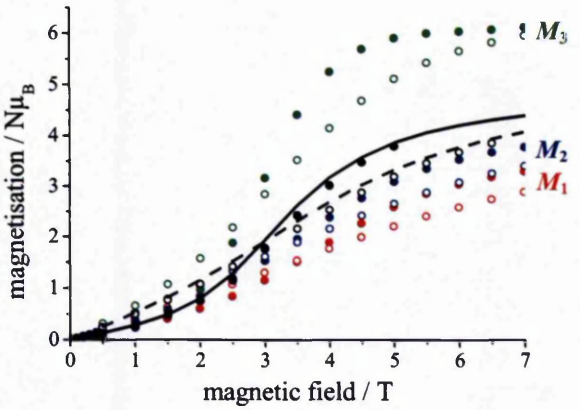

Figure III.18: Field dependent magnetisation of **6** along the three principal magnetic axes at 1.8 K (solid) and 4 K (ring). Strong anisotropy is observed in the saturation of the magnetisation and in the magnetic field, which shows the inflection point. The principal average (line solid: 2 K, dash: 4 K) overlays well with the powder experiment (black).

Anisotropy is observed in both the saturation value of the magnetisation, a direct measure of the slope of the Zeeman splitting (or "*g*"-value), and the field of inflection, a direct measure of the exchange interaction. The lowest inflection point at 2.75 T, and hence strongest magnetic exchange is again observed for M_3 along *b*. Values of 3.35 T and 3.65 T have been obtained for M_1 and M_2, respectively. This time measurements were performed in 0.5 T steps, however the magnetisation was measured at four different temperatures and all curves overlay at one inflection point. Extrapolation allows for the determination of the inflection point with only a small error of ± 0.1 T despite the comparably large field steps (Appendix 3.6).

A particularly strong difference is observed in the slope of the Zeeman splitting. If an effective "*g*"-value was to be assigned to the three principal directions, the following numbers are observed for an effective "triplet" "S_{eff}" = 1: "$g_{eff,1}$" ≥ 3.3, "$g_{eff,2}$" ≥ 3.8, "$g_{eff,3}$" = 6.2. A comparably strong anisotropy has been observed from the saturation of the magnetisation of the axial monomer **1** discussed in Chapter II with effective "*g*-values" of "g_{xx}" = "g_{yy}" = 5.58, "g_{zz}" = 2.50. This supports the above observation that the orientation of the molecules within the crystal does not lead to a strong cancellation of the single ion anisotropies. For **1** and **6** similar average effective "*g*"-values of "*g*" = 4.55 and "g_{eff}" = 4.4 are obtained, respectively.

III.3 Electron paramagnetic resonance spectroscopy on cobalt(II) dimetallics

Electron paramagnetic resonance spectroscopy is a very sensitive tool to investigate magnetic exchange interactions. In other examples it has been shown that EPR spectroscopy can clearly identify magnetic exchange interactions that are too weak to be detected with a commercial SQUID magnetometer.[87] Furthermore, several recent studies have used EPR spectroscopy to determine the physical origin of anisotropy effects, for example quantum tunnelling of magnetisation.[19,21,117] Especially in the presence of the highly anisotropic cobalt(II) ion, EPR spectroscopy is a promising tool to investigate anisotropic exchange between the metal ions. Surprisingly, to our knowledge, there are *no* examples reported of EPR spectroscopy on exchange coupled octahedral cobalt(II) ions to date. We are only aware of one other example studied by Hill and *co*-workers who have performed single crystal EPR spectroscopy on the ferromagnetically coupled heterocubane $[Co(hmp)(dmb)Cl]_4$[118] (where dmb = 3,3-dimethyl-1-butanol and Hhmp = 2-hydroxy-methylpyridine) and on its diamagnetic zinc analogue doped with cobalt(II) ions for the determination of the single ion properties.[119]

Antiferromagnetic exchange interactions observed in six (**3**, **5-9**) out of the seven dimetallics are weak, but have been detected undoubtedly with SQUID measurements. For the ferromagnetic example (**4**) on the other hand, the magnetic exchange is so weak that only a very small increase in χT is detected at magnetic fields ≤ 0.1 T, while at 0.5 and 1 T the ferromagnetic coupling is masked by effects due to splitting in zero field. From magnetic measurements alone, it is not possible to claim confidently the observation of exchange interactions in **4**. In the following sections multifrequency EPR spectra on powder and single crystal samples of **4** are discussed, which prove the ferromagnetic exchange interactions, and allow for an in-depth analysis of the low lying energy manifold.

The interesting results obtained for **4** encouraged the extension of the study on dimetallic compounds with EPR to an antiferromagnetic example, and Q- and W-band spectra will also be presented for the antiferromagnetic analogue **3**.

III.3.1. EPR spectroscopy on powder samples of 3 and 4

Low temperature (1.63 – 30 K) multifrequency EPR spectra have been recorded between 9.4 and 345 GHz on immobilized powder samples. Figure III.19 shows spectra recorded at X-band, Q-band and W-band frequencies. In Figure III.20 high-field EPR spectra (HFEPR) are plotted, which have been measured at the GHMFL in Grenoble in collaboration with Dr. Anne-Laure Barra.

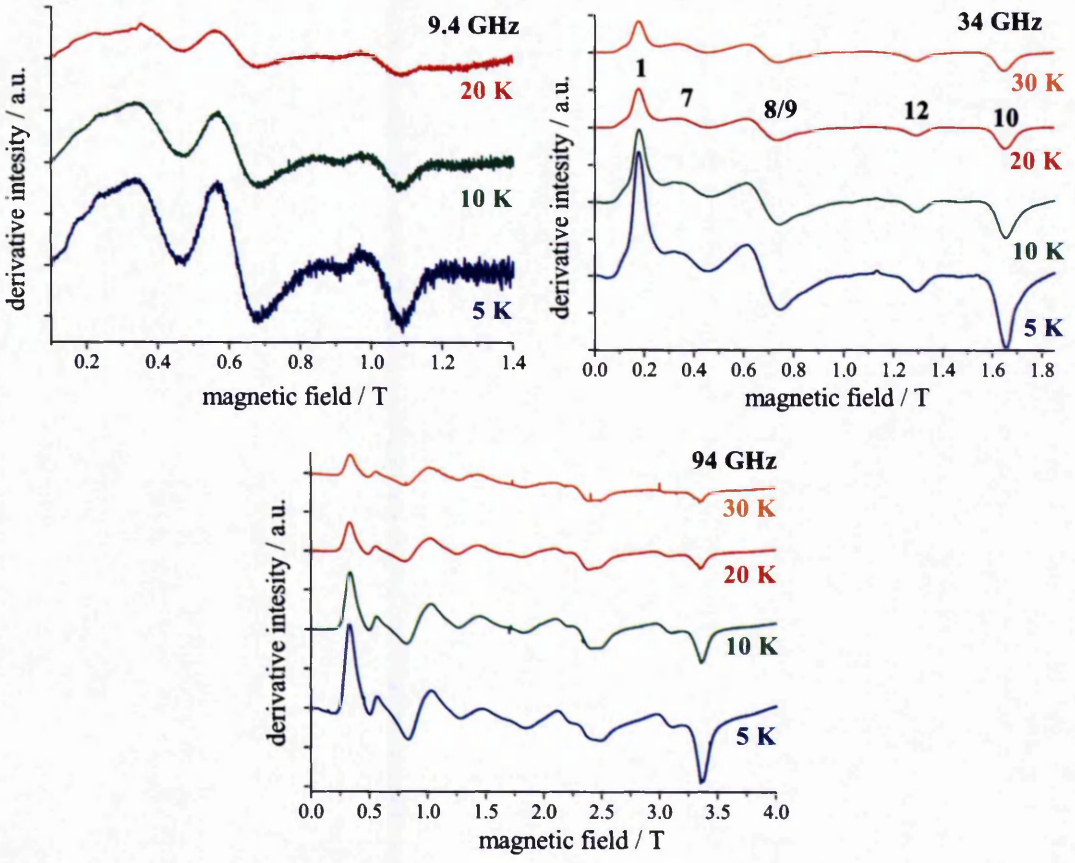

Figure III.19: Variable temperature X-band, Q-band and W-band spectra on powder samples of **4** fixed in eicosane. Numbers in the Q-band spectrum at 20 K relate to transitions in the single crystal EPR spectra of **4** (Section III.3.2).

The spectra are very rich with up to 12 transitions and immediately show that the transitions must occur between energy levels arising from exchange coupling between the two cobalt(II) ions. In the absence of metal hyperfine interactions, uncoupled cobalt(II) ions show a maximum of three transitions from anisotropic Zeeman splitting of the ground Kramers doublet as shown for the monometallic **1** in

Chapter II, and also for a cobalt(II) ion within a Ga_7Co ring (**12**) in Section IV.2, where the ligand environment is more similar to the one in **4**.

At frequencies ≥ 94 GHz all spectra are centred on "g_{eff}" ~ 4 as expected for cobalt(II) ions and reminiscent of spectra arising from a spin-triplet with unusual fine splitting and *g*-anisotropy. The overall form of the spectra appears to support the simple picture of an effective "triplet" arising from the coupling between the lowest Kramers doublets of the two cobalt(II) ions.

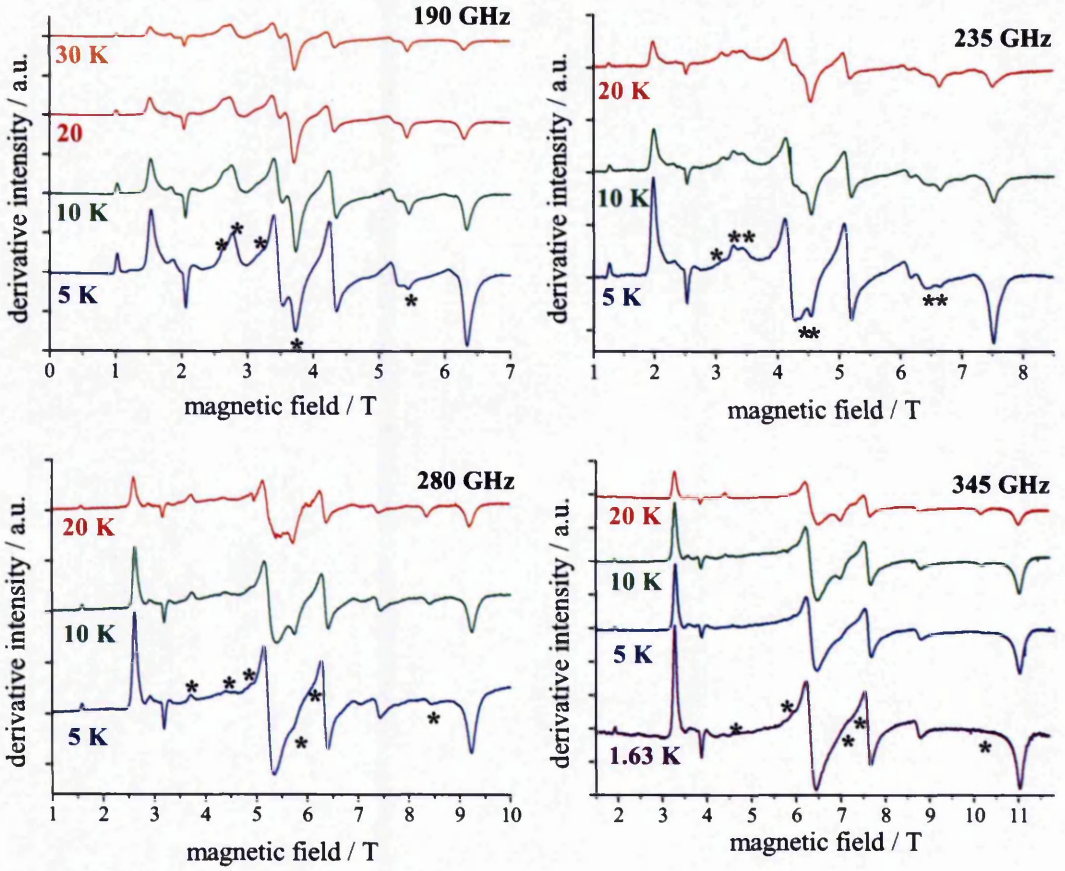

Figure III.20: Variable temperature HFEPR spectra recorded at the GHMFL in Grenoble on a powder sample of **4** pressed into a pellet. The star indicates hot transitions.

Significant temperature dependence, which increases with the applied magnetic field, has been observed. In Appendix 3.7 the high frequency spectra (190 – 345 GHz) are normalized to the strong low field transition 2 (Table III.5) allowing for a better assignment of cold transitions from the lowest energy level, and hot (star) transitions originating from higher energy levels. It is important to note, that at frequencies < 285 GHz all features are present at 5 K, although signals marked with a star gain higher relative intensity upon raising the temperature. In Figure III.8 the

magnetisation of **4** has shown a very clear saturation above 3 T, which indicates a good isolation of the ground energy manifold from further excited states. In Section III.4 inelastic neutron scattering (INS) will confirm this observation. Hence, transitions observed at with EPR spectroscopy at 5 K must arise from the same manifold, and the temperature dependence cannot be attributed to the population of further excited states. Nevertheless, at temperatures below 10 K hot transitions are lost at higher EPR frequencies and only reappear at higher temperatures. The effect can be explained with the strong Zeeman splitting in high magnetic fields: While at a low magnetic field the thermal energy at 5 K is sufficient to (partly) populate all energy levels within the ground multiplet, the strong splitting at high magnetic fields leads to a thermal population of only the lowest multiplet levels at 5 K. Upon raising the temperature the remaining energy levels are populated and the corresponding transitions reappear in the spectrum.

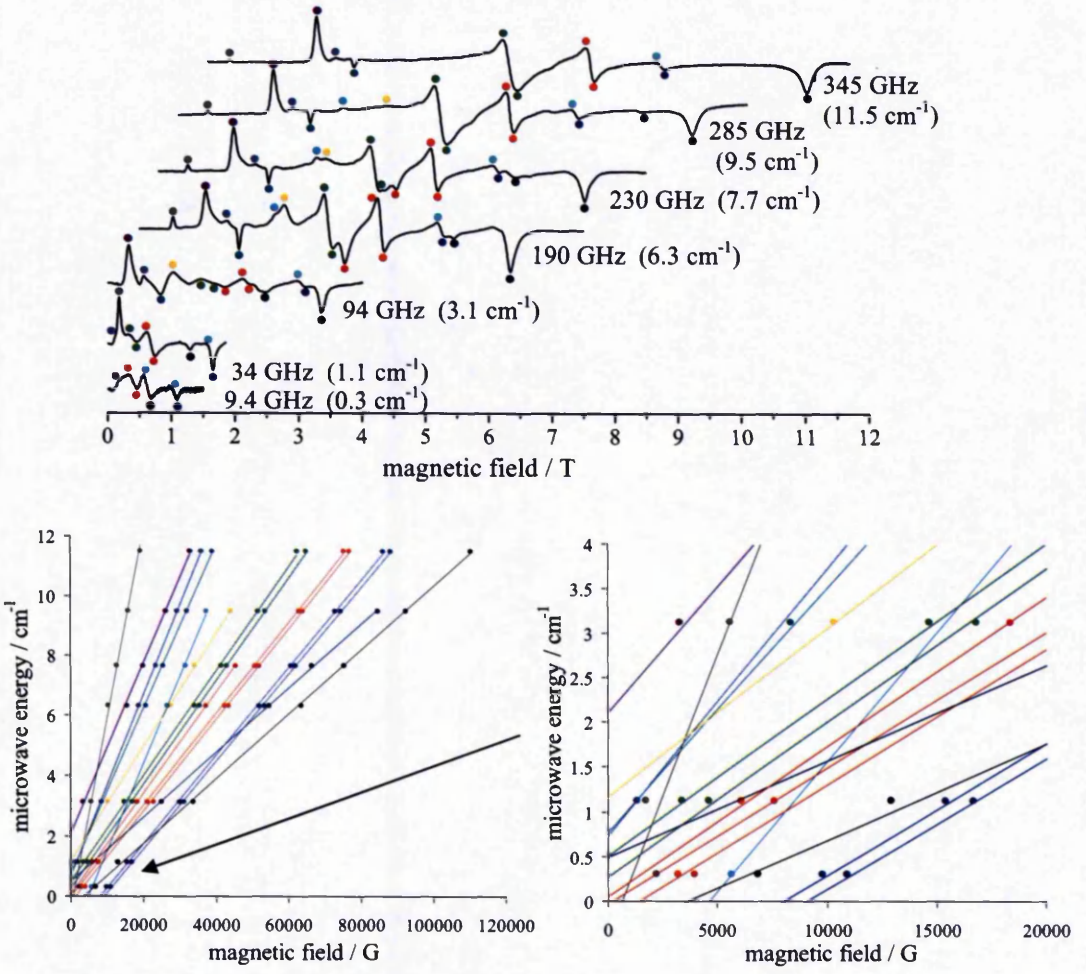

Figure III.21: Linear dependence of the resonance magnetic field of **4** on the microwave frequency at 5 K, the coloured dots in the 5 K spectra correspond to the colour in the energy *vs.* magnetic field graph. The right hand panel is an expansion of low field/energy region.

In Figure III.21 the dependence of the resonance magnetic field on the microwave energy is plotted for 12 resonance field positions (Table III.5) in the different spectra at 5 K. Certainly down to Q-band, possibly even down to X-band, linear frequency dependence is observed. However, at the lower frequencies it is difficult to assign the transitions due to overlap of excitations, hence the assignment at X-band may or may not be valid. Considering the strong anisotropy of cobalt(II) ions arising from spin-orbit coupling and mixing from upper terms into the ground $^4T_{1g}$ term, which introduces non-linearity into the Zeeman splitting, such a high degree of linearity was not expected.

Table III.5 summarises the effective "*g*"-values obtained from the slope of the energy *vs.* magnetic field plot. Apart from transition 1 with "g_{eff}" = 13.48, all other "*g*"-values are within the range of 2.3 – 6.4, similar to the values of 3.3 – 6.2 observed for **6** with single crystal SQUID experiments. The low field (or in spin-only EPR terminology "half-field") transition indicates a spin forbidden $\Delta m = \pm 2$ transition, which appears partly allowed in **4**.

	"g_{eff}"-value (slope/μ_B)	Splitting in ZF / cm^{-1} (*y*-intercept)	Goodness of linear fit R^2
1	13.48	(-0.41)	0.9927
2	6.07	2.10	0.9992
3	6.38	0.73	0.9999
4	5.88	0.77	0.9995
5*	6.19	(-1.13)	0.9995
6*	4.05	1.16	0.9997
7	3.75	0.51	0.9995
7	3.70	0.27	0.9998
8*	3.60	0.05	0.9999
9	3.26	(-0.03)	0.9991
9	3.25	(-0.22)	0.9994
10	3.14	(-1.17)	0.9998
10	3.11	(-1.31)	0.9999
11*	2.29	(-0.50)	0.9996
12	2.30	(-0.39)	0.9997

Table III.5: "g_{eff}"-values and splitting in zero-field obtained from linear regression of the frequency dependent resonance field in **4**. Parentheses indicate physically meaningless negative energies at zero-field. Stars label hot transitions.

Extrapolation of the linear regression back to zero-field may allow for the splitting at zero-field to be estimated. For a number of transitions this value is negative, which is physically meaningless. At small magnetic fields non-linearity in the frequency

dependence of the resonance magnetic field is expected.[117,120] Although it is important not to over-interpret what can be drawn from the linear extrapolations to zero-field, it is worth comparing the obtained positive energies to the transitions observed by INS on $\mathbf{4}^{D}$ presented in Section III.4, which are 0.8 cm^{-1}, 1.6 cm^{-1} and 2.4 cm^{-1}. Exactly corresponding numbers cannot be found within the zero-field energies determined from the EPR spectra, but the only positive energies above the INS resolution limit of *ca.* 0.5 cm^{-1} lie between 0.7 and 2.1 cm^{-1}, which are in a comparable order to the observations from INS.

For some transitions the splitting at zero-field exceeds the microwave energy in the lower frequency measurements. Hence it is not possible to observe transition 2 and 6 at Q-band (ν = 1.13 cm^{-1}) and only a small number of excitations can be induced at X-band (ν = 0.3 cm^{-1}).

Strictly, transitions between different "spin-states" should be forbidden due to the EPR selection rules of $\Delta m_S = \pm 1$ and $\Delta S = 0$. However **4** is not a spin-only system and inter-multiplet transitions may be partly allowed through spin-orbit coupling and mixing of wavefunctions.

For the antiferromagnetic analogue **3**, a similar situation is expected. Figure III.22 shows the Q- and W-band spectra of **3** between 5 and 20 K. Hot transitions in the W-band spectrum are again marked with a star.

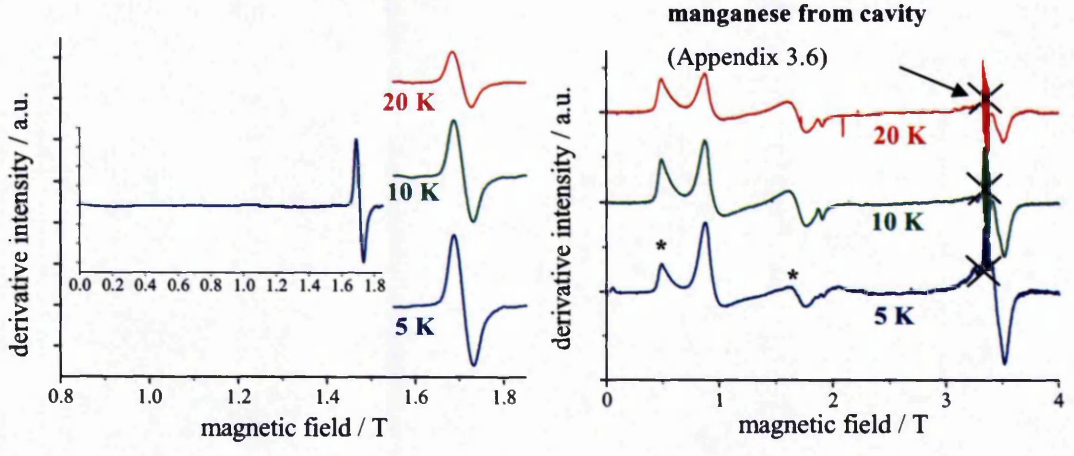

Figure III.22: Variable temperature Q-band and W-band spectra on powder samples of **3** immobilized in eicosane. Stars mark hot transitions.

Transitions at W-band correspond to "g_{eff}"-values of 13.64, 7.7, 4.0 and 1.9. Again a transition with the very large "g_{eff}"-value of 13.64 indicates a partly allowed spin

forbidden $\Delta m = 2$ excitation. For the remaining transitions a slightly larger spread is observed, indicating a stronger splitting in zero-field than observed in **4**. This is confirmed by the Q-band spectrum of **3**, which only shows a transition at very high field. Therefore, any energy splitting at zero-field must be larger than the microwave energy at Q-band of 1.13 cm^{-1}. Further confirmation has been obtained from INS measurements on the deuterated derivative $\mathbf{3}^{D}$, which has shown splittings in zero-field ≥ 1.9 cm^{-1} (Section III.4).

Overall, the multifrequency EPR spectra of **3** and **4** seem to confirm the model of the coupling between two Kramers doublets to give rise to a singlet and a triplet state. Further interpretation will be discussed together with the results from single crystal EPR spectroscopy on **4** in Section III.3.2, INS on $\mathbf{3}^{D}$ and $\mathbf{4}^{D}$ in Section III.4, and the concluding model in Section III.5.

III.3.2. Single crystal EPR spectroscopy of 4

The previous section on powder EPR spectroscopy has shown that in the case of **4** more detailed information on the electronic structure of the system can be obtained from EPR in comparison to the less sensitive SQUID magnetometry. Furthermore, single crystal measurements on a SQUID could only provide information on the orientation of the principal magnetic axes with respect to the crystal structure, while additional low temperature measurements were prohibited by the instability of large crystals at low temperatures. Fortunately it was possible to obtain a full set of single crystal data by EPR spectroscopy to investigate the anisotropy within the system.
Q-band frequency was chosen for the single crystal EPR study. The information from Q-band EPR spectroscopy will be limited by the available exciting energy (*ca.* 1.13 cm^{-1}), which is less than some of the energy differences in zero field as seen in Figure III.21 and Table III.5. Nevertheless, apart from one major transition 2 in Table III.5, the majority of the signals observed at W-band and higher frequencies are still present at Q-band, although not as well resolved. Single crystal experiments are more readily performed at Q-band than at W-band due to the larger cavity, which allows for larger sample dimensions, and a higher stability of the instrument to

temperature changes, which occur during sample rotation. No significant temperature dependence has been observed for the Q-band spectra on powder samples, and more importantly, multifrequency studies reported in the previous section have shown that all transitions observed up to 30 K correspond to the same ground multiplet, and no further excited states are populated at this temperature. For practical reasons all rotational studies have consequently been performed at 20 K rather than 5 K.

Figures III.23 – III.25 show the 20 K single crystal EPR spectra of **4** in the three orthogonal planes a^*b, a/a^*c and bc, respectively, with $a^* = b \times c$. For details on the setup of the single crystal experiment see also Section VI.3.3. From mounting and comparison between the spectra in the different planes, the crystallographic axes can be assigned to the spectra, relating the anisotropy to the molecular orientation in the crystal. An error of ± 5° on the crystal position is estimated for manual mounting and 10° steps on a goniometer with *ca.* 2° accuracy.

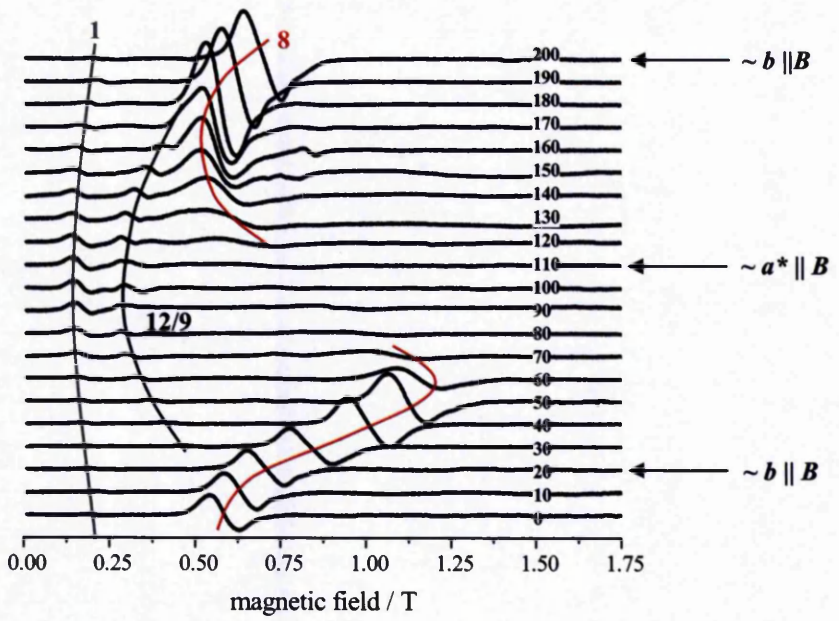

Figure III.23: Q-band single crystal EPR spectra measured at 20 K during rotation of **4** in the a^*b-plane. From crystal mounting and comparison to the other planes the approximate positions of a^* and b have been determined.

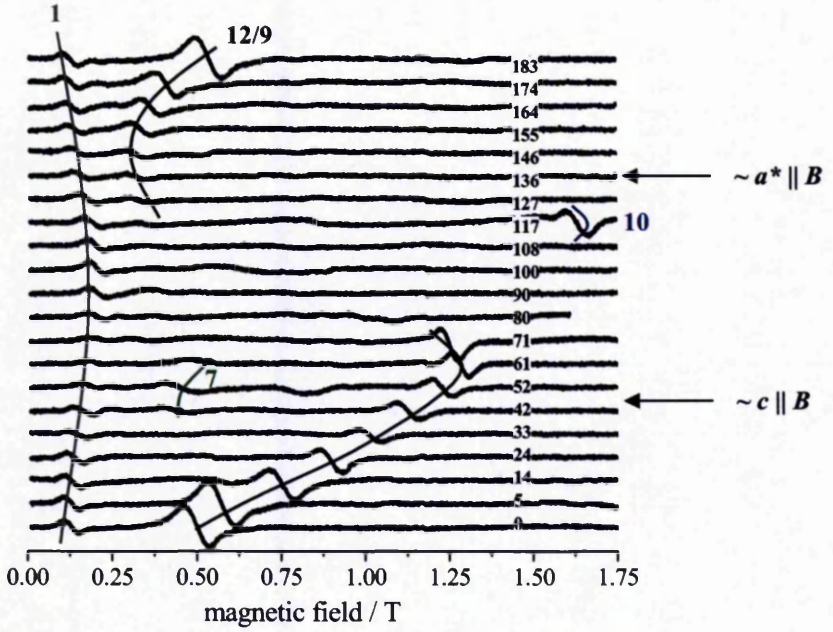

Figure III.24: Q-band single crystal EPR spectra measured at 20 K during rotation of **4** in the *ac*-plane. From crystal mounting and comparison to the other planes the approximate positions of *c* and *a** have been determined.

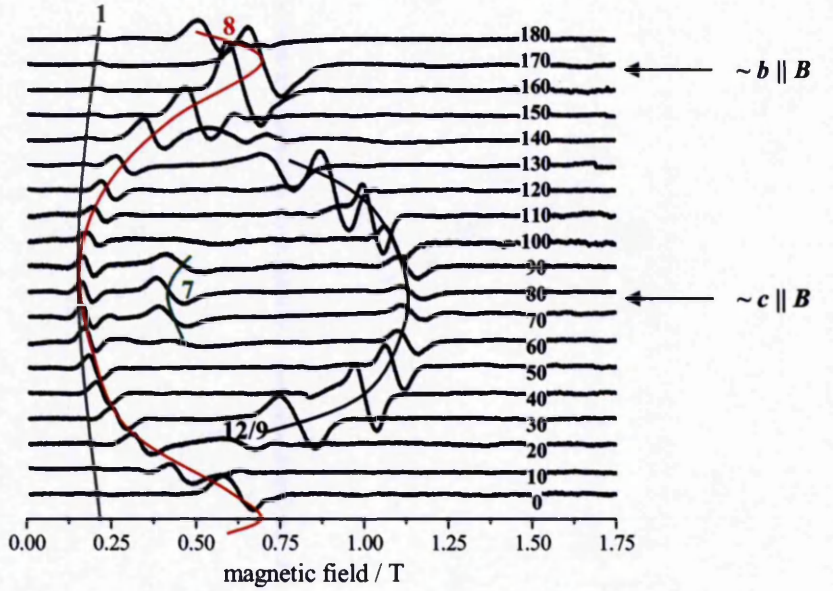

Figure III.25: Q-band single crystal EPR spectra measured at 20 K during rotation of **4** in the *bc*-plane. From crystal mounting and comparison to the other planes the approximate positions of *b* and *c* have been determined.

Five features (1: "g_{eff}" = 13.48, 7: "g_{eff}" = 7.73 8: "g_{eff}" = 3.60 overlaying with 9: "g_{eff}" = 3.26, 12: "g_{eff}" =2.30 10: "g_{eff}" = 3.13) have been observed in the powder spectrum of **4** (Figure III.19 and Table III.5). Coloured lines in Figures III.23 – III.25 visualize the angular dependence of the corresponding transitions in the three

orthogonal planes. Transitions 9 and 12 correspond to a transition between the same energy levels as shown in Section III.5.

In the following, the single crystal EPR spectra are discussed in two steps:

1. Transitions in the three orthogonal crystal planes are related to transitions in the multifrequency powder EPR spectra.
2. The anisotropy within the three planes is related to the crystal structure.

The single crystal spectra are dominated by transitions 8 and 12, which show the highest relative intensities and strongest dependence on the crystal orientation.

Transition 8 occurs in both the a^*b- and the bc-plane; the corresponding "g_{eff}"-values vary between 4.3 and 2.1 in the a^*b-plane, and between 13.5 and 3.5 in the bc-plane. In both planes the extrema are separated by *ca.* 90° and transition 8 overlays with transition 12 along the unique b-axis at a magnetic field of *ca.* 7000 G. This transition is present in the powder spectrum at *ca.* 6800 G and the corresponding "g_{eff}"-value lies between 3.6 (transition 8) and 3.25 (transition 12/9). Around a^*, where the contribution from b becomes small, transition 8 vanishes.

Transition 12 is present in all three planes and shows a strong angle dependence in the a^*c- and bc-plane, while the angle dependence in the a^*b-plane is weak compared to that of transition 8. The strongest anisotropy is observed in the a^*c-plane, where "g_{eff}"-values vary between *ca.* 1.9 and 7.5 with a separation of *ca.* 90°. In the powder spectrum, the high field extreme of transition 12 (*ca.* 12880 G) is observed at *ca.* 12900 G. Between a^* and c the appearance of transition 12 is interrupted, but only in one direction. In the a^*b-plane transition 12 varies little with the angle of rotation, and its weak intensity is comparable to the "spin-forbidden" transition 1. This may indicate that transition 12 violates the EPR selection rules in this plane, but becomes partly allowed due to spin-orbit coupling and mixing of wavefunctions. In the bc-plane transition 12 varies between "g_{eff}" ~ 2.1 along c and "g_{eff}" ~ 3.5 along b

Transition 1 is present in all three planes and shows little angle dependence. Such behaviour is characteristic of forbidden "half-field" transitions, hence transitions with $\Delta m = \pm 2$, in accord with the high "g_{eff}"-value.

The remaining two transitions 7 and 10 only appear in very specific positions. Transition 7 is observed along the c-axis in the a^*c- and bc-plane. In the bc-plane, 7

shows strongest intensity along *c* and disappears within the next 20° in either direction. Transitions occur between *ca.* 4200 and 5000 G, the minimum corresponds to the transition in the powder spectrum at *ca.* 4000 G. Transition 10 is only observed in one spectrum 20° away from *a** moving towards *c*. Measurements 180° away from this position and with smaller angle steps in the area of ± 10° have shown that the transition is observed reproducibly, but only seen in this particular position ± *ca.* 6°. In either direction the signal is immediately broadened and shifted to slightly lower field. The sharpest transition occurs at the maximum field of *ca.* 16322 G (centre of the derivative signal) and is observed as a strong transition in the powder spectrum at 16524 G (minimum of the absorption shaped signal).

Figure III.26 shows the crystal packing of **4** in different rotational orientations with highlighted cobalt-oxygen-cobalt atoms and bonds down the *c* axis in the *a*b*-plane. Depth cue shows lighter molecules in the front and dark molecules further back; wedges indicate the perspective of the cobalt-cobalt vector. The principal axis *b* runs perpendicular to the cobalt-cobalt vector and through the central oxygen of the bridging water molecule, relating the two cobalt(II) centres by C_2 symmetry. All molecules are magnetically equivalent within the crystal packing. The vector *a** corresponds to the projection of the cobalt-cobalt vector into the *a*b*-plane. Spectra in the *a*b*-plane are dominated by transition 8, which exhibits turning points *between* the crystallographic axes *ca.* ± 50° away from *a** and *ca.* ± 40° away from *b*. ± 41° away from *b* in either direction the projections of the water-cobalt-bonds into the *a*b*-plane become perpendicular to *B* (images 2 and 4 in Figure III.26). It is interesting to note that the two orientations have very different spectral responses, even though they correspond to very similar structural orientations. This difference must arise from the orientation of the principal magnetic axes with respect to the molecular structure. By symmetry one of the principal molecular magnetic axes (here defined as *x* following conventions of the model in Section III.5) aligns with the unique crystal axis *b* in a monoclinic crystal system.[3] From single crystal magnetic measurements in the *ac*-plane (Section III.2.2) it appears that the cobalt-cobalt vector plays an important role on the anisotropy of the system. Therefore three principal axes may be assigned as: *b* (by symmetry), the cobalt-cobalt vector (from single crystal magnetic properties), and the cross product of the two (Figure III.27).

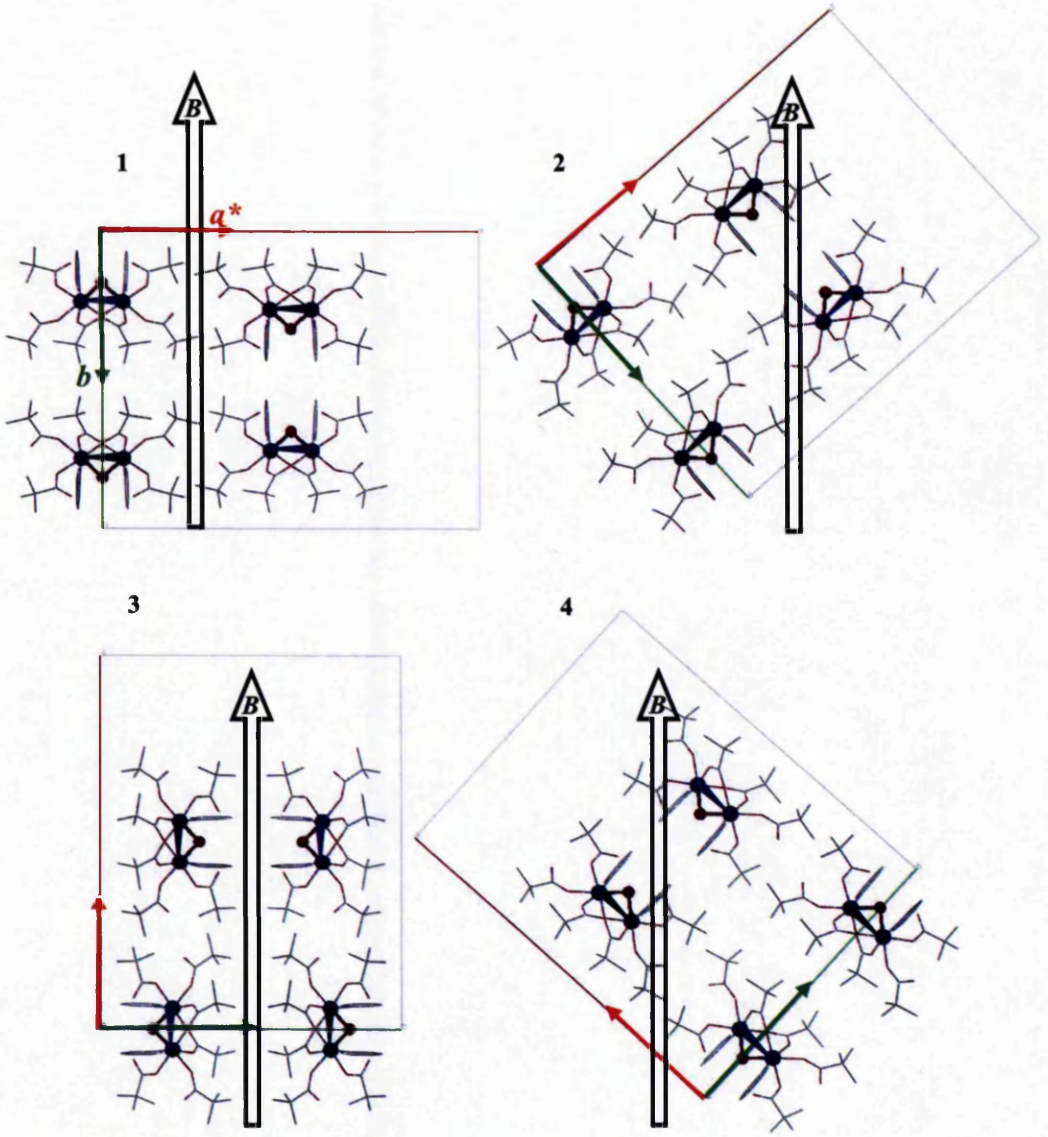

Figure III.26: Orientation of the molecules of **4** in the a^*b-plane with respect to the magnetic field B during rotation around c. Orientations: $b \parallel B$, 41° rotation left; $a^* \parallel B$, 49° rotation left.

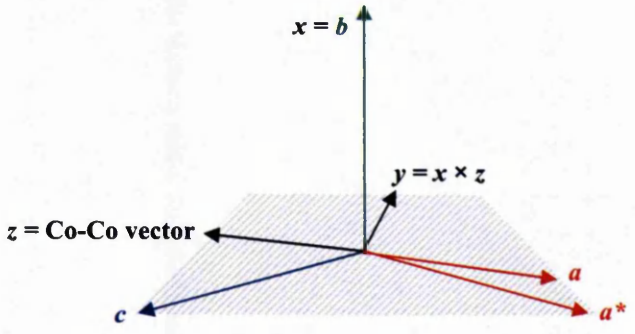

Figure III.27: Proposed principal magnetic axes for **4** from single crystal magnetic measurements and EPR spectroscopy.

At this stage, the assignment is a pure hypothesis; however, throughout the following discussions and in Section III.5 it will become clear that complementary experimental data can indeed be explained within this axis framework.

Along $b = x$, contributions from y and z are small. When moving towards a^* as depicted in Figure III.26, the projection of x onto B points in the opposite direction to the magnetic field, while the projections of y and z onto B are oriented parallel to B. After a 90° turn in contrast, the projections of all three vectors x, y, z onto B point in the same magnetic field direction. Significant difference in the intensities of transition 8 may even allow for going a step further: Maximum intensity is achieved with $x = b$ parallel B, where the contributions from y and z are small. Intensities remain strong, as long as the angle between b and the magnetic field is smaller than 45°, hence x remains the major component projected onto B. Further rotation leads to a major influence from y and z, until around a^* the contribution from x becomes small and the transition disappears. In conclusion, transition 8 is closely related to the principal direction $x = b$.

Transition 12 shows its turning points along the axes in the a^*b-plane, with a minimum resonance magnetic field along a^* and a maximum magnetic resonance field for the overlap with transition 8 along b. In contrast to transition 8, maximum intensity of 12 is observed along a^* and the transition weakens towards b. This indicates, that transition 12 either corresponds to the cobalt-cobalt vector z or the orthogonal y or both. Overall the intensity of 12 is relatively weak in this plane, indicating that this transition may only be partly allowed in this orientation.

Figure III.28 shows different orientations of the molecules in the second measurement plane a/a^*c during rotation around b. Both cobalt ions per molecule are located in the ac-plane, + and – indicate whether the corresponding water molecules lie above or below, respectively.

The rotation axis b is oriented perpendicular to the magnetic field at any measurement angle, hence the contribution from b is expected to be small in the a^*c-plane. Consequently transition 8, which is related to the principal direction $x = b$, does not appear in spectra recorded in the a^*c-plane. Spectra in the a^*c-plane are dominated by transition 12, which exhibits off-axis turning points in this plane. The strongest intensity of 12 is observed *ca.* 40° away from c at the inflection point of the angle dependence, where the field is aligned perpendicular to the cobalt-cobalt vector

(image 4 in Figure III.28). The intensities of the spectra agree with observations in the previous plane, where spectra have shown maximum intensities along *b*, hence orthogonal to the cobalt-cobalt vector. 90° away from this orientation (image 2 in Figure III.28) the magnetic field is oriented parallel to the cobalt-cobalt vector and spectroscopically only the forbidden transition 1 is still observed.

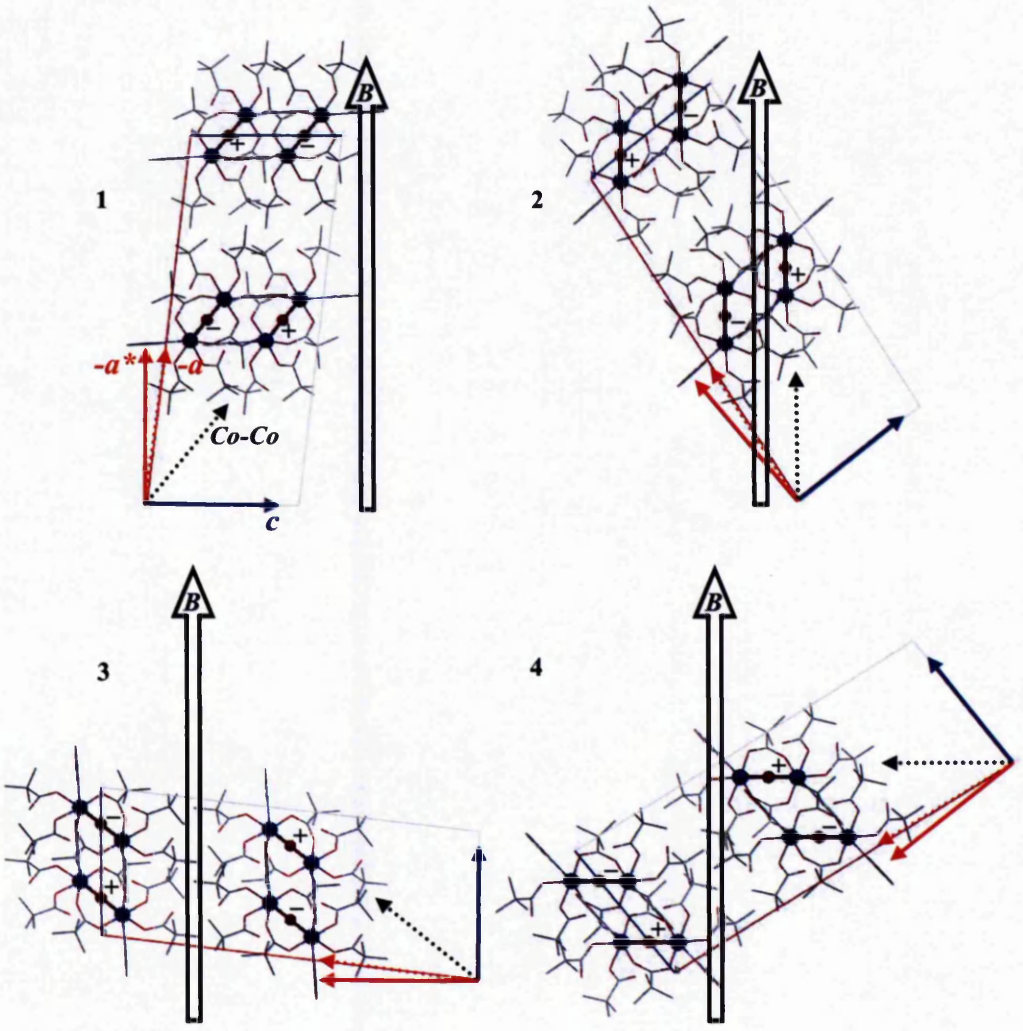

Figure III.28: Orientation of the molecules of **4** in the *a*/*a***c*-plane with respect to the magnetic field *B* during rotation around *b*. Orientations: *a** || *B*, 39° rotation left; *c* || *B*, 39° rotation left.

From spectra in the *a***b*-plane transition 12 has been assigned to the *y* or *z* component. The disappearance of 12 along *x* in the *a***c*-plane appears to allow for further constraints, and transition 12 with "g_{eff}" = 2.30 may be related to the principal *y* direction, perpendicular to the cobalt-cobalt vector. However, this assumption is not consistent with results from single crystal SQUID measurements on **4** (Section

III.2.2), which have related the largest molecular magnetisation and hence the *largest* effective "g_{eff}"-value to the *y*-direction ($\chi_y = \chi_2$). Consequently the small "g_{eff}"-value of transition 12 should correspond to the cobalt-cobalt vector *z* with $\chi_z = \chi_1$ in the single crystal susceptibility measurements. As mentioned in the beginning of this section, the information from Q-band EPR-spectroscopy is limited by the exciting energy, but also by the 2 T range of the Q-band magnet. Calculations of the corresponding Zeeman splitting in Section III.5 will show that the origin for the disappearance of 12 along *z* does not lie in the orientation of the molecules, but in the large magnetic field required to induce resonance conditions, which exceeds the range of the Q-band magnet.

The two intermediate positions, observed as turning points in the angular dependence of the resonance magnetic field, correspond to very similar crystallographic orientations, but, similar to the previous plane of measurement, exhibit very different spectroscopic responses. Within the accuracy of 10° steps, the turning points correspond roughly to the positions where the cobalt-cobalt vector is tilted by 45° with respect to the magnetic field. The spectral properties can again be related to the projection of the principal magnetic responses onto the magnetic field. Strongest intensity is observed where *y* is parallel *B*, and intensities remain strong, as long as the angle between *y* and the magnetic field does not exceed 45°. Larger angles lead to a weakening in the *y* contribution and, because transition 12 is not observed along *z*, the signal disappears.

Only in the *bc*-plane do turning points correspond to the crystallographic axes and, within the experimental error, changes in resonance magnetic field and intensity occur symmetrically from *c* to ± *b*. Figure III.29 shows the crystal packing of **4** down *a** in the *bc*-plane in different rotation orientations, where *b* corresponds to *x* and *c* to the projection of the cobalt-cobalt vector *z* into the *bc*-plane. Along *c* the maximum resonance magnetic field is observed for transition 12 and the minimum resonance magnetic fields for transitions 7 and 8. Along *b* transition 8 and 12 become one strong transition, which is also observed in the powder spectrum. Within the experimental error, transition 12 exhibits maximum intensity *ca.* ± 45° away from the two turning points. These orientations correspond to the images 2 and 4 in Figure III.29, where the projections of *y* and *z* are tilted 45° from *B*.

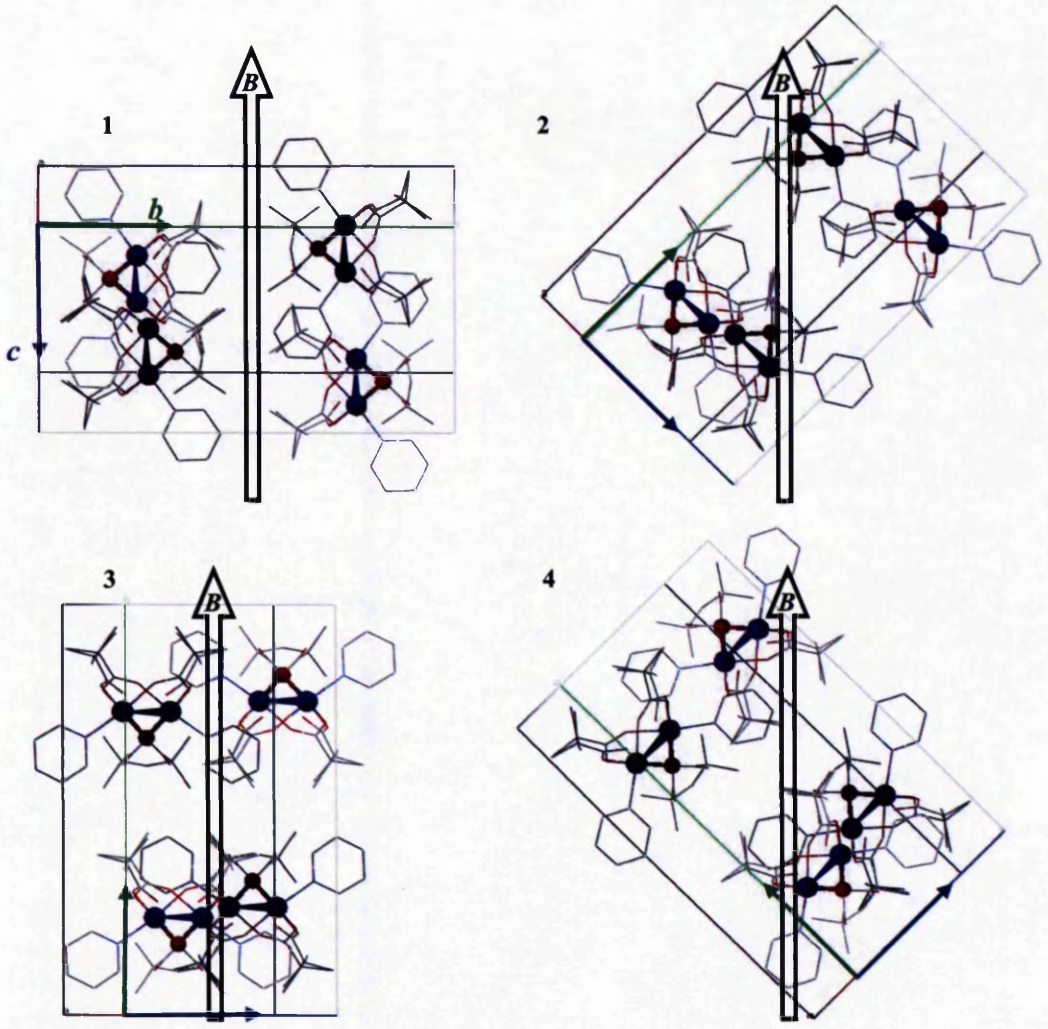

Figure III.29: Orientation of the molecules of **4** in the *bc*-plane with respect to the magnetic field *B* during rotation around *a**. Orientations: *b* || *B*, 45° rotation left; *c* || *B*, 45° rotation left

Moving from *c* towards *b*, the amplitude of transition 12 increased for angles < ± 45° and subsequently decreases for angles > ± 45°. Broadening of the spectral features arising from overlap with transition 8 does not allow detailed analysis of the intensity of 12 around *b*.

Transition 8, related to $x = b$, increases steadily in intensity when moving from *c* towards *b*. Similar to the behaviour of transition 12, a broadening is observed around *b*, where transitions 9 and 12 interfere. Along *c*, *b* is oriented perpendicular to the magnetic field, and its contribution is expected to be small. Nevertheless, transition 8 is still weakly observed, although with much smaller intensity than along *b*.

In contrast, transition 7 is strongest along *c* and its intensity weakens until disappearance when moving *ca.* ± 30° away from *c*.

In summary, single crystal EPR spectroscopy at Q-band frequency on **4** has allowed for the major transitions observed in the multi-frequency powder experiment to be assigned to the principal magnetic and spectroscopic axes:

a) Transitions 8 and 9, with effective powder "g_{eff}"-values of 3.60 and 3.25, respectively, corresponds to the contributions along $x = b$.

b) Transition 12, with a powder "g_{eff}"-value of 2.30 corresponds to the contribution along z, the cobalt-cobalt vector.

c) The two transitions 7 and 10 are only observed in very specific positions, which may indicate that they are not part of the allowed inter-triplet spectrum, but arise from inter-multiplet transitions that become partly allowed in certain orientations.

d) Transition 1 has been confirmed to be a "forbidden" $\Delta m = \pm 2$ transition.

One major transition (2, in Table III.5), which is observed with "g_{eff}" = 6.07 at higher frequency, is missing in the Q-band single crystal and powder spectra, because the corresponding splitting at zero field exceeds Q-band frequencies. This transition completes the "triplet"-like structure of the EPR spectra and may be assigned to the remaining principal direction y, the cross product between $x = b$ and the cobalt-cobalt vector z.

III.4 Inelastic neutron scattering on cobalt(II) dimetallics

Inelastic neutron scattering (INS) is a powerful experimental tool for investigations into molecular energy manifolds, as it provides direct access to the energy splitting, in both zero and applied magnetic fields. [99,102,121-124] In Section III.3 it was shown that back-extrapolation of the energy *vs.* magnetic field plots from EPR spectroscopy may allow for the zero-field energies to be determined in **4**, however non-linearity at low field may be present and confident results can only be obtained from a direct measurement at zero-field. With a different set of selection rules ($\Delta S = 0, \pm 1$ and $\Delta m_S = 0, \pm 1$) that allows for the observation of both intra- and inter-multiplet transitions, INS is a complementary technique to EPR spectroscopy. Consequently, transitions, which for EPR spectroscopy on **3** and **4** may have only been partly allowed by the influence of spin-orbit mixing from upper levels, become allowed in INS. Additionally INS allows for the measurement of the intensity with respect to the

scattering vector, Q. This Q-dependence allows for the discrimination between various types of magnetic transitions, reducing ambiguity from any assignment of spectroscopic transitions.

A major source of background noise in INS data is strong incoherent nuclear scattering of hydrogen.[125] To avoid this problem, fully deuterated derivatives of **3** and **4** have been synthesized, and kindly provided for measurements by Dr. Grigore Timco of The University of Manchester. Details on the synthetic procedure of $\mathbf{3}^{D}$ and $\mathbf{4}^{D}$ can be found in Appendix 3.1. INS experiments have been carried out in collaboration with Dr. Richard Mole at the Technische Universität München / Germany (FRM II), on the cold neutron chopper spectrometer TofTof.[103]

Figure III.30 shows the INS spectra of $\mathbf{3}^{D}$ between 4 and 16 K using 6.0 Å neutrons. Five magnetic transitions are well resolved between 11.3 cm^{-1} and 1.9 cm^{-1} on both the energy loss and the energy gain side. All transitions have been fitted as Gaussian peaks. The spectra show significant temperature dependence. Similar to the EPR spectroscopy on **4**, all transitions are present at 4 K, but some gain higher intensity with increasing temperature. This is consistent with a ground multiplet, sufficiently separated from any further excited states at temperatures up to at least 30 K. From comparison of the relative intensities in Figure III.30, cold and hot (star) transitions are readily assigned.

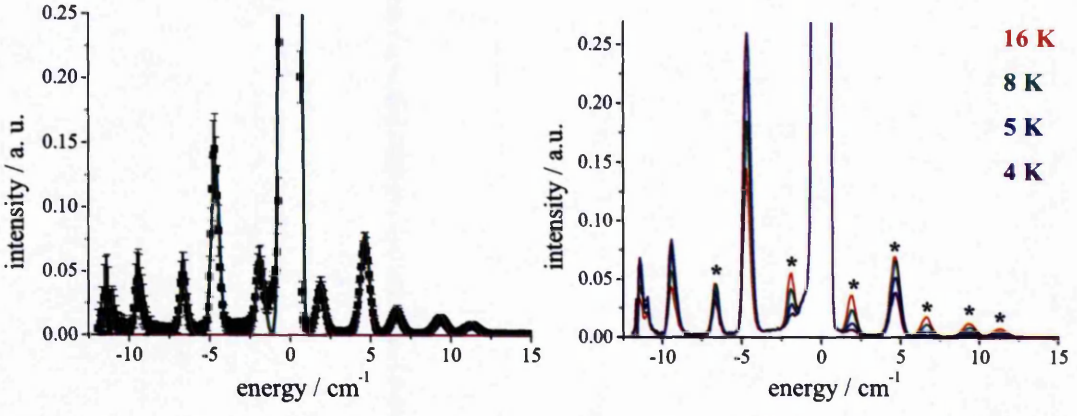

Figure III.30: INS spectrum of $\mathbf{3}^{D}$ obtained with 6.0 Å neutrons. Left: 16 K spectrum with error bars and a Gaussian fit. (Green: Gaussian fit, blue Gaussians: cold transitions, red Gaussians: hot transitions) Right: Variable temperature studies between 4 and 16 K. Stars indicate hot transitions.

Figure III.30 shows an energy diagram corresponding to the observed ten transitions, labelled a - j. The sum of transition energies b/i + e/f and c/h + d/g add up to that of transitions a/j within a four level energy diagram.

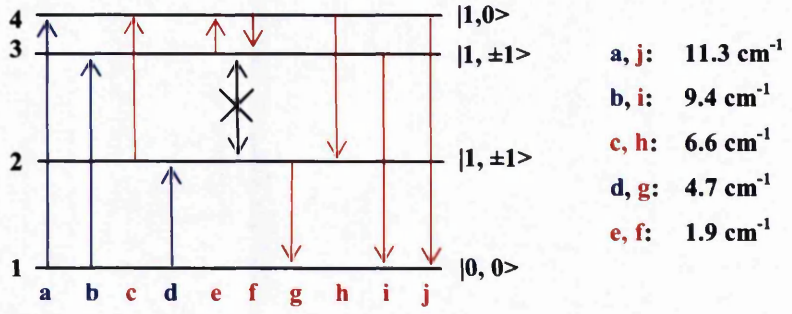

Figure III.31: Energy level diagram illustrating the INS transitions of 3^D.

Only one excitation, namely between level 2 and 3, is not observed. Before interpreting the missing transition, it is important to analyse the temperature dependence quantitatively, because the energy difference between level 2 and 3 is 4.7 cm^{-1}, the same as the difference between level 1 and 2. The transition could therefore overlap with transitions d and g. Because a hot transition from level 2 to 3 is less likely than a cold transition from 1 to 2, analysis of the temperature dependence in comparison with the Boltzmann population should allow for the 4.7 cm^{-1} transition to be assigned.

Figure III.32 shows the calculated Boltzmann population of the energy levels in Figure III.31 in comparison to the temperature dependence of the relative experimental peak intensities. All calculated transition probabilities (solid lines) have been normalized individually to the experimental data points at 16 K. Within the experimental error the temperature dependence of all transitions is reproduced well by the calculation. The dotted line shows the transition probability if the 4.7 cm^{-1} transition is a hot transition from 2 to 3 or 3 to 2. Especially in the second plot for transition g it is clear that the 4.7 cm^{-1} transition corresponds exclusively to the transition between level 2 and 1 (solid) and the transition between 3 and 4 (dash) is indeed not observed. The first plot for transition d supports this conclusion even though not as unambiguously.

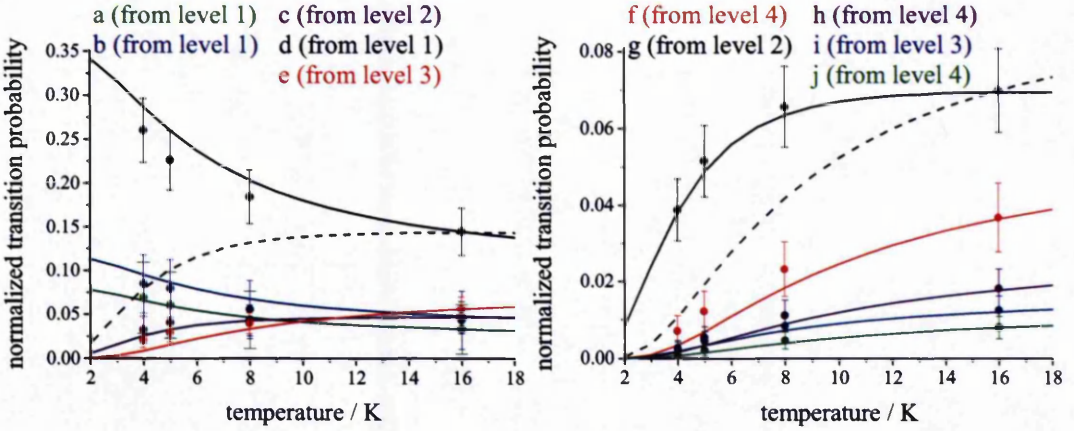

Figure III.32: Transition probabilities of $\mathbf{3}^{D}$ calculated from the Boltzmann population of the different energy levels in Figure III.31. All calculations are normalized individually to the 16 K data points. See text for the explanation of the dashed lines.

The explanation for the missing transition simply relates to the INS selection rules. The four level system is believed to arise from a "singlet" ground state and an excited "triplet" where all degeneracy is lifted; hence the missing excitation must correspond to the only conventionally INS forbidden transition with $\Delta m = 2$ between |1, -1> and |1, +1>. Together with the knowledge that **3** exhibits a non-magnetic ground state, wavefunctions can be assigned within the simplified effective model as indicated in Figure III.31.

From INS, distinction between |1, -1> and |1, +1> is not possible, however in the beginning of this section the scattering vector Q was mentioned, which influences the intensity of INS transitions. This analysis is particularly useful in the discrimination between different spin multiplets, which exhibit different Q-dependences and should allow for a confirmation of the magnetic ground state. If the energy level scheme in Figure III.31 is correct, and a simple model of an effective ground "singlet" and excited "triplet" is valid, the Q-dependence of the signals should represent this assignment.

In Appendix 3.9 the basic scattering theory used to calculate the Q-dependence of $\mathbf{3}^{D}$ and $\mathbf{4}^{D}$ is summarized. Several different contributions influence the Q-dependence: the Debye-Waller factor, the ionic form factor and the interference term, which is related to the inter-ion distance in the molecule.[99,102] The cobalt-cobalt distance R is known from the crystal structure as 3.4275(11) Å (at 150 K), and consequently the form factor of the dimetallic for the Δ"S_{eff}" = 0 and Δ"S_{eff}" = 1 case can be predicted.

The experimental Q-dependence of **3** at 4 K and the calculated expectations for Δ"S_{eff}" = 0 and Δ"S_{eff}" = 1 are shown in Figure III.33. It is immediately obvious that the overall fit to the form factor is not excellent; nevertheless the general trends are correct.

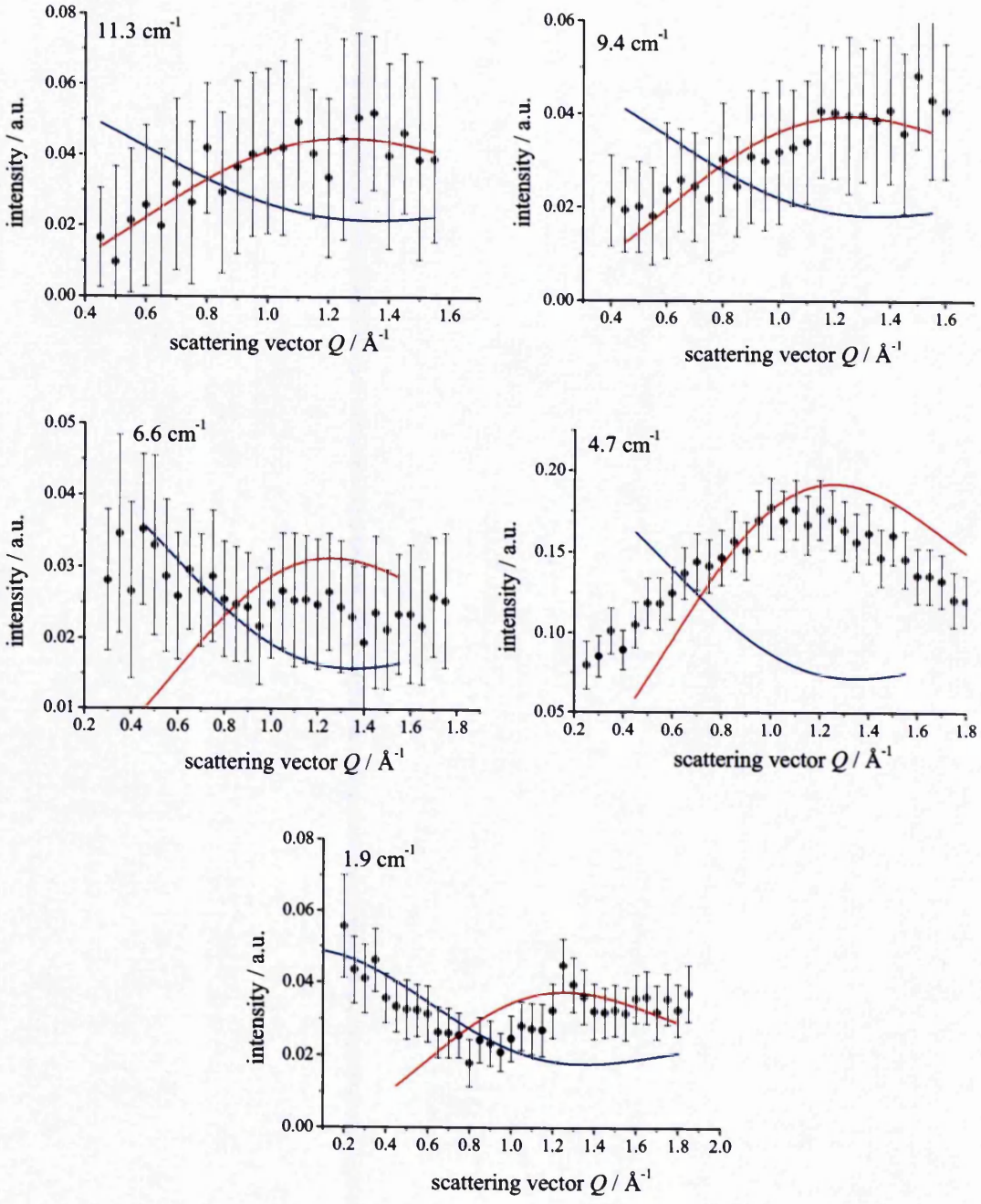

Figure III.33: Calculation of the Q-dependence in $\mathbf{3}^{D}$. Black: experimental data, red: calculation for Δ"S_{eff}" = 0, blue: calculations for Δ"S_{eff}" = 1.

The main reason for the deviation of the calculation from the experimental data is the dipole approximation of the single ion form factor.[99] This model is based on spin-only theory with $s = {}^1/_2$ ions and not suitable for the application to spin-orbit wavefunctions, because the orbital angular momentum has significant influence on the single ion form factor. The interference term (see Appendix 3.9) on the other hand, arises from the geometry of the ion and will thus hold true. In the low Q limit, $\sin(QR)/QR$ converges towards 1, thus for Δ"S_{eff}" = 0 the interference term converges towards 2, while for Δ"S_{eff}" = 1 the interference term converges towards 0. Thus we can assign the transitions solely on the behavior at low Q in Figure III.33. Calculated red lines correspond to Δ"S_{eff}" = 0 transitions, while Δ"S_{eff}" = 1 transitions are plotted in blue. Comparison of the low Q experimental data confirms indeed the assignment in Figure III.31 with a non-magnetic ground state: All cold transitions show a decrease at low Q indicating a Δ"S_{eff}" = 1 transition and hence a transition between a non-magnetic ground state and either of the three excited "triplet" levels. The remaining two hot transitions show increasing intensity at low Q indicating an inter-"triplet" transition with Δ"S_{eff}" = 0.

INS spectra on $\mathbf{4}^{D}$ have initially been recorded using 3.8 Å neutrons and were thought to show a magnetic excitation at approximately 8 cm^{-1}, while above 16 cm^{-1} a second series of excitations has been observed. Figure III.34 shows a two dimensional graphic representation of the INS intensities of **4** at 20 K as a function of energy and scattering vector. At high Q a group of phonon modes have been observed for energies above 16 cm^{-1}. The assignment has been based on both the Q-value and the temperature dependence: phonons are a result of neutrons being scattered by the nuclei. There is a Q^2 dependence to the form factor because of the point nature of the nuclei. Furthermore, phonons decrease in intensity with decreasing temperature as shown in Figure III.35.

The excitation at 8 cm^{-1} (Figure III.34) occurs at low Q, however the feature has not been observed in the neutron energy gain spectrum at any recorded temperature, nor does the peak on the energy loss side show any temperature dependence. Furthermore this transition is not observed in the 6 Å spectra (see below), indicating that this signal is caused by some spurious scattering or bad results associated with the low angle detectors.

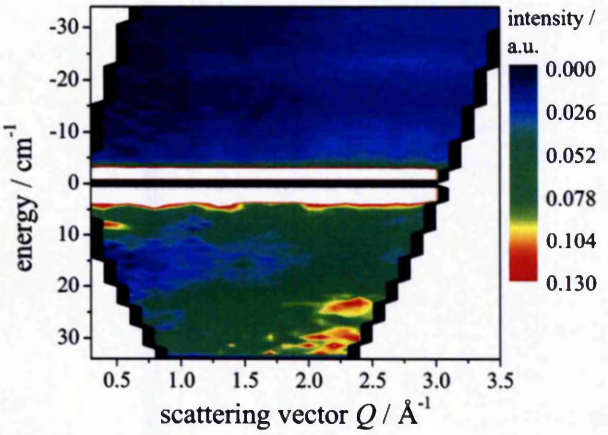

Figure III.34: 2D plot of transition energy *vs.* scattering vector Q and intensity at 20 K for $\mathbf{4}^{D}$ obtained with 3.8 Å neutrons. Excitations due to phonons are clearly seen above $Q = 2$ Å^{-1} and above 16 cm^{-1}. The spurious scattering associated with the magnetic excitations is at 8 cm^{-1} around $Q = 0.5$ Å^{-1}.

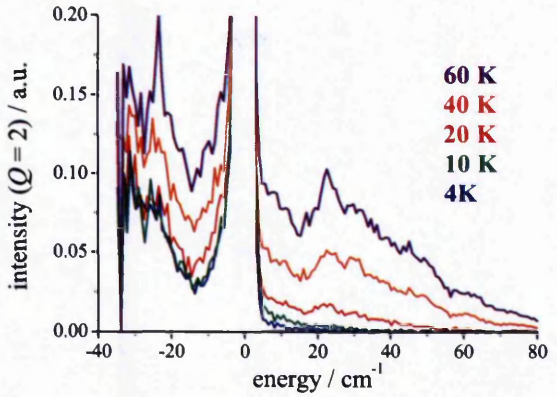

Figure III.35: Variable temperature plot of the intensity of $\mathbf{4}^{D}$ at $Q = 2$ obtained with 3.8 Å neutrons, indicating that these excitations are phonons and not magnetic in nature.

What is of more interest is what has *not* been seen in the 3.8 Å measurements: Up to the maximum recorded temperature of 60 K *no* excitations have been observed at high energy transfer in the neutron energy gain spectrum, indicating that there are no allowed transitions in the energy range up to this temperature. However, potential hot transitions would be weak as occupation of upper levels will be low and could be obscured by the observed phonons at higher energy. Overall, this confirms experimentally that the energy manifold arising from coupling the two Kramers' doublets is indeed very well isolated from further excited states. Together with the saturation of the magnetisation in all of the investigated dimetallics, this observation justifies the treatment of the low temperature magnetic and spectroscopic properties

as a multiplet arising from the interactions of only the lowest Kramers doublets of the two cobalt(II) ions.

Figure III.36 shows the INS spectra of $\mathbf{4}^{D}$ between 4 and 20 K recorded with 6.0 Å neutrons. At this wavelength only the low Q-region is detected and it was anticipated that only magnetic excitations are observed in this region. Integrating over the entire Q-range of interest revealed three peaks on both the energy loss, as well as the energy gain side. All transitions have been fitted with Gaussians. Two overlapping transitions occur at 1.6 and 2.4 cm^{-1}, and an unresolved shoulder is observed on the elastic peak at 0.8 cm^{-1}. These peaks show a strong Q-dependence with decreasing intensity for an increasing scattering vector Q, indicating that they are magnetic in nature.

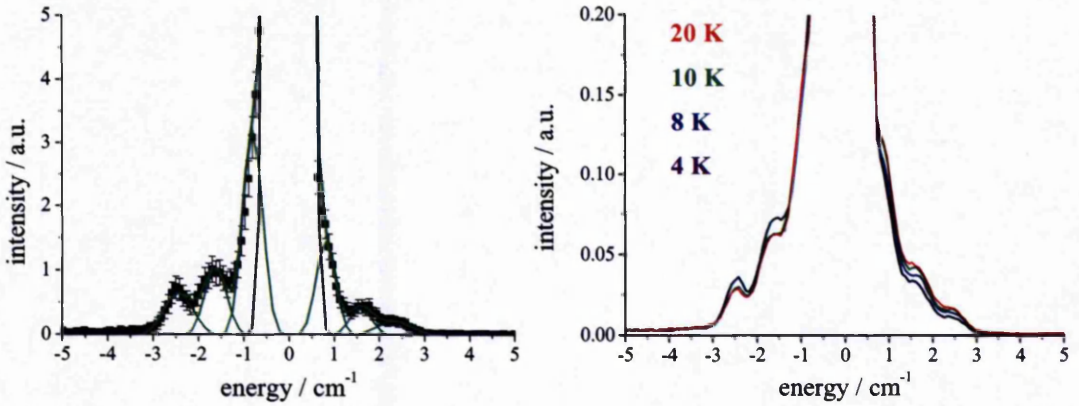

Figure III.36: INS spectrum of $\mathbf{4}^{D}$ obtained with 6 Å neutrons. Left: 4 K spectrum with error bars and a Gaussian fit (green) Right: Variable temperature studies between 4 and 20 K integrated over all Q.

As expected, all three energy levels are populated at 4 K, which allows for a thermal population of $3kT$ = 8.4 cm^{-1}, and only very weak temperature dependence is observed. Within the experimental error it is not possible exclusively to assign cold and hot transitions. Nevertheless the higher intensities for both the -2.4 cm^{-1} and the -1.6 cm^{-1} transition on the neutron energy loss side at 4 K, compared to identical intensities observed between 8 and 20 K, strongly suggest a cold transition in both cases. The unresolved shoulder on the elastic peak at -0.8 cm^{-1} cannot be assigned to either a hot or a cold transition from temperature dependence, but its energy corresponds exactly to the difference between the two cold transitions, and is likely to be the corresponding hot transition. Two energy level diagrams are proposed for the three transitions in Figure III.37. In model I an axial three level system is

proposed, while model II shows a completely rhombic case with equidistant splittings between all four energy levels.

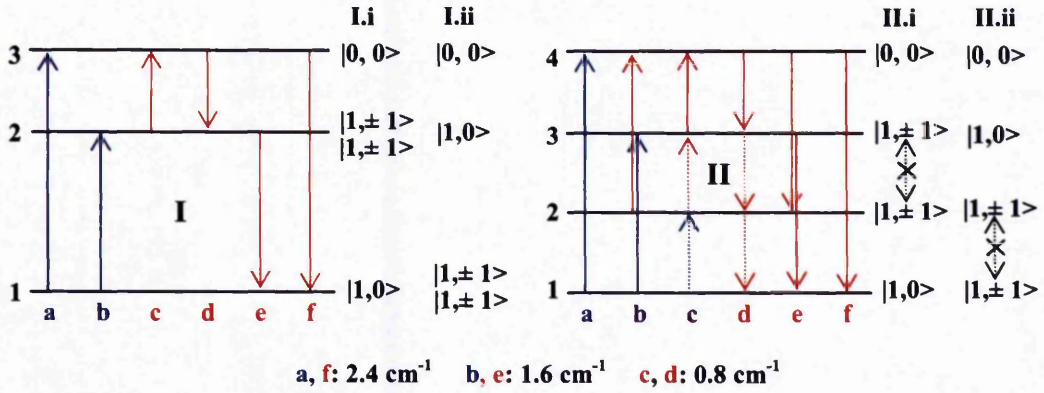

Figure III.37: Energy level diagrams proposed from the INS transitions observed in $\mathbf{4}^{D}$. Model I: axial, model II: completely rhombic

From magnetic measurements it is known that **4** exhibits ferromagnetic interactions, hence levels corresponding to the effective "triplet" state are lower in energy than the effective "singlet" level. However, neither magnetism nor INS allow for the *m* levels to be assigned within the effective triplet. For I the two possibilities, i and ii, are shown in Figure III.37. Theoretically, there are three possibilities to assign *m* states to the three triplet energy levels in II; however, only for two of them (i, ii) is transition b an allowed cold transition. Depending on the order of the *m* states, one of the transitions between level 1 and 2 or level 2 and 3 should be INS forbidden as seen for $\mathbf{3}^{D}$.

Figure III.38 shows the calculated transition probabilities for the three transitions in model I, and for the five transitions in model II, each for case i and ii. For model I, both cold transitions at -2.4 and -1.6 cm^{-1} and the corresponding transitions on the neutron energy gain side are reproduced well within the experimental error. However, neither of the two cases can reproduce the temperature dependence of the transitions at ± 0.8 cm^{-1}. Significantly different results are obtained for the calculations within model II. The ± 2.4 cm^{-1} transitions are reproduced well as transitions between level 1 and 4 in both cases. For II.i experimental data points lie between the pure cold and pure hot transition extremes for the ± 1.6 and ± 0.8 cm^{-1} excitations. This is expected if the two experimental peaks are each arising from a mixture of two transitions with identical energy separation.

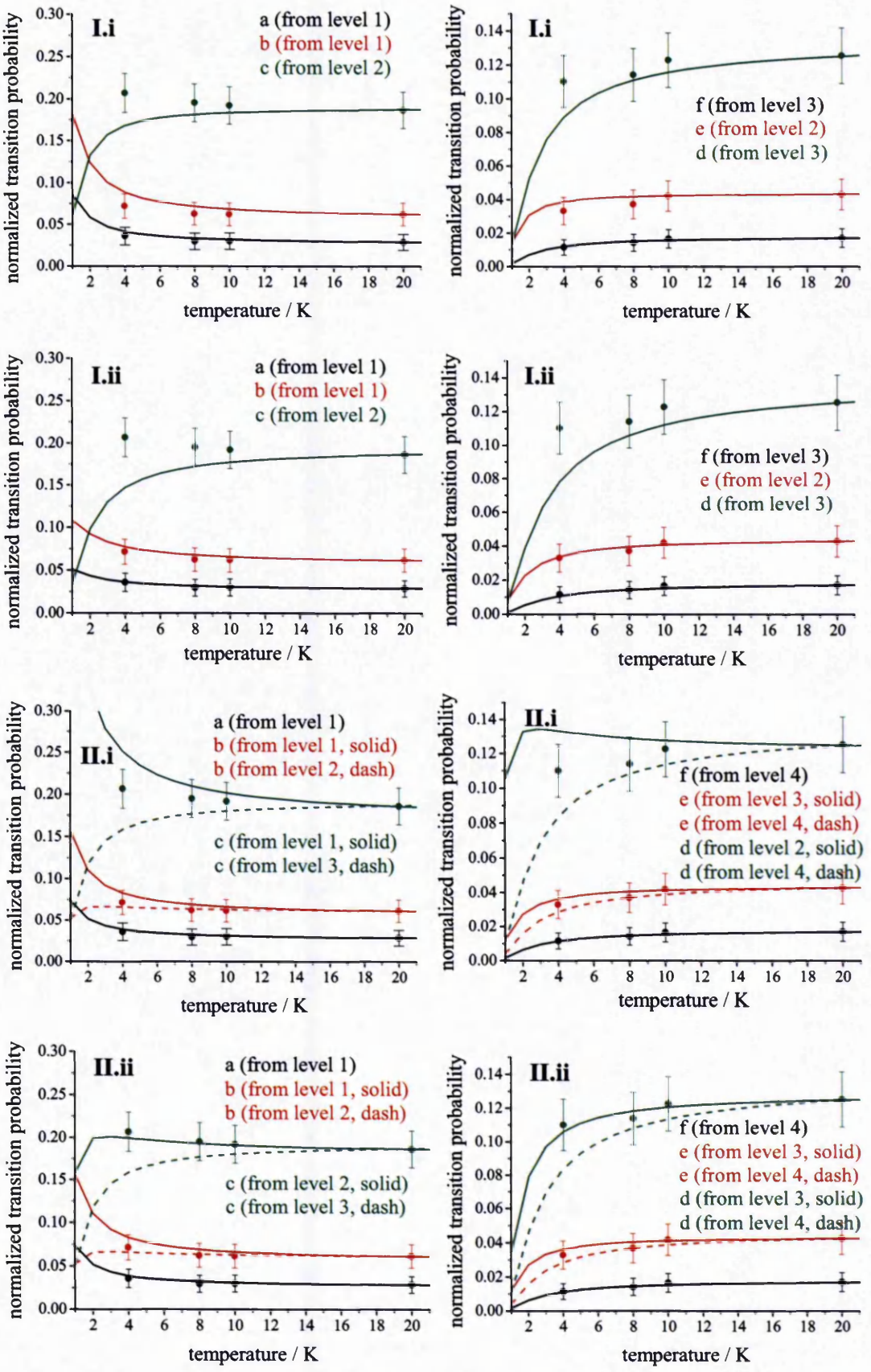

Figure III.38: Transition probability of 4^D calculated from the Boltzmann population of the different energy diagrams in Figure III.37. Calculations are normalized to the 20 K data points.

For II.ii experimental data appear to support only four out of the five transitions, with transition c/d only occurring between level 2 and 3. At 4 K all energy levels are sufficiently populated, and there is no reason why the fifth allowed transitions may be missing.

Overall the comparison of the four possibilities favours model II.i; however, measurements at lower temperature and higher resolution are scheduled to resolve the 0.8 cm^{-1} transition and to assign the energy levels more confidently.

For the antiferromagnetic analogue **3** it was possible to confirm the non-magnetic "singlet" ground state and a degenerate excited "triplet" from the Q-dependence of the transitions at low Q. Similar calculations have been performed for $\mathbf{4}^{D}$ and the results are plotted in Figure III.39.

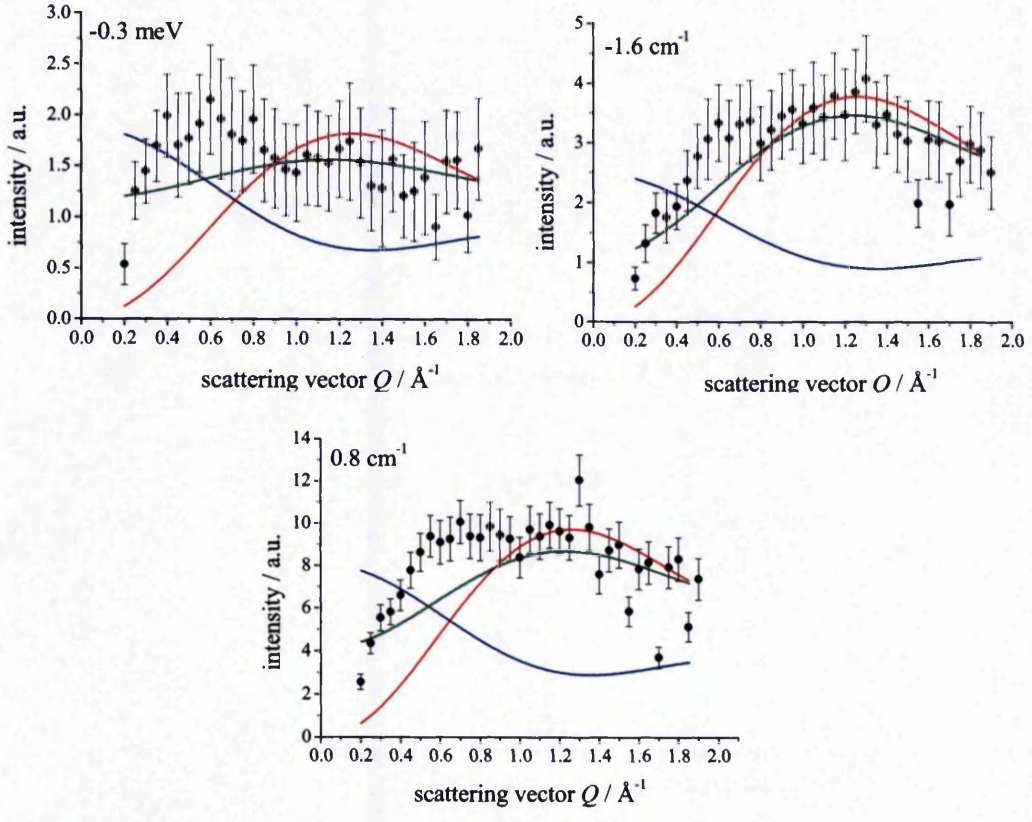

Figure III.39: Calculation of the Q-dependence in $\mathbf{4}^{D}$. Black: experimental data, red: calculation for Δ"S_{eff}" = 0, blue: calculations for Δ"S_{eff}" = 1, green: mixture of Δ"S_{eff}" = 0 and 1.

The 0.8 cm^{-1} data in Figure III.39 are integrated in the region 0.8 ± 0.2 cm^{-1}. This range was chosen to minimise the amount of overlap from adjacent excitations, whilst retaining good statistics. For all calculations the blue line corresponds to

Δ"S_{eff}" = 0, the red line to Δ"S_{eff}" = 1. Finally the green line is a mixture of the two with weighting coefficients of the two components refined, as the occupancy of the upper level is unknown. The observed fractions for Δ"S_{eff}" = 1 : Δ"S_{eff}" = 0 are 0.7 : 0.3 (0.8 cm^{-1}), 0.76 : 0.23 (1.6 cm^{-1}) and 0.6 : 0.4 (2.4 cm^{-1}). Similar to the antiferromagnetically coupled dimetallic $\mathbf{3}^{D}$ the experimental Q-dependence at low Q for $\mathbf{4}^{D}$ shows poor agreement with this simple model, however, the overall trend can be compared. It is interesting to note, that all three transitions decrease in intensity at low Q. The Q-dependent contributions to the observed scattering are essentially a produce of the ionic from factor and the interference term. The ionic from factor is always described by an exponential decrease, thus as Q is reduced, this term increases. In the case of "S_{eff}" = 0, the interference term converges to 2 at low Q, while for "S_{eff}" = 1, the interference term converges to zero. Consequently the experimental data suggest that all transitions have an "S_{eff}" = 1 component. The simplest interpretation would be a singlet ground state, however this ignores the possibility of any hot transitions having an "S_{eff}" = 0 component. Furthermore, magnetic measurements have unambiguously shown a magnetic ground state of **4**. The only model that can reproduce these results is a complete lift of the degeneracy in the ground "triplet" according to model II in Figure III.37 with equidistant splitting between the different energy levels. For the 1.6 cm^{-1} and the 0.8 cm^{-1} transition in model II, an overlap of an intra-"triplet" and "triplet"-"singlet" transition is expected. This agrees well with the overall broad shape of the experimental Q-dependence, which appears to reflect a mixture between a pure Δ"S_{eff}" = 0 and Δ"S_{eff}" = 1 transition. A Q-dependence that suggests a system described by model II is also consistent with the weak temperature dependence, which has favoured model II.i (Figure III.38). In any of the simple models in Figure III.37 the 2.4 cm^{-1} excitation is expected to be a pure "triplet"-"singlet" transition, despite its apparent partly Δ"S_{eff}" = 0 character observed experimentally. This may indicate some mixing between the different states. In Section III.5.2 an example is discussed whereby strong "g_{eff}" –anisotropy, as observed for **4** by EPR spectroscopy, can indeed induce mixing between different "spin" states. This does of course not change the energy in zero-field, but changes the character of the wavefunctions and may explain the Q-dependence of the transition.

In conclusion INS has provided the energy levels of $\mathbf{3}^{D}$ and $\mathbf{4}^{D}$ at zero fields. Both experiments confirm a four level energy manifold arising from the coupling of the lowest Kramers doublets of two cobalt(II) ions. Experiments up to 60 K at 3.8 Å have not shown any further magnetic transitions confirming the isolation of the ground multiplet at low temperatures. Energies and temperature dependence in $\mathbf{3}^{D}$ have shown a complete lifting of the degeneracy in the effective "triplet" leading to a rhombic system.

Overall the simple model also appears to allow for a first analysis of the Q-dependence of the different excitations, however the experimental data are not modelled well and further work is required on the model, in particular to describe the ionic form factor, which significantly depends on the contribution from the orbital angular momentum. Nevertheless both weak temperature dependence as well as the overall shape of the Q-dependence in $\mathbf{4}^{D}$ point towards a lifting of all degeneracy in the effective "triplet" leading to a completely rhombic system, consistent with the rhombic splitting observed unambiguously in $\mathbf{3}^{D}$.

III.5 Semi-quantitative effective model

The interpretation of magnetic and spectroscopic properties of cobalt(II) dimetallics in the previous sections has shown that a simple picture of two effective Kramers doublets interacting to give an effective "singlet" and "triplet" state allows for a qualitative analysis and provides a first understanding of the systems. In this Section, those results have been combined to form the basis of a semi-quantitative interpretation, which can explain the different complementary results on different compounds simultaneously. The choice of model does not aim for a complete quantitative interpretation of the simulated magnetic and spectroscopic properties; rather a cross-linking of different information on the electronic structure from different experiments into an overall valid and simple physical picture is sought.

III.5.1. Assignment of parameters to the INS transitions at zero-field

INS has provided the low lying energy manifold for $\mathbf{3}^{D}$ and $\mathbf{4}^{D}$ at zero field. Considering the simple effective model of two Kramers doublets interacting *via* exchange interactions, using a simple isotropic Heisenberg-Dirac-van-Vleck Hamiltonian $\hat{H}_{HDvV}$ (Equation I.2) for two "s" = $^1/_2$ centres and an effective Zeeman Hamiltonian (Equation I.4) for an effective triplet "S_{eff}" = 1 as introduced in Section I.1.1, Hamiltonian parameters can be assigned to the simulated the energy splittings in zero-field: An exchange parameter "J" splits the single ion Kramers doublets into an effective singlet and an effective triplet. "D_{eff}" and "E_{eff}" parameters then are used to generate a rhombic splitting of the triplet in order to reproduce the energy splittings observed experimentally with INS. Tables III.6 and III.7 show the parameters that have been assigned to **3** and **4**, respectively, based on INS,. Temperature dependence of the INS transitions of $\mathbf{3}^{D}$ has clearly determined the sign of "D_{eff}" to be negative. Both, positive and negative values for "E_{eff}" are possible. In $\mathbf{4}^{D}$ such constraints are not unambiguously possible from INS. Two axial and four rhombic combinations have to be considered, although analysis of the temperature dependence (Section III.4) favours the parameter set "D_{eff}" = +1.2 cm^{-1} and "E_{eff}" = ± 0.4 cm^{-1}.

"J"	"D_{eff}"	"E_{eff}"
- 4.23	- 4.25	±2.35

Table III.6: "J", "D_{eff}" and "E_{eff}" parameters from the zero-field energies obtained by INS on $\mathbf{3}^{D}$.

"J"	"D_{eff}"	"E_{eff}"
0.80	±1.60	0
0.80	±1.20	0.40
0.80	±1.20	-0.40

Table III.7: "J", "D_{eff}" and "E_{eff}" parameters from the zero-field energies obtained by INS on $\mathbf{4}^{D}$.

Formally, isotropic exchange interactions lead to a splitting between the effective "singlet" and "triplet" states, whilst zero-field splitting parameters "D_{eff}" and "E_{eff}" account for the anisotropy of the system. This is *not* a physically correct interpretation. Rather, anisotropy is introduced through anisotropic exchange

interactions between the two Kramers doublets leading to a total lifting of the degeneracy in the effective "triplet" at zero field. Nevertheless, those parameters provide a simple mathematical tool to generate the observed energy manifold at zero-field, and to estimate the evolution of the energy levels in a magnetic field.

Compound **4** is either axial or completely rhombic with $|"E_{eff}"| = {}^1/_3 |"D_{eff}"|$, although a rhombic case is favoured from analysis of preliminary INS results. Conventionally this is also the definition of the maximum value of E, however in compound **3** $|"E_{eff}"|$ exceeds this condition. This apparent violation of the rule can be explained with the origin of the anisotropy. Conventionally "D_{eff}" and "E_{eff}" are defined as zero-field splitting parameters, which describe zero-field splitting arising from the influence of second order spin-orbit coupling terms on the spin-function. As mentioned earlier, in **3** and **4** anisotropy arises from anisotropic exchange coupling between the two spin-orbit Kramers doublets, and conditions derived for conventional "D_{eff}" and "E_{eff}" parameters may not be applicable here. It is also important to note that the anisotropy parameters "D_{eff}" and "E_{eff}" are of the same order as the isotropic exchange parameter "J". In spin-only systems, isotropic exchange is usually the major component to the magnetic properties, while anisotropic exchange is often treated as a perturbation on the isotropic system. For the exchange coupling between the cobalt(II) ions, this is clearly not the case, rather isotropic and anisotropic exchange appear to contribute in a similar order. This can be related to the spin-orbit character of the wavefunctions, which results in a very anisotropic Zeeman splitting of the corresponding energy levels in a magnetic field and hence a very anisotropic exchange interaction.

III.5.2. Calculation of the Zeeman splitting of 4, and assignment of HFEPR transitions to the low lying energy manifold

In the previous section, effective "D_{eff}" and "E_{eff}" parameters have been assigned to the INS transitions of **4**. Furthermore, single crystal EPR spectroscopy (Section III.3.2) has provided principal "g_{eff}"-values for the anisotropic Zeeman splitting.

Using those values, the Zeeman splitting of the different energy levels of the effective "triplet" can be calculated (for equations see Appendix 3.10).[3] In addition, the effective "singlet" has to be considered. While inter-multiplet transitions conventionally violate the EPR selection rule of $\Delta S = 0$, mixing of the spin-orbit functions may well lead to partly allowed transitions between all four energy levels of the low lying manifold. In a (very crude) first approximation the "singlet" energy level was considered diamagnetic with a constant energy in all field directions.

All six parameter combinations of axial and rhombic anisotropy listed in Table III.7 have been tested and compared to the HFEPR spectra, which are assumed to show transitions in a linear region of the Zeeman splitting. For axial symmetry, $|\text{“}D_{\text{eff}}\text{”}| = 1.6\ \text{cm}^{-1}$ exceeds the microwave energy of $1.13\ \text{cm}^{-1}$ at Q-band frequency, which leads to a loss of two out of three inter-triplet transitions. Experimentally two out of three inter-triplet transitions are observed (transition 8 and 12 in Section III.3), indicating rhombic rather than axial symmetry.

For positive "D_{eff}" and "E_{eff}", transitions 8 and 12 collapse to one transition along x in the calculated Zeeman diagram. This behaviour has been confirmed in the single crystal spectra, where transition 8 and 12 collapse along the unique symmetry axis b. Conventionally the principal direction associated with the overlap between the two transitions is defined as x, the principal "$\mathbf{g}_{\text{eff}}$"-matrix frame has therefore been chosen for principal x parallel to b. Furthermore, relative intensities depend greatly on the sign of "D_{eff}" and "E_{eff}", and the strong temperature dependence of the HFEPR spectra allows for a confident assignment of the sign to the parameters, consistent with the indications from the weak temperature dependence of the INS peak intensities. The best reproduction of the experimental spectra has been observed for a completely rhombic system with "$g_{\text{eff},xx}$" = 3.43, "$g_{\text{eff},yy}$" = 6.13, "$g_{\text{eff},zz}$" = 2.30, "D_{eff}" = $1.2\ \text{cm}^{-1}$, and "E_{eff}" = $0.4\ \text{cm}^{-1}$ (Figure III.40). It is important to note that the sign of "D_{eff}" depends on the definition of the axis systems. Identical transitions can be calculated for "$g_{\text{eff},xx}$" = 2.30, "$g_{\text{eff},yy}$" = 3.43, "$g_{\text{eff},zz}$" = 6.13, "D_{eff}" = $-1.2\ \text{cm}^{-1}$, and "E_{eff}" = $0.4\ \text{cm}^{-1}$, where transitions 8 and 12 collapse at "g_{eff}"= 3.43 along y. However, as mentioned earlier, the conventional assignment was chosen for this study.

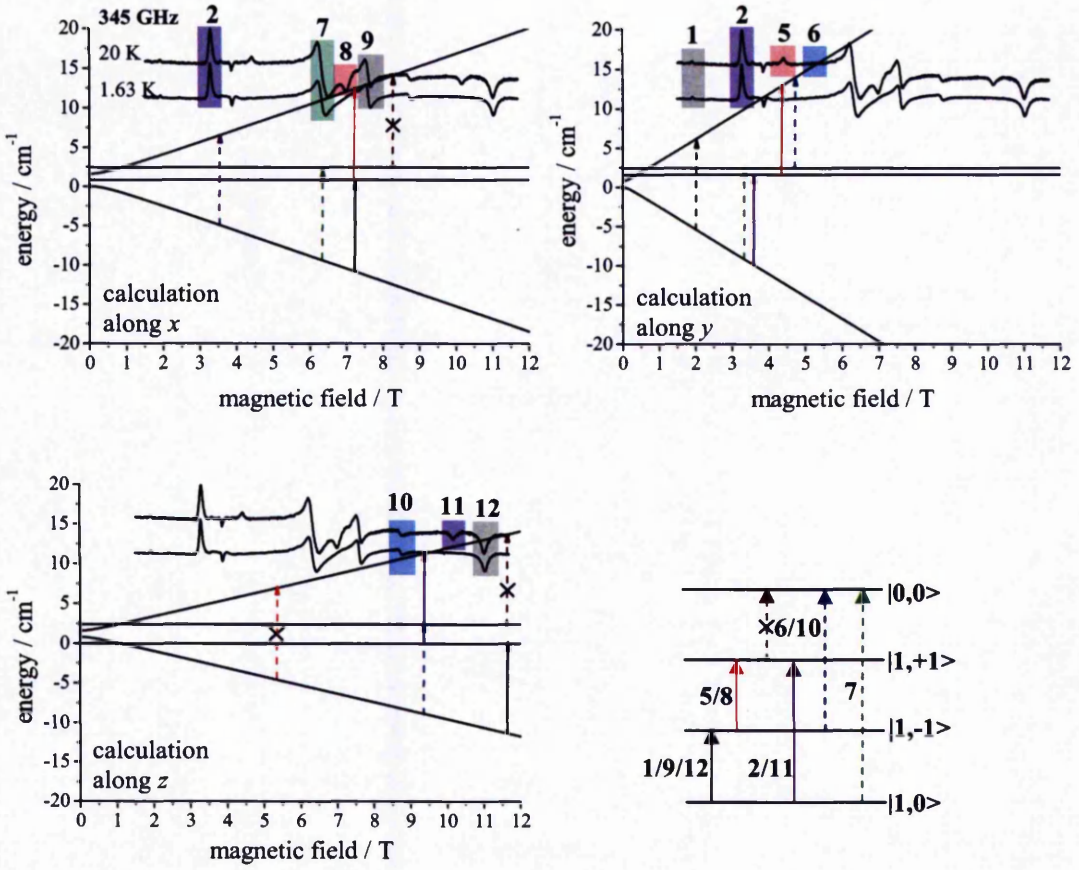

Figure III.40: Calculated Zeeman splitting of **4** along the three principal magnetic axes for "$g_{eff,xx}$" = 3.43, "$g_{eff,yy}$" = 6.13, "$g_{eff,zz}$" = 2.30, "D_{eff}" = 1.2 cm^{-1}, and "E_{eff}" = 0.4 cm^{-1}. Arrows indicate transitions at 345 GHz in comparison to the 345 GHz spectrum at 5 K and 20 K. Bottom right: Zero field energy diagram with corresponding transitions. See text and Table III.5 for explanation of labelling of transitions.

Initially the Zeeman splitting was calculated for "$g_{eff,xx}$" = 3.25, "$g_{eff,yy}$" = 6.07, "$g_{eff,zz}$" = 2.30, which have been assigned from the single crystal spectra in Section III.3.2. Once the remaining transitions in the experimental HFEPR spectra had been assigned, those initial values, restricted to the limited transitions observed at Q-band, were adjusted to account for all six inter-triplet transitions in the different field directions. The new principal effective "g_{eff}"-values have been calculated as an average between the pairs of "g_{eff}"-values obtained from the linear regression of the HFEPR for transitions representing the same orientation (Figure III.41). From the field dependent magnetisation measurements (Section III.2.1) an effective average "g_{eff}"-value of *ca.* 3.75 is observed, which falls slightly under the average of the principal "g_{eff}"-values from EPR spectroscopy.

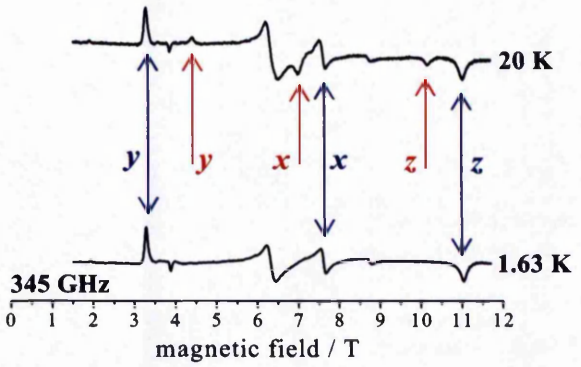

Figure III.41: Assignment of hot (red) and cold (blue) transitions in the HFEPR powder spectra at 345 GHz to the contributions from different orientations with respect to the magnetic field.

The calculated Zeeman diagram explains ten out of the twelve features observed experimentally. Figure III.40 shows an energy level diagram at zero-field with the ten possible transitions. The main inter-"triplet" transitions 2 = 11, 8 = 5 and 12 = 9 = 1 appear to be equally allowed, depending on the magnetic field direction, consistent with observations in completely rhombic spin-only systems with $E = {}^{D}/_{3}$.[3] In accord with single crystal EPR, the calculated Zeeman diagrams predict the presence of transition 8 = 5 in two directions (x and y), while transition 12 = 9 = 1 is present in all three directions, however, only formally allowed along x and z. This agrees with the weak signal and small angle dependence of 12 in the ba^*-plane compared to transition 8. Transition 2 = 11 is not found in the single crystal spectra, because the splitting of the corresponding energy levels at zero-field (ΔE = 1.6 cm^{-1}) exceeds the Q-band microwave frequency of 1.13 cm^{-1}.

As expected, not only the conventionally allowed transitions, but also inter-multiplet transitions (7, 10 = 6) are observed. In the powder spectra at high magnetic field, but also in the Q-band spectra, transitions 7 and 10 are present as well resolved cold transitions (Figures III.19 and III.20). Both transitions are also present in the single crystal Q-band spectra, but only in very specific orientations (Figures III.24 and III.25). This is in agreement with the inter-multiplet character of those excitations. The lack of cancellation effects due to the forbidden character of the transitions in most orientations, leads to the strong intensity in the powder spectra compared to the formally allowed transitions.

In all three principal directions the calculated transitions are slightly shifted with respect to the experimental resonance magnetic fields. The linear frequency dependence at high magnetic fields has allowed for the "g_{eff}"-values to be determined precisely, hence the deviation must arise from insufficiency of the model, rather than an error in determining the parameters. Comparison of experiment and calculation along *x* in Figure III.40 shows that transitions 8 and 9 = 12 do not actually overlap in the experimental spectrum, but are slightly shifted in resonance. The difference in field is however relatively small compared to the bandwidth, and hence not resolved at Q-band where the two transitions appear to overlap along *x*.

A linear frequency dependence of the resonance field at the same time as a deviation of the experimental transitions from a linear symmetrical Zeeman splitting is only possible, if energy levels evolve (nearly) linearly with the magnetic field, but the slope of corresponding ± *m* levels deviates between +*m* and –*m*, averaging to the observed "g_{eff}"-values. AOM calculations on the spin-orbit wavefunctions of **1** and **5** indeed confirm this proposed behaviour with a significantly stronger slope of the "$-^1/_2$" level compared to the "$+^1/_2$" level along *xy*.

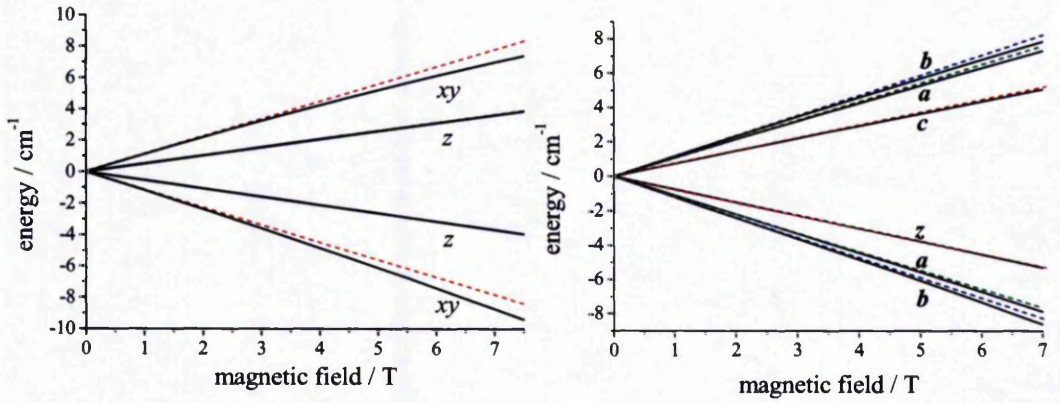

Figure III.42: Zeeman splitting obtained for the monometallic **1** and for one of the single cobalt centres of the dimetallic **5**. Dashed coloured lines represent a linear symmetrical Zeeman splitting with identical magnitudes to emphasize the curvature of the energy levels.

Figure III.42 shows the Zeeman splitting obtained from AOM calculations on the monometallic **1** (left, for parameters see Section II.3.2) and on one of the two cobalt centres in the dimetallic **5** (right, for parameters see Appendix 3.4). Dashed coloured lines represent a linear symmetrical Zeeman splitting to emphasize the curvature of the energy levels. In the monometallic **1**, a symmetrical Zeeman splitting is observed

along *z*. In the *xy*-plane differences occur in the steepness of the slope and an additional small deviation from the linearity of the field dependence. Experimental evidence was also found by the apparent field dependence of "g" in the magnetisation *vs.* magnetic field plot: At higher magnetic fields the system is dominated by the "-1/2" level only and thus requires a larger average effective "g_{eff}"-value that at small magnetic field where both "±1/2" levels are populated. In the dimetallic **5**, small deviations from a linear, symmetrical Zeeman splitting are observed in all three directions from AOM. While the deviation is small compared to the overall anisotropy, at high field a significant shift in the EPR transitions can be expected. At lower fields the deviation will not be resolved.

Furthermore, a simple model shows how the strong "g"-anisotropy can introduce mixing between different multiplets in the case of non-co-linearity between the single ion principal axes, even in the absence of any splitting in zero-field. Figure III.43 shows the calculated Zeeman splitting of a four level system arising from isotropic exchange coupling between two spins "s" = $^1/_2$ with "J" = 0.8 cm^{-1} "g_{xx}" = 3.43, "g_{yy}" = 6.13 and "g_{zz}" = 2.30 in Equation III.2 along the *z* (left) and *y* (right) axis.

$$\hat{H} = -2J\hat{s}_{\text{eff},1}\hat{s}_{\text{eff},2} + \sum_i \mu_B \vec{B}\mathbf{g}_{\text{eff},i}\hat{s}_{\text{eff},i} \qquad \text{(III.2)}$$

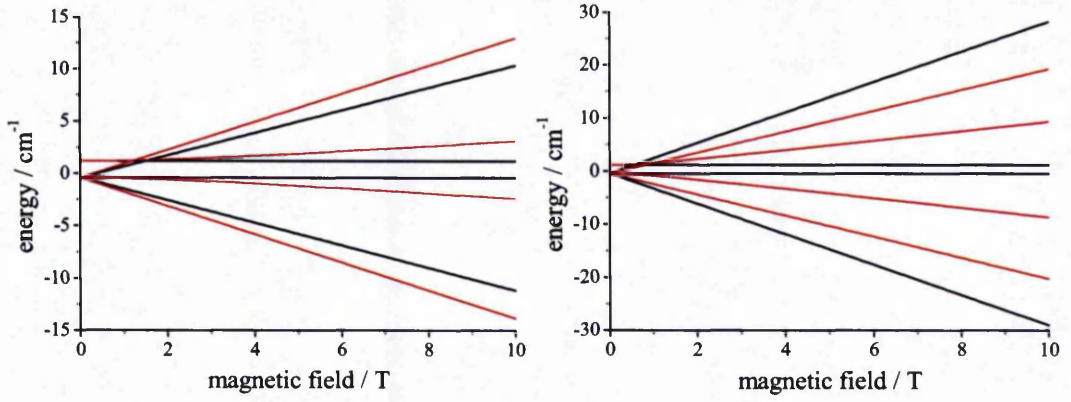

Figure III.43: Demonstration of the mixing effect induced by strong "g"-anisotropy along *z* (left) and *y* (right). Black: Calculation of the Zeeman splitting for co-linear "**g**"-matrices on "s_1" and "s_2"; red: Zeeman splitting after a rotation of matrix "$\mathbf{g}_2$" by 90° around *z*. ("J" = 0.8 cm^{-1}, "g_{xx}" = 3.43, "g_{yy}" = 6.13 and "g_{zz}" = 2.30).

In the first calculation (black) the orientation of the two "**g**"-matrices is co-linear, while for the second case (red) a 90° rotation around *z* was performed. In the latter, strong mixing between effective "singlet" and "triplet" leads to a significant field dependence on the $|S, m>$ levels with $m = 0$.

Preliminary *ab-initio* crystal field calculations performed by Prof. Chibotaru and *co*-workers at the University of Leuven/Belgium indeed support non-co-linear single ion "**g**"-matrices in **4** (Appendix 3.5).

From the relative shift of the experimentally observed transitions from the calculated line in Figure III.40, the curvature of the energy levels can be estimated. Along *x*, transition 8 is observed experimentally at a lower magnetic field than calculated, while transition 9 is observed in a higher magnetic field. This indicates an "inward" bending of the ground energy level |1, 0> and an "outward" bending of the highest triplet energy level |1, +1> in comparison to a linear symmetrical Zeeman splitting. Transition 2 is observed at slightly lower energy than calculated, which suggests a non-linearity of level |1, +1> that is larger than for ground level |1, 0>. Transition 7 is reproduced reasonably well, indicating that in case of a bent ground level |1, 0>, the effective "singlet" level |0, 0> may also show a field dependence, leading to a slightly positive Zeeman slope. Along *y* the hot transition 5 is reproduced reasonably well, while the cold transitions 1 and 2 are observed at slightly lower magnetic fields than predicted. This indicates a curvature of the ground energy level |1, 0> towards lower energies than in the linear case. Level |1, -1> and |1, +1> are both expected to show a deviation from the linear case, too, and the good reproduction of the experimental transition 5 suggests that both energy levels differ from the linear case by a similar amount. Along *z*, the two cold transitions 10 and 12 are observed at a lower magnetic field than predicted from the calculation. The hot transition 11 on the other hand, occurs at a higher magnetic field. All signals are shifted by a similar amount indicating a consistent curvature similar to the observations from AOM calculations, where the energy levels bend towards a lower energy compared with a linear case.

At low magnetic fields the model fails. Experimentally observed Q-band and even W-band transitions are not well reproduced by the simple effective model, apart from the overlap of transition 8 and 12 along *x* (Appendix 3.11). It is not surprising that the simple model only accounts for the linear region of the Zeeman splitting at high

magnetic fields, because the calculated curvature of the energy levels at low magnetic fields is based on a very different physical origin (second-order spin-orbit coupling effect) than present in the cobalt(II) dimetallics (spin-orbit wavefunctions leading to anisotropic exchange). Here calculations using the true spin-orbit wave-functions are required.

Nevertheless some important information can be drawn from the calculations at low magnetic fields. Along the cobalt-cobalt vector *z*, where transition 12 is expected, the Zeeman splitting does not allow for transition 12 to be observed in a field range ≤ 2 T (limit of the Q-band Elexsys magnet). This explains the absence of transition 12 in the single crystal spectrum along z. Rotation away from this axis in the *ac*-plane leads to contributions from *y* (with "$g_{\text{eff},yy}$" = 6.13), hence the Zeeman splitting increases and transition 12 becomes observable again.

III.5.3. Calculation of the Zeeman splitting of 3

Based on the successful application of the simple effective model, which can explain both INS and multifrequency EPR transitions in **4**, similar calculations have been carried out on **3**.

Effective parameters have been derived directly from INS (Section III.5.1) to simulate the splitting in zero-field. The three principal effective "g_{eff}"-values have been adjusted to gain the best simulation of the experimentally observed cold and hot transitions at W-band: "$g_{\text{eff},xx}$" = 5.6, "$g_{\text{eff},yy}$" = 3.9, "$g_{\text{eff},zz}$" = 3.0, "D_{eff}" = -4.35, and "E_{eff}" = 2.35. Again, relative intensities have allowed for the sign of the zero-field splitting parameters to be determined. Figure III.44 shows the calculated Zeeman splitting of **3**, where arrows indicate transitions at 94 GHz in comparison to the 94 GHz spectrum at 5 K.

Overall the three estimated "g_{eff}"-values are in the order of those obtained for compounds **1**, **4** and **6** experimentally. However, in the previous section the validity of the simple effective model at low magnetic fields (even at W-band) has been questioned. Furthermore a curvature of the energy levels away from the calculated symmetrical linear development has been observed. Nevertheless, comparison of different possible combinations has shown that, even though absolute numbers have

to be treated carefully, the relative magnitude of "g_{eff}" ("$g_{eff,xx}$" > "$g_{eff,yy}$" > "$g_{eff,zz}$") and the sign of "E_{eff}" can be assigned.

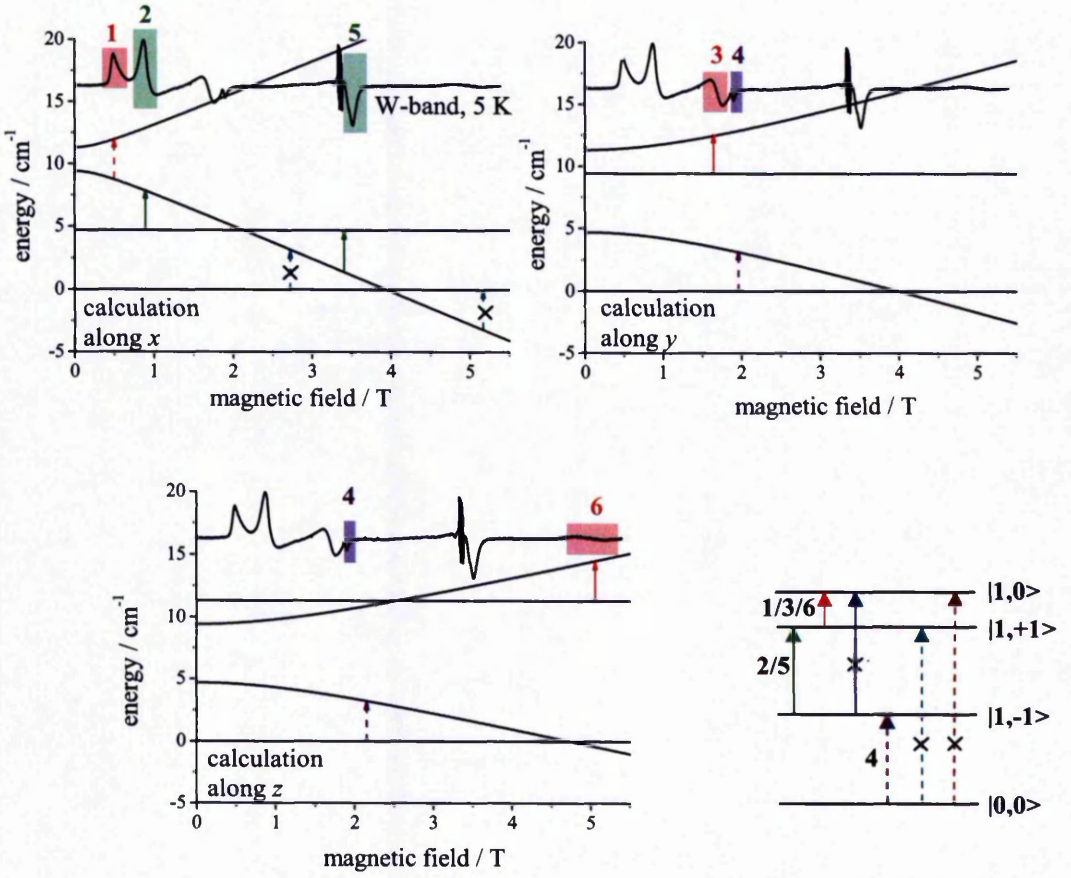

Figure III.44: Calculated Zeeman splitting of **3** along the three principal magnetic axes for "$g_{eff,xx}$" = 5.6, "$g_{eff,yy}$" = 3.9, "$g_{eff,zz}$" = 3.0, "D_{eff}" = -4.35, and "E_{eff}" = 2.35. Arrows indicate transitions at 345 GHz in comparison to the 345 GHz spectrum at 5 K. Bottom right: Zero field energy diagram with corresponding transitions.

The result is in agreement with the ground energy manifold in **4**, which has also been simulated best for a positive "E_{eff}". The sign of "D_{eff}" is opposite in the two different compounds; however with respect to the splitting in zero-field, this represents a consistent picture of $m = \pm 1$ levels enclosed between the $m = 0$ levels from the effective "singlet" and triplet". The energy diagram in Figure III.44 shows that only two out of the three transitions expected from the effective triplet are observed in **3**. This is readily understood, because the separation of level |1, -1> and |1, 0> in Figure III.44 at zero field exceeds the microwave energy at W-band and excitation is not possible. One inter-multiplet transition (4) is observed weakly between the |0, 0> and |1,-1> level, which appears to become partly allowed along y and z. The

corresponding transition has also been observed in **4** along *z* and *y* (10 = 6, Figure III.40), showing again the consistency between the two examples.

III.5.4. Calculation of the magnetic properties from the anisotropic Zeeman splitting in 3 and 4

To complete the comparison of the semi-quantitative model to the experimental observations, the low temperature magnetic properties of **4** and **3** have been calculated from the four level Zeeman diagrams developed in Sections III.5.2 and III.5.3, respectively.

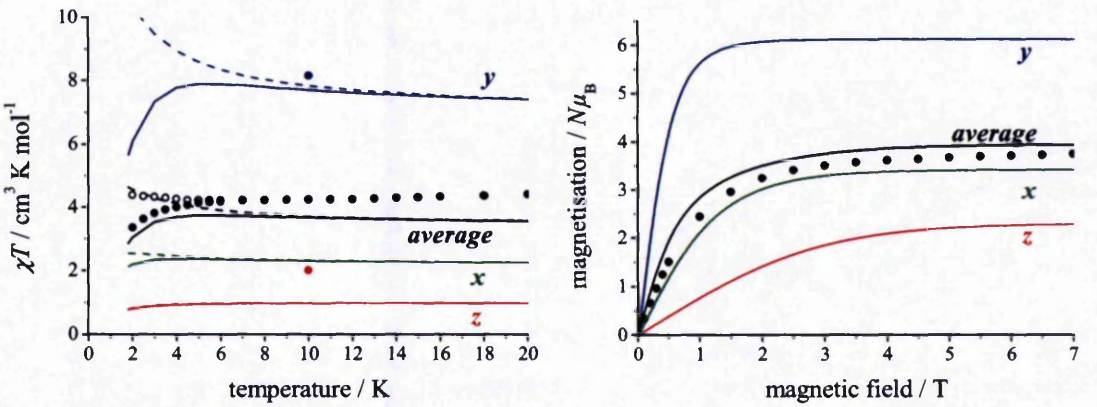

Figure III.45: Calculated magnetic properties of **4** along the principal magnetic axes for "$g_{eff,xx}$" = 3.43, "$g_{eff,yy}$" = 6.13, "$g_{eff,zz}$" = 2.30, "D_{eff}" = 1.2 cm^{-1}, and "E_{eff}" = 0.4 cm^{-1}. Left: χT at 1 T (solid) and 0.1 T (dash), right: magnetisation at 1.8 K. The principal average is a good estimate of the powder experiment (χT: dot: 1 T, circle 0.1 T; magnetisation: dot 1.8 K)

For each principal direction, the principal magnetisation and susceptibility has been calculated from Equations II.4 and II.5. The average of the three principal directions has been compared to the magnetic properties of the powder samples. Figure III.45 shows calculated and experimental magnetic properties of **4**. The average magnetisation compares well to the experimental results at all magnetic fields. The small constant overall deviation of the calculation from the experimental results may either represent the limitation of the model, or arise from a small experimental error. INS, EPR and SQUID measurements have been performed on different sample

batches of deuterated and hydrogenated samples, and small differences may be possible.

Some discrepancy is observed for the calculation of the temperature dependent susceptibility between 2 and 20 K. While the overall curvature of χT and the field dependence between 0.1 T and 1 T at low field is reproduced well, the absolute calculated numbers are lower than the experimental values. The magnetic susceptibility is extremely sensitive to the anisotropy of the system. Figure III.46 shows the same calculation, but with an average "g_{eff}"-value of 3.97 rather than the principal values. Here, the average susceptibility is even lower than in the anisotropic calculation. The average magnetisation is less sensitive to the "g_{eff}"-anisotropy, although the overall curvature of the experimental data is reproduced slightly better with anisotropic "g_{eff}"-values.

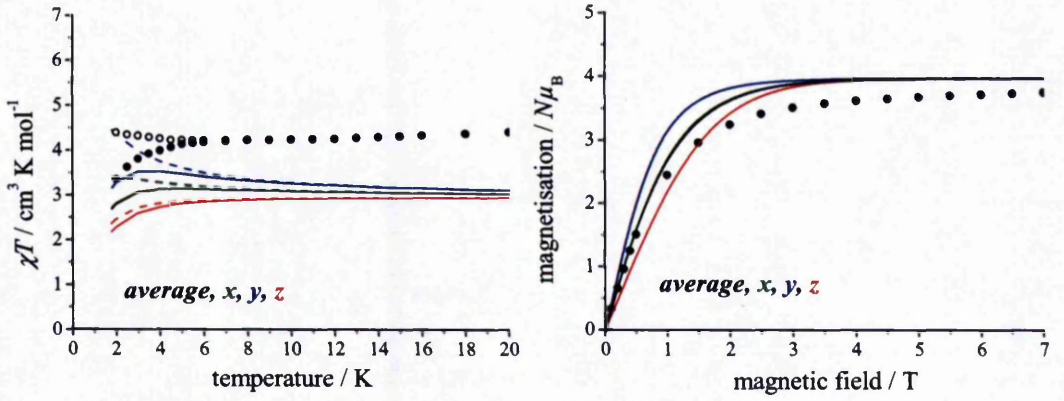

Figure III.46: Calculated magnetic properties of **4** along the principal magnetic axes for "$g_{eff,xx}$" = "$g_{eff,yy}$" = "$g_{eff,zz}$" = 3.97, "D_{eff}" = 1.2 cm^{-1}, and "E_{eff}" = 0.4 cm^{-1}. Left: χT at 1 T (solid) and 0.1 T (dash), right: magnetisation at 1.8 K.

In the previous sections the limitation of the simple effective model at low magnetic fields has been discussed. The correct curvature of the energy of spin-orbit wavefunctions in low magnetic fields is not reproduced correctly with the model equations, and such deviations are potentially very important for the anisotropy observed in the magnetic susceptibility.

Despite the limitation of the model, two single crystal data points in the *ac*-plane (maximum and minimum of the 10 K rotation plot, see Section III.2.2) confirm the magnitude and direction of the anisotropy calculated for **4**. Furthermore, the calculations confirm observations in Section III.2.2, where the apparent difference in

the ferromagnetic exchange contribution has been mentioned. In the single crystal SQUID experiment (Section III.2.2) only a minor decrease has been obtained for $\chi_2 T = \chi_y T$ between 300 and 10 K. Spin-orbit coupling is expected to induce a much stronger decrease, indicating that ferromagnetic exchange in the direction of $\chi_2 = \chi_y$ must be significantly stronger than the average observed in the powder. In comparison to the powder or principal average, the calculations indicate strong ferromagnetic exchange interaction along y and a weak ferromagnetic exchange along x, both lie perpendicular to the cobalt-cobalt vector. Along z and hence the cobalt-cobalt vector, very weak antiferromagnetic exchange, if any, is observed.

Figure III.47 shows the calculated magnetic properties of **3** in comparison to the experimental results on powder samples.

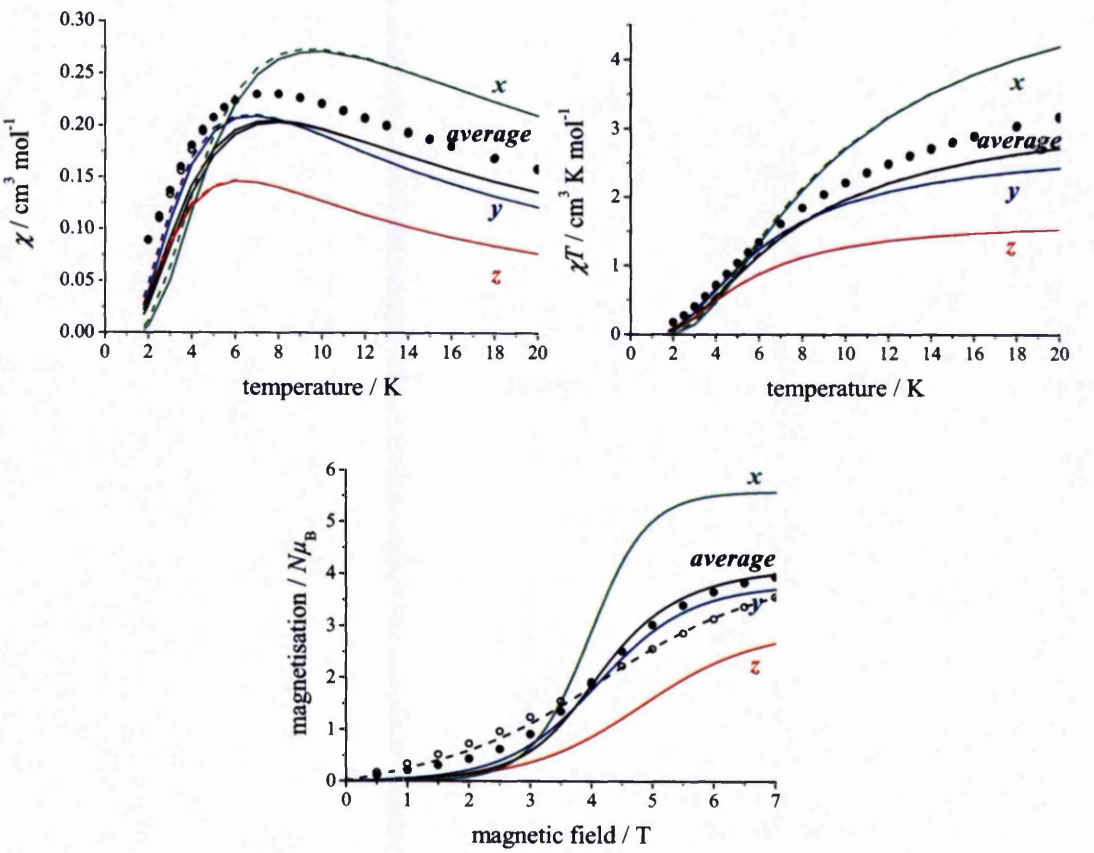

Figure III.47: Calculated magnetic properties of **3** along the principal magnetic axes for "$g_{eff,xx}$" = 5.6, "$g_{eff,yy}$" = 3.9, "$g_{eff,zz}$" = 3.0, "D_{eff}" = -4.35 cm^{-1}, and "E_{eff}" = 2.35 cm^{-1}. Top: χ and χT at 1 T (solid) and 0.1 T (dash), bottom: magnetisation at 1.8 K. The principal average is a good estimate of the powder experiment (χT: dot: 1 T, circle 0.1 T; magnetisation: dot 1.8 K, circle 4 K).

Again, the trend of the temperature dependent susceptibility, especially the temperature of χ_{max} is reproduced well, but the absolute calculated values are below the experimental observations. The field dependent magnetisation is reproduced extremely well above 4 T, the inflection point of the sigmoidal curve. At this point the linear region of the Zeeman splitting has been reached and the model describes the system well. At low magnetic fields the model is limited and does not reproduce the correct field dependence of the energy levels. While in **4** the ground energy level is magnetic, **3** exhibits a diamagnetic ground state, and hence the system is more sensitive to the population differences of the remaining energy levels. Small deviations from the model may lead to a significant difference in the calculated magnetisation at low magnetic fields. Similar to discussions on the HFEPR of **4** a steeper increase, and hence an earlier population of excited states in **3** than predicted from the calculations may indicate curving of the "triplet" energy levels towards lower energies, consistent with the AOM calculations (Section III.5.2). Furthermore, mixing induced through the strong "g_{eff}"-anisotropy may lead to a certain field dependence and magnetic character of the effective ground "singlet" itself, leading to an increase of the field dependent magnetisation until the level crossing occurs.

III.6 Conclusions

Seven octahedral cobalt(II) dimetallics have been studied with complementary techniques such as SQUID and torque magnetometry, EPR spectroscopy and INS on powder and single crystal samples. Such experiments provide high resolution experimental data in order to investigate the anisotropy of magnetic exchange interactions between the two spin-orbit cobalt(II) ions. Low temperature experimental results were interpreted on the basis of a simple effective model taking into account only the ground Kramers doublets of octahedral cobalt(II) interacting to give rise to an effective "singlet" and "triplet state".

Magnetic measurements have shown antiferromagnetic exchange interactions for six (**3**, **5**–**9**) out of the seven examples, while the dimetallic **4** is characterized by weak ferromagnetic exchange coupling. No structure-related trends were found, which indicate a reason for the inversion of the magnetic properties in **3** and **4** despite the

almost identical molecular structure. The origin is believed to lie in the electronic structure, which is extremely sensitive to small changes in the ligand field, due to the strong anisotropy of the single ions.

Single crystal rotational studies by magnetometry in selected crystallographic planes of the ferromagnetically and two antiferromagnetically coupled dimetallics have provided the orientation of the principal molecular magnetic axes. Strong anisotropy has been observed in all cases, which manifests in particular in the strong "*g*"-anisotropy that has also been discussed in Chapter II. In addition, the peak temperature of χ and the inflection point of a level crossing observed in single crystal low temperature magnetic measurements on **5** have shown that anisotropy is also present in the exchange interactions. An even more pronounced effect is present in **4**, where calculations and preliminary single crystal magnetic measurements indicate very weak antiferromagnetic exchange along the cobalt-cobalt vector, and ferromagnetic exchange in the orthogonal directions.

To our knowledge, no EPR spectra on exchange coupled cobalt(II) system have been reported to date. Here multifrequency EPR spectra on two dimetallics, and the first rotational study on an exchange coupled cobalt(II) system (**4**) were presented. Overall the experimental spectra are very rich and confirm the magnetic exchange interactions between the ground Kramers doublets of the cobalt(II) ions obtained in magnetic measurements, in particular in the case of **4**, where SQUID magnetometry is not sensitive enough to prove the weak ferromagnetic interactions unambiguously. Multifrequency EPR spectroscopy on **4** has shown a high degree of linearity in the frequency dependence of the resonance magnetic field, down to at least 34 maybe even 9.4 GHz. Such linearity was not expected from a spin-orbit system and this observation is very important because it shows that despite the spin-orbit character of the wave functions, the system exhibits a frequency dependence, which appears to have strong similarities to a spin-only *g*-value.

The temperature dependence of electronic transitions observed with both EPR spectroscopy and INS have confirmed the isolation of the ground multiplet from further excited energy levels by a separation of at least 60 K, the essential condition to interpret the low temperature magnetic properties of cobalt(II) ions based on the ground Kramers doublets only. Consistent results have been found in calculations of

the single ion eigenvalues with the AOM and *ab-initio* methods, which predict an energy gap between the two lowest Kramers doublets of > 150 cm^{-1}.

Single crystal EPR spectroscopy at Q-band frequency on **4** has allowed for the assignment of the "triplet" transitions and the corresponding "g_{eff}"-values observed in the multi-frequency powder experiment to the principal magnetic and spectroscopic axes ("$g_{eff,xx}$" = 3.43, "$g_{eff,yy}$" = 6.13, "$g_{eff,zz}$" = 2.30). Together with the zero-field energies observed experimentally with INS, the Zeeman splittings of **3** and **4** were calculated on the basis of a very simple effective model: Exchange coupling with J = -4.23 cm^{-1} (**3**) and J = 0.8 cm^{-1} (**4**) between two "s" = $^1/_2$ doublets leads to an effective "singlet" and "triplet" state, where all degeneracy is lifted. As a result it has indeed been possible to simulate semi-quantitatively the EPR transition energies in **3** and **4**, and to calculate the magnetic properties of the two compounds with the same parameters. In particular in the case of **4** it is worth emphasizing again that the Zeeman splitting was not fitted, but calculated solely from experimental observables and reproduces complementary results from SQUID magnetometry, EPR spectroscopy and INS *simultaneously*. Deviations of the calculation from the experimental data were expected, and are not the result of bad parameters, but the limitation of the over-simplified model, which was never aimed to result in a fully quantitative interpretation of the experimental data. The main discrepancy is, as expected, a non-symmetrical Zeeman spitting in the real systems. A linear frequency dependence of the resonance field at the same time as a deviation of the experimental transitions from a linear symmetrical Zeeman splitting is only possible, if energy levels evolve (nearly) linearly with the magnetic field, but the slope of corresponding $\pm m$ levels deviates between $+m$ and $-m$, averaging to the observed "g_{eff}"-values. Comparison of the linearly modelled Zeeman effect to the actual transition energies obtained with EPR spectroscopy points towards a Zeeman splitting reminiscent of the single ion properties obtained in Chapter II, and potential inter multiplet mixing due to the strong "g"-anisotropy of the single ions.

Chapter IV

Studies on antiferromagnetically coupled hetero-metallic rings

Antiferromagnetically coupled heterometallic rings have been investigated intensively during the past five years, because such compounds have been suggested for applications in quantum computing (see Section I.3).[75,77,80,90]

Most heterometallic rings exhibit a paramagnetic ground state, and within families of isostructural compounds, magnetic and electronic properties of ground and excited states can be tuned, whilst retaining a constant geometric and chemical environment. The electronic structure arising from magnetic exchange interactions within the circle of metal ions has been investigated thoroughly by complementary techniques such as SQUID and high-field torque magnetometry,[73,90] specific heat measurements,[78,90] EPR, MCD and XMCD spectroscopy,[89,94,126] and inelastic neutron scattering[92,93] on various different examples. However, so far, most studies on heterometallic chromium rings have been focused on systems that do not exhibit a first order orbital angular momentum. In the following sections different cobalt(II) containing heterometallic rings are studied to investigate the influence of the large single ion anisotropy of octahedral cobalt(II) on the magnetic and spectroscopic properties of the ring. To gain a good understanding of the individual components and their contribution to the overall physical properties, several isostructural compounds have been compared:

$[(C_2H_5)_2NH_2][Cr_7ZnF_8(O_2CC(CH_3)_3)_{16}]$	(Cr_7Zn, **10**)	chromium-chromium
$[(CH_3)_2NH_2][Cr_7CdF_8(O_2CC(CH_3)_3)_{16}]$	(Cr_7Cd, **11**)	exchange
$[(CH_3)_2NH_2][Ga_7CoF_8(O_2CC(CH_3)_3)_{16}]$	(Ga_7Co, **12**)	single ion cobalt(II)
$[(CH_3)_2NH_2][Cr_7NiF_8(O_2CC(CH_3)_3)_{16}]$	(Cr_7Ni, **13**)	spin only chromium-nickel system for comparison
$[(CH_3)_2NH_2][Cr_7CoF_8(O_2CC(CH_3)_3)_{16}]$	(Cr_7Co, **14**)	chromium-cobalt system

In a subsequent project, heterometallic rings templated around imidazolium cations have been studied, some of which contain more than one divalent hetero-ion. In the first instance chromium-nickel compounds have been studied intensively to

understand the properties of rings with more than one heteroion on the isostructural spin-only systems before moving on to the theoretically more challenging cobalt(II) derivatives:

[2,4-DiMe-ImidH][$Cr_7M^{II}F_8(O_2CC(CH_3)_3)_{16}$] ($Cr_7Ni$, (**15**), Cr_7Co, (**16**))

[ImidH]$_2$[$Cr_6M^{II}_2F_8(O_2CC(CH_3)_3)_{16}$] ($Cr_6Ni_2$ (**17**), Cr_6Co_2 (**18**))

[1-Bz-ImidH]$_2$[$Cr_7M^{II}_2F_9(O_2CC(CH_3)_3)_{18}$] ($Cr_7Ni_2$ (**19**), Cr_7Co_2 (**20**))

IV.1 Brief structural description of heterometallic rings

All heterometallic rings that are described in this Ph.D. thesis were synthesised and kindly provided for measurements by Dr. Grigore Timco of the University of Manchester. Details on synthetic procedure and crystallographic data are given in Appendix 4.1.

Chemically the eleven compounds (**10** – **20**) are very similar. In all systems the metal ions are located in an almost planar octagon and bridged by a fluoride ion and two deprotonated pivalic acid molecules. Half of the pivalates are located within the ring plane (equatorial), the remaining pivalates alternate perpendicularly above and below the ring (axial). The carboxylate functionality provides delocalised π-electrons and hence a pathway for magnetic superexchange around the circle of metal ions. The mono- or bivalent anionic rings are templated around one or two protonated amines respectively, for charge balance.

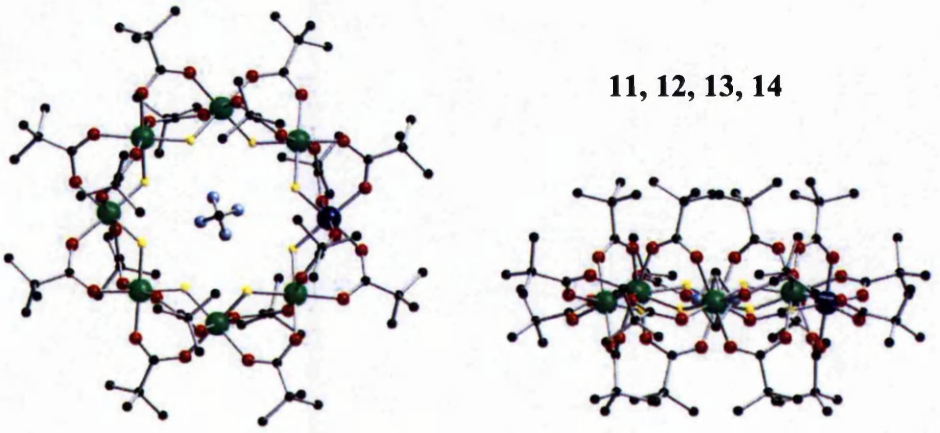

Figure IV.1: Top and side view of the isostructural rings [$(CH_3)_2NH_2$][$M^{III}_7M^{II}F_8(O_2CC(CH_3)_3)_{16}$] ($M^{III}$ = Cr, M^{II} = Cd (**11**), M^{III} = Ga, M^{II} = Co (**12**), M^{III} = Cr, M^{II} = Ni (**13**), M^{III} = Cr, M^{II} = Co (**14**)), *I4*: $a = b = 19.8514(7)$ Å, $c = 16.1783(7)$ Å, $V = 6345.9(4)$ Å^3, $Z = 2$[73]

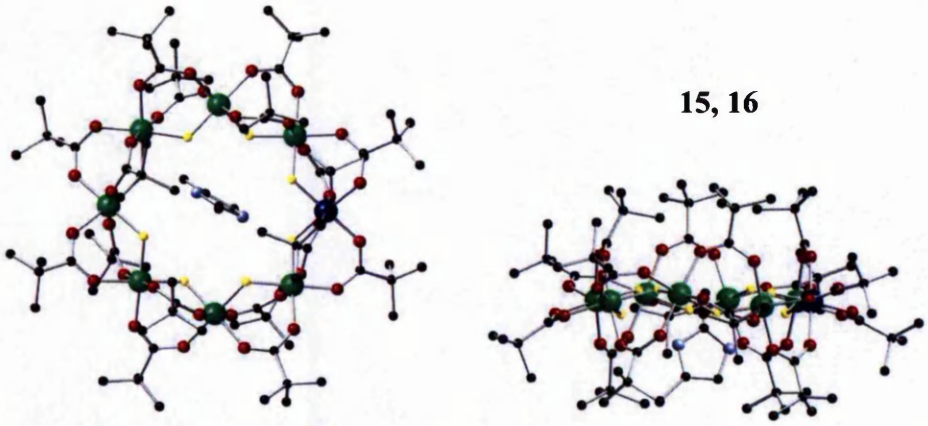

15: *I2/a*, a = 34.899(3) Å, b = 16.5196(4) Å, c = 44.0704(15) Å, β = 111.673(3)°, V = 23611.2 Å^3, Z = 8. **16**: *C2/c*, a = 45.042(8) Å, b = 16.5349(4) Å, c = 34.959(7) Å, β = 114.529(7)°, V = 23687(6) Å^3, Z = 8

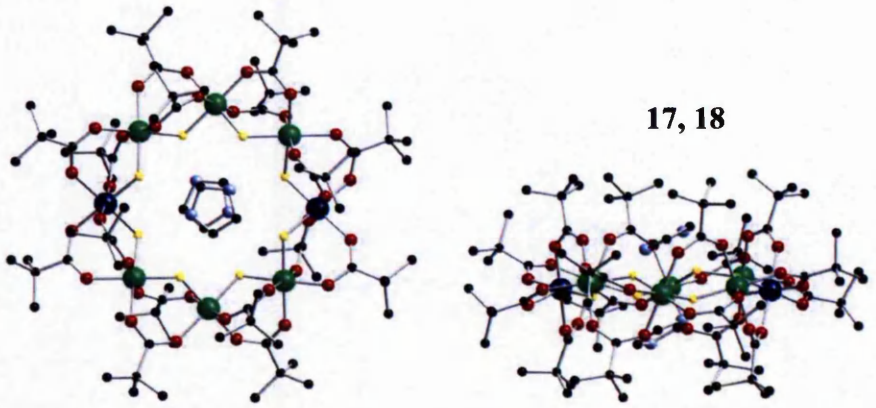

17: *P21/c*, a = 24.9795(5) Å, b = 16.6454(3) Å, c = 31.0755(6) Å, β = 111.147(2)°, V = 12050.9 Å^3, Z = 4, **18**: isostructural

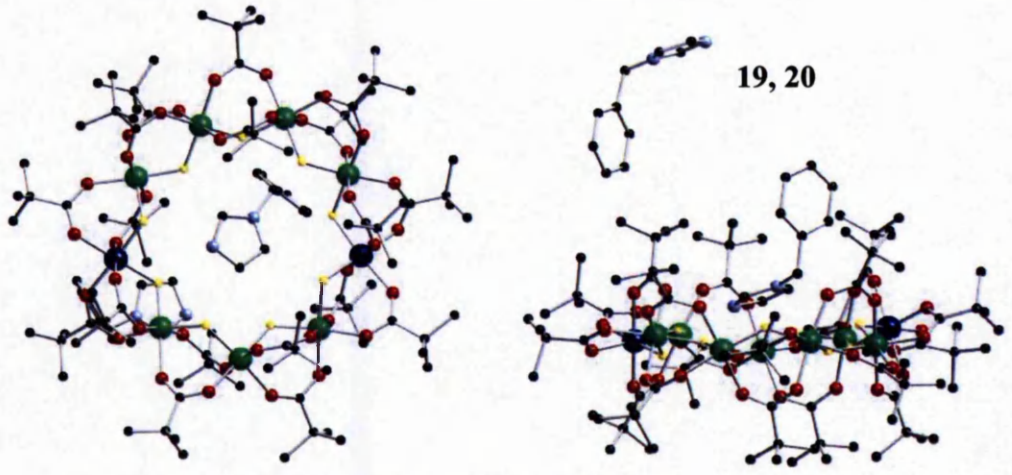

19: *C2*, Z = 2; a = 28.2803(14) Å, b = 19.8054(10) Å, c = 13.8581(12) Å, β = 106.439(6), V = 7444.7(8) Å^3, Z = 2. **20**: isostructural

Figure IV.2: Top and side view of isostructural pairs: [2,4-DiMe-ImidH][$Cr_7M^{II}F_8(O_2CC(CH_3)_3)_{16}$] ($Cr_7Ni$ (**15**) Cr_7Co (**16**)), [ImidH]$_2$[$Cr_6M^{II}{}_2F_8(O_2CC(CH_3)_3)_{16}$] ($Cr_6Ni_2$ (**17**), Cr_6Co_2 (**18**)), [1-Bz-ImidH]$_2$[$Cr_7M^{II}{}_2F_9(O_2CC(CH_3)_3)_{18}$] ($Cr_7Ni_2$ (**19**), Cr_7Co_2 (**20**))

Figures IV.1 and IV.2 show the crystallographic structures of the ten heterometallic rings **11** - **20**. In all cases the hetero-ions are disordered over all possible sites, and in the images the coloured location of the hetero atom has been chosen arbitrarily. The metal content of the heterometallic rings was determined by elemental analysis confirming the presence of one or two hetero-ions as indicated.

Compound **11** – **14** are isostructural. Molecule **10** only differs in the templating ammonium cation ($[(C_2H_5)_2NH_2]^+$ instead of $[(CH_3)_2NH_2]^+$ and consequently different crystal packing), which does not change the overall powder magnetic properties of the compound in comparison to **11**.

In compounds **15** – **20** imidazolium cations function as templates for the heterometallic rings. Again the pairs of cobalt and nickel derivatives crystallize isostructurally.

For the odd membered rings **19** and **20** the alternating arrangement of the axial pivalates above and below the metal plane is interrupted in one position. (Figure IV.3) The two pivalate molecules between ion 5 and 6 both lie on the vertex between the horizontal and vertical position. The different geometry may influence the magnetic exchange interaction in comparison to the remaining pairs of ions. From crystallographic studies it is not possible to distinguish if positions 5 and 6 are occupied by chromium or nickel/cobalt ions or both.

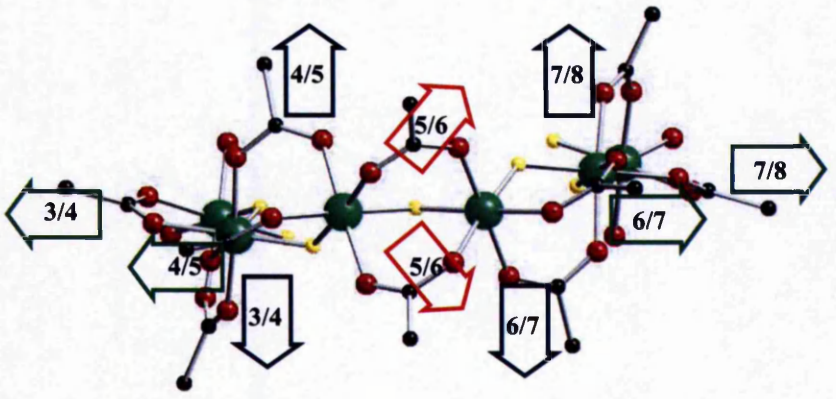

Figure IV.3: Geometry of the pivalate bridges in **19** and **20**. Green: in the ring plane, blue: alternating above and below the ring plane, red: between atom 5 and 6 the alteration is interrupted and both pivalates are located on the vertex between a horizontal and vertical orientation.

IV.2 Influence of the anisotropic cobalt(II) ion on the physical properties of heterometallic rings

The magnetic properties of $[R_2NH_2][Cr_7M^{II}F_8(O_2CC(CH_3)_3)_{16}]$ with M^{II} = Ni, Co, Cd, Mn and Fe have been reported in 2003.[73] The effect of the strong anisotropy of cobalt(II) ions on magnetic exchange interactions between chromium(III) and cobalt(II) ions and hence on the overall magnetic properties of the ring system, forms the central question in the following section. Cr_7Co (**14**) has been investigated systematically by comparison with isostructural compounds providing information of the single ion contributions.

Prior to this Ph.D. project the contribution of the chromium ions to the magnetic properties of heterometallic rings has been intensively studied by Dr. Stergios Piligkos on $[R_2NH_2][Cr_7M^{II}F_8(O_2CC(CH_3)_3)_{16}]$, where the paramagnetic hetero-ion is replaced with a diamagnetic zinc (**10**) or cadmium (**11**) ion. Multifrequency EPR spectroscopy on powder and single crystal samples of **11** have provided detailed spin-Hamiltonian parameters such as chromium-chromium exchange, chromium single ion *g*-values and zero-field splitting.[89,91,127] Replacing the chromium(III) ions with diamagnetic gallium(III) allows for the study of the cobalt(II) contribution in identical ligand field surroundings, hence the isostructural Ga_7Co ring (**12**) was synthesized. Both the contributions from chromium(III) and cobalt(II), as well as a comparison with the widely studied, magnetically simpler isostructural nickel derivative **13**, will be a major step towards the interpretation of the magnetic properties of **14**.

IV.2.1 Contributions from chromium and cobalt to the properties of the rings studied separately on Cr_7Zn/Cd and Ga_7Co

The experimental and calculated temperature dependent susceptibility of Cr_7Zn (**10**) has been investigated by Piligkos and a chromium-chromium exchange interaction of *ca.* -5.9 cm^{-1} has been reported.[127] At room temperature $\chi T \sim 11.3$ cm^3 K mol^{-1} is slightly lower than expected for seven uncoupled chromium spins $s = {}^3/_2$ with g =

1.96 (χT = 12.6 cm^3 K mol^{-1}). However, the temperature dependent susceptibility in Figure IV.4 is not fully saturated yet, and the small deviation may arise from unpopulated high energy levels, which do not contribute to the magnetic moment at room temperature.

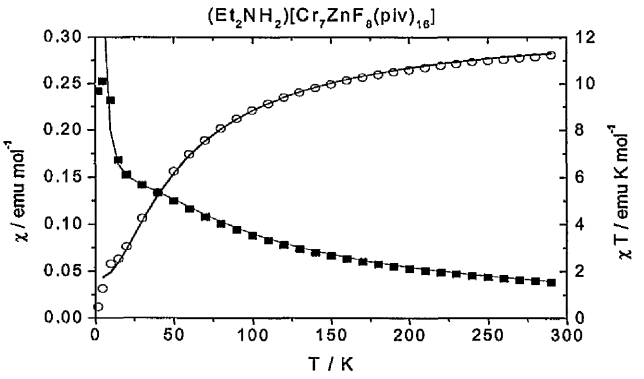

Figure IV.4: Magnetic properties of Cr_7Zn (**10**) reported by Piligkos,[73,127] square: χ, ring: χT, line: best fit with the parameters $J_{(Cr\text{-}Cr)}$ = -5.9 cm^{-1} and $J_{(Cr\text{-}Zn)}$ = 0

Much more sensitive to the electronic structure, and therefore to the spin-Hamiltionian parameters than SQUID mangetometry, is EPR spectroscopy. Piligkos has reported multifrequency EPR spectroscopy on powder and single crystal samples of Cr_7Cd (**11**).[89,91,127] Figure IV.5 (left) shows the experimental Q-band EPR spectrum on a powder sample of **11** and its simulation with a conventional spin-Hamiltonian in the strong exchange limit (SEL), *viz.* Equation I.4 with $g_{eff,xx} = g_{eff,yy}$ =1.955, $g_{eff,zz}$ = 1.945, for all spin states, $D_{eff,3/2}$ = -0.41 cm^{-1}, $E_{eff,3/2}$ = -0.041 cm^{-1}, $D_{eff,5/2}$ = 0.04 cm^{-1}, and $E_{eff,5/2}$ not determined.

The strong exchange limit (SEL) has been introduced in Section I.1.1 and is based on exchange interactions, which are strong, compared to the single ion anisotropy. Effective zero-field splitting parameters are used to parameterize anisotropy in the resulting effective total spin-states. Ground and excited state spin-states are modelled independently in this most widely used approach to model EPR spectra on exchange coupled oligomers. The spectrum has been reproduced reasonably well within the SEL by summation over the contributions from ground and first excited state separately.

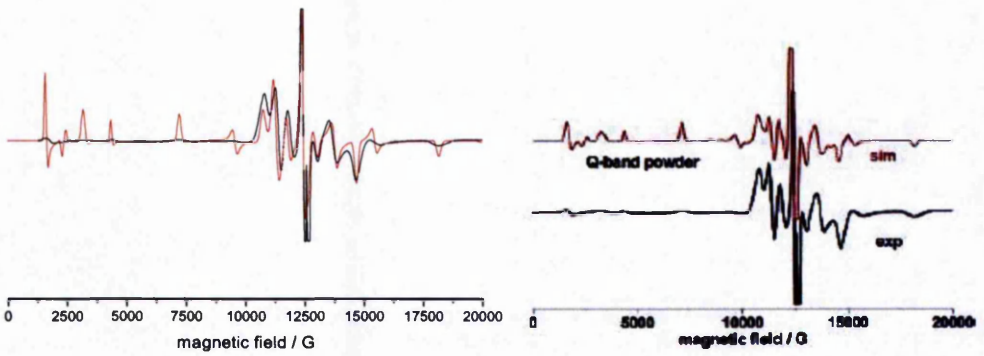

Figure IV.5: Experimental EPR powder spectrum of Cr_7Cd (**11**) (black) and simulation (red) at 34.05 GHz, isotropic Gaussian linewidth of 100G. Left: SEL with spin-Hamiltonian parameters: $g_{eff,xx} = g_{eff,yy} = 1.955$, $g_{eff,zz} = 1.945$, for all spin states, $D_{eff,3/2} = -0.41$ cm^{-1}, $E_{eff,3/2} = -0.041$ cm^{-1}, $D_{eff,5/2} = 0.04$ cm^{-1}, $E_{eff,5/2}$ not determined.[127] Right: microscopic spin-Hamiltonian with: $J_{Cr\text{-}Cr} = -5.800$ cm^{-1}, $g_{Cr} = 1.960$, $D_{Cr} = -0.145$ cm^{-1}, $D_{Cr\text{-}Cr} = -0.098$ cm^{-1}.[89]

An even better agreement has been obtained by extending the model to the use of a microscopic spin-Hamiltonian to determine the single ion parameters for the chromium ions (Figure IV.5 right, Equation IV.1).[89,91] The following parameters are reported for individual chromium ions with $s_i = {}^3/_2$: $J_{Cr\text{-}Cr} = -5.800$ cm^{-1} (isotropic exchange), $g_{Cr} = 1.960$, $D_{Cr} = -0.145$ cm^{-1} (axial zero-field splitting), $D_{Cr\text{-}Cr} = -0.098$ cm^{-1} (anisotropic exchange). In a more recent publication the D parameters have been adjusted to fit not only the transitions in Cr_7Cd, but simultaneously in Cr_7Ni ($D_{Cr} = -0.134$ cm^{-1}, $D_{Cr\text{-}Cr} = -0.106$ cm^{-1}).[91]

$$\hat{H} = \sum_i \mu_B \vec{B} \mathbf{R}^*_{g,i} \begin{pmatrix} g_{xx,i} & 0 & 0 \\ 0 & g_{yy,i} & 0 \\ 0 & 0 & g_{zz,i} \end{pmatrix} \mathbf{R}^{-1}_{g,i} \hat{s}_i + \sum_i \hat{s}_i \mathbf{R}^*_{D,ii} \begin{pmatrix} -D_i/3 & 0 & 0 \\ 0 & -D_i/3 & 0 \\ 0 & 0 & 2D_i/3 \end{pmatrix} \mathbf{R}^{-1}_{D,ii} \hat{s}_i$$
$$+ \sum_{i,j>j} -2\hat{s}_i J_{ij} \hat{s}_j + \sum_{i,j>j} \hat{s}_i \mathbf{R}^*_{D,ii} \begin{pmatrix} -D_{ij} & 0 & 0 \\ 0 & -D_{ij} & 0 \\ 0 & 0 & 2D_{ij} \end{pmatrix} \mathbf{R}^{-1}_{D,ii} \hat{s}_i \qquad \text{(IV.1)}$$

To investigate the cobalt(II) site in the heterometallic rings, temperature dependent susceptibility and field dependent magnetisation, as well as Q-band and W-band EPR spectra of Ga_7Co (**12**) have been measured. (Figures IV.6 and IV.7)

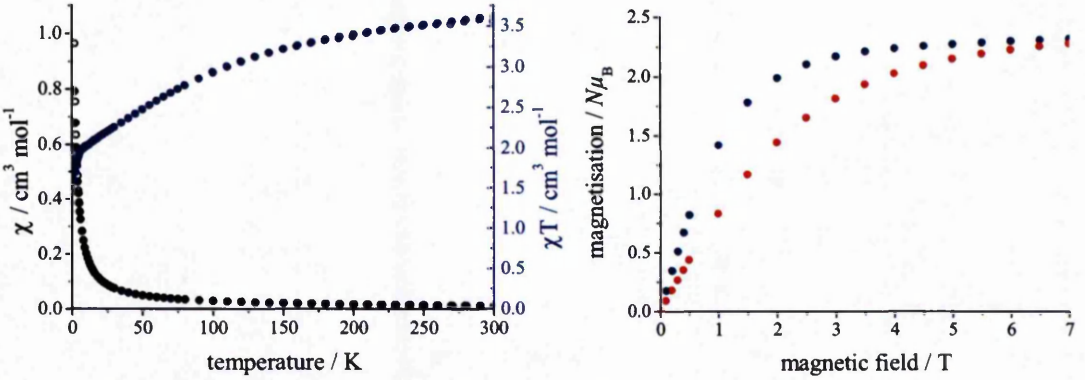

Figure IV.6: Magnetic properties of Ga_7Co (**12**) measured on a powder sample fixed in eicosane. Left: temperature dependent susceptibility at 1 T (dot) and 0.1 T (ring), right: field dependent magnetisation at 2 K (blue) and 4 K (red).

Compound **12** shows the typical magnetic behaviour for a monometallic cobalt(II) ion in an octahedral ligand field (compare Section II.2). Both high and low temperature susceptibility ($\chi T_{300\,K}$ = 3.61 cm^3 K mol^{-1}, $\chi T_{2\,K}$ = 1.92 cm^3 K mol^{-1}), the decrease of χT upon cooling due to first order spin-orbit coupling, and the high saturation value of the magnetisation (M = 2.32 $N\mu_B$) are evidence for the strong orbital contribution to the magnetic properties.

The Q-band and W-band EPR spectra show identical features at both frequencies and no significant temperature dependence up to 20 K, which indicates a ground (spin-orbit) state isolated from further excited states by a minimum of 50 cm^{-1}.

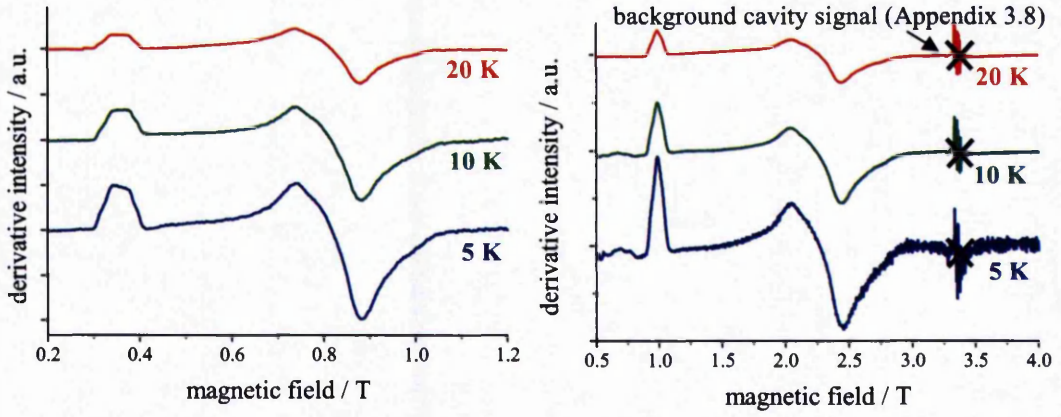

Figure IV.7: Variable temperature EPR spectra of Ga_7Co (**12**). Left: Q-band, right: W-band

The broad, very anisotropic spectra have an average pseudo "g"-value of *ca.* 4.3, and show strong axial or even slightly rhombic anisotropy with one component "g" ~ 6.8

and two components with "g" ~ 2.9. To ascertain whether those transitions are characteristic features of heterometallic gallium-cobalt rings, the Q-band EPR spectrum was also been collected for a ring templated around a different ammonium cation $[C_3H_7NH_2][Ga_7CoF_8(O_2CC(CH_3)_3)_{16}]$ and the same anisotropy with similar values ("g" ~ 6.8 and 2.9) was observed (Appendix 4.2).

The almost rectangular shape of the envelope of the parallel component at Q-band frequency is characteristic for hyperfine coupling in the order of the spectral linewidth. Figure IV.8 shows the experimental spectrum and its calculated second derivative. The spectra are overlaid with a simulation for a pseudo spin "s" = $^1/_2$, "g_{xx}" = 2.69, "g_{yy}" = 3.01, "g_{zz}" = 6.79, a linewidth of 130 G and a hyperfine splitting of A = 70 G modelled with second order contribution effects. The shape of either derivative is not reproduced well, but from the second derivative spectrum a good estimation of the cobalt(II) hyperfine splitting is possible.

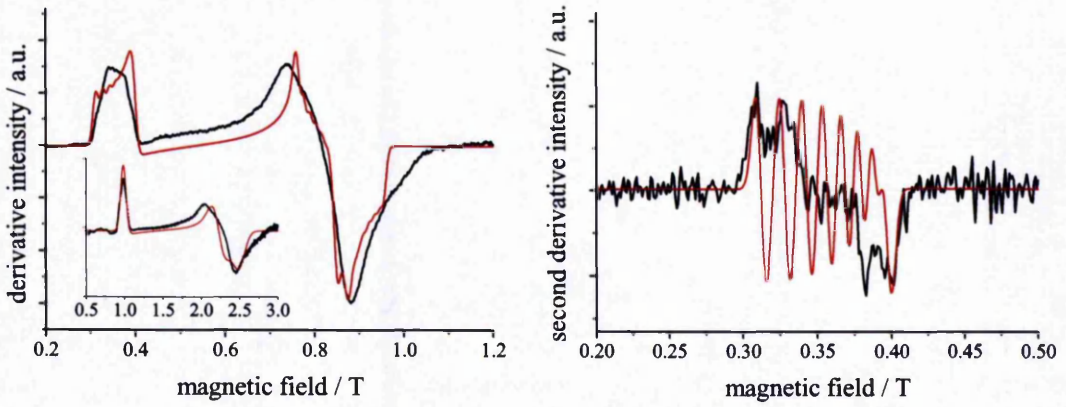

Figure IV.8: Left: first derivative Q-band spectrum of Ga_7Co (**12**), right: low field region of the second derivative spectrum calculated from the experimental spectrum. Simulation (red) for "s" = $^1/_2$, "g_{xx}" = 2.69, "g_{yy}" = 3.01, "g_{zz}" = 6.79, A = 70 G, linewidth: 130 G; Inset left: W-band spectrum and simulation for the above $\mathbf{g}_{eff}$-matrix, no hyperfine coupling, anisotropic linewidth xy: 1500 G, z = 700 G.

The over simplified model assumes hyperfine coupling between the cobalt nuclear spin of $^7/_2$ and an electron spin of $^1/_2$ although for the actual system the magnetic moment of $^1/_2$ is not a spin but a spin-orbit doublet. This may explain the deviation of the calculated spectral shape from the experimental observation. Furthermore the experimental spectrum is characterised by an anisotropic linewidth. The xy region of the spectrum is significantly more broadened than the simulation of 130 G that reproduces the z width in both first and second derivative spectra. Nevertheless the shape of the envelope in the xy region reproduces roughly the observed shape of the

signal indicating that this shape of signal is also influenced significantly by the observed hyperfine coupling. Slight *xy* anisotropy has been introduced; however the experimental spectrum indicates that even stronger anisotropy may be necessary. Compound **12** crystallizes in a tetragonal space group and by symmetry constraints the overall anisotropy should be limited to axial splitting. However, if an individual ring is considered, the introduction of M^{II} breaks the axial symmetry and rhombicity is possible. Nevertheless it is possible to obtain an overall axial anisotropy of the compound even though the electronic structure at the eight individual metal sites can be rhombic. The spectrum is too broad and influenced by too many components to determine exact values for "g_{xx}" and "g_{yy}" in the simplified effective model. The linewidth of the parallel component at W-band frequency is about 700 G and the much smaller hyperfine splitting is not resolved. The inset in Figure IV.8 shows the simulation of the W-band spectrum with the same effective "**g**"-matrix, no hyperfine coupling and anisotropic linewidth (*xy*: 1500 G, *z*: 700 G).

In previous chapters it has been shown that treatment of low temperature magnetic and spectroscopic properties of cobalt(II) as an effective "*s*" = $^1/_2$ can give a qualitative answer, but is not sufficient to understand fully the observed behaviour. One important aspect is the orientation of the magnetic axis on the cobalt centre with respect to the ligand field. The strong single ion anisotropy of cobalt(II) ions leads to a high sensitivity to the ligand field orientation, and the angular overlap model has been used to investigate the influence of the ligand field on the Zeeman anisotropy in gallium-cobalt ring. A quantitative reproduction of the single ion EPR spectrum with AOM was not attempted, because the number of free variables *i.e.* e_σ and anisotropic e_π parameters for the carboxylate oxygen and fluoride atoms is too large to fit against powder magnetic and spectroscopic properties. Nevertheless the method can be used to estimate the direction of the anisotropy, which depends to a large extent on the ligand field geometry. Geometrically two non-equivalent metal sites are present in the Ga_7Co ring, and identical calculations have been performed for both geometries within the tetragonal crystal axes frame. AOM parameters have been fixed to the set of parameters derived for the dimetallic **5** (Appendix 3.4) and anisotropic contribution from the carboxylate π-orbitals are treated in the same way. For details on the ligand field matrix and the orientation of the π-orbitals see also Section VI.4.1. Figure IV.9 shows the resulting calculated spectra in comparison to the

experimental observations. The experimentally observed anisotropy is reproduced surprisingly well by the sum of the calculations for the two individual centres, considering the parameters have been taken from a very different compound (e.g. oxygen instead of fluoride).

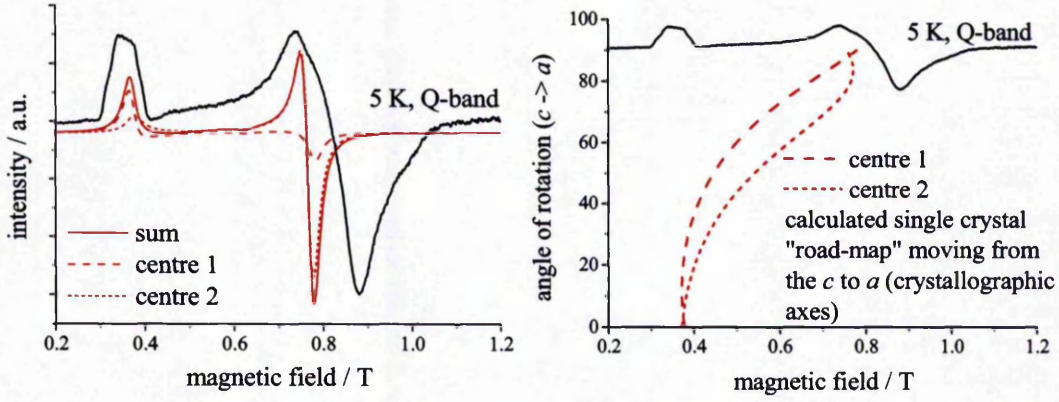

Figure IV.9: Left: Calculation of the EPR spectrum of Ga_7Co (**12**) with the AOM for the two possible cobalt(II) sites. All parameters are fixed to values obtained for the dimetallics **4** and **5**: $e_\sigma = 4160$ cm^{-1} (all), $e_{\pi x} = 300$ cm^{-1} (carboxylate), $e_{\pi y} = 500$ cm^{-1} (carboxylate), Racah $B = 840$ cm^{-1}, $C = 3860$ cm^{-1}, $\zeta = 515$ cm^{-1} (free ion), linewidth: 200 G. Right: calculated single crystal line position for a 90° rotation from the crystallographic axis *c* to *a*.

The *LIGFIELD*[110] software allows for the determination of the single crystal line positions (Figure IV.9, right) and calculations have been performed for a 90° rotation from the crystallographic axis *c* to *a*. The tetragonal crystal structure of **12** is highly symmetric and all molecular rings are packed in the same orientation. The tetragonal axis *c* runs perpendicular to the heterometallic rings, while the *ab*-plane is aligned with the ring plane. The two EPR signals can be assigned to the overall molecular principal directions: The low field signal at ca. 3500 G (Q-band) corresponds to the tetragonal axis, while the contribution at 8000 G (Q-band) can be assigned to contributions within the ring plane. Hence a very strong Zeeman splitting ("*g*" ~ 6.8) is obtained along the tetragonal axis, while a more moderate Zeeman splitting ("*g*" ~ 2.9) is obtained in the ring plane. This "g" anisotropy is consistent with that obtained for the dimetallic **4**, where the smallest Zeeman splitting ("$g_{eff,zz}$" = 2.30) was also obtained along the cobalt-cobalt vector, hence the direction with magnetic exchange mediated by two bridging carboxylate and a bridging water molecule similar to the ring plane geometry.

IV.2.2 Studies of Cr_7Co in comparison to the spin-only analogue Cr_7Ni

The temperature dependent susceptibility and field dependent magnetisation of Cr_7Co (**14**) have been re-measured and the results confirm the previously reported magnetic data on this compound[73] (Figure IV.10).

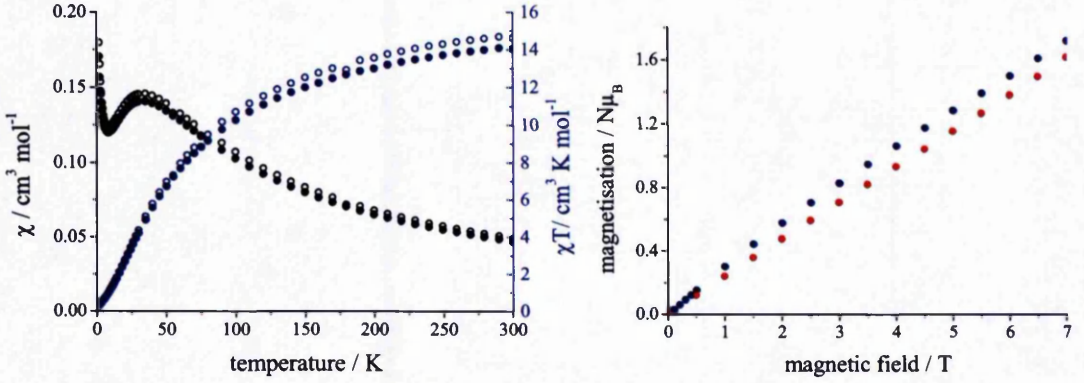

Figure IV.10: Magnetic properties of Cr_7Co (**14**) measured on a powder sample. Left: temperature dependent susceptibility at 1 T (dot) and 0.1 T (ring), right: field dependent magnetisation at 2 K (blue) and 4 K (red).

At room temperature magnetic exchange is masked due to equal population of all magnetic states and the magnetic susceptibility can be estimated as a simple addition of the single ion contributions from chromium (Cr_7Zn or Cr_7Cd) and cobalt(II) (Ga_7Co). The experimentally observed value of $\chi T_{300\,K}$ = 14.0 – 14.6 cm^3 K mol^{-1} is lower than the expectation value of χT = 16.2 cm^3 K mol^{-1} for seven uncoupled spin-only chromium ions (s = $^3/_2$, g = 1.96) and one cobalt(II) ion with spin and orbital angular momentum (s = $^3/_2$, l = 3, g = 2.00), but only slightly lower than the sum of the room temperature contributions taken directly from the analogues Cr_7Zn (Figure IV.4) and Ga_7Co (Figure IV.6), respectively leading to $\chi T_{300\,K}$ = 14.9 cm^3 K mol^{-1}. Again saturation of χT is not yet reached at 300 K, indicating that not all magnetically relevant energy levels are populated at room temperature. Upon cooling, the effect of antiferromagnetic coupling is observed below the ordering temperature of 30 K, leading to a diamagnetic ground state of the molecule. As discussed in previous chapters, the orbital angular momentum of octahedral

cobalt(II) ions leads to a splitting of the $^4T_{1g}$ ground term into a ground Kramers doublet and excited states. Qualitatively one could expect a paramagnetic total ground state of ~ 1 cm^3 K mol^{-1} arising from the antiferromagnetic coupling of seven chromium spins $s = {}^3/_2$ with an effective moment of ${}^1/_2$ from cobalt(II). However, the χT value at 2 K ($\chi T_{2\ K}$ = 0.36 cm^3 K mol^{-1}) indicates a diamagnetic ground state together with partial population of one or more low lying excited states. The constant increase in the magnetisation (Figure IV.10) with the application of a magnetic field confirms the presence of a diamagnetic ground state and close low lying excited states, which can easily be populated even at 2 K. It is clear, that the treatment of cobalt(II) as a pseudo spin "*s*" = ${}^1/_2$ within the heterometallic ring is *not* a valid approach to interpret the exchange interaction between the chromium and cobalt ions – not even in a qualitative manner.

Despite the introduction of a spin-orbit ion, the overall magnetic properties of Cr_7Co (**14**) are very similar to those of the Cr_7Ni (**13**) analogue. The original data on **13** have not been available for comparison, but in Figure IV.11 the temperature dependent susceptibility of **14** is plotted in comparison to the original data published in 2003 on $[(C_2H_5)_2NH_2][Cr_7CoF_8(O_2CC(CH_3)_3)_{16}]$ (**14a**) and the nickel analogue $[(C_2H_5)_2NH_2]$-$[Cr_7NiF_8(O_2CC(CH_3)_3)_{16}]$ (**13a**).[73]

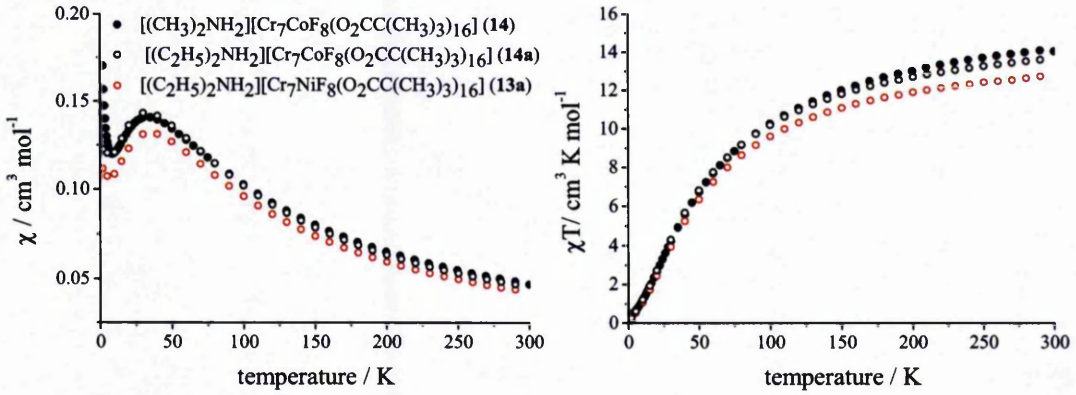

Figure IV.11: Temperature dependent susceptibility of **14** in comparison to **13a** and **14a**. Identical behaviour of **14** and **14a** validates a direct comparison of **14** and **13a**.[73]

Compounds **14** and **14a** are identical, apart from the templating ammonium cation $[(CH_3)_2NH_2]^+$ that has been replaced with $[(C_2H_5)_2NH_2]^+$. As expected no difference in the magnetic properties of **14** and **14a** is observed from the change in the templating cation. The small deviation between the high temperature susceptibilities

may arise from differences in measurement methods and diamagnetic corrections, which can influence the weaker magnetic response at high temperature in particular. The good agreement in the presence of a stronger signal in the SQUID at low temperature confirms the identical behaviour of the two compounds and validates a direct comparison between Cr_7Co **14** and Cr_7Ni **13a**.

The small number of points at low temperature (Figure IV.11) does not allow for a precise determination of the temperature of the peak in χ for **13a**, but the estimated value of 35 K is slightly higher than for the maximum observed in **14** at 33 K, indicating a slightly smaller exchange interaction between chromium and cobalt compared to chromium and nickel. Also useful is a comparison with Cr_7Zn (Figure IV.4), where a weak plateau is observed around 30 – 35 K. The overall magnetic exchange interactions in all three compounds are clearly dominated by the chromium-chromium exchange and only weakly influenced by the hetero-ion. Despite the strong orbital momentum observed for the cobalt ion in the hetero-site of the ring systems (Ga_7Co) in powder magnetic measurements, any potential influence is masked by the chromium ions in Cr_7Co rings.

A more promising technique to study the influence of the cobalt(II) ion on the exchange interactions within the ring is EPR spectroscopy. However, when performing multifrequency EPR spectroscopy on Cr_7Co (**14**) (and subsequently on several other heterometallic chromium-cobalt rings) it appeared that spin relaxation processes on the time-scale of EPR spectroscopy do not allow for the collection of sufficiently resolved and intense EPR spectra. This observation is very disappointing because EPR spectroscopy can potentially provide a more detailed insight into the electronic structure of the low lying magnetic states. The only other technique which allows for the direct observation of the low lying magnetic energy levels is inelastic neutron scattering (INS). Mr. Michael Baker[128] and collaborators have performed INS experiments on the deuterated derivative $\mathbf{14}^{D}$. The obtained cold (blue) and hot (red) transitions are shown in Figure IV.12.

Magnetic measurements have shown that **14** exhibits a diamagnetic "S_{eff}" = 0 molecular ground state. A first assignment of the excited "spin-states" could be "S_{eff}" = 1, 2 and 3 with increasing energy in zero-field. However, in Section III.4 analysis of INS on the dimetallic **3** has indicated, that the INS selection rule $\Delta m_S = \pm 1$ still

holds for the spin-orbit cobalt(II) system. If this is also true for $\Delta S = \pm 1$, transition II cannot correspond to a "S_{eff}" = 0 to "S_{eff}" = 2 excitation. Should transitions I to III correspond to only two "spin-states", splitting in zero-field seems remarkably large. A large splitting of the effective triplet has also been seen in **3** with a maximum energy separation of 6.6 cm^{-1}, however **3** contains of two interacting spin-orbit ions, while in **14** the majority of ions exhibit a quenched orbital angular momentum and a splitting as large as 11.2 cm^{-1} may not be expected.

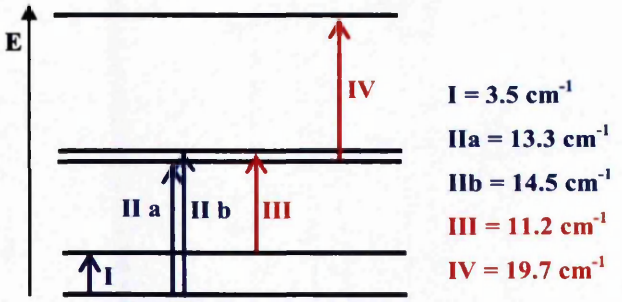

Figure IV.12: Magnetic cold (blue) and hot (red) transitions observed by Baker *et al.*[128] with INS on a powder sample of compound **14**^{D}.

Further analysis especially of the Q-dependence of the magnetic transitions is necessary to assign effective "spin-states" to the INS transitions, which may then allow for a more detailed analysis of the magnetic properties of **14**.

IV.3 Physical properties of heterometallic chromium rings with more than one hetero atom

In the following section, a selection of cobalt(II) containing heterometallic rings are studied in comparison to their magnetically simpler spin-only nickel(II) analogues:

[2,4-DiMe-ImidH][$Cr_7M^{II}F_8(O_2CC(CH_3)_3)_{16}$] ($Cr_7Ni$, (**15**), Cr_7Co, (**16**))
[ImidH]$_2$[$Cr_6M^{II}{}_2F_8(O_2CC(CH_3)_3)_{16}$] ($Cr_6Ni_2$ (**17**), Cr_6Co_2 (**18**))
[1-Bz-ImidH]$_2$[$Cr_7M^{II}{}_2F_9(O_2CC(CH_3)_3)_{18}$] ($Cr_7Ni_2$ (**19**), Cr_7Co_2 (**20**))

Stepwise analysis of the six compounds offers a promising route towards the theoretical challenges: Compounds **15** and **16** only differ from **13** and **14** in the

templating cation. A very similar magnetic and spectroscopic behaviour is expected and will ensure that replacing the secondary amine with imidazole derivatives does not change the magnetic properties of the ring. A second heteroatom is introduced in the compounds Cr_6Ni_2 (**17**) and Cr_6Co_2 (**18**), while the total number of eight metal ions remains constant. In most cases it is not possible to identify the heteroatoms crystallographically and for $M^{III}_7M^{II}$ rings the heteroatom M^{II} is usually disordered over all possible sites. This raises an interesting question for the $M^{III}_6M^{II}_2$ rings, where different magnetic ground states can be expected for different positions of the heteroatoms with respect to each other. Magnetic and spectroscopic techniques will allow constraints on the possible isomer or isomeric mixtures in the compounds. The nine-membered metal rings Cr_7Ni_2 (**19**) and Cr_7Co_2 (**20**) exhibit an additional difficulty. In odd numbered rings strictly antiferromagnetic coupling between the paramagnetic ions is not possible. Two alternatives can be discussed: Similar exchange between all metal ions will lead to a certain degree of spin frustration in the magnetic exchange coupling. A Möbius strip-like spin frustration has been found previously in a Cr_8Ni ring.[129] With respect to the distorted geometry at metal 5 and 6 (see Section IV.1) it is also possible that the associated exchange coupling is significantly different from that in the remaining pairs of ions, preventing spin frustration for the rest of the ring. A quantitative analysis of the magnetic and spectroscopic properties characterising the chromium-nickel rings **15**, **17** and **19** has been carried out using the software *MAGPACK* [130]and *EPR Sim.*[131] The overall magnetic properties are compared to the cobalt analogues **16**, **18** and **20** to gain a qualitative understanding of the influence of cobalt(II) on the ring systems.

IV.3.1 Magnetic and spectroscopic properties of Cr_7Ni, Cr_6Ni_2 and Cr_7Ni_2

The magnetic properties of Cr_7Ni (**15**) are shown in Figure IV.13. The temperature dependent susceptibility is identical to that obtained for **13a**[73] (see also Figure IV.11) and the compound shows the characteristic behaviour for the family of Cr_7Ni rings with an overall antiferromagnetic exchange between the chromium and nickel

ions. χT = 13.2 cm^3 K mol^{-1} at room temperature agrees with the contribution of seven chromium and one nickel ions. Upon cooling, antiferromagnetic exchange is observed with a peak in χ at *ca.* 33 K. The magnetic properties have been modelled using *MAGPACK* based on an isotropic Heisenberg-Dirac-van-Vleck exchange Hamiltonian (Equation I.2 and I.3 without ZFS term) with a single isotropic exchange parameter J = -5.8 cm^{-1} that has previously been found experimentally with INS.[92] The temperature dependent susceptibility is calculated with a g_{eff}-value of g_{eff} = 2.02, while for the field dependent magnetisation the contributions from a ground $S_{eff} = {}^1/_2$ with g_{eff} = 1.77 and excited states with g_{eff} = 2.02 are simulated individually, and as a weighted average.

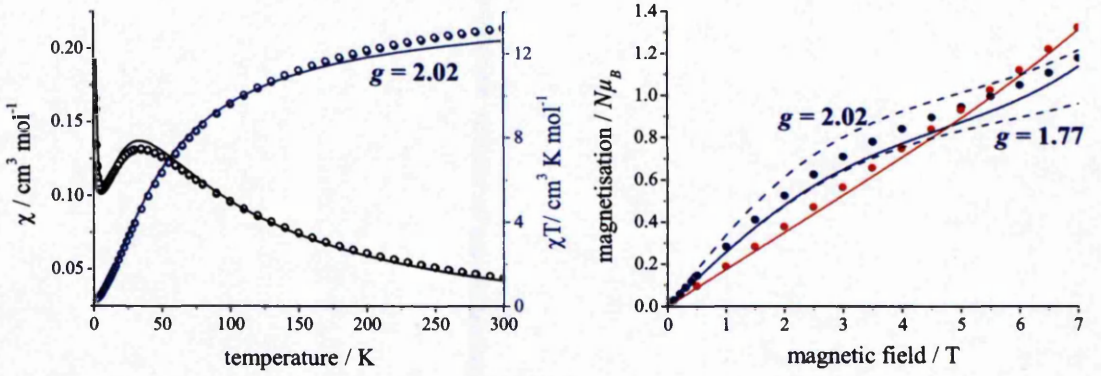

Figure IV.13: Magnetic properties of Cr_7Ni (**15**) measured on a powder sample. Left: temperature dependent susceptibility at 1 T (dot) and 0.1 T (ring), calculation for J = -5.8 cm^{-1}, g_{eff} = 2.02 (solid). Right: field dependent magnetisation at 2 K (blue) and 4 K (red), calculation for J = -5.8 cm^{-1} and g_{eff} = 2.02 or g_{eff} = 1.77 (dash) and a Boltzmann weighted average (solid)

The exact g-value for the calculation of magnetic properties can be obtained experimentally by EPR spectroscopy. The Q-band EPR spectrum at 5 K (Figure IV.14) is dominated by a slightly axial transition at $g_{eff} \sim 1.78$ and has been modelled with a conventional Hamiltonian in the strong exchange limit (SEL, Equation I.4)[3] for a total spin of $S_{eff} = {}^1/_2$, arising from antiferromagnetic coupling between one nickel and seven chromium ions.

In his Ph.D. Thesis Piligkos reports how vector coupling of the single ion **g**-matrices for chromium and nickel gives rise to the unusually low **g**-matrix characteristic for the $S_{eff} = {}^1/_2$ ground state of the heterometallic systems.[127] The principal values of $g_{eff,xx} = g_{eff,yy}$ = 1.775, $g_{eff,zz}$ = 1.735 ($g_{eff,xx} = g_{eff,yy}$ = 1.78, $g_{eff,zz}$ = 1.74 reported by Piligkos on compound **13**) average to an isotropic g_{eff}-value of 1.76.

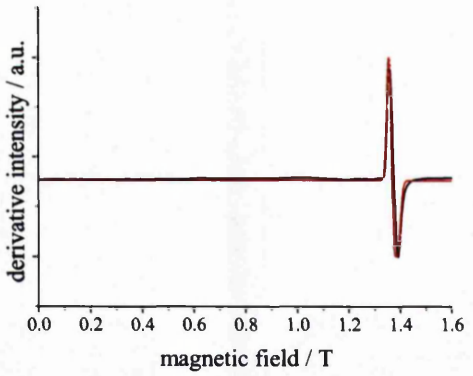

Figure IV.14: EPR spectrum of **15** at 5 K (black) and simulation for a total spin $S_{eff} = {}^1/_2$ and a total **g**-matrix with principal components $g_{eff,xx} = g_{eff,yy} = 1.775$, $g_{eff,zz} = 1.735$ (red)

Piligkos further reports the spin-Hamiltonian parameters of the next two low lying excited states $S_{eff} = {}^3/_2$ and $S_{eff} = {}^5/_2$ with principal **g**-matrix components of $g_{eff,xx} = g_{eff,yy} = 2.00$ and $g_{eff,zz} = 2.05$.[127] Figure IV.15 shows an expansion of the Q-band EPR spectrum of **15** at different temperatures.

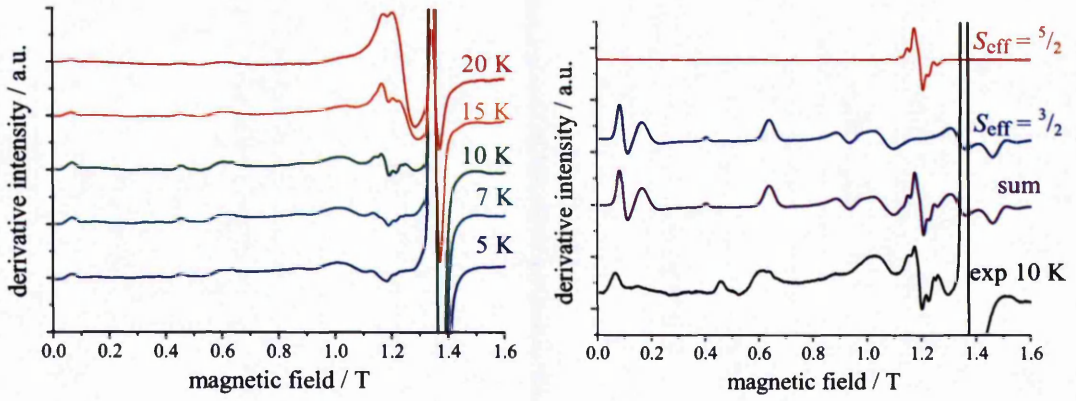

Figure IV.15: Left: Expansion of the EPR spectrum of **15** between 5 and 20 K measured on a powder sample. Right: Simulation of excited state transitions at 10 K for $S_{eff} = {}^3/_2$, $g_{eff,xx} = g_{eff,yy} = 2.01$, $g_{eff,zz} = 2.06$, $D_{eff,3/2} = 0.47$, $E_{eff,3/2} = 0.055$, Gaussian linewidth of 300 G and $S_{eff} = {}^5/_2$, $g_{eff,xx} = g_{eff,yy} = 2.01$, $g_{eff,zz} = 2.06$, $D_{eff,5/2} = 0.023$ $E_{eff,5/2} = 0$, Gaussian linewidth of 100 G.

Transitions within both the $S_{eff} = {}^3/_2$ and $S_{eff} = {}^5/_2$ levels grow in intensity with increasing temperature. The weak excitations at 10 K have been modelled for contributions from two excited levels with a conventional Zeeman Hamiltonian and total spins $S_{eff} = {}^3/_2$ and $S_{eff} = {}^5/_2$, respectively. In contrast to the axial symmetry of compound **13** studied by Piligkos,[127] **15** is rhombic and the introduction of an *E*

parameter into the simulation is necessary for the S_{eff} = $^3/_2$ level. The *g*-values obtained from the Q-band EPR spectra of **15** are very similar to those of compound **13** (see Table IV.1), where studies were based on the simultaneous simulation of multifrequency experiments on both powder and single crystal samples and hence the confidence in absolute numbers is much larger. For the calculation of the magnetic properties the average isotropic *g*-values were derived from Piligkos' studies with g_{eff} = 1.77 and 2.02 for ground and excited state transitions, respectively.

Compound: S_{eff}	$g_{eff,xx/yy}$value	$g_{eff,zz}$	$D_{eff,S}$ / cm^{-1}	$E_{eff,S}$ / cm^{-1}
15: $^1/_2$	1.775	1.735	n/a	n/a
13: $^1/_2$	1.78	1.74	n/a	n/a
15: $^3/_2$	2.01	2.06	0.47	0.055
13: $^3/_2$	2.00	2.05	0.56	0
15: $^5/_2$	2.01	2.06	0.023	0
13: $^5/_2$	2.00	2.05	0.14	0

Table IV.1: Spin-Hamiltonian parameters of **15** in comparison to those found by Piligkos on **13**.[127]

The different contributions from ground and excited energy levels lead to an apparent field and temperature dependent g_{eff}-value, which is best observed in the magnetisation *vs.* magnetic field plot (Figure IV.13). Below 2 T simulations with either g_{eff} = 1.77 or g_{eff} = 2.02 show that the system is better described with the smaller g_{eff}-value and hence dominated by ground state population, although a partial contribution from excited states is already observed. The gradually increasing Zeeman splitting with increasing magnetic field leads to an increase in the population of further energy levels and the larger g_{eff}-value becomes progressively more important. At *ca.* 4.5 T a level crossing is observed, above which the response of the system is dominated by excited states with g_{eff} = 2.02. *MAGPACK* only allows for the input of a single isotropic *g*-value for all spin-states. The Boltzmann weighted average of the contributions from the different spin-states with different *g*-values was calculated manually in *Origin* including the four lowest spin-states (for details see Section VI.4.3). The calculated mean magnetisation is slightly lower than the experimental observation, but the overall curvature is reproduced very well. For the temperature dependent susceptibility the small g_{eff} value of the ground state is only relevant at very low temperatures, whilst at higher temperatures the system is

dominated by excited states, hence the susceptibility has been modelled with a single $g_{eff} = 2.02$ over the entire temperature range.

As expected, analysis of the magnetic and spectroscopic properties of **15** in comparison with **13** has shown that the replacement of the secondary amine with an imidazolium cation does not change the magnetic properties of the ring system. Chromium-chromium and chromium-nickel exchange interactions of **15** within the ring system can be modelled sufficiently accurately with only one fixed (from INS) isotropic exchange parameter J = -5.8 cm^{-1} using g_{eff}-values obtained from EPR. Moving on to heterometallic ring systems with two nickel ions, it should be possible to translate this concept by assuming the same uniform exchange.

The first example is $[Cr_6Ni_2F_8(O_2CC(CH_3)_3)_{16}]$ (**17**) with six chromium and two nickel ions. Crystallographically the location of the nickel ions cannot be determined. Considering the metal sites only, the sequence of chromium and nickel ions on the ring can lead to four different isomers (Figure IV.16).

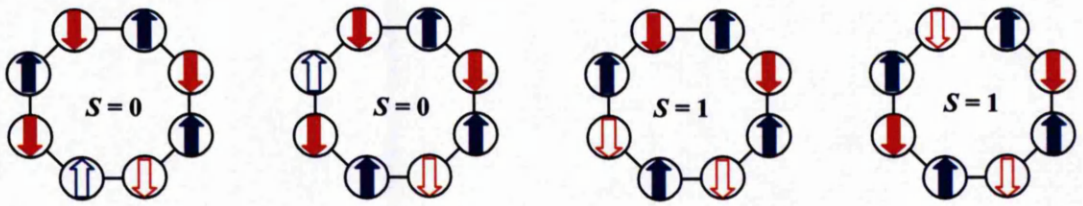

Figure IV.16: Four different possible isomers of $[Cr_6Ni_2F_8(O_2CC(CH_3)_3)_{16}]$ (**17**) leading to magnetic ground states of $S_{eff} = 0$ or $S_{eff} = 1$. (Solid: Cr(III) $s = {}^3/_2$, empty: Ni(II) $s = 1$)

A simple picture of a "spin-up" and a "spin-down" sub-lattice visualizes the resulting magnetic ground states for the different isomers: The antiferromagnetically coupled single ion spins are divided into two sub-lattices grouping together spins with the same orientation. If both nickel ions are placed on the same sub-lattice, the eight single ion spins couple antiferromagnetically to a molecular ground state of $S_{eff} = 1$, while location of the nickel ions on different sub-lattices leads to a diamagnetic molecular ground state $S_{eff} = 0$. A division into sub-lattices becomes particularly important in the context of spin projection and will be discussed further at a later stage of this chapter.

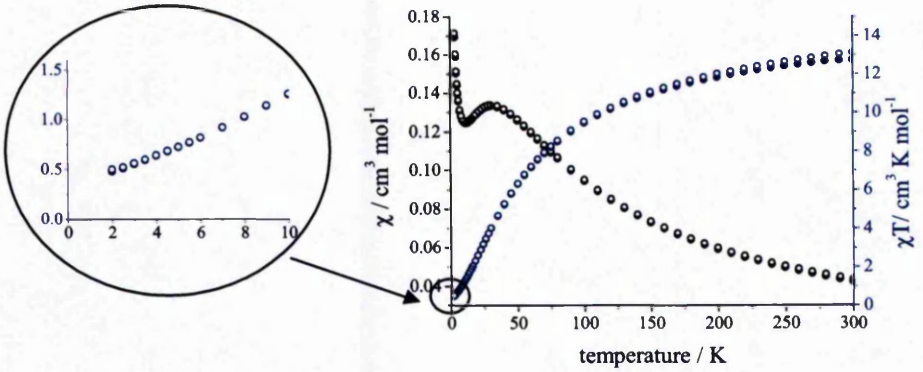

Figure IV.17: Temperature dependent susceptibility of Cr_6Ni_2 (**17**) at 1 T (dot) and 0.1 T (ring). Expansion: χT at 2 K indicates a mixture of isomers with $S_{eff} = 0$ and $S_{eff} = 1$.

Figure IV.17 shows the temperature dependent susceptibility of Cr_6Ni_2. As expected, the system behaves similarly to Cr_7Ni with a room temperature value of χT_{300K} = 12.70 cm^3 K mol^{-1}, slightly higher than 12.01 cm^3 K mol^{-1} for six chromium and two nickel ions, and a maximum in χ at 30 K. At base temperature the experimentally observed susceptibility ($\chi T_{2\ K}$ = 0.48 cm^3 K mol^{-1}) appears to represent an average between the expectation values for $S_{eff} = 0$ ($\chi T = 0$) and $S_{eff} = 1$ (χT = 1 cm^3 K mol^{-1} for $g_{eff} = 2.0$), a first indication of the presence of different isomers in the compound.

In contrast to SQUID magnetometry, EPR spectroscopy shows the *sum* of all isomers with ground and excited state transitions. Figure IV.18 shows the very complex EPR spectra of **17** at Q- and W-band frequencies between 5 and 20 K.

A quantitative analysis of the EPR spectra is challenging because of multiple contributions, hence it is helpful to start with a qualitative assignment of different spectral regions to transitions from spin states of different isomers. For two isomers the transitions within the ground state S_{eff} = 1 are present strongly at 5 K and decrease in intensity to higher temperature. Transitions within the first excited state $S_{eff} = 2$, presumably of the same molecules, grow in at higher temperatures. Analysis of the relative intensities at different temperatures allows for a second pair of weak $S_{eff} = 1$ transitions to be assigned to excited state transitions arising from two isomers with an EPR silent $S_{eff} = 0$ ground state.

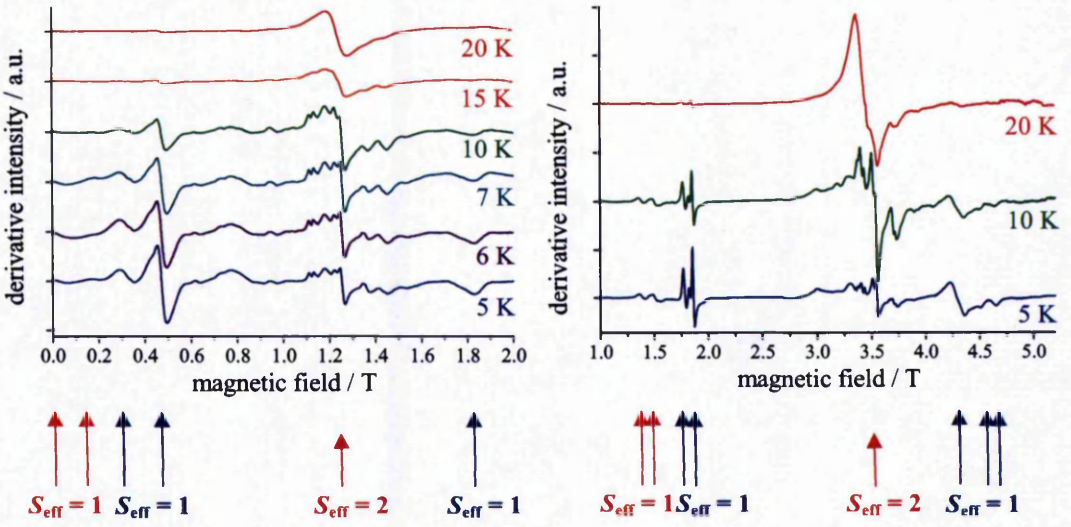

Figure IV.18: Variable temperature Q-band (left) and W-band (right) EPR spectra of a powder sample of Cr_6Ni_2 (**17**). Ground (blue) and excited state (red) transitions are observed from four different isomers, two with $S_{eff} = 0$ and two with $S_{eff} = 1$ ground state.

Confidence in spin-Hamiltonian parameters is only achieved if the spectra at both frequencies can be simulated with the same unique set of parameters. For six individual contributions to the overall spectrum, over-interpretation especially through introduction of rhombic anisotropy is a big problem. Figure IV.19 shows a possible assignment of g_{eff}- and $|D_{eff}|$-values to the ground state $S_{eff} = 1$ transitions in the Q- and W-band spectra. The strong transitions in the centre of the calculated spectrum are experimentally not observed. Introduction of rhombicity into the calculation weakens and moves the central transitions significantly (Figure IV.19, right). However, the spectra are too complex to assign confidently any E_{eff} parameters to the $S_{eff} = 1$ contributions. Any g_{eff}-anisotropy would also over-interpret the experimental spectra. Therefore, the quantitative interpretation has been restricted to the determination of g_{eff} and $|D_{eff}|$ for the two $S_{eff} = 1$ contributions and even here the absolute values have to be treated with caution because any introduction of rhombicity will also slightly influence the outer transitions determined by $|D_{eff}|$. The plotted simulations have been calculated with a negative D_{eff}-value; however, the complex spectra do not allow for the sign of D_{eff} to be determined. Relative intensities are strongly dependent on the sign of D_{eff}, while the positions of the lines stay constant, so that $|D_{eff}|$ seems a good estimate of the zero field splitting within the different spin states.

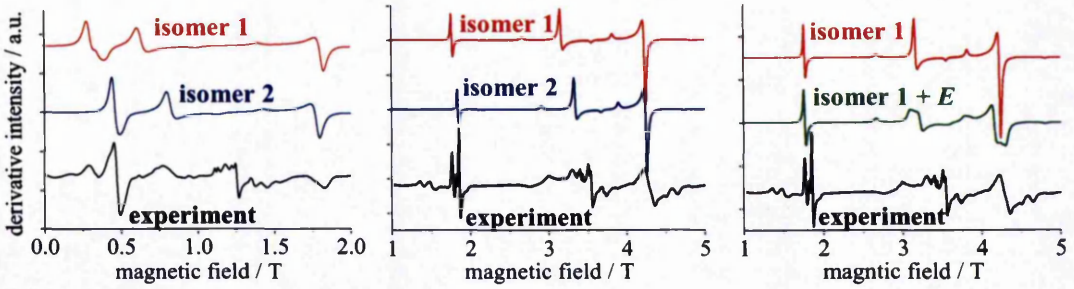

Figure IV.19: Simulations of contributions from two different isomers to the Q-band (left) and W-band (middle and right) EPR spectra of **17** at 5 K. Left and middle: $S_{eff} = 1$: $g_{eff,1} = 1.80$, $D_{eff,1} = -0.90$ cm^{-1} $g_{eff,2} = 1.76$, $D_{eff,2} = -0.75$ cm^{-1} Right: Introduction of additional rhombic anisotropy for isomer 1, $E_{eff,1} = -0.04$ cm^{-1}

The two excited state $S_{eff} = 1$ transitions are too weak to be parameterized quantitatively, because the high field part of the spectral components cannot be recognised. For at least one of the two isomers the Q-band spectrum shows a zero field transition, which defines the energy of D_{eff} to be very similar to the microwave energy of 1.13 cm^{-1}. D_{eff} for the second isomer appears to be even larger from the W-band spectrum. In both cases g can be estimated as *ca.* 2.1 to allow for such low field transitions. The central transitions arising from the $S_{eff} = 2$ excited state have not been modelled. The parameters for the two isomers appear to be similar and require axial or even rhombic symmetry. It is not possible to distinguish between the two isomers, nor hence confidently to assign spin-Hamiltonian parameters to the transitions that reproduce both Q- and W-band EPR spectra. Nevertheless, it is possible to estimate $g_{eff} \sim 1.95$ and $|D_{eff}| < 0.08$ from spectra at the two frequencies.

It is interesting to note that in complete analogy to **15** and **13** very low g_{eff}-values < 1.8 are observed for the $S_{eff} = 1$ ground state transitions in **17**, while excited state transitions for $S_{eff} = 1$ and $S_{eff} = 2$ are characterised by g-values around 2. A vector coupling method can explain the low g_{eff}-value in **13** arising from the single ion values $g_{Cr} = 1.96$ and $g_{Ni} = 2.23$ within the antiferromagnetically coupled ring. The same method has been used to predict g_{eff}-values for the different isomers of **17** using Equation IV.2.[132]

The $\mathbf{g}_{eff}$-matrix of the total spin state S_{eff} is expressed as a linear combination of the individual **g**-matrices assigned to the spin states. All coefficients are calculated from a pair-wise coupling of spins (for details see Appendix 4.3).

$$\mathbf{g}_{Seff} = c_1\mathbf{g}_A + c_2\mathbf{g}_B \qquad \text{(IV.2)}$$

$\mathbf{g}_{Seff}$ = g-matrix of the total spin S_{eff} and $\mathbf{g}_{A/B}$ g-matrix of spin states A and B

For a ring of eight atoms a coupling scheme has to be chosen to define the order in which the single ion spins are coupled. Previous studies on other homo and heterometallic ring systems have shown that vector coupling based on a division of the ring into its "spin-up" and "spin-down" sub-lattices successfully generates the expected spin states[133-135] (Figure IV.20). In this coupling scheme, spins *within* a sub-lattice are coupled in a ferromagnetic fashion first, and in a final step the antiferromagnetic interaction between the two sub-lattices is introduced.

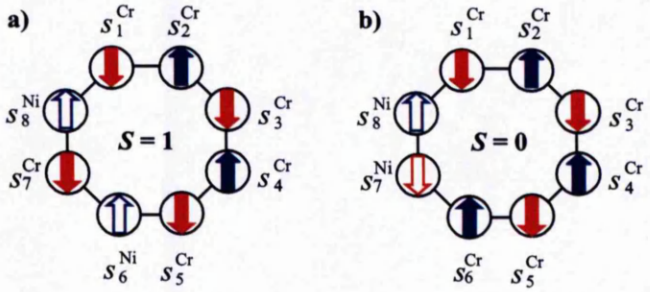

Figure IV.20: Vector coupling scheme dividing the eight metal centres into two sub-lattices with either spin up (blue) or spin down (red). Solid: Cr(III), empty: Ni(II)

Through pair-wise coupling the wavefunction can be expressed as:

$$|s_1\, s_3\, s_{13}\, s_5\, s_7\, s_{57}\, s_{1357}\, s_2\, s_4\, s_{24}\, s_6\, s_8\, s_{68}\, s_{2468}\, S\, M>$$

For the calculation of *g*, the order of coupling *within* the sub-lattice does not make a difference, hence identical values are obtained for:

$$|s_1\, s_3\, s_{13}\, s_5\, s_{135}\, s_7\, s_{1357}\, s_2\, s_4\, s_{24}\, s_6\, s_{246}\, s_8\, s_{2468}\, S\, M>$$

a)	Experiment g_{Seff}	Vector coupling g_{Seff}	b)	Experiment g_{Seff}	Vector coupling g_{Seff}
$S_{eff} = 1$	1.80 1.76	1.69	$S_{eff} = 0$	not relevant	
$S_{eff} = 2$	~ 1.95	1.91	$S_{eff} = 1$	2.1	2.01

Table IV.2: Comparison between experimentally observed g_{eff}-values of Cr_6Ni_2 and their calculation by vector coupling method from the single ion *g*-values g_{Cr} = 1.96 and g_{Ni} = 2.23.

In Table IV.2 calculated and experimentally observed g_{eff}-values for ground and first excited spin states are listed. For all three spin-states the calculated *g*-values are slightly lower than experimentally observed, but overall the vector coupling model

provides a good explanation for the experimentally observed *g*-values, and confidence in the correct assignment of multiple transitions to contributions from different isomers.

In accord with the presence of multiple isomers observed by EPR spectroscopy, it is not possible to reproduce the magnetic properties of **17** for either a pure $S_{eff} = 0$ or $S_{eff} = 1$ spin ground state. The best agreement is achieved with 2:1 mixture of $S_{eff} = 1$ to $S_{eff} = 0$. Figure IV.21 shows the calculated magnetic properties for $S_{eff} = 0$ or $S_{eff} = 1$ and different ratios for a mixture of the two, with an isotropic exchange parameter $J = -5.8$ cm^{-1} (fixed from **13** and **15**). The g_{eff} parameters were adopted from the EPR spectra as follow: At low temperatures, hence relevant for the field dependent magnetisation at 2 and 4 K and for the very low temperature susceptibility, both ground and the excited state g_{eff}-values have to be taken into account separately. *MAGPACK* only allows for the input of one isotropic *g*-value for all spin states. This is sufficient for the isomers with an $S_{eff} = 0$ ground state. A single excited state g_{eff}-value of 2.03 (average from excited state g_{eff}-values obtained by EPR) was used for the calculation. In the case of isomers with an $S_{eff} = 1$ ground state, a Boltzmann weighted calculation was performed manually on the basis of the four lowest spin-states to account for the ground and excited state values of $g_{eff,S=1} = 1.78$ and $g_{eff,S=2} = 1.95$, respectively (for details see Section VI.4.3). The temperature dependent susceptibility between 2 and 300 K was calculated with an average g_{eff}-value of $g_{eff,S=1} \sim 2.03$ based on only excited state contributions. This is not valid at very low temperature, but reproduces the overall temperature dependence well. Below 15 K a separate calculation has been performed, in which a Boltzmann weighting of the two g_{eff}-values was taken into account within the four lowest spin-states.

Figure IV.21 shows the resulting calculated magnetic properties in comparison with the experimental data. A slight variation in the spin-Hamiltonian parameters may also allow for the reproduction of the temperature dependent susceptibility as a pure $S_{eff} = 1$ system, but from the field dependent magnetisation it is immediately obvious that such a model is not at all valid. The field dependent magnetisation is most sensitive to contributions from different isomers with different magnetic ground states. It is worth emphasizing here that the magnetic properties have *not* been fitted, but calculated with only fixed parameters that have been derived from previous compounds or measurements. This allows for the isomeric ratio to be varied in order

to simulate the magnetic properties of the compound. Figure IV.21 shows the result for a 1:1, 2:1 and 3:1 mixture of isomers with an $S_{eff} = 1$ or $S_{eff} = 0$ ground state, respectively. The experimental data are best reproduced with a 2:1 excess of isomers where the nickel ions are located on the same sub-lattice. Similar calculations of the low temperature susceptibility confirm this observation and the experimental data are fitted well with a 2:1 isomeric ratio. Above 10 K the fit becomes poor, due to the insufficient number of excited states included in the calculation. At higher temperatures the individual contribution from the ground state with its low g_{eff}-value becomes negligible, and the temperature dependent susceptibility has been reproduced well with an average $g_{eff} = 2.03$ for a 2:1 isomeric ratio.

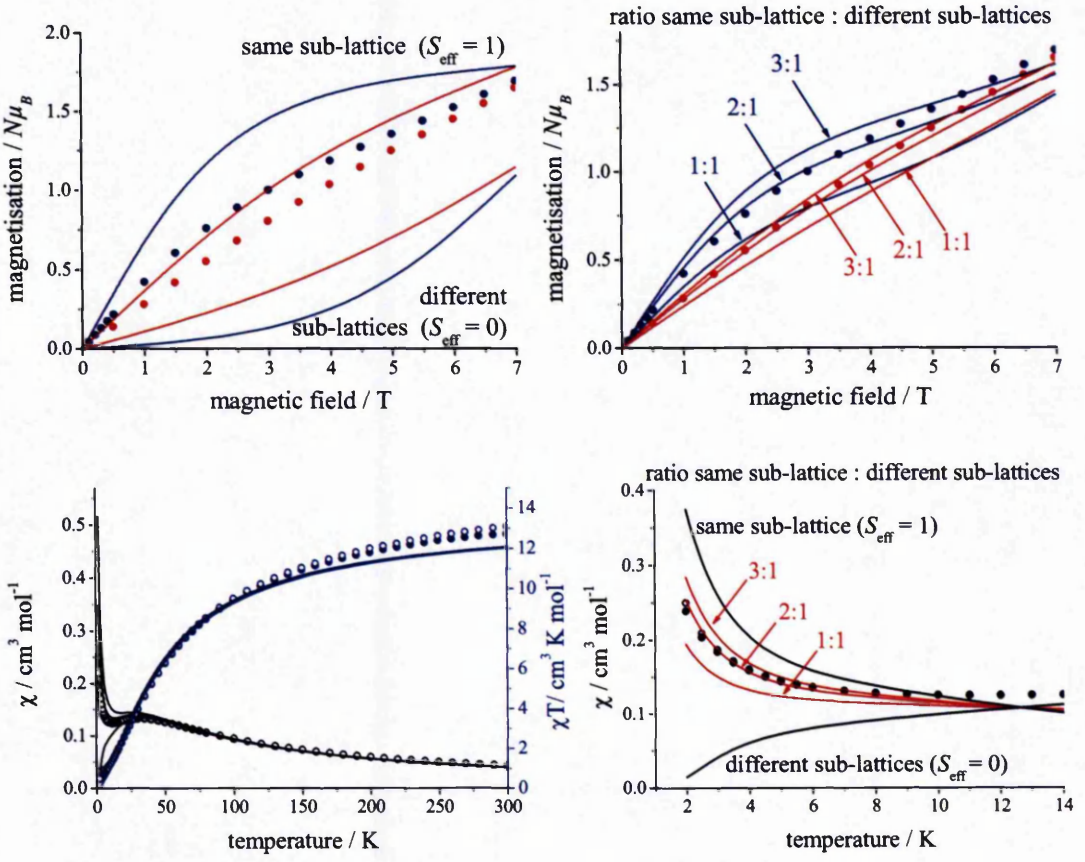

Figure IV.21: Top: field dependent magnetisation of **17**. Blue: 2 K, red: 4 K, lines: calculation with $J = -5.8cm^{-1}$ for separate isomers and isomeric mixture using effective g_{eff}-values as explained in the text. Bottom: temperature dependent susceptibility of **17**. Dot: 1T, ring: 0.1 T. Left: calculation with $J = -5.8cm^{-1}$ and geff = 2.03 for separate isomers and an isomeric mixture, right: Boltzmann weighted inclusion of different g_{eff}-values as explained in the text for separate isomers and isomeric mixtures.

The experimental field dependent magnetisation is reproduced very well up to *ca.* 3.5 T, above which a deviation of the calculation from the experiment occurs. Such discrepancy suggests non-linearity in the Zeeman splitting, which can be introduced by mixing of spin states for example through anisotropic exchange. EPR spectroscopy on **13** has clearly shown the presence of anisotropic chromium-chromium and chromium-nickel exchange as well as single ion zero field splitting for both ions.[91] The isotropic exchange Hamiltonian used to calculate the magnetic properties does not account for any form of anisotropy and hence the calculated Zeeman splitting is linear and cannot reproduce the real field dependence of the different spin states. An extended version of the software *MAGPACK* does allow for anisotropy parameters to be considered, however for a system with eight metal ions the number of matrix elements exceeds the limit of the software.

Even more complicated than Cr_6Ni_2, is the odd numbered ring Cr_7Ni_2 (**19**) with seven chromium and two nickel ions. Again different positional isomers can lead to different magnetic ground states, but additionally spin frustration has to be considered, because full antiferromagnetic coupling in odd numbered ring systems cannot be achieved.

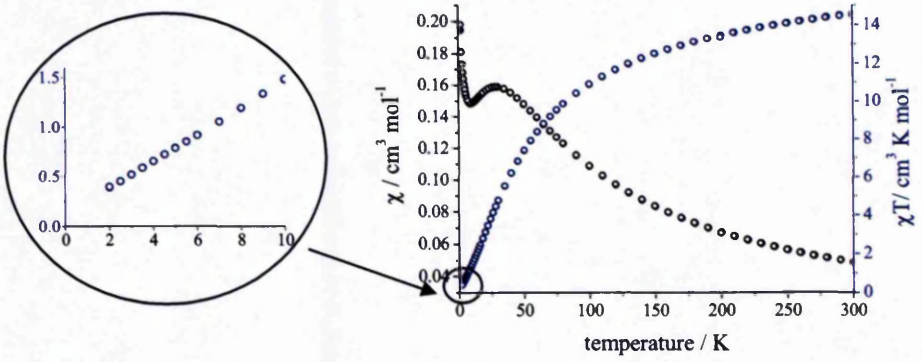

Figure IV.22: Temperature dependent susceptibility of Cr_7Ni_2 (**19**) at 1 T (dot) and 0.1 T (ring). Expansion: at 2 K χT appears to arise from a spin ground state of $S_{eff} = {}^1/_2$.

Figure IV.22 shows the temperature dependent susceptibility of Cr_7Ni_2 (**19**). The overall magnetic properties are very similar to those of Cr_6Ni_2 and Cr_7Ni with a room temperature susceptibility of χT_{300K} = 14.56 cm^3 K mol^{-1}, slightly higher than that expected for seven chromium and two nickel ions (calculated χT = 13. 63 cm^3 K

mol^{-1}). The maximum in χ at 28 K again indicates a very similar order of antiferromagnetic exchange interactions. The base temperature susceptibility of $\chi T_{2\,K}$ = 0.395 cm^3 K mol^{-1} suggests the presence of only one spin ground state $S_{eff} = {}^1/_2$ (χT = 0.375 cm^3 K mol^{-1} for g_{eff} = 2.0).

EPR spectra were collected at Q- and W-band frequencies between 5 and 20 K (Figure IV.23). At Q-band only two very broad features occur, at 5 K centred on g_{eff} ~ 1.76, and one broad feature at 20 K around g_{eff} = 1.98. The anisotropy of the high field feature is better resolved in the 5 K W-band spectrum, while at 20 K the spectrum is again dominated by an isotropic broad signal at g_{eff} ~ 2. Temperature dependence allows for the assignment of spectral regions to ground and excited state transitions.

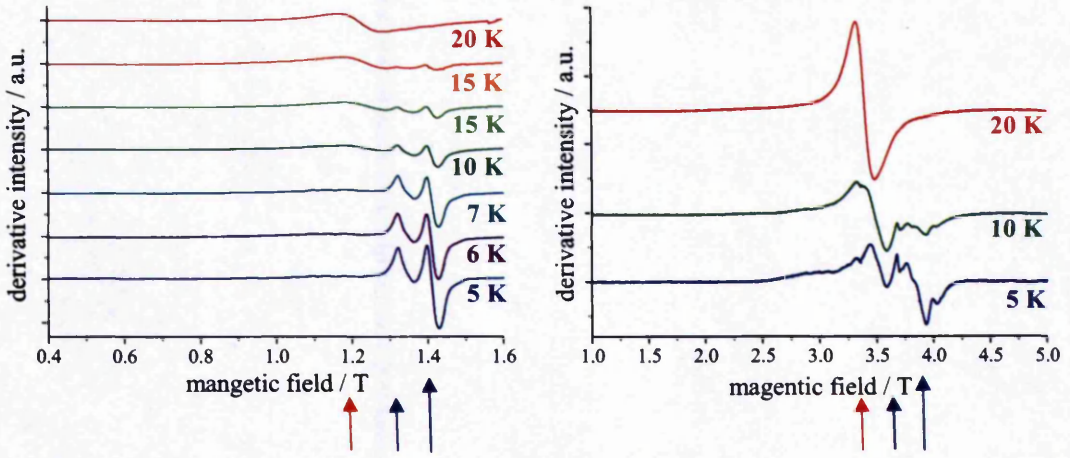

Figure IV.23: Variable temperature Q-band (left) and W-band (right) EPR spectra of a powder sample of Cr_7Ni_2 (**19**). Ground (blue) and excited state (red) transitions are assigned from temperature dependence.

Two different coupling schemes can be discussed for the magnetic exchange interaction in C_7Ni_2:

1. Interruption of the overall antiferromagnetic exchange and hence the presence of different isomers, which can have either $S_{eff} = {}^1/_2$, ${}^3/_2$ or ${}^5/_2$ ground states, depending on the positions of chromium and nickel ions in the ring.
2. Identical antiferromagnetic exchange between all chromium and nickel ions causing spin frustration, which leads to an $S_{eff} = {}^1/_2$ ground state.

First, an interruption of the antiferromagnetic coupling at one point in the ring is considered, based on the structural difference in the ligand bridges of one ion pair (Section IV.1). Figure IV.24 shows the three possible ground states in Cr_7Ni_2 based on division of the chromium-nickel ring into sub-lattices.

a) If the two nickel ions are placed on different sub-lattices, coupling leads to an overall magnetic ground state of $S_{eff} = {}^3/_2$.

b) If both nickel ions are placed on the four ion sub-lattice, a magnetic ground state of $S_{eff} = {}^5/_2$ is expected, while

c) placement on the five ion sub-lattice results in an $S_{eff} = {}^1/_2$ ground state.

Similar to Cr_6Ni_2 the magnetic and spectroscopy properties are expected to be an average or sum of the individual isomers, respectively.

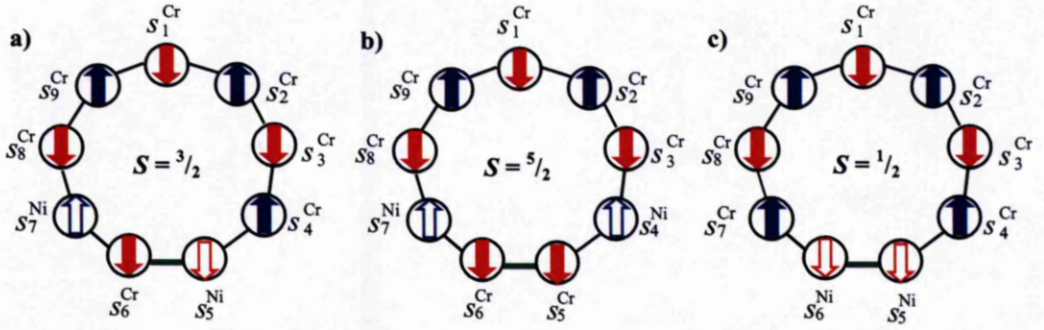

Figure IV.24: Three different possible ground states of Cr_7Ni_2 (**19**) depending on the location of the nickel ions in the ring. For each ground state different isomers are possible. (Full: Cr(III) s = 3/2, empty: Ni(II) s = 1) Green: interruption of the antiferromagnetic coupling

The above options are easy to visualize and plausible with respect to the structure; however it is questionable if a sudden change to a ferromagnetic coupling as pictured for case a) and b) (Figure IV.24) is likely, based on the similar and antiferromagnetic chromium-chromium and chromium-nickel exchange observed in **13**, **15** and **17**. Only the particular isomer shown for case c), with ferromagnetic coupling between the neighbouring nickel ions, allows for both chromium-chromium and chromium-nickel exchange to remain antiferromagnetic. On the other hand deviations in the chromium-chromium and chromium-nickel exchange have been found in the nine membered Cr_8Ni ring, where the chromium-nickel exchange appears to be much larger than the chromium-chromium exchange.[129] Consequently all possibilities have been taken into account for the interpretation of the EPR spectra.

The experimental EPR spectra of **19** show one set of ground state features at g_{eff} ~ 1.76 and excited state features at g_{eff} ~ 1.95. Vector coupling has successfully reproduced the ground and excited state g-values for Cr_7Ni and Cr_6Ni_2. The coupling scheme is based on pure antiferromagnetic and ferromagnetic exchange and does not account for any spin frustration. However it may be useful to distinguish between the different ground states and isomers shown in Figure IV.24. Table IV.3 shows the calculated g_{eff}-values for different coupling schemes. For coupling scheme a, where the two nickel ions are placed on different sub-lattices, a small difference is observed depending on the coupling order within the five ion sub-lattice.

1) $|s_{Cr}\, s_{Cr}\, s_{CrCr}\, s_{Cr}\, s_{Cr}\, s_{CrCr}\, s_{CrCrCrCr}\, s_{Ni}\, s_{CrCrCrCrNi}\, s_{Cr}\, s_{Cr}\, s_{CrCr}\, s_{Cr}\, s_{Ni}\, s_{CrNi} s_{CrCrCrNi}\, S\, M>$

2) $|s_{Cr}\, s_{Cr}\, s_{CrCr}\, s_{Cr}\, s_{Ni}\, s_{CrNi}\, s_{CrCrCrNi}\, s_{Cr}\, s_{CrCrCrNiCr}\, s_{Cr}\, s_{Cr}\, s_{CrCr}\, s_{Cr}\, s_{Ni}\, s_{CrNi} s_{CrCrCrNi}\, S\, M>$

If both nickel ions are placed on the same sub-lattice, the coupling order within the sub-lattice does not influence the resulting g_{Seff}.

spin state	Vector coupling g_{Seff} a) 1) ($^3/_2$)	Vector coupling g_{Seff} a) 2) ($^3/_2$)	Vector coupling g_{Seff} b) ($^1/_2$)	Vector coupling g_{Seff} c) ($^5/_2$)
$S_{eff} = {}^1/_2$			2.375	
$S_{eff} = {}^3/_2$	1.975	2.161	2.076	
$S_{eff} = {}^5/_2$	1.992	2.088		1.794
$S_{eff} = {}^7/_2$				1.894

Table IV.3: Calculated g_{eff}-values obtained for Cr_7Ni_2 by vector coupling method from the single ion g-values g_{Cr} = 1.96 and g_{Ni} = 2.23. Models a), b), c) from Figure IV.24; 1) and 2) from text above.

Overall it is clear, that the three ground states give rise to three very different g_{eff}-values. For $S_{eff} = {}^1/_2$ a high g_{eff}-value of *ca.* 2.38, for $S_{eff} = {}^3/_2$, a value close to the chromium g_{eff}-value of 1.98 and for $S_{eff} = {}^5/_2$ a low g_{eff}-value of g_{eff} ~ 1.79 has been calculated. All excited state transitions are expected between g_{eff} = 1.9 and 2.1 similar to previous observations on Cr_7Ni and Cr_6Ni_2. If the vector coupling model is applicable for Cr_7Ni_2, it indicates that the ground state transitions arise from an $S_{eff} = {}^5/_2$ ground state only, because only in this scheme is a g_{eff}-value < 1.8 achieved. Ground state transitions around g_{eff}-values of 2.0 and 2.38 are experimentally not observed. The excited state transitions at g_{eff} = 1.95 could potentially belong to any of the above spin states.

The brief analysis of the magnetic properties in the beginning of this section (Figure IV.22) has already shown that the low temperature susceptibility cannot be explained by a pure $S_{eff} = {}^5/_2$ ground state, but appears to favour a pure $S_{eff} = {}^1/_2$ ground state. So far for Cr_7Ni and Cr_6Ni_2, magnetic and spectroscopic properties have been very consistent and the discrepancy indicates that a model with discontinuation of the antiferromagnetic coupling is not valid for Cr_7Ni_2.

The second option to interpret the magnetic and spectroscopic properties of **19** is the assumption of a spin frustrated system similar to Cr_8Ni for which a Möbius strip-like spin frustration has been found (Figure IV.25).[129] The authors report calculations, which have shown that the Cr_8 chain is antiferromagnetically coupled, leading to antiparallel orientation of the edges. As soon as chromium-nickel exchange is introduced into the model, the edges of the chromium chain are twisted to achieve a parallel or antiparallel orientation with the nickel ion, depending on the sign of the chromium-nickel exchange. For $J_{CrCr} >> J_{CrNi}$ the spin frustration is mainly localised on the nickel site, while $J_{CrNi} >> J_{CrCr}$ leads to spin frustration on the chromium chain. The overall ground state of Cr_8Ni has been found to be 0.

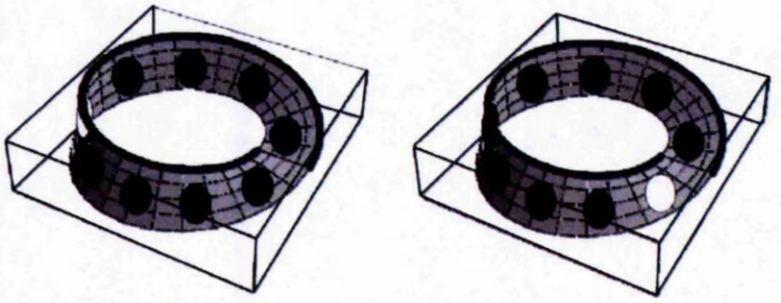

Figure IV.25: Representation of the spin frustration in Cr_8Ni as a Möbius strip, with the white circle as the Ni site, and black circles as Cr. Left: $J_{CrCr} << J_{CrNi}$, the ''knot'' is on the chromium spin chain; right: $J_{CrCr} >> J_{CrNi}$ and the ''knot'' is on the nickel site. The ''knot'' is the point at which the upper line is discontinuous.[129]

Qualitatively this idea can be directly translated to Cr_7Ni_2. No matter which position the nickel ions occupy with respect to each other, the overall ground state of the molecule will always be a spin doublet in accord with magnetic measurements. For an odd-numbered homometallic ring, a degenerate pair of ground state spin-doublets is expected, however, analysis at a later stage will show that such degeneracy can be lifted in heterometallic systems. On the contrary, the ground state transitions in the

EPR spectrum are very anisotropic and cannot be explained by genuine g_{eff}-anisotropy in a spin doublet. Again, spin frustration must be taken into account here. On antiferromagnetically coupled iron triangles and a triangle-based Fe_9 oligomer, unusual EPR spectra have been observed previously on such spin frustrated ground doublets.[136,137] Antisymmetric Dzyaloshinsky – Moria interactions can lift the degeneracy of the doublets and lead to mixing of the associated wavefunctions. In consequence EPR transitions are no longer intra doublet transitions and hence the assigned "g_{eff}-values" not genuine molecular g-values and can be significantly more anisotropic than usual.

Despite the indication of a pure $S_{eff} = {}^1/_2$ ground state from the low temperature susceptibility, the magnetic properties cannot be simulated with a single isomer. Interestingly, calculations for different chromium-nickel sequences indeed lead to very different magnetic responses, even though the magnetic ground state corresponds to a doublet arising from spin frustration in all cases. Four different isomers have to be considered:

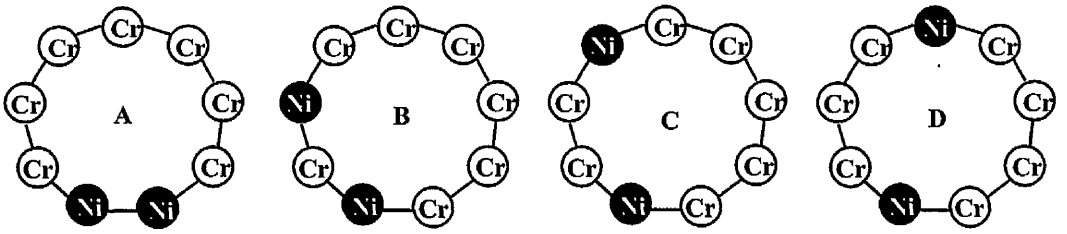

Figure IV.26: Four different isomers of Cr_7Ni_2 leading to different magnetic responses, despite the common doublet ground state arising from spin frustration within the ring. All exchange interactions are considered isotropic and uniform.

Similar to **17**, at low temperatures both ground and the excited state g_{eff}-values have to be taken into account separately. A Boltzmann weighted calculation was performed manually on the basis of the four lowest spin-states to account for the ground and excited state values of $g_{eff,ground\ state} = 1.76$ and $g_{eff,excited\ state} = 2.04$, respectively for each isomer (for details see Section VI.4.3). Initially the excited state g_{eff}-value was fixed to 1.98 (Appendix 4.4) from the broad excited state transition at 20 K in the EPR spectra, however a higher g_{eff}-value is needed to reproduce the magnetic properties quantitatively. The g_{eff}-value was adjusted to the experimental χT values between 2 and 100 K, a region that has previously been reproduced well

by the calculations on **15** and **17**. The temperature dependent susceptibility between 2 and 300 K was calculated with g_{eff} = 2.04 based on the excited state contributions only. This is not valid at very low temperature, but reproduces the overall temperature dependence well.

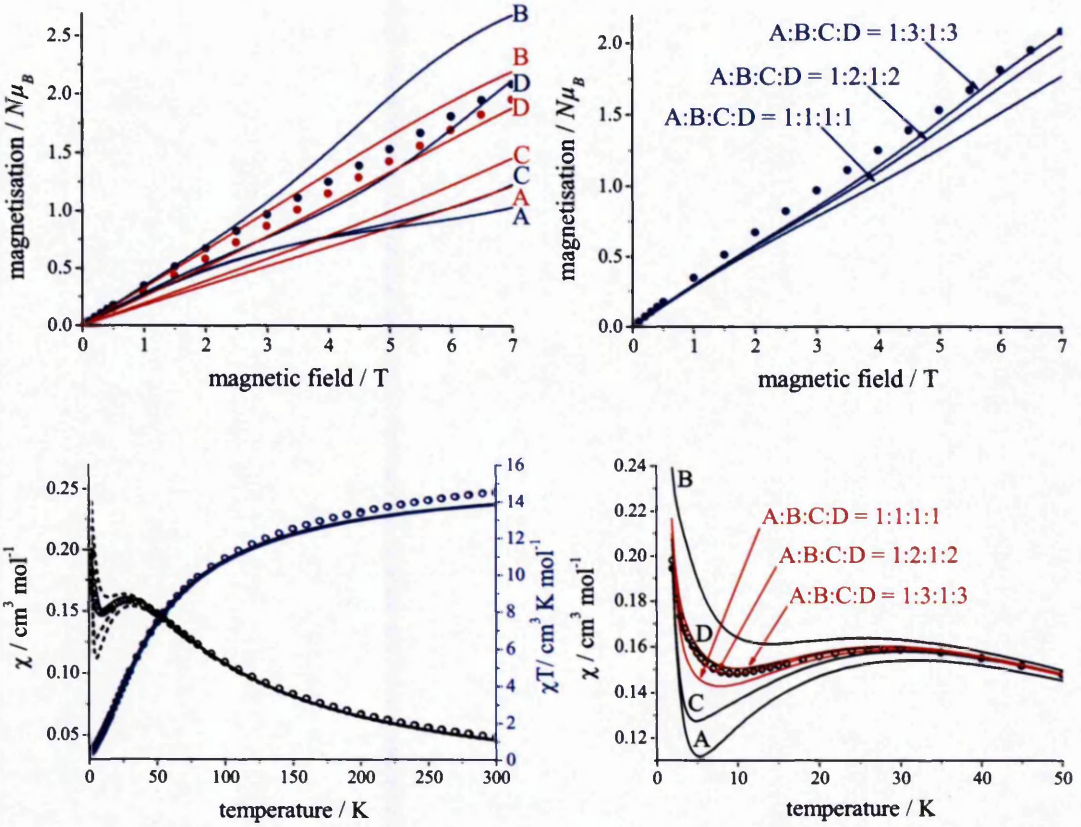

Figure IV.27: Top: field dependent magnetisation of **19**. Blue: 2 K, red: 4 K, lines: calculation with J = -5.8cm^{-1} for separate isomers and isomeric mixture using effective g_{eff}-values as explained in the text. Bottom: temperature dependent susceptibility of **19**. Dot: 1 T, ring: 0.1 T. Calculation with J = -5.8cm^{-1} and g_{eff} = 2.04 for separate isomers and an A:B:C:D = 1:2:1:2 isomeric mixture (right: expansion of the low temperature region)

Figure IV.27 shows the calculation of the magnetic susceptibility and magnetisation on **19** for the individual isomers and for isomeric mixtures with the isotropic exchange parameter J = -5.8. Again the field dependent magnetisation in particular shows the difference of the individual isomers. Surprisingly, the temperature dependent susceptibility is simulated best with the single isomer D (see Figure IV.26); however the curvature of the magnetisation *vs.* field plot of isomer D deviates significantly from the experimental data, indicating the presence of more than one isomer. Four different isomers provide a multitude of different possibilities

for isomeric mixtures and ratios, and on the basis of the experimental data an unambiguous assignment is not possible.

Nevertheless, the overall shape of the magnetisation *vs.* field plot strongly indicates a composition of A:B:C:D *ca.* 1:2:1:2. The absolute values of the calculated magnetisation are slightly lower than the experimental data. A similar problem has been observed for **15**, where the curvature of the magnetisation is reproduced correctly, but the absolute values are too small, even though in those calculations only fixed parameters were used (Figure IV.13). The isomeric composition can be confirmed by the temperature dependent susceptibility, which is also reproduced well for a 1:2:1:2 ratio. It is interesting to note that this isomeric ratio is very similar to that observed in **17**. In both compounds, a 2:1 excess of isomers with a stronger magnetic moment, and hence nickel ions on the same sub-lattice (counting the shortest distance in **19**), has been found.

To understand the origin of the different responses from the four different isomers, the eigenvalues and eigenfunctions of the molecular spin-states have been analysed. All isomers have an effective molecular spin ground state of $S_{eff} = {}^{1}/_{2}$, hence deviation of the magnetic properties of the different isomers must arise from low lying excited states. For an odd numbered homometallic ring, the ground state is expected to be a degenerate pair of spin doublets. This degeneracy is lifted in **19** and a very different low lying energy manifold is indeed observed for the different models A - D.

Level	Model A		Model B		Model C		Model D	
	E / cm^{-1}	S_{eff}	E / cm^{-1}	S_{eff}	E / cm^{-1}	S_{eff}	E / cm^{-1}	S_{eff}
10	27.06	${}^{5}/_{2}$	26.84	${}^{3}/_{2}$	27.93	${}^{1}/_{2}$	26.56	${}^{3}/_{2}$
9	26.73	${}^{5}/_{2}$	25.04	${}^{1}/_{2}$	26.67	${}^{5}/_{2}$	25.99	${}^{1}/_{2}$
8	25.83	${}^{1}/_{2}$	24.48	${}^{1}/_{2}$	25.63	${}^{3}/_{2}$	24.94	${}^{1}/_{2}$
7	23.12	${}^{1}/_{2}$	24.04	${}^{5}/_{2}$	25.53	${}^{5}/_{2}$	24.44	${}^{5}/_{2}$
6	22.54	${}^{3}/_{2}$	21.24	${}^{3}/_{2}$	24.43	${}^{1}/_{2}$	23.08	${}^{5}/_{2}$
5	17.08	${}^{3}/_{2}$	19.50	${}^{5}/_{2}$	19.24	${}^{3}/_{2}$	20.55	${}^{3}/_{2}$
4	12.10	${}^{3}/_{2}$	12.59	${}^{3}/_{2}$	11.71	${}^{3}/_{2}$	12.51	${}^{3}/_{2}$
3	10.93	${}^{3}/_{2}$	9.32	${}^{1}/_{2}$	9.57	${}^{3}/_{2}$	8.48	${}^{1}/_{2}$
2	3.00	${}^{1}/_{2}$	4.87	${}^{3}/_{2}$	6.67	${}^{1}/_{2}$	6.70	${}^{3}/_{2}$
1	0	${}^{1}/_{2}$	0	${}^{1}/_{2}$	0	${}^{1}/_{2}$	0	${}^{1}/_{2}$

Table IV.4: Lowest ten spin-states and eigenvalues calculated with *MAGPACK* for the four isomers of Cr_7Ni_2 with a uniform, isotropic exchange parameter $J = -5.8$ cm$_1$.

Table IV.4 summarizes the calculated eigenvalues for the ten lowest spin-states. Not only does the energy difference between ground and excited states vary between the models, the *order* of the spin-states varies, too.

A simple model based on exchange coupled fragments helps to illustrate the origin of those differences. Let us first select the largest insulated chain of chromium ions Cr_n not directly connected to any nickel ion. For cyclic odd numbered chains (n = odd), the resulting ground state spin in case of antiferromagnetic coupling is $S_{eff} = {}^1/_2$, for even number chains (n = even) the spins couple to an effective ground state of zero. The remaining fragment is $Cr_{7-n}Ni_2$, and for an identical antiferromagnetic exchange parameter J the resulting spin ground states will be 0 or ${}^1/_2$ depending on the value of n. Table IV.4 summarizes the spin-states for the different fragments. Next the fragments are coupled together, again in antiferromagnetic fashion. The ground state spin of Cr_n is coupled to ground and first excited spin of $Cr_{7-n}Ni_2$, leading to the lowest three Cr_7Ni_2 spin-states in model A and C, and the lowest two spin-states in model B and D. Finally the first excited spin-state of Cr_n is coupled to the ground state of $Cr_{7-n}Ni_2$.

	A	B	C	D
Cr_n	Cr_5	Cr_4	Cr_3	Cr_2
$S_{Cr,n,1}$	${}^1/_2$	0	${}^1/_2$	0
$S_{Cr,n,2}$	${}^3/_2$	1	${}^3/_2$	1
$Cr_{7-n}Ni_2$	Cr_2Ni_2	Cr_3Ni_2	Cr_4Ni_2	Cr_5Ni_2
$S_{Cr,7-n,Ni2,1}$	0	${}^1/_2$	0	${}^1/_2$
$S_{Cr,7-n,Ni2,2}$	1	${}^3/_2$	1	${}^3/_2$
$S_{Cr,n,1} + S_{Cr,7-n,Ni2,1}$	${}^1/_2$	${}^1/_2$	${}^1/_2$	${}^1/_2$
$S_{Cr,n,1} + S_{Cr,7-n,Ni2,2}$	${}^1/_2$ ${}^3/_2$	${}^3/_2$	${}^1/_2$ ${}^3/_2$	${}^3/_2$
$S_{Cr,n,2} + S_{Cr,7-n,Ni2,1}$	${}^3/_2$	${}^1/_2$ ${}^3/_2$	${}^3/_2$	${}^1/_2$ ${}^3/_2$

Table IV.5: Coupling scheme based on coupling of chromium and chromium-nickel cyclic chain fragments leading to the four lowest spin-states of Cr_7Ni_2.

The simple model does not explain yet, why the energies of the spin-states model A and C or model B and D differ. In addition it assumes an order of coupling the fragments and may need more refinements. However, it illustrates nicely, how the different order in the spin-states can arise from a simple coupling scheme, and that degeneracy of the spin-doublets is no longer expected for a heterometallic odd-number antiferromagnetically coupled ring.

Overall EPR spectroscopy and SQUID magnetometry have consistently shown that **17** and **19**, despite each being crystallographically and analytically pure compounds, contain different Cr_6Ni_2 and Cr_7Ni_2 positional isomers with different magnetic properties. Exchange interactions in all three compounds, Cr_7Ni (**15**), Cr_6Ni_2 (**17**) and the odd numbered ring Cr_7Ni_2 (**19**) have been interpreted with a unique isotropic exchange parameter of J = -5.8 cm^{-1}. Spin frustration in the odd-numbered ring **19** leads to the interesting effect that all positional isomers exhibit different magnetic properties, while in the even-numbered ring **17** differentiation is only possible between isomers where nickel ions are located on the same or different sub-lattices.

IV.3.2 Magnetic and spectroscopic properties of Cr_7Co, Cr_6Co_2 and Cr_7Co_2

The magnetic properties of the chromium-nickel ring systems even with two hetero-ions are dominated by the isotropic chromium-chromium exchange and from observations in Section IV.2 it is expected that the cobalt derivatives behave overall very similarly to the nickel analogues. Figures IV.28 – IV.30 show the magnetic properties of the three antiferromagnetically coupled chromium-cobalt rings Cr_7Co (**16**), Cr_6Co_2 (**18**), and Cr_7Co_2 (**20**). At room temperature the following contributions can be calculated from the single ion chromium(III) and cobalt(II) properties obtained experimentally for **10** and **12** at 300 K: (Figures IV.4 and IV.6)

Cr_7Co: $\chi T_{300\,K}$ = 15.11 cm^3 K mol^{-1} (calculation), 14.91 cm^3 K mol^{-1} (experiment)
Cr_6Co_2: $\chi T_{300\,K}$ = 17.08 cm^3 K mol^{-1} (calculation), 16.12 cm^3 K mol^{-1} (experiment)
Cr_7Co_2: $\chi T_{300\,K}$ = 18.72 cm^3 K mol^{-1} (calculation), 19.85 cm^3 K mol^{-1} (experiment)

For all three compounds, the room temperature susceptibility corresponds roughly to the predicted values. Values higher than the calculation have also been observed for Cr_6Ni_2 and Cr_7Ni_2 in a similar order.

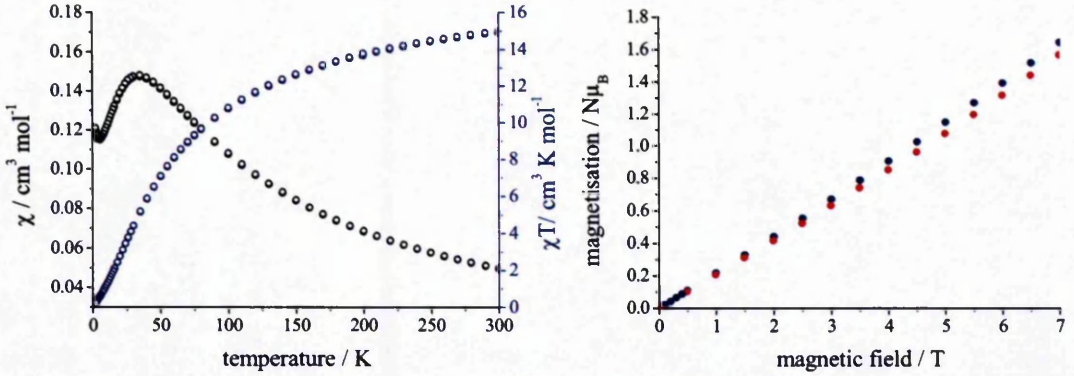

Figure IV.28: Magnetic properties of Cr_7Co (**16**) measured on a powder sample. Left: temperature dependent susceptibility at 1 T (dot) and 0.1 T (ring), right: field dependent magnetisation at 2 K (blue) and 4 K (red).

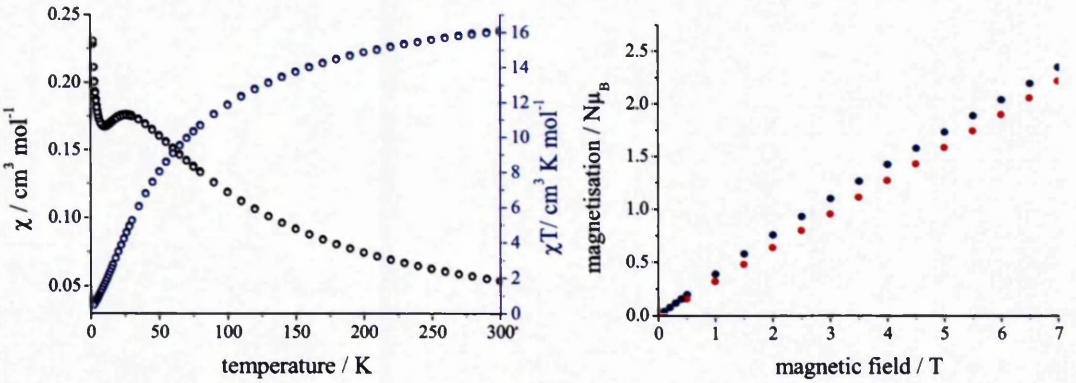

Figure IV.29: Magnetic properties of Cr_6Co_2 (**18**) measured on a powder sample. Left: temperature dependent susceptibility at 1 T (dot) and 0.1 T (ring), right: field dependent magnetisation at 2 K (blue) and 4 K (red).

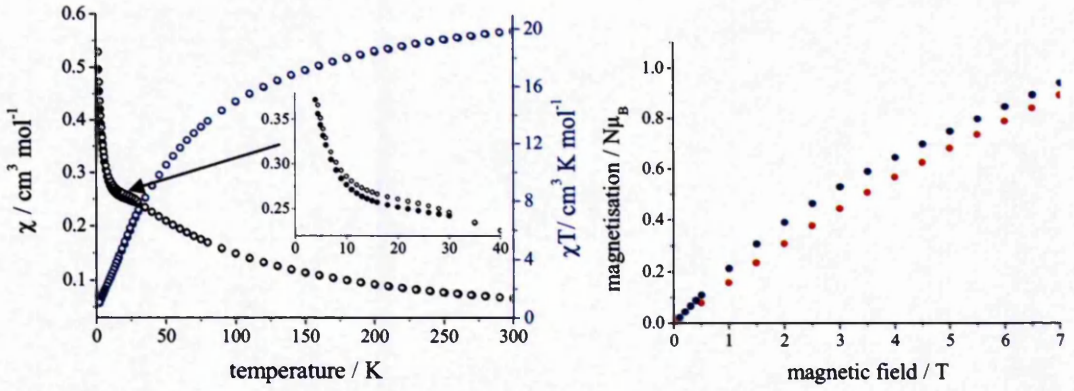

Figure IV.30: Magnetic properties of Cr_7Co_2 (**20**) measured on a powder sample. Left: temperature dependent susceptibility at 1 T (dot) and 0.1 T (ring), right: field dependent magnetisation at 2 K (blue) and 4 K (red). Inset: expansion of χ at low temperature.

The temperature of the maximum in χ in all three compounds (30 K (**16**), 26 K (**18**), 22K (**20**)) is slightly lower than that of the nickel derivatives compounds (33 K (**15**), 38 K (**17**), 28 K (**19**)), indicating a slightly weaker exchange interaction between chromium and cobalt compared to chromium and nickel. Similar indications have also been found for Cr_7Ni (**13a**) and Cr_7Co (**14**) in Section IV.2.2.

Antiferromagnetic coupling leads to a diamagnetic ground state in Cr_7Co (**16**) and Cr_6Co_2 (**18**) with low lying excited states, resulting in a base temperature susceptibility of χT_{2K} = 0.24 and 0.46 cm^3 K mol^{-1}, respectively. This model is supported by the steady increase of the magnetisation with the magnetic field. For Cr_7Co_2 (**20**) an $S = {}^3/_2$ ground state with χT_{2K} = 1.875 cm^3 K mol^{-1} is expected should the overall antiferromagnetic interaction be interrupted in one place (compare also Figure IV.24 for Cr_7Ni_2). Experimentally a significantly lower value of χT_{2K} = 0.99 cm^3 K mol^{-1} is observed, indicating a spin-frustrated system with a doublet ground state similar to Cr_7Ni_2. Base temperature χT is expected to be around 0.375 cm^3 K mol^{-1} for a spin doublet. However, a slightly higher value than expected is in fact obtained for all three chromium-cobalt rings: Ground states with χT = 0 at low temperature are expected for Cr_7Co (**14**, **16**) and Cr_6Co_2 (**18**), but values of 0.34 cm^3 K mol^{-1}, 0.24 cm^3 K mol^{-1}, and 0.46 cm^3 K mol^{-1} are obtained, respectively. It appears that each cobalt ion raises the spin-only expectation value by *ca.* 0.25 cm^3 K mol^{-1} in the three compounds. It is possible that low lying excited states, which are partly populated at 2 K may contribute to the low temperature susceptibility. However, a more important explanation is the influence of the orbital angular momentum onto the ground state. Indeed, a rise of +0.17 cm^3 K mol^{-1} at 2 K is obtained for the Ga_7Co ring. The paramagnetic ground state of Cr_7Ni_2 is confirmed by the slight curving in the field dependent magnetisation. A clear plateau is not observed, because low lying excited states are partially populated at 2 K and mask the saturation of the magnetisation.

Interestingly, the peak shape of the susceptibility changes when moving from Cr_7Co (**16**) over Cr_6Co_2 (**18**) to Cr_7Co_2 (**20**). While in **16** behaviour much like the nickel derivative **15** is observed, in compound **18** the peak intensity is significantly smaller and has weakened to a plateau shape in **20**. In fact, the overall shape of χ in Cr_7Co_2 is very reminiscent of the observations in Cr_7Zn (Figure IV.4). In addition, a small field dependence is observed in **20** at the plateau between the 0.1 T and 1 T measurement

(Inset in Figure IV.30). It is difficult to draw distinct conclusions about the shape of the susceptibility at this point, because the curvature of both low temperature susceptibility as well as low temperature magnetisation depend greatly on the isomeric mixture as seen for Cr_6Ni_2 and Cr_7Ni_2. However, the significant change might be a further indication that the introduction of a second cobalt(II) ion into the ring leads to a more pronounced influence of the orbital contribution from cobalt(II).

EPR spectroscopy on **17** and **19** has provided a good insight into the different isomers and their anisotropy present in the ring compounds. Unfortunately, spin relaxation processes in the chromium-cobalt rings appear to be in the order of the EPR time-scale and prevent similar investigations on compounds **18** and **20** by EPR spectroscopy. While spin relaxation hinders investigation with EPR spectroscopy, it promotes investigation with NMR and Dr. E. Carolina Sañudo has obtained very well resolved paramagnetic NMR spectra of chromium-cobalt rings.[138] In collaboration with Sañudo paramagnetic NMR spectra have been collected for the three imidazolium templated chromium-cobalt rings **16**, **18** and **20** to gain information on the isomers present in solution. Figures IV.31 and IV.32 (see also the corresponding Tables IV.6 and IV.7) show the paramagnetic NMR spectra of **16** and **18** respectively. The NMR spectrum of Cr_7Co_2 (**20**) is not conclusive and either shows the presence of many isomers or a decomposition of the species in solution.

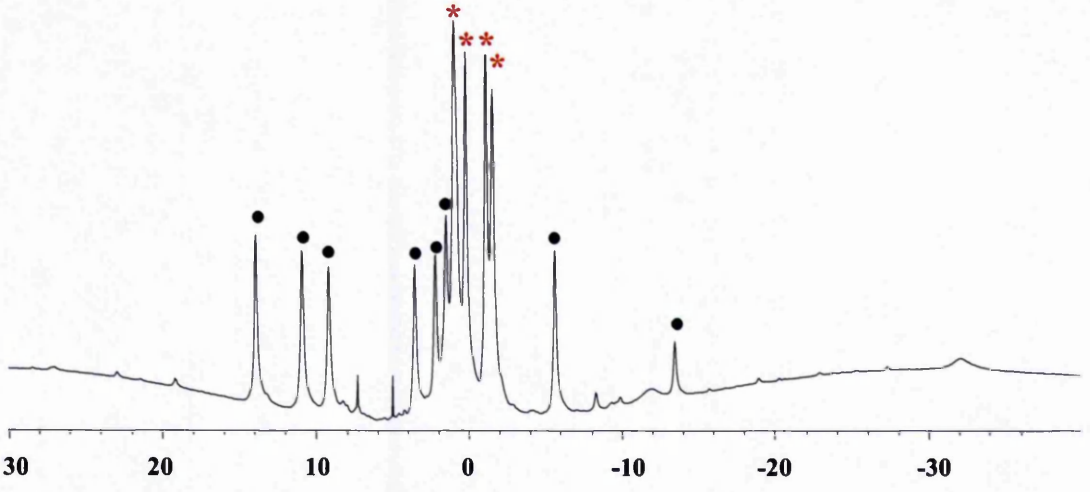

Figure IV.31: 300 MHz paramagnetic NMR spectrum of Cr_7Co (**16**) in $CDCl_3$ at room temperature.

δ / ppm	13.91	10.90	9.19	3.53	2.23	1.54	0.97
integral	9 H	9 H	9 H	9 H	9 H	9 H	27 H
	1 axial pivalate (9 H) per singlet						1 ax. 2 eq. piv

δ / ppm	0.27	-1.06	-1.63	-5.62	-13.52
integral	18 H	18 H	18 H	9 H	
	2 equatorial pivalates per singlet			1 ax. piv.	probably imidazolium methyl groups

Table IV.6: Peak positions corresponding to the NMR spectrum of Cr_7Co (**16**) in Figure IV.31. Chemical shifts have been calibrated to the $CHCl_3$ impurity in $CDCl_3$.

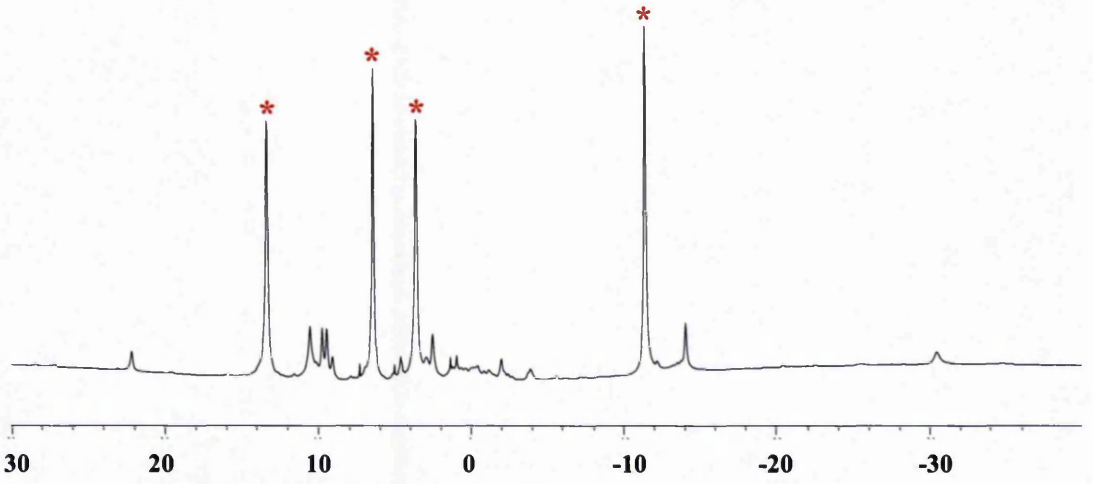

Figure IV.32: 300 MHz paramagnetic NMR spectrum of Cr_6Co_2 (**18**) in $CDCl_3$ at room temperature.

δ / ppm	13.34	6.22	3.59	-11.40	-30.49	-46.65	-91.75	-117.59	-120.85
integral	36 H	36 H	36 H	36 H					
	4 pivalates per singlet				probably imidazolium methyl groups			probably imidazolium NH	

Table IV.7: Peak positions corresponding to the NMR spectrum of Cr_6Co_2 (**18**) in Figure IV.32. Chemical shifts have been calibrated to the $CHCl_3$ impurity in $CDCl_3$.

16 shows 12 singlets corresponding to the t-butyl groups of the pivalic acid, indicating 12 NMR inequivalent pivalate ligands. Rapid rotation of the t-butyl group and the three methyl groups within leads to a NMR equivalence of all nine t-butyl hydrogen atoms at room temperature. Eight of the pivalates are arranged in the ring plane (equatorial), the remaining eight alter above and below the plane (axial) as depicted in Figure IV.33. Within the ring plane, pairs of equatorial pivalates are equivalent (indicated by letters), the symmetry is defined by the hetero atom (red).

The results are four signals with an intensity corresponding to two pivalic acid *t*-butyl groups. Those four peaks are indicated with a red star in Figure IV.31. The remaining eight axial pivalates are inequivalent and give rise to another eight signals with an intensity corresponding to one pivalic acid t-butyl group (black dots in Figure IV.31).

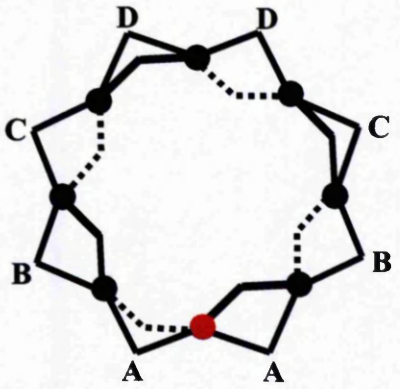

Figure IV.33: Schematic representation of the NMR equivalent and inequivalent pivalate ligands in **16**. Four singlets arise from pairs of equivalent equatorial pivalates A, B, C and D. All axial pivalates are inequivalent and give rise to eight individual methyl singlets.

The NMR spectrum of Cr_6Co_2 (**18**) is clearly dominated by one very symmetric species. Figure IV.34 indicates schematically the four environments leading to the four strong singlets (red star in Figure IV.31). An isomer with hetero-ions on opposite positions within the ring is the only arrangement that can give rise to only four NMR signals.

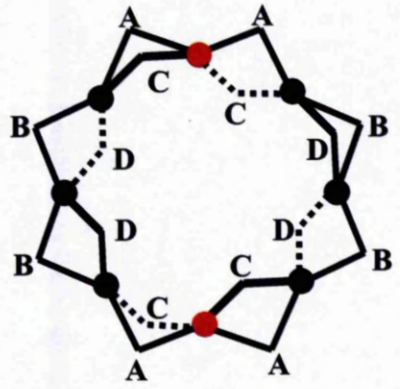

Figure IV.34: Schematic representation of the NMR equivalent and inequivalent pivalate ligands in **18**. Two singlets arise from groups of four equivalent equatorial pivalates A and B, and two signals from groups of four equivalent axial pivalates C and D.

A number of weak signals confirm the presence of at least one more isomer; however the intensities of those signals are too weak to identify the chromium-cobalt sequence. From integration a ratio of *ca.* 4:1 is estimated for the two isomers.
In comparison with the EPR spectra of Cr_6Ni_2 it seems surprising that one isomer appears to have such dominance in Cr_6Co_2, while the nickel analogue is characterised by at least two, and according to the EPR more likely four isomers. However, it could be possible that some isomer(s) might not be seen by NMR because their electronic structure leads to a cancelling of the beneficial (relaxation time) effect of Co especially in the case of adjacent cobalt ions. Consistent, is the excess of isomers with hetero-ions located on the same sub-lattice, although for Cr_6Ni_2 only a 2:1 excess is observed. However a direct comparison between solution and solid state may not necessarily be adequate.

IV.4 Conclusions

In the first part of this chapter, the contribution of the anisotropic spin-orbit ion cobalt(II) to the magnetic properties of heterometallic chromium rings has been reported by comparing Cr_7Co to the isostructural derivatives Cr_7Cd / Cr_7Zn, Ga_7Co and the spin-only analogue Cr_7Ni.
Magnetic measurements and multifrequency EPR spectroscopy on Ga_7Co have allowed for the investigation of the single ion properties of cobalt(II) within the ligand field geometry of the heterometallic rings, in addition to Piligkos' studies on Cr_7Cd, which provide the contributions from the Cr_7 segment. The magnetic properties of Ga_7Co reflect the typical response of a single cobalt(II) ion in an octahedral ligand field with an unquenched orbital angular momentum. From the calculated second derivative spectrum, it has been possible to observe the cobalt(II) hyperfine splitting of 70 G. Very strong anisotropy was obtained by Q-band and W-band EPR spectroscopy. Furthermore, calculations of the EPR spectrum and single crystal line positions with the angular overlap model (AOM) have allowed for the two transitions to be assigned to the molecular structure. While a strong Zeeman splitting ("g" = 6.8) occurs along the tetragonal symmetry axis perpendicular to the ring plane, the Zeeman splitting within the ring plane is moderate ("g" = 2.9). Both

the magnitude, as well as the direction of the anisotropy is consistent with observations on the dimetallic **4** (Chapter III). This shows the importance of the ligand field geometry on the anisotropy of single cobalt(II) ions. In both compounds, the metal ions are surrounded by pairs of bridging carboxylates and bridging oxygen (**4**) or fluoride (**12**) forming a face sharing octahedral connectivity between the metal ions. Such similar geometry leads to a very similar magnetic anisotropy.

Despite the strong anisotropy of the single cobalt(II) ion in the heterometallic ring compounds, the powder magnetic properties of the Cr_7Co ring are very similar to those of the spin-only nickel analogue Cr_7Ni. Overall the low temperature magnetic properties are clearly dominated by the exchange coupled chromium ions, and any anisotropic effects of cobalt(II) are masked, at least in a powder experiment. Only at room temperature the orbital momentum of cobalt(II) becomes apparent, leading to the typical rise in χT compared to spin-only ions. It is interesting to note, that Cr_7Co exhibits a diamagnetic ground state. In Chapter III, cobalt(II) dimetallics have been treated as pairs of interacting pseudo spins, to a first approximation very successfully. If such a pseudo spin of $^1/_2$ was to interact with the seven chromium spins of $^3/_2$, an effective ground state of 1 could be expected. This idea is clearly not supported by the experimental observations and shows that such a simple model cannot be generalized to magnetic interactions between spin-only and spin-orbit ions.

In the second part of this chapter, studies on heterometallic rings with one or two hetero-ions templated around imidazolium cations are reported. Prior to the theoretically challenging chromium-cobalt rings, the isostructural spin-only nickel derivatives have been investigated in detail with SQUID magnetometry and EPR spectroscopy.

Replacement of the secondary ammonium cation in Cr_7Ni (**13**) with the imidazolium cation in Cr_7Ni (**15**) has not shown any influence on the magnetic properties of the well studied Cr_7Ni systems, but a small rhombicity was noticed in the excited state EPR transitions reflecting the reduced symmetry of the monoclinic crystal structure of **15** in comparison to the tetragonal structure of **13**. Nevertheless, the uniform exchange parameter of $J = -5.8$ cm^{-1} (fixed from INS)[92] and the isotropic g_{eff}-values are consistent between the two compounds within the strong exchange limit. On this basis, exchange interactions in the heterometallic chromium-nickel rings with two

metal ions, Cr_6Ni_2 (**17**) and also the odd numbered ring Cr_7Ni_2 (**19**) were interpreted successfully with the same uniform isotropic exchange parameter of J = -5.8 cm^{-1} and g_{eff}-values obtained experimentally by EPR spectroscopy for the molecular spin-states in the strong exchange limit.

Both EPR spectroscopy and SQUID magnetometry have consistently shown that **17** and **19**, despite each being crystallographically and analytically a pure compound, contain different Cr_6Ni_2 and Cr_7Ni_2 positional isomers with different magnetic properties depending on the chromium-nickel sequence. Although a complete quantitative simulation of the EPR spectra has not been possible in all cases, a good estimate of the g_{eff}-values and the zero field splitting parameters of the different spin-states in different isomers has been achieved. Vector coupling based on a division of the ring into its "spin-up" and "spin-down" sub-lattices has allowed for the expected g_{eff}-values of **17** to be calculated in each isomer and supports the assignment of different spectral features to different isomers. The low temperature magnetic properties have proved most sensitive to the isomeric ratio and were calculated for each individual isomer with only *fixed* parameters obtained from other experiments, allowing for the isomeric ratio to be varied in order to fit the magnetic properties. For both compounds a *ca.* 2:1 excess of isomers with nickel ions on the same sub-lattice (counting along the shortest distance in **19**) was found.

The uniform chromium-chromium and chromium-nickel exchange leads to spin frustration in the odd-numbered Cr_7Ni_2 ring. While for a homometallic compound the ground state is characterised by a degenerate pair of spin-doublets, such degeneracy is no longer present in the heterometallic system. Although a doublet ground state has been found for all isomers, the energy and more importantly the order of excited spin-states depends greatly on the chromium-nickel sequence leading to four magnetically different positional isomers.

Finally, on the basis of the results for the spin-only chromium-nickel rings, the cobalt systems have been investigated. The powder magnetic properties of Cr_7Co, Cr_6Co_2 and Cr_7Co_2 are very similar to those of the nickel analogues, but indicate a slightly weaker chromium-cobalt exchange compared to chromium-nickel interactions. Again a diamagnetic ground state is observed for the even-numbered rings, while a paramagnetic doublet ground state was found for Cr_7Co_2, showing again spin-frustration similar to Cr_7Ni_2. In all cases the low temperature magnetic susceptibility is slightly higher than expected for spin-only systems, the effect is more pronounced

in the compounds with two cobalt(II) ions, and indicates that the orbital momentum is still influencing the magnetic properties of the ground state. No resolved EPR spectra have been obtained on any chromium-cobalt rings, probably due to spin-relaxation mechanisms on the order of the EPR-timescales, but high resolution paramagnetic NMR spectra in solution at room temperature were recorded. The spectrum of Cr_6Co_2 confirms the excess of isomers with heterometals on the same sub-lattice, but a much larger excess of *ca.* 4:1 of a single isomer was obtained in solution.

Chapter V

Concluding remarks

Exchange coupled octahedral cobalt(II) coordination compounds exhibit particularly challenging magnetic properties arising from first order spin-orbit coupling of the cobalt(II) single ions, which does not allow for a conventional spin-only treatment of the magnetic exchange interactions. But whilst spin-orbit coupling complicates life for a magneto-chemist, it leads to a very strong single ion anisotropy, which is the key to many interesting and important physical properties related to potential applications of molecule-based magnetic devices. The goal of this Ph.D. research was the direct *experimental observation* of this anisotropy in order to provide high quality complementary data, against which theoretical models can be tested. Only through experimental results, particularly on single crystals, can a better understanding of the magnetic exchange coupling between metal ions with an unquenched orbital angular momentum be achieved.

Dimetallic compounds are the smallest, hence most "simple", exchange coupled unit, and in this Ph.D. Thesis complementary studies such as SQUID and torque magnetometry, EPR spectroscopy and INS on powder and single crystal samples of a series of structurally very closely related octahedral cobalt(II) dimetallics (six antiferromagnetically (AF) coupled dimetallics (**3**, **5** – **9**) and one ferromagnetically (F) coupled example (**4**) have been presented.

However, prior to the study of exchange coupled systems, the monometallic compound $[Co(C_5H_5NO)_6](NO_3)_2$ (**1**) has been used as a test compound both for experimental routines such as single crystal SQUID magnetometry, as well as for modelling studies using two different approaches: a simple effective treatment of cobalt(II) as a pseudo "s" = $^1/_2$, and a ligand field approach based on the angular overlap model (AOM). Successful and consistent reproduction of both experimental and computational studies reported previously on **1**[104] has provided high confidence in both experimental and computational routines. Furthermore, important observations have been drawn from the calculations regarding the sensitivity of the calculated magnetic properties to changes in the AOM parameters. It appears that the

anisotropy of the Zeeman splitting in the ground doublet, which is responsible for low temperature magnetic properties, is hardly affected by changes in the strength of the metal-ligand bonds and hence the absolute values of e_σ and e_π, providing the sign and magnitude of $\Delta e_\pi = e_{\pi x} - e_{\pi y}$ is correct. The orbitals involved in anisotropic π-interactions are defined by the e_π parameters and the corresponding ψ angle, thus the magnitude and direction of the anisotropy of the systems depends almost entirely on Δe_π and its sign in particular. The parameter *cannot* be obtained from powder experimental data, but requires single crystal studies.

In addition, characteristic single ion properties extracted from the monometallic compound have provided useful information for the treatment of cobalt(II) ions within exchange coupled systems. Most *low temperature* experimental observations on exchange coupled cobalt(II) dimetallics reported in this Ph.D. Thesis have been interpreted with a simple effective model on the basis of exchange coupling between the lowest Kramers doublets of the two cobalt(II) ions, giving rise to an effective "singlet" and "triplet" state. This model requires a well isolated ground state of the single ions from higher (excited) states. From AOM calculations, a sufficient energy difference between the ground and first excited doublet of *ca.* 60 cm^{-1} has been found in **1**; subsequent calculations with the AOM on the dimetallic **5** (AF) has suggested an even larger energy gap of > 150 cm^{-1} in the dimetallics, consistent with preliminary *ab-initio* calculations of the ligand field in **4** (F). Experimentally the sufficient isolation of the ground multiplet from further excited energy levels was also confirmed by the temperature dependence of excitations observed by both EPR spectroscopy and INS on the dimetallics **3** (AF) and **4** (F). INS on **4** has not shown any further excited states up to at least 60 K. Consequently the use of very anisotropic effective "g"-values (2.5 – 4.7), which account for the orbital contribution to the Zeeman splitting of the ground doublet, has reproduced approximately the anisotropy of the monometallic **1** in both EPR spectra and magnetic properties at low temperature, and has justified an equivalent treatment for the dimetallics. It is important to emphasise again that octahedral cobalt(II) does behave as a doublet magnetic moment at low temperatures, despite the real cobalt(II) spin $s = {}^3/_2$, but the wavefunctions are spin-orbit functions, and hence a quantitative reproduction with a pseudo-spin model is not possible. Deviations of the model have been observed for the monometallic **1** and manifest in particular in the Zeeman

splitting, which is not linearly symmetrical as assumed in the model. For the interpretation of the dimetallics similar deviations were *expected*, but can be explained and discussed on the basis of ligand field calculations with the AOM.

Single crystal rotational studies using a SQUID magnetometer in selected crystallographic planes of different cobalt(II) dimetallics have provided the orientation of the principal magnetic axes with respect to the molecular structure. Strong anisotropy has been observed in all cases, which manifests in particular in the Zeeman splitting or "g"-anisotropy ("g_{eff}" = 2.3 – 6.2). Single crystal low temperature magnetic measurements on **5** (AF) have shown, that anisotropy is also present in the exchange interactions. An even more pronounced effect has been found for **4** (F), where calculations and low temperature rotational studies with a SQUID have indicated very weak antiferromagnetic exchange along the cobalt-cobalt vector, and ferromagnetic exchange interactions in the other orthogonal directions. This is a very important observation, because many theoretical models (see Section I.2) are based on the assumption that the orbital contribution towards the magnetic exchange is quenched. Even though such models account for spin-orbit coupling in the Zeeman terms *via* anisotropic **g**-matrices, the exchange interaction is handled isotropically. In particular in the case of **4** such a treatment does not seem adequate to explain the experimental observation. The significant differences between different orientations, hence different exchange pathways, are reminiscent of the model developed by Gerloch *et al.*, introduced in Section I.2. The authors define distinct "exchange active" orbital pairs and corresponding exchange parameters. In contrast to an isotropic treatment of exchange, those selected exchange pathways will depend greatly on the orbital contribution to the particular wavefunctions. For Gerloch *et al.*'s antiferromagnetically coupled dimetallic $[Co_2(O_2CC_6H_5)_4L_2]$ (L = 4-methyl-quinoline) the calculated and experimental minimum susceptibility was found along the cobalt-cobalt vector of the dimetallic; exactly the same orientation of the minimum susceptibility was found for the dimetallic **4**. This seems very significant, because the local geometry of the cobalt (II) ions in Gerloch's dimetallic is square pyramidal, with four donor ligands at 90° to the cobalt-cobalt vector, whereas in **4**, the link is approximately co-facial.

In collaboration with Prof. Chibotaru at the University of Leuven / Belgium, the manifold of experimental data is currently being analysed against a theoretical model based on calculations of the ligand field interactions with *ab-initio* methods, and

exchange interactions within the Lines model.[25,70] Previously Chibotaru *et al.* have successfully modelled the powder magnetic properties of cobalt(II) oligomers, and extension to single crystal data will now be possible. Again, exchange interactions are treated isotropically within this model approach, and it will be informative to compare results from the calculations to the anisotropic exchange interactions observed experimentally. Furthermore, analysis with an approach similar to that of Gerloch *et al.* may be very instructive, in order to introduce anisotropy into the exchange interactions.

Very detailed information on the anisotropy of the dimetallics has also been obtained from multifrequency EPR spectroscopy between 9.4 and 345 GHz, and the first single crystal rotational EPR study on an exchange coupled cobalt(II) dimetallic. It was possible to assign the "triplet" transitions of **4** (F) and the corresponding "g_{eff}"-values of "$g_{eff,xx}$" = 3.43 "$g_{eff,yy}$" = 6.13 "$g_{eff,zz}$" = 2.30 observed in the multi-frequency powder experiment to the principal magnetic and spectroscopic axes, where x is the unique C_2 symmetry axis, z the cobalt-cobalt vector and y the cross product of the two. Together with the zero-field energies (0, 4.7 cm^{-1}, 9.4 cm^{-1},11.3 cm^{-1} in $\mathbf{3}^D$ and 0, 0.8 cm^{-1}, 1.6 cm^{-1}, 2.4 cm^{-1} in $\mathbf{4}^D$) observed experimentally with INS, the Zeeman splitting of **3** (AF) and **4** (F) was calculated on the basis of a very simple effective model of two pseudo "s" = $^1/_2$ interacting to give a "singlet" and "triplet" state, where all degeneracy is lifted. *Simultaneously* magnetic properties, EPR spectroscopy and INS have been calculated successfully in a semi-quantitative fashion, in the case of **4** solely from experimental observables without any fitting parameters. Interestingly, the model predicts a weak antiferromagnetic exchange in **4** along the cobalt-cobalt vector and ferromagnetic interactions in orthogonal directions, despite the use of a single isotropic exchange parameter of J = +0.8 cm^{-1}. The (expected) limitation of the over-simplified model shows itself particularly in the comparison of the linearly modelled Zeeman effect to the actual transition energies obtained with EPR spectroscopy. On the other hand, a surprisingly linear frequency dependence of the resonance fields in **4** has indicated that, despite the spin-orbit character of the wavefunctions, the system exhibits a frequency dependence, which appears to have strong similarities to a spin-only g-value. In addition an apparent field dependence of the "g"-value was found experimentally from the magnetisation of the monometallic **1**. Those observations can only be explained consistently, if energy levels evolve (nearly) linearly with the magnetic field, but the slope of

corresponding ± m levels deviates between $+m$ and $-m$ averaging in the effective "g_{eff}"-value obtained from HFEPR. Theoretical calculations with the AOM have confirmed this behaviour. In addition, preliminary *ab-initio* calculations have shown that the single ion "**g**"-matrices within the dimetallics are non-collinear. Together with the strong anisotropy, mixing between "spin"-states can be expected. Experimentally, indications for such mixing have been found with EPR spectroscopy in the Zeeman splitting, and from INS in the Q-dependence of **4**. Studies on other (spin-only) systems have shown, that the origin of enhanced quantum tunnelling of the magnetisation can often be attributed to mixing between spin-states.[19-21] Observations in the dimetallics may give a first experimental indication of the reason for the fast quantum tunnelling observed in cobalt(II) molecular magnets showing a "butterfly"-shaped hysteresis, which collapses at zero field.[17,18]

In the third section of this Ph.D. Thesis, heterometallic rings with one or more heteroatoms were studied for two aspects: The influence of the anisotropic cobalt(II) ion on the overall magnetic properties of the rings, and the isomeric composition of heterometallic rings with more than one heteroatom. For the second part in particular, detailed studies on spin-only nickel analogues were carried out to gain a good understanding of the spin-only system prior to the analysis of the theoretically more challenging chromium-cobalt rings.

Three chromium-nickel rings Cr_7Ni, Cr_6Ni_2 and Cr_7Ni_2 templated around one or two imidazolium cations have been studied, and their magnetic properties have been reproduced with a uniform chromium-chromium and chromium-nickel exchange parameter of J = -5.8 cm^{-1} reported previously from INS[92] and g_{eff}-values obtained experimentally by EPR spectroscopy for the molecular spin-states in the strong exchange limit. For the first time, an odd numbered heterometallic ring with two hetero-ions has been studied. Strict antiferromagnetic coupling with a uniform chromium-chromium and chromium-nickel exchange is not possible, thus spin-frustration occurs in the Cr_7Ni_2 ring. For a homometallic compound a ground state characterised by a degenerate pair of spin-doublets is expected, however such degeneracy was not found in the heterometallic system. The energy and, more importantly, the order of excited spin-states were found to depend greatly on the chromium-nickel sequence. Indeed calculations with a uniform exchange parameter have shown four different magnetic responses for the four positional isomers of

Cr_7Ni_2. The main difference occurs in the excited spin-states: while all four isomers are characterized by a doublet ground state, a doublet first excited state was only obtained for two isomers, while the remaining two isomers exhibit a first excited state of $^3/_2$.

Both EPR spectroscopy and SQUID magnetometry have consistently shown that Cr_6Ni_2 and Cr_7Ni_2 contain different positional isomers with different magnetic properties depending on the chromium-nickel sequence. EPR spectroscopy has shown the different contributions from different isomers, and a good estimate of the g_{eff}-values and the zero-field splitting parameters of the different spin-states in different isomers has been obtained. Vector coupling based on a division of the ring into its "spin-up" and "spin-down" sub-lattices has allowed for the expected g_{eff}-values of the even-numbered Cr_6Ni_2 to be calculated in each isomer and supports the assignment of different spectral features to different isomers. The low temperature magnetic properties have proved most sensitive to the isomeric ratio and were calculated for each individual isomer with only *fixed* parameters obtained from other experiments, allowing for the isomeric ratio to be varied in order to fit the magnetic properties. For both compounds a *ca.* 2:1 excess of isomers with nickel ions on the same sub-lattice (counting along the shortest distance in Cr_7Ni_2) was found. This is a nice example of how the combination of complementary techniques can provide important information on the studied system: While the additive EPR spectroscopy has allowed for the individual isomers to be identified and parameterized, the averaging SQUID magnetometry has allowed for the isomeric ratio to be determined. Paramagnetic NMR spectroscopy on Cr_6Co_2 confirms the excess of isomers with heterometals on the same sub-lattice found for the chromium-nickel rings for the chromium-cobalt analogue, but a different isomeric ratio of *ca.* 4:1 was obtained for the chromium-cobalt ring in solution.

The single ion magnetic properties of cobalt(II) within the heterometallic rings have been studied on Ga_7Co, which reflects the typical response of a strongly anisotropic single cobalt(II) ion in an octahedral ligand field with an unquenched orbital angular momentum, similar to the monometallic **1**. Both the magnitude, as well as the direction of the anisotropy have been found to be consistent with observations on the dimetallic **4** (F). In both **4** and Ga_7Co the cobalt(II) ions are bridged by two carboxylate ligands and a water molecule or fluoride ion, respectively. In **4**, the

smallest Zeeman splitting ("g_{eff}" = 2.3) has been found along the cobalt-cobalt vector consistent with the small Zeeman splitting ("g_{eff}" ~ 2.9) of Ga_7Co in the ring plane. Along the tetragonal axis of the Ga_7Co ring, a much larger Zeeman splitting ("g_{eff}" ~ 6.8) comparable to the maximum Zeeman splitting in **4** ("g_{eff}" ~ 6.13) has been found. Despite the strong anisotropy of the single cobalt(II) ion in the heterometallic ring compounds, the overall powder magnetic properties of the heterometallic rings are dominated by the exchange coupled chromium ions. Consequently the magnetic properties of the cobalt-chromium rings Cr_7Co, Cr_6Co_2 and Cr_7Co_2 have been found to behave very similarly to those of the isostructural spin-only nickel analogues, although based on the peak temperature of χ the chromium-cobalt exchange appears to be slightly weaker than the chromium-nickel interactions. However, the properties of the cobalt(II) ions are manifest in observable fluid NMR spectra (which cannot be obtained on the nickel analogues), therefore the spin-orbit component of the electronic wavefunctions must have a profound effect on the relaxation properties of the nuclear wavefunctions. Although potential influences of the anisotropic cobalt(II) ions on the magnetic exchange are masked by the dominating chromium-chromium exchange, the orbital contribution of cobalt(II) can be observed at room temperature through the characteristic increase in χT also found in Ga_7Co, as well as a small, but consistent, increase at low temperature compared to spin-only expectations.

A non-magnetic ground state has been found in the even-numbered chromium-cobalt rings Cr_7Co and Cr_6Co_2. Unless the two cobalt(II) ions in Cr_6Co_2 are adjacent, this does not agree with the treatment of cobalt(II) as a pseudo spin of $^1/_2$ at low temperature. The major Cr_6Co_2 isomer found in solution has shown cobalt(II) ions located on opposite positions on the ring, hence a dominance of Cr_6Co_2 with adjacent cobalt(II) ions in the solid state is unlikely. The non magnetic ground state shows that a simple effective model cannot be generalized to magnetic interactions between spin-only and spin-orbit ions. In fact, the ground state of the Cr_7Co ring appears to favour the behaviour of cobalt(II) as a real spin $s = {}^3/_2$, which may suggest a quenching of the orbital angular momentum contribution to the exchange pathway between a spin-only and a spin-orbit ion. However, further studies, particularly on single crystals, are required to draw final conclusions. By analogy to Cr_7Ni_2, a paramagnetic ground doublet has been found for Cr_7Co_2, showing again spin-frustration in the odd-numbered ring.

In conclusion, complementary measurement techniques have been used very successfully on single crystal and powder samples of extended families of structurally very similar compounds. The results have provided detailed insight into the magnetic properties of exchange coupled cobalt(II) compounds, and heterometallic chromium-cobalt and chromium-nickel rings with one or more hetero atom. Experimental evidence has been found for the strong anisotropic Zeeman splitting of cobalt(II) ions and for the anisotropic exchange in cobalt(II) dimetallics, with a particular importance of the direct cobalt-cobalt vector. A new simple model of coupling effective spins to produce effective parameters has provided an easy and successful access to the calculation of the magnetic and spectroscopic properties simultaneously. In a polymetallic, where cobalt(II) is the minority spin, the orbital contribution is diminished. Nevertheless an important contribution to the molecular wavefunctions is manifest in particular in the possibility of recording paramagnetic NMR spectra on chromium-cobalt rings.

Chapter VI

Experimental and computational details

VI.1 General procedures and instrumentation

VI.1.1 Chemicals

All chemicals were purchased from Acros, Fisher Scientific, Fluka, Lancaster or Aldrich and used without further purification. Air or moisture sensitive reactions were carried out using Schlenk techniques under a dinitrogen atmosphere. Solvents were dried by standard distillation procedures and stored under a dinitrogen atmosphere.

VI.1.2 X-Ray diffraction

Crystallographic data were collected with an Oxford Diffraction XCalibur2 diffractometer. Structures were solved and refined by direct methods using SHELXTL[139] and completed by iterative cycles of ΔF syntheses and full-matrix least-squares refinement. Refinement of F^2 was against all reflections. All non-hydrogen atoms were refined anisotropically. Hydrogen atoms, if not found experimentally, were included in idealized positions.
All crystal structures relevant for this Thesis are available in cif format on the accompanying disc.

VI.1.3 Magnetic measurements

Powder and single crystal magnetic measurements were carried out on a commercial 7 T Quantum Design MPMS-XL SQUID magnetometer. To prevent powder samples from orienting in strong magnetic fields, compounds **1, 14** and all cobalt(II) dimetallics were fixed in wax (eicosane, Aldrich) unless stated otherwise.

Single crystal experiments were performed with a Quantum Design single crystal rotator device. Crystals were fixed to the holder with a small drop of cryogenic grease (AP 101, Apiezon). An external motor allows for the rotation of the sample perpendicular to the magnetic field direction.

All powder and single crystal magnetic properties were calculated per mole and corrected for the diamagnetism of the holder and wax. The diamagnetic susceptibility of the compound was calculated from Pascal constants[1,2] and subtracted from the experimental value.

Magnetic torque experiments were carried out at the Institute of Physics in Modena in collaboration with Prof. Marco Affronte. Data were collected on a Quantum Design PPMS thin lever torque magnetometer at 2 K. The sample was fixed on the lever of a silicon device with a small drop of cryogenic grease. 360° rotation perpendicular to the magnetic field was achieved with an external motor.

VI.1.4 Electron paramagnetic resonance (EPR) spectroscopy

K- and Q-band EPR spectra were recorded on a Bruker Elexsys Spectrometer, equipped with a 2 T Bruker electro magnet and an Oxford Instruments helium cryostat. S- and X- band EPR spectra were measured on a Bruker EMX system, equipped with a 1.5 T Varian electro magnet and an Oxford Instruments helium cryostat.

W-band EPR spectra were recorded on a Bruker Elexsys Spectrometer equipped with a 6 T superconducting magnet and a helium cryostat, both manufactured by Oxford Instruments.

Baseline corrections have been applied where necessary and possible without manipulation of the spectral features.

HFEPR spectra were collected at the GHMFL in Grenoble in collaboration with Dr. Anne-Laure Barra on a home-built spectrometer that allows for frequencies between 53 GHz and 1 THz, equipped with a 12 T superconducting magnet, and a helium cryostat allowing for temperatures between 1.5 and 300 K.

VI.1.5 Inelastic neutron scattering (INS)

INS experiments were performed in collaboration with Dr. Richard Mole on a multi-chopper time of flight instrument TofTof at FRM-II of the Technische Universität München / Germany (beamline scientist: Dr. Tobias Unruh).[103] The sample was placed in an annular can of outer radius 1.2 cm, with sample thickness of 0.1 cm, and placed in a CCR (closed cycle refrigerator) type cryostat. Data were collected between 4 and 60 K (**4**) or 4 and 20 K (**3**) using 3.8 Å (**4**) and 6 Å (**3**, **4**) neutrons. Data were normalised to a vanadium sample and background-subtracted using an empty can. An absorption correction was also made. All data corrections were made using the *IDA* software suite.[140]

VI.1.6 Nuclear magnetic resonance (NMR) spectroscopy

Paramagnetic proton NMR spectra (^{1}H NMR) spectra were recorded on a Varian INOVA Unity 300 (300 MHz) spectrometer at room temperature.

VI.1.7 Magnetic circular dichroism (MCD) spectroscopy

MCD spectra on **4** were recorded by Dr. Justin Bradley at The University of East Anglia, Norwich/UK. Identical MCD spectra were observed for samples pressed in a KBr disks and samples mulled in nujol, sandwiched between quartz plates. Low light transmittance outside the UV-visible region prevented further measurements on KBr disks, while spectra in nujol showed much improved transmittance. Spectra have been recorded at variable fields up to 5 T in the temperature range 1.7 to 20 K. For high temperature comparison, spectra were also recorded in full field at 75 K. The absorption spectrum of the mulled sample between quartz plates was calibrated against that of a 10 mmol mull in a 1 mm pathlength cuvette in order to convert the intensity of the differential MCD spectra into $\Delta\varepsilon$.

VI.2 Synthetic routes

VI.2.1 Monometallic cobalt(II) compound 1

$[Co(C_5H_5NO)_6](NO_3)_2$ (1)

$C_{30}H_{30}CoN_8O_{12}$ **RM = 753.1 g mol^{-1}**

$[Co(C_5H_5NO)_6](NO_3)_2$ was prepared following O'Connor *et al*:[105]

Large red diamond shaped crystals are observed from the red solution after a few days at 5°C.

Elemental analysis: %, calculated for $C_{30}H_{30}CoN_8O_{12}$: C: 47.82, H: 4.01, N: 14.87, found: C: 47.60, H: 3.68, N: 14.58

X-Ray: hexagonal *R3*, $a = 12.4142(21)$ Å, $c = 18.0012(2)$ Å, $V = 2402.53$ Å^3

VI.2.2 Dimetallic cobalt(II) compounds 3 – 9

The deuterated dimetallics $\mathbf{3}^D$ and $\mathbf{4}^D$ for INS studies were synthesised and kindly provided for measurements by Dr. Grigore Timco at The University of Manchester. Details on the synthetic procedure are described in Appendix 3.1.

$[Co_2(H_2O)(O_2CC(CH_3)_3)_4(HO_2CC(CH_3)_3)_4]$ (3)

$C_{40}H_{78}Co_2O_{17}$ **RM = 948.9 g mol^{-1}**

3 was prepared following Winpenny *et al*.[113] Large pink needle-like crystals were observed from the cold deep purple solution after a few days.

Elemental analysis: %, calculated for $C_{40}H_{78}Co_2O_{17}$: C: 50.63, H: 8.29, found: C: 50.56, H: 8.43

X-Ray: monoclinic: $P2_1/n$, $a = 12.149(4)$ Å, $b = 20.027(7)$ Å, $c = 23.097(8)$ Å, $\beta = 103.410(7)°$, $V = 5466.47$ Å^3, $Z = 4$[113]

$[Co_2(H_2O)(O_2CC(CH_3)_3)_4(HO_2CC(CH_3)_3)_2(py)_2]$ (4)

$C_{40}H_{68}Co_2N_2O_{13}$ **RM = 902.8 g mol^{-1}**

4 was prepared from **3** following Winpenny *et al.*[113]

4 precipitated as a pink microcrystalline powder, larger pink crystals were obtained from the filtered solution after 4 days at 5°C.

Elemental analysis: %, calculated for $C_{40}H_{68}Co_2O_{13}$: C: 53.21, H: 7.59, N: 3.10, found: C: 53.35, H: 7.79, N: 3.13

X-Ray: monoclinic *C2/c*, a = 24.715(2) Å, b = 19.5088(19) Å, c = 9.8201(10) Å, β = 96.725(2)°, V = 4702.2(8) Å^3, Z = 4.[113]

$[Co_2(H_2O)(O_2CCH_3)_4(tmen)_2]$ (5)

$C_{20}H_{46}Co_2N_4O_9$ **RM = 604.5 g mol^{-1}**

5 was prepared following Turpeinen *et al.*[112]

Fine, needle-like pink crystals of **5** were collected by filtration and the remaining solution left at room temperature for further crystallization. Large pink crystals were obtained after a few days.

Elemental analysis: %, calculated for $C_{20}H_{46}Co_2N_4O_9$: C: 39.74; H: 7.67, N: 9.27, found: C: 39.10, H: 7.91, N: 9.05

X-Ray: orthorhombic: *Pbca*, a = 12.056(3) Å, b = 15.917(5)° Å, c = 31.33(1) Å, V = 6012.08 Å^3, Z = 8[112]

General method for the synthesis of $[Co_2(H_2O)(O_2CR)_4$-$(tmen)_2]$ (6 – 9)

6 - 9 were prepared following the synthetic method towards $[Co_2(H_2O)(O_2CCH_2Cl)_4$-$(tmen)_2]$ reported by Turpeinen *et al.*[112]

Fresh cobalt(II) carbonate (1.00 g, 8.41 mmol) and two equivalents of carboxylic acid (16.82 mmol) were suspended in ethanol (20 mL) and heated to reflux until most cobalt(II) carbonate dissolved. The pink solution was filtered hot to remove undissolved cobalt carbonate. Subsequently tetramethylethylene diamine (1.27 mL, 8.41 mmol) were added dropwise to the warm solution. A first pink microcrystalline precipitate of $[Co_2(H_2O)(O_2CR)_4(tmen)_2]$ was collected by filtration, larger crystals were obtained from the remaining solutions after few days.

$[Co_2(H_2O)(O_2CCH2Cl)_4(tmen)_2]$ (6)

$C_{20}H_{42}Co_2N_4O_9Cl_4$ **RM = 742.3 g mol^{-1}**

Elemental analysis: %, calculated for $C_{20}H_{42}Co_2N_4O_9Cl_4$: C: 32.36; H: 5.70, N: 7.55, found: C: 32.26, H: 7.95.67, N: 7.36

X-Ray: monoclinic: $P2_1/c$, a = 15.7872(3) Å, b = 12.8814(2) Å, c = 15.2748(3) Å, β = 91.126(2)°, V = 3105.7 Å^3, Z = 4

A **6_Co2AcClTmen.cif** containing the full crystallographic data is available on the accompanying disc.

$[Co_2(H_2O)(O_2CCHCl_2)_4(tmen)_2]$ (7)

$C_{20}H_{38}Co_2N_4O_9Cl_8$ **RM = 880.03 g mol^{-1}**

Elemental analysis: %, calculated for $C_{20}H_{38}Co_2N_4O_9Cl_8$: C: 27.30; H: 4.35, N: 6.37, found: C: 27.02, H: 4.25, N: 6.22

X-Ray: triclinic: *P P-1*, a = 9.736(1) Å, b = 11.792(2) Å, c = 16.771(2) Å, α = 78.96(1)°, β = 105.56(1)°, γ = 95.41(1)°, V = 1818.66 Å^3, Z = 2

$[Co_2(H_2O)(O_2C(CH_3))_4(tmen)_2]$ (8)

$C_{32}H_{70}Co_2N_4O_9$ **RM = 772.79 g mol^{-1}**

Elemental analysis: %, calculated for $C_{32}H_{70}Co_2N_4O_9$: C: 49.73; H: 9.13, N: 7.25, found: C: 49.57, H: 9.30, N: 7.15

X-Ray: monoclinic: *P21*/c, a = 11.404(<1) Å, b = 21.870(1) Å, c = 34.735(1) Å, β = 90.12(<1)°, V = 8662.90 Å^3, Z = 8

$[Co_2(H_2O)(O_2CC_6H_5)_4(tmen)_2]$ (9)

$C_{40}H_{54}Co_2N_4O_9$ **RM = 852.7 g mol^{-1}**

Elemental analysis: %, calculated for $C_{40}H_{54}Co_2N_4O_9$: C: 56.34; H: 6.38, N: 6.58, found: C: 56.40, H: 6.43, N: 6.52

X-Ray: triclinic *P-1*, a = 10.7281(3) Å, b = 11.6789(4) Å, c = 17.1733(5) Å, α = 106.092(3)°, β = 91.135(2)° γ = 93.160(2)°, V = 2062.85 Å^3, Z = 2

A **9_Co2BenzTmen.cif** containing the full crystallographic data is available on the accompanying disc.

VI.2.3 Heterometallic rings

All heterometallic rings that are described in this Ph.D. thesis were synthesised and kindly provided for measurements by Dr Grigore Timco of The University of Manchester. Details of the synthetic procedure are available in Appendix 5.1.

VI.3 Single crystal experiments

VI.3.1 General procedure to relate the crystal morphology to the crystallographic unit cell

For known crystallographic structures the *crystal movie configuration* tool of the *CrysAlis RED* software[141] allows the crystal faces to be indexed, and hence the crystallographic unit cell axes can be related to the crystal morphology.

Accurate determination of absolute magnetic intensities on a commercial Quantum Design MPMS SQUID magnetometer requires a sufficiently large amount of sample (ideally *ca.* 10 mg) to ensure a strong paramagnetic signal compared to the molecular and instrumental diamagnetic contributions. Such large crystals exceed the dimensions of the camera lens on the X-ray diffractometer. Hence the indexing process was performed twice for each compound: on a smaller crystal (dimensions: *ca.* $1 \times 1 \times 0.2$ mm, collection at 100 K), which allows for the determination of all crystal faces, and on the large crystal for single crystal magnetic experiments, which only allows for a small part of the crystal to be indexed. In the case of the large crystals, unit cell determination and capture of the movie were carried out at room temperature to prevent the formation of ice on the crystal surface in the conventional nitrogen cooling stream. Comparison of the two experiments allowed for a confident assignment of the remaining faces for the large crystals.

VI.3.2 Single crystal SQUID magnetometry on 1

1 forms large, diamond-shaped crystals, in which the bottom and top face are given by the *hkl* vectors (-1 0 -1) and (1 0 1), respectively and include the unit cell axis *b*. The four sides of the crystal are formed by the planes (1 -1 -1) and (-1 1 1) including no axis, and (0 -1 1) and (0 1 -1) including the unit cell axis *a*. No crystal face aligns with the unique unit cell axis *c* (see Figure VI.1).

For SQUID measurements, a single crystal of 15.92 mg (dimensions: ~ 3 × 3 × 1 mm) was used. The crystal morphology of **1** only allows for a precise mounting of *b* parallel or perpendicular to the magnetic field *B*. Fortunately, the anisotropy of the principal susceptibility in uniaxial crystal systems (here *R3*) is completely defined by two independent diagonal elements of the susceptibility tensor $\chi_c = \chi_{\parallel}$ and $\chi_a = \chi_b = \chi_{\perp}$, the whole crystal *ab*-plane being isotropic throughout.

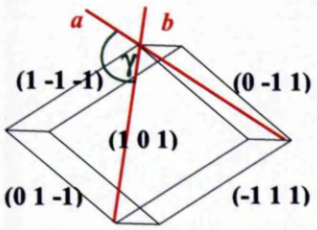

Figure VI.1: Indexed crystal faces and unit cell axes of **1**.

A virtual axis *a**, the cross product of *b* and *c*, can be projected onto the *ab*-plane (Figure VI.2), with a susceptibility $\chi_{a^*} = \chi_{\perp}$.

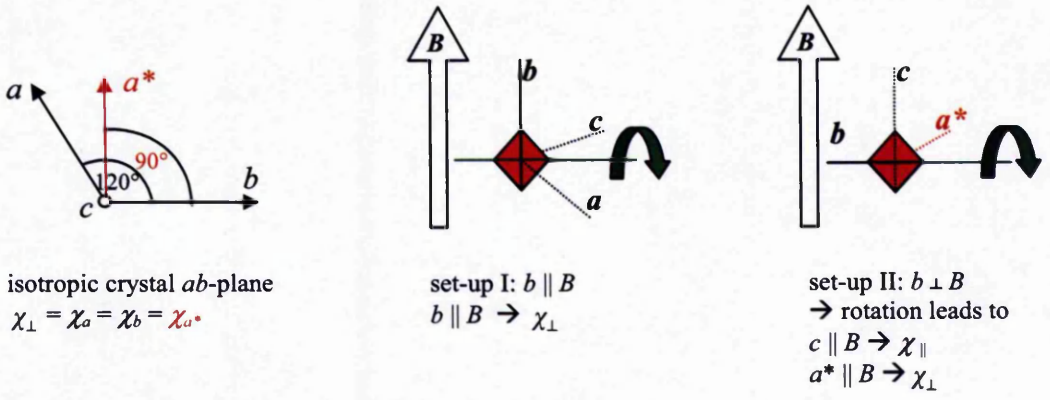

isotropic crystal *ab*-plane
$\chi_{\perp} = \chi_a = \chi_b = \chi_{a^*}$

set-up I: $b \parallel B$
$b \parallel B \rightarrow \chi_{\perp}$

set-up II: $b \perp B$
→ rotation leads to
$c \parallel B \rightarrow \chi_{\parallel}$
$a^* \parallel B \rightarrow \chi_{\perp}$

Figure VI.2: Set-up of the single crystal susceptibility measurements on **1**.

Figure VI.2 illustrates the two set-ups for the single crystal experiment. After observation of $\chi_\perp$ from set-up I, $\chi_\perp$ can be identified on a rotational plot (χ vs. rotation angle) in set-up II, giving $\chi_\parallel$ in the positions ± 90° from $\chi_\perp$. In both set-ups, the susceptibility was measured *vs.* the angle of a 360 degree rotation in a 1 T magnetic field at both 300 and 10 K. For a correct alignment of the crystal with respect to the magnetic field, symmetrical sinusoidal angular dependence is expected.

Further control is given by the double measurement of $\chi_\perp$, which is observed in both of the two independent mountings, and by comparison to the powder magnetic measurement that represents a weighted average over all possible orientations ($\chi_{powder} = 2\chi_\perp + \chi_\parallel$). The high quality of the experimental data can be deduced from Figure VI.3, which shows symmetrical angular dependence, identical values for $\chi_\perp$ in both set-ups and agreement with the powder experiment.

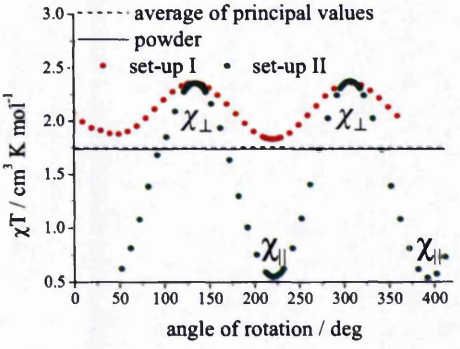

Figure VI.3: Angular dependence of the single crystal susceptibility of **1** at 1 T and 10 K.

VI.3.3 Single crystal SQUID, torque and EPR measurements on 4

4 crystallizes as deformed hexagons, where the flat bottom and top face form the *bc*-plane described by the *hkl* vectors (1 0 0) and (-1 0 0).

In one direction the adjacent faces are characterised by (-1 -1 0) and (-1 1 0), defining the direction of *c* within the *bc*-plane. The unique axis *b* is orthogonal to *c* by definition in monoclinic space groups, as depicted in Figure VI.4. The crystal morphology did not allow for *c* to be determined from the crystal shape, every crystal had to be indexed individually for single crystal experiments.

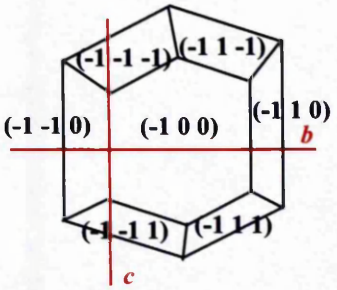

Figure VI.4: Indexed crystal faces and unit cell axes of **4**.

For **SQUID magnetometry**, a single crystal of 2.89 mg (dimensions: $\sim 2 \times 2 \times 1$ mm) was used. The paramagnetic signal from such a small sample volume is too weak for quantitative measurements, in particular at room temperature, because the paramagnetic response is in the order of the diamagnetic corrections. Only relative intensities can be compared. Figure VI.5 shows the set-up for the rotational experiment in the *ac* plane.

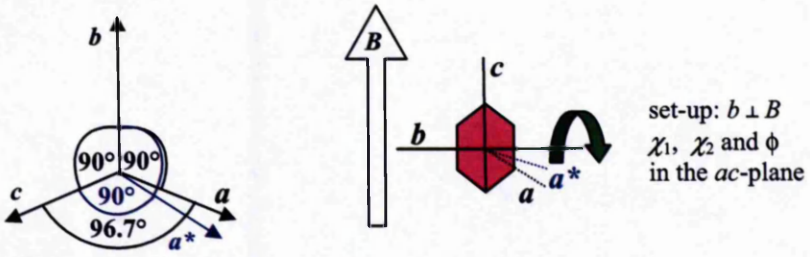

Figure VI.5: Set-up of the single crystal susceptibility measurements on **4**.

For **torque magnetometry** very small crystals with dimensions ≤ 0.2 mm in all directions were used. Such small samples make indexing of the faces on an X-ray diffractometer and subsequent correct mounting on the torque cantilever very difficult, and it proved simpler to use the anisotropy obtained from the torque itself to align the crystals. Three experiments were performed, each with the assumption of *c* along one of the three crystal sides. Figures VI.6 and VI.7 show that two of the three rotations exhibit identical behaviour with a smaller anisotropy than observed in the third set-up. These results were expected and show, that in case a) and b) the crystal was aligned along either of the edges (1 0 0) / (-1 -1 1) or (1 0 0) / (-1 1 1) where rotation around the orthogonal vector did not result in principal magnetic responses. In c) the crystal was oriented correctly along *c* and rotation around the orthogonal *b* leads to the anisotropy within the *ac* plane.

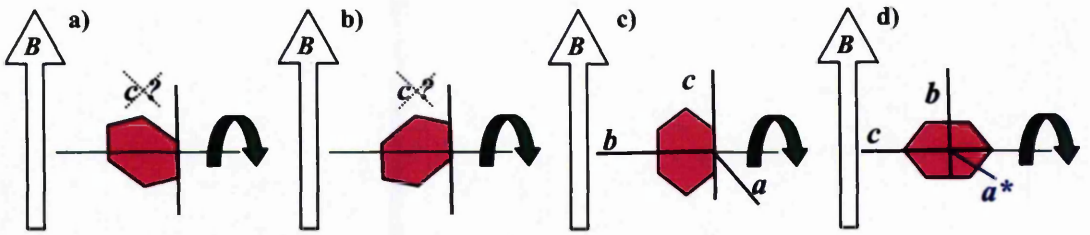

Figure VI.6: a) – c): Set-ups to determine the crystallographic axes of **4** with torque magnetormetry, c) and d) rotational studies to measure the crystal anisotropy in the *ac*-plane and *ba** plane.

Having determined the crystallographic axis with respect to the crystal morphology, in the fourth set-up d) the crystal was rotated around *c*, resulting in the anisotropy of the *ba**-plane, with a* being the cross product of *b* and *c*.

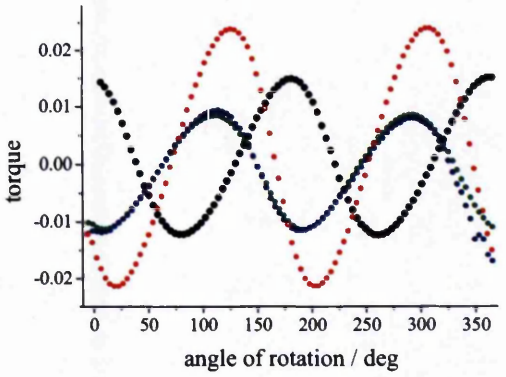

Figure VI.7: Rotational studies of **4** with a cantilever torque at a magnetic field of 1 T in the different set-ups depicted in Figure VI.6: a) blue, b) green, c) black (*ac* plane), d) red (*ba** plane).

In addition to the magnetic measurements, **single crystal EPR** studies were carried out on **4** at Q-band. Crystals were mounted on custom-designed quartz rods with a diameter of 0.9 mm and placed into a Q-band quartz sample tube as depicted in Figure VI.8. The images show the three set-ups for the measurement of the anisotropy in three orthogonal planes. For set-up I and II the rod had a flat face for vertical mounting of the crystal, while for set-up III a polished bottom surface allowed for horizontal mounting of the crystal. The sample was rotated manually in 10° steps with a goniometer of 2° accuracy. The error introduced through mounting of the small crystal on the sample stud under a microscope and the goniometer was estimated to be ± 5°.

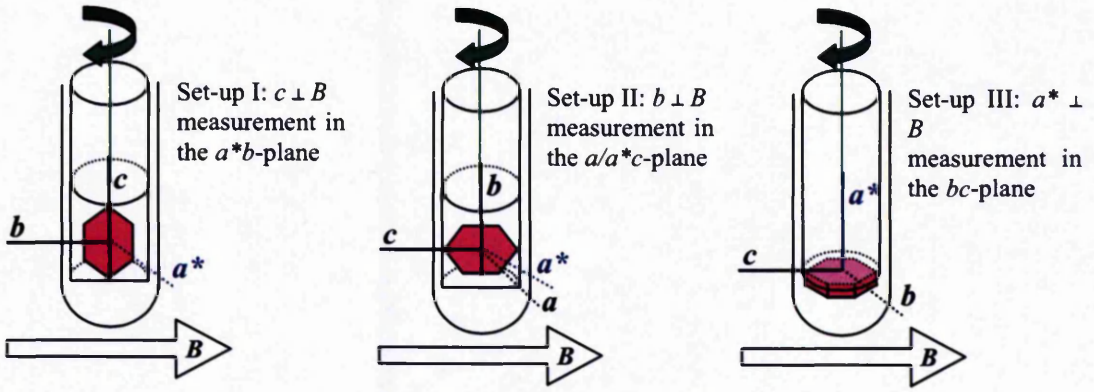

Figure VI.8: Set-ups for single crystal EPR spectroscopy on **4** in three different orthogonal planes.

Measurement in three orthogonal planes led to a double measurement along all three orthogonal axes a^*, b and c. This double measurement was used to identify the spectra corresponding to the crystal axes. From crystal mounting in set-up I, a^* was expected at *ca.* 135° and c at *ca.* 45° (see Figure III.23), while in set-up II a^* was expected at *ca.* 110° and b at *ca.* 20° and 200° (see Figure III.24). In set-up III it was not possible to adjust the directions of the b and c axes with respect to the magnetic field and the crystal axes in Figure III.25 were determined purely from comparison with the first two planes. Reproducibility of related spectral orientations in different planes is more reliable than the rough estimation of the starting position, and the assignment of the crystal directions from comparison of the spectra agreed surprisingly well with the expectations from the mounting of the crystal.

VI.3.4 Single crystal SQUID magnetometry on 5

The indexed crystal faces and the unit cell axes of **5** with respect to the crystal morphology are shown in Figure VI.9.

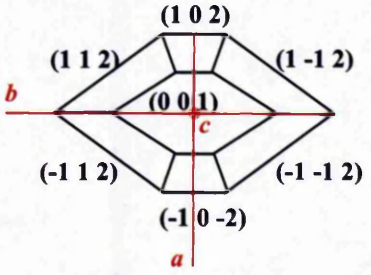

Figure VI.9: Indexed crystal faces and unit cell axes of **5**.

The *ab*-plane forms the top and bottom of the crystal with the *hkl* vectors (0 0 1) and (0 0 -1); *c* is vertically pointing out of the *ab*-plane. The *b* axis runs along the elongated side of the crystals, *c* by definition is perpendicular to *b*.

The crystal morphology allowed an easy alignment of the crystal axes with respect to an applied magnetic field. For orthorhombic crystal systems, the three different principal susceptibilities along the three crystal axes can be observed with just two measurement set-ups, which are illustrated in Figure VI.10.

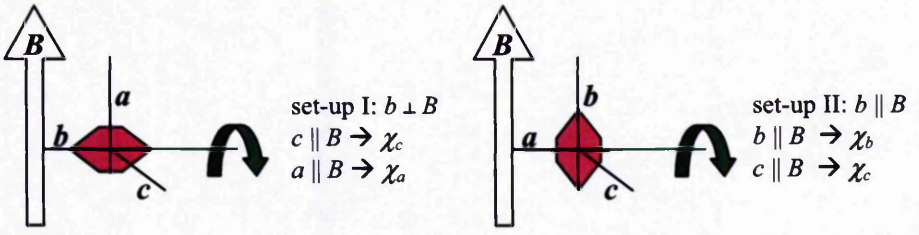

Figure VI.10: Set-ups for the single crystal susceptibility measurements on **5**.

Rotation around *b* as shown in set-up I allowed for the measurement of the anisotropy in the *ac*-plane including the two principal directions. In set-up II, rotation around *a* resulted in the *bc* anisotropy. From the double measurement of χ_c the quality of the manual mounting was estimated.

Initially the measurement of the angular dependence was started at 10 K, however crystals fractured in two attempts and powder remained. Controlled cooling of a new sample while measuring the minimum and maximum susceptibility at 300 K, 200 K, 100 K, and below in 10 K steps, gave a fracture temperature of the crystal between 40 and 30 K as shown in Figure VI.11.

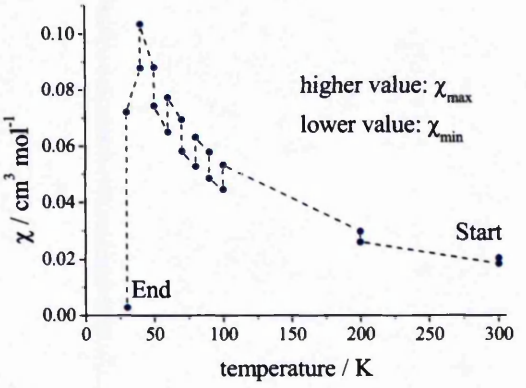

Figure VI.11: Temperature dependent maximum and minimum susceptibility of **5**; the crystal fractures between 40 and 30 K.

To ensure the crystal remained stable, all further measurements were carried out above 50 K. Figure VI.12 shows the angle dependence of the anisotropy in the *ac* and *bc* plane at 1 T and 50 K. In both set-ups identical values for χ_c were obtained, which confirmed the precise mounting of the crystal in both measurements. Powder measurement and the average of the principal values agree reasonably well at 50 K. The good agreement is more obvious in the χT vs. T plot in Figure III.13. Both double measurement of χ_c and comparison with the powder experiment provided high confidence in the absolute values of the single crystal susceptibility.

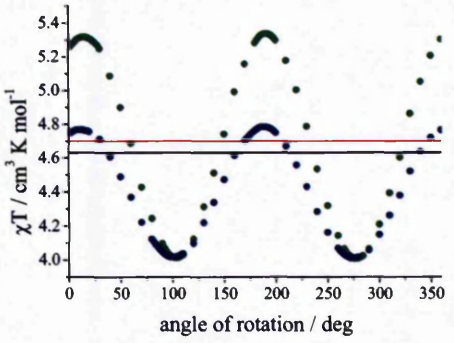

Figure VI.12: Angular dependence of the single crystal susceptibility of **5** at 1 T and 50 K. Green: *bc*-plane, blue: *ac*-plane, red: principal average at 50 K, black: powder at 50 K.

VI.3.5 Single crystal SQUID magnetometry on 6

The monoclinic compound **6** crystallizes in a needle-like fashion where *a* runs along the needle direction, while *b* and *c* run through the body diagonals as drawn in Figure VI.13.

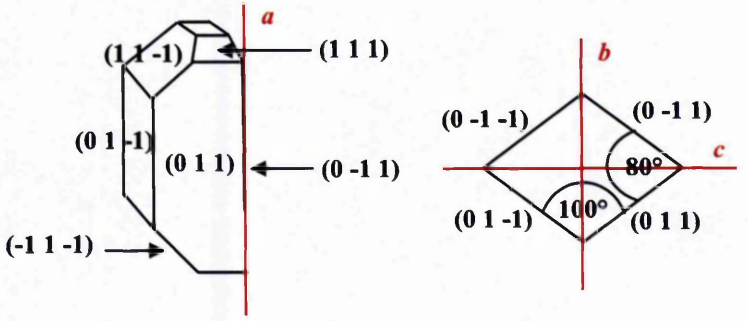

Figure VI.13: Indexed crystal faces and unit cell axes of **6**.

This morphology complicated the mounting of the crystal on the SQUID sample holder, because rotation around the unique axis *b* could only be achieved if the crystal was mounted on the 80° edge. To accomplish a precise mounting a small custom-designed Teflon holder was used, where an 80° v-shaped groove allowed for a perfect fit of the crystal. Figure VI.14 shows the two different set-ups, which were required to measure along all three principal magnetic directions. The monoclinic angle β is almost 90° in this example and within the experimental error of "mounting by eye" the 1.1° difference was negligible. Therefore for the second set-up *a* was assumed to be orthogonal to *b* and *c*. The symmetrical angle dependence in the *bc*-plane and the very good agreement between principal average and powder shown in Figures III.15, III.17 and III.18 confirmed that the crystal was mounted sufficiently accurately and the above assumption was valid in case of **6**.

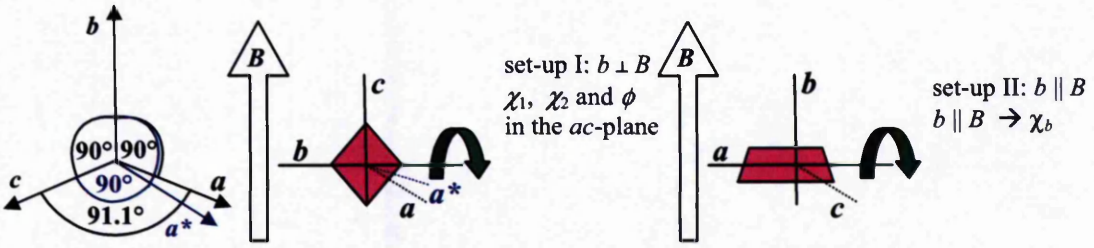

Figure VI.14: Set-ups of the single crystal susceptibility measurements on **6**. Rotation around *b* allowed for the principal magnetic axis χ_1 and χ_2 to be determined with respect to the crystallographic axis *a* and *c*.

VI.4 Computational details

VI.4.1 Determination of the ligand field matrices for AOM

The angular overlap model (AOM) is based on a parameterisation of the metal-ligand bond interaction after a precise definition of the ligand positions within a chosen axes frame. To simulate the molecular magnetic anisotropy, the ligand positions are expressed as polar coordinates (θ, ϕ) within the principal magnetic axes system. The origin of the coordinate system is defined as the central cobalt(II) ion. In this set-up the magnetic axes are defined as *X*: $\theta = 90$, $\phi = 0$, *Y*: $\theta = 90$, $\phi = 90$, *Z*: $\theta = 0$, $\phi = 0$.

In addition to the ligand positions, the orientations of π-orbitals on the ligands have to be defined to account for anisotropic metal-ligand interactions. The *AOMX*[109] software implements the calculation of a third angle ψ, which defines a local axis frame on the ligands. A dummy atom is introduced into the AOM ligand matrix, which forms a plane with the ligand donor atom and the central metal atom. By default, the calculated ψ-angle places the local y axis, and hence the $e_{\pi y}$ contribution of the ligand, perpendicular to the ligand-metal-dummy-atom plane. All polar coordinates of ligand atoms were determined with the crystallography software *Mercury*[142] using the *measure angle* and *measure torsion* tool.

$[Co(C_5H_5NO)_6](NO_3)_2$ (1)

In the highly symmetric compound **1** the principal magnetic orientations are defined as $XY = ab = \perp$ and $Z = c = ||$. The cobalt(II) centres are placed on the crystal unit cell corners and the polar coordinates of the ligand atoms within the coordinate system $XYZ \equiv ab^*c$ with $b^* = a \times c$ are easily determined, see Table VI.1.

The orientations of the two π-orbitals on the pyridine-N-oxide ligand are defined by the rotational angle ψ, which places a local y axis on the ligand ($e_{\pi y}$ contribution) with respect to the metal-ligand bond vector (local z axis). To account for the sp^2 hybridized oxygen with a partial conjugation into the pyridine ring, ψ has been calculated for π_y perpendicular to the Co – O – N plane (Figure VI.15, Table VI.1).

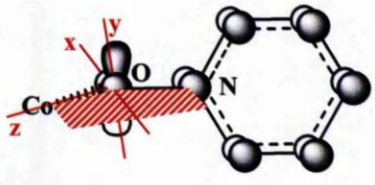

Figure VI.15: Schematic diagram showing the orientation of the π-orbitals of pyridine-N-oxide.

Ligand	θ	ϕ	ψ		Dummy	θ	ϕ
pyO	54.67	16.74	111.507653		pyO-N	49.49	45.93
pyO	54.67	136.74	111.507653		pyO-N	49.49	165.93
pyO	54.67	256.74	111.507653		pyO-N	49.49	285.93
pyO	125.33	76.74	68.492347		pyO-N	130.51	105.93
pyO	125.33	196.74	68.492347		pyO-N	130.51	225.93
pyO	125.33	316.74	68.492347		pyO-N	130.51	345.93

Table VI.1: Polar coordinates defining the ligand positions of **1** within the framework of the principal magnetic axes *XYZ*.

$[Co_2(H_2O)(O_2CCH_3)_4(tmen)_2]$ (5)

In the orthorhombic system **5** the magnetic axes are defined as $X = a$, $Y = b$ and $Z = c$. Along the three principal molecular directions, the different molecules in the unit cell are magnetically equivalent, but the two individual cobalt centres are not related by symmetry and have to be considered individually. π-interactions were taken into account for the three acetate oxygen atoms coordinated to the cobalt centres. The carboxylate carbon atom was used as a dummy-atom to define the local axis frame for the π-contributions. π_x corresponds to the free electron pair on the oxygen, while π_y defines the delocalized π-orbital on the carboxylate functionality. Figure VI.16 shows the nomenclature of the different atoms in the molecule and the orientation of the π-orbitals on the oxygen atoms.

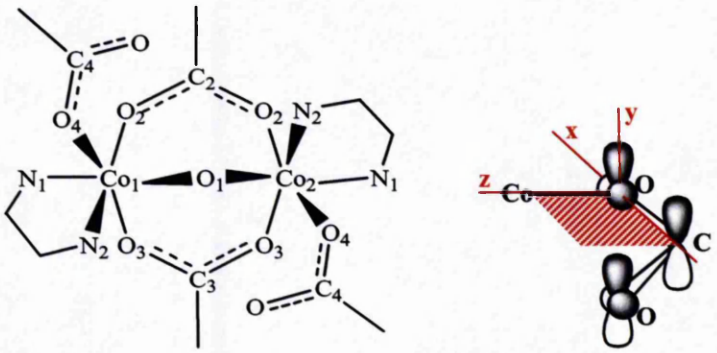

Figure VI.16: Schematic diagram showing the nomenclature of the two cobalt(II) centres and the orientation of the π-orbitals of the carboxylate oxygen atoms in **5**.

The polar coordinates of the different atoms within the principal *XYZ* axes system are listed in Table VI.2.

Ligand	θ	ϕ	ψ
H_2O-O1	149.15	58.91	0
ac-O2	60.16	73.79	333.883254
ac-O3	80.85	334.38	62.975950
ac-O4	121.56	249.00	14.270133
N1	30.99	234.59	0
N2	89.53	161.57	0

Dummy	θ	ϕ
ac-C2	75.51	66.21
ac-C3	88.65	349.20
ac-C4	138.99	255.72

Cobalt centre 1

Ligand	θ	ϕ	ψ
H_2O-O1	89.75	203.74	0
ac-O2	34.41	114.71	111.033106
ac-O3	58.41	299.57	241.103696
ac-O4	122.19	116.58	123.469742
N1	92.51	25.86	0
N2	148.42	306.95	0

Dummy	θ	ϕ
ac-C2	31.95	145.14
ac-C3	51.82	281.40
ac-C4	110.28	133.83

Cobalt centre 2

Table VI.2: Polar coordinates defining the ligand positions of **5** within the framework of the principal magnetic axes *XYZ* and atom labelling in Figure VI.16.

$[(CH_3)_2NH_2][Ga_7CoF_8(O_2CC(CH_3)_3)_{16}]$ (12)

Compound **12** crystallizes in the tetragonal space group I4, where the magnetic axes are defined as $XY = ab = \perp$ and $Z = c = ||$. Crystallographically the eight membered ring is created by symmetry from only two different metal sites (M1 and M2), which alternate within the ring. AOM calculations have been carried out for both metal sites, because from crystallography it is not known which of the sites is occupied by the cobalt(II) ion. Figure VI.17 and Table VI.3 show the polar coordinates of the different ligands within the framework of the magnetic axis *XYZ*.

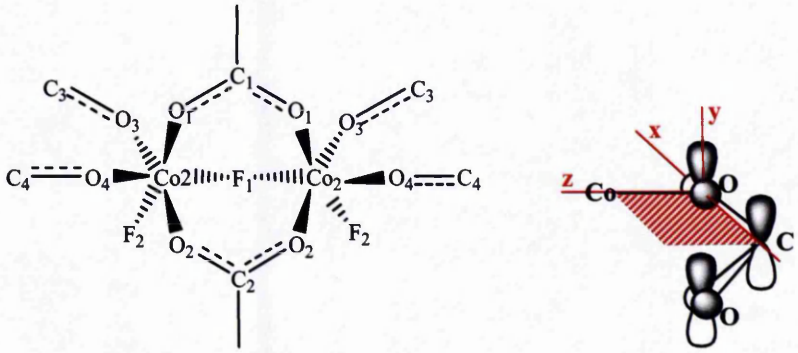

Figure VI.17: Schematic diagram of a ring fraction showing the nomenclature for the two possible cobalt(II) sites and the orientation of the π-orbitals of the carboxylate oxygen in **12**.

Ligand	θ	ϕ	ψ	Dummy	θ	ϕ
piv-O1	68.90	225.34	311.153083	piv-C1	82.46	210.46
piv-O2	159.59	201.68	258.182699	piv-C2	150.43	164.06
piv-O3	22.35	25.36	337.512195	piv-C3	42.08	13.78
piv-O4	98.91	310.29	59.637038	piv-C4	107.32	326.04
F1	82.19	131.09	-	**Cobalt site 1**		
F2	111.56	48.20	-			

Ligand	θ	ϕ	ψ	Dummy	θ	ϕ
piv-O1	80.67	264.84	123.124916	piv-C1	70.76	281.70
piv-O2	157.58	342.49	205.298246	piv-C2	138.84	329.78
piv-O3	20.76	157.78	280.388421	piv-C3	29.02	120.98
piv-O4	111.59	180.21	231.010048	piv-C4	98.42	164.67
F1	68.25	2.70	-	**Cobalt site 2**		
F2	97.49	85.96	-			

Table VI.3: Polar coordinates defining the ligand positions of **12** within the framework of the principal magnetic axes *XYZ* and atom labelling in Figure VI.17.

VI.4.2 Calculation of high temperature magnetic properties from AOM eigenvalues

The *AOMX* output contains eigenvalues and eigenfunctions for the 120 energy levels arising from a d^7 *d*-orbital configuration. Calculations were performed for a zero field case, as well as a magnetic field of 0.5 – 7.5 T in steps of 0.5 T oriented along the principal magnetic axes of the molecule (*XYZ*). By *AOMX* default, all eigenvalues are defined by the lowest energy ($E_1 = 0$ always) resulting in a deformed Zeeman splitting in an energy *vs.* magnetic field plot. Therefore, the program was modified slightly to allow for the energies to be defined by the zero field ground state energy for all calculations. Using the *differentiate* tool in *Origin*[143] the first derivative $\partial E_n / \partial \vec{H}$ was calculated from the Zeeman splitting. Equation VI.1 shows the *Origin* algorithm applied to calculate the derivative function of discrete data points.

$$f'(x_i) = \frac{1}{2}\left(\frac{y_{i+1} - y_i}{x_{i+1} - x_i} + \frac{y_i - y_{i-1}}{x_i - x_{x-1}}\right) \qquad \text{(VI.1)}$$

The magnetic properties were calculated from Equations II.4 and II.5 in a self-written routine in *Mathematica*[111] (Appendix 2.1 and accompanying disc). No magnetic exchange interactions were introduced at this stage. At high temperature weak magnetic exchange is masked by equal population of low lying energy levels, and the high temperature susceptibility of the dimetallics was calculated as a simple sum of the contributions from the two cobalt(II) ions.

VI.4.3 Calculation of the low temperature magnetic properties of antiferromagnetically coupled heterometallic rings.

In Section IV.3.1 the magnetic properties of heterometallic chromium-nickel rings have been simulated using *MAGPACK*.[130] To account for the different Zeeman splitting of different spin-states obtained experimentally with EPR spectroscopy, the

low temperature magnetic properties of the rings have been calculated manually using *Origin*. *MAGPACK* provides eigenvalues of all effective spin-states arising from the magnetic coupling of the eight (or nine) magnetic ions. Table VI.4 shows the four lowest energy levels for the three compounds Cr_7Ni (**15**), Cr_6Ni_2 (**17**) and Cr_7Ni_2 (**19**).

	model	E_1 / cm^{-1}	$S_{eff,1}$	E_2 / cm^{-1}	$S_{eff,2}$	E_3 / cm^{-1}	$S_{eff,3}$	E_4 / cm^{-1}	$S_{eff,4}$
Cr_7Ni		0	$^1/_2$	9.65	$^3/_2$	23.54	$^1/_2$	25.66	$^5/_2$
Cr_6Ni_2	same sub-lattice	0	1	12.66	2	18.04	0	20.04	0
	different sub-lattices	0	0	6.47	1	19.40	2	27.26	1
Cr_7Ni_2	A	0	$^1/_2$	3.00	$^1/_2$	10.93	$^3/_2$	12.10	$^3/_2$
	B	0	$^1/_2$	4.87	$^3/_2$	9.32	$^1/_2$	12.59	$^3/_2$
	C	0	$^1/_2$	6.67	$^1/_2$	9.57	$^3/_2$	11.71	$^3/_2$
	D	0	$^1/_2$	6.70	$^3/_2$	8.48	$^1/_2$	12.51	$^3/_2$

Table VI.4: Four lowest effective spin-states and eigenvalues of the chromium-nickel rings arising from the antiferromagnetic coupling of the metal ions. Calculations were performed using *MAGPACK* with an isotropic exchange parameter J = -5.8 cm^{-1}.

For each energy level the isotropic field dependence was calculated from Equation VI.2 using the appropriate g_{eff}-value determined by EPR spectroscopy for the particular spin-state.

$$E = \mu_B \vec{B} m_{Seff} g_{eff} \qquad \text{(VI.2)}$$

The first derivative $\frac{\partial E}{\partial \vec{B}}$ was calculated from Equation VI.1 and the magnetic properties from Equations II.4 and II.5.

References

[1] F. E. Mabbs, D. J. Machin, *Magnetism and Transition Metal Complexes*, Chapman and Hall, London, **1973**.

[2] O. Kahn, *Molecular Magnetism*, VCH, New York, Weinheim, Cambridge, **1993**.

[3] F. E. Mabbs, D. Collison, *Electron Paramagnetic Resonance of d Transition Metal Compounds*, Elsevier, Amsterdam, **1992**.

[4] R. Sessoli, D. Gatteschi, A. Caneschi, M. A. Novak, *Nature* **1993**, *365*.

[5] L. Thomas, F. Lionti, R. Ballou, D. Gatteschi, R. Sessoli, B. Barbara, *Nature* **1996**, *383*, 145.

[6] C. Coulon, H. Miyasaka, R. Clérac, *Struct. Bond.* **2006**, *122*, 163.

[7] A. Caneschi, D. Gatteschi, N. Lalioti, R. Sessoli, L. Sorace, V. Tangoulis, A. Vindigni, *Chem. Eur. J.* **2002**, 286.

[8] D. M. Low, L. F. Jones, A. Bell, E. K. Brechin, T. Mallah, E. Riviere, S. J. Teat, E. J. L. McInnes, *Angew. Chem. Int. Ed.* **2003**, *42*, 3781.

[9] R. Shaw, R. H. Laye, L. F. Jones, D. M. Low, C. Talbot-Eeckelaers, Q. Wei, C. J. Milios, S. J. Teat, M. Helliwell, J. Raftery, M. Evangelisti, M. Affronte, D. Collison, E. K. Brechin, E. J. L. McInnes, *Inorg. Chem.* **2007**, *46*, 4968.

[10] M. Evangelisti, A. Candini, A. Ghirri, M. Affronte, S. Piligkos, E. K. Brechin, E. J. L. McInnes, *Polyhedron* **2005**, *24*, 2573.

[11] R. Shaw, I. S. Tidmarsh, R. H. Laye, B. Breeze, M. Helliwell, E. K. Brechin, S. L. Heath, M. Murrie, S. Ochsenbein, H. U. Güdel, E. J. L. McInnes, *J. Chem. Soc., Chem. Commun.* **2004**, 1418.

[12] L. Lisnard, F. Tuna, A. Candini, M. Affronte, R. E. P. Winpenny, E. J. L. McInnes, *Angew. Chem. Int. Ed.* **2008**, *47*, 9695.

[13] S. Carretta, P. Santini, G. Amoretti, M. Affronte, A. Candini, I. S. Tidmarsh, R. H. Laye, E. J. L. McInnes, *Phys. Rev. Lett.* **2006**, *97*, 207201.

[14] J. Tang, I. Hewitt, N. T. Madhu, G. Chastanet, W. Wernsdorfer, C. E. Anson, C. Benelli, R. Sessoli, A. K. Powell, *Angew. Chem. Int. Ed.* **2006**, *45*, 1729.

[15] J. Luzon, K. Bernot, I. J. Hewitt, C. E. Anson, A. K. Powell, R. Sessoli, *Phys. Rev. Lett.* **2008**, *100*, 247205.

[16] M. Trif, F. Troiani, D. Stepanenko, D. Loss, *Phys. Rev. Lett.* **2008**, *101*, 217201.

[17] S. J. Langley, M. Helliwell, R. Sessoli, P. Rosa, W. Wernsdorfer, R. E. P. Winpenny, *Chem. Commun.* **2005**, 5029.

[18] K. W. Galloway, A. M. Whyte, W. Wernsdorfer, J. Sanchez-Benitez, K. V. Kamenev, A. Parkin, R. D. Peacock, M. Murrie, *Inorg. Chem.* **2008**, *47*, 7438.

[19] A. Wilson, E. C. Yang, D. N. Hendrickson, S. Hill, *Polyhedron* **2007**, *26*, 2065.

[20] A. L. Barra, A. Caneschi, A. Cornia, D. Gatteschi, L. Gorini, L. P. Heiniger, R. Sessoli, L. Soracet, *J. Am. Chem. Soc.* **2007**, *129*, 10754.

[21] A. Wilson, J. Lawrence, E. C. Yang, M. Nakano, D. N. Hendrickson, S. Hill, *Phys. Rev. B* **2006**, *74*.

[22] B. N. Figgis, M. A. Hitchman, *Ligand Field Theory and Its Applications*, Wiley-VCH, New York, **2000**.

[23] J. S. Griffith, *The Theory of Transition-Metal Ions*, Cambridge University Press, Cambridge, **1961**.

[24] C. J. Ballhausen, *Introduction to Ligand Field Theory*, McGraw-Hill Book Company, Inc., New York, **1962**.

[25] M. E. Lines, *J. Chem. Phys.* **1971**, *55*, 2977.

[26] C. E. Schäffer, C. K. Jørgensen, *Mol. Phys.* **1965**, *9*, 401.

[27] M. Gerloch, *Magnetism and Ligand-field Analysis*, Cambridge University Press, Cambridge, **1983**.

[28] A. Bencini, C. Benelli, D. Gatteschi, *Coord. Chem. Rev.* **1984**, *60*, 131.

[29] D. Reinen, *Coord. Chem. Rev.* **1998**, *175*, 91.

[30] P. E. Hoggard, *Coord. Chem. Rev.* **1986**, *70*, 85.

[31] A. Bencini, I. Ciofini, M. G. Uytterhoeven, *Inorg. Chim. Acta* **1998**, *274*, 90.

[32] J.-N. Rebilly, G. Charron, E. Revière, R. Guillot, A.-L. Barra, M. D. Serrano, J. van Slageren, T. Mallah, *Chem. Eur. J.* **2008**, *14*, 1169.

[33] G. Charron, F. Bellot, F. Cisnetti, G. Pelosi, J.-N. Rebilly, E. Revière, A.-L. Barra, T. Mallah, C. Policar, *Chem. Eur. J.* **2007**, *13*, 2774.

[34] T. B. Mikhailova, I. G. Fomina, A. A. Sidorov, I. F. Golovaneva, G. G. Aleksandrov, V. M. Novotortsev, V. N. Ikorskii, I. L. Eremenko, *Russ. J. Inorg. Chem.* **2003**, *48*, 1505.

[35] G. G. Aleksandrov, I. G. Fomina, A. A. Sidorov, T. B. Mikhailove, V. I. Zhilov, V. N. Ikorskii, V. M. Novotortsev, I. L. Eremenko, I. I. Moiseev, *Russ. Chem. Bull., Int. Ed.* **2004**, *53*, 1200.

[36] I. G. Fomina, A. A. Sidorov, G. G. Aleksandrov, V. I. Zhilov, V. N. Ikorskii, V. M. Novotortsev, I. L. Eremenko, I. I. Moiseev, *Russ. Chem. Bull., Int. Ed.* **2004**, *53*, 118.

[37] T. B. Mikhailova, A. E. Malkov, A. A. Sidorov, I. G. Fomina, G. G. Aleksandrov, I. F. Golovaneva, V. M. Demyanovich, V. M. Novotortsev, V. N. Ikorskii, I. L. Eremenko, *Russ. J. Inorg. Chem.* **2002**, *47*, 1680.

[38] U. Turpeinen, R. Hämäläinen, J. Reedijk, *Polyhedron* **1987**, *6*, 1603.

[39] D. A. Brown, W. Errington, W. K. Glass, W. Haase, T. J. Kemp, H. Nimir, S. M. Ostrovsky, R. Werner, *Inorg. Chem.* **2001**, *40*, 5962.

[40] A. D. Brown, W. K. Glass, N. J. Firtzpatrick, T. J. Kemp, W. Errington, G. J. Clarkson, W. Haase, F. Karsten, A. H. Mahdy, *Inorg. Chim. Acta* **2004**, *357*, 1411.

[41] A. D. Brown, W. K. Glass, N. J. Firtzpatrick, T. J. Kemp, W. Errington, G. J. Clarkson, W. Haase, F. Karsten, A. H. Mahdy, *Inorg. Chim. Acta* **2005**, *358*, 2454.

[42] G. de Munno, M. Julve, F. Lloret, J. Faus, A. Caneschi, *J. Chem. Soc., Dalton Trans.* **1994**, 1175.

[43] S. Petit, G. Pilet, D. Luneau, L. F. Chibotaru, L. Ungur, *Dalton Trans.* **2007**, 4582.

[44] O. F. Ikotun, W. Ouellette, F. Lloret, P. E. Kruger, M. Julve, R. P. Doyle, *Eur. J. Inorg. Chem.* **2008**, 2691.

[45] S. M. Ostrovsky, K. Falk, J. Pelikan, A. D. Brown, Z. Tomkowicz, W. Haase, *Inorg. Chem.* **2006**, *45*, 688.

[46] S. M. Ostrovsky, R. Werner, D. A. Brown, W. Haase, *Chem. Phys. Lett.* **2002**, *353*, 290.

[47] M. J. Hossain, M. Yamasaki, M. Mikuriya, A. Kuribayashi, H. Sakiyama, *Inorg. Chem.* **2002**, *41*, 4058.

[48] H. Sakiyama, R. Ito, H. Kumagai, K. Inoue, M. Sakamoto, Y. Nishida, M. Yamasaki, *Eur. J. Inorg. Chem.* **2001**, 2027.

[49] E.-C. Yang, D. N. Hendrickson, W. Wernsdorfer, M. Nakano, L. N. Zakharov, R. D. Sommer, A. L. Rheingold, M. Ledezma-Gairaud, G. Christou, *J. Appl. Phys.* **2002**, *91*, 7382.

[50] A. Ferguson, A. Parkin, J. Sanchez-Benitez, K. Kamenev, W. Wernsdorfer, M. Murrie, *Chem. Commun.* **2007**, 3473.

[51] O. Waldmann, M. Ruben, P. Müller, J. M. Lehn, *Inorg. Chem.* **2006**, *45*, 6535.

[52] P. D. Boyd, M. Gerloch, J. H. Harding, R. G. Woolley, *Proc. Roy. Soc. Lond. A.* **1978**, *360*, 191.

[53] F. Lloret, M. Julve, J. Cano, R. Ruiz-García, P. Emilio, *Inorg. Chim. Acta* **2008**, *361*, 3432.

[54] O. Fabelo, J. Pasán, F. Lloret, M. Julve, C. Ruiz-Pérez, *Inorg. Chem.* **2008**, *47*, 3568.

[55] H. Sakiyama, *Inorg. Chim. Acta* **2006**, *359*, 2097.

[56] H. Sakiyama, R. Ito, H. Kumagai, K. Inoue, M. Sakamoto, Y. Nishida, M. Yamasaki, *Eur. J. Inorg. Chem.* **2001**, 2705.

[57] H. Sakiyama, *J. Chem. Software* **2001**, *7*, 171.

[58] K. Tone, H. Sakiyama, M. Mikuriya, M. Yamasaki, Y. Nishida, *Inorg. Chem. Commun.* **2007**, *10*, 944.

[59] A. V. Palii, B. S. Tsukerblat, E. Coronado, J. M. Clemente-Juan, J. J. Borrás-Almenar, *Inorg. Chem.* **2003**, *42*, 2455.

[60] J. M. Clemente, H. Andres, M. Aebersold, J. J. Borrás-Almenar, E. Coronado, H. U. Güdel, H. Büttner, G. Kearly, *Inorg. Chem.* **1997**, *36*, 2244.

[61] J. M. Clemente-Juan, E. Coronado, A. Gaita-Ariño, C. Giménez-Saiz, H. U. Güdel, A. Sieber, R. Bircher, H. Mutka, *Inorg. Chem.* **2005**, *44*, 3389.

[62] C. J. Gómez-García, E. Coronado, J. J. Borrás-Almenar, M. Aebersold, H. U. Güdel, H. Mutka, *Physica B* **1992**, *180 & 181*, 238.

[63] H. Andres, J. M. Clemente-Juan, R. Basler, M. Aebersold, H.-U. Güdel, J. J. Borrás-Almenar, A. Gaita, E. Coronado, H. Büttner, S. Janssen, *Inorg. Chem.* **2001**, *40*, 1943.

[64] H. Andres, J. M. Clemente-Juan, M. Aebersold, H. U. Güdel, E. Coronado, H. Büttner, G. Kearly, J. Melero, R. Burriel, *J. Am. Chem. Soc.* **1999**, *121*, 10028.

[65] J. M. Clemente-Juan, E. Coronado, A. Forment-Aliaga, J. Galán-Mascarós, C. Giménez-Saiz, C. J. Gómez-García, *Inorg. Chem.* **2004**, *43*.

[66] J. J. Borrás-Almenar, J. M. Clemente-Juan, E. Coronado, A. V. Palii, B. S. Tsukerblat, *Chem. Phys.* **2001**, *274*, 131.

[67] J. J. Borrás-Almenar, J. M. Clemente-Juan, E. Coronado, A. V. Palii, B. S. Tsukerblat, *Chem. Phys.* **2001**, *274*, 145.

[68] A. V. Palii, B. S. Tsukerblat, E. Coronado, J. M. Clemente-Juan, J. J. Borrás-Almenar, *Polyhedron* **2003**, *22*, 2537.

[69] A. V. Palii, B. S. Tsukerblat, E. Coronado, J. M. Clemente-Juan, J. J. Borrás-Almenar, *J. Chem. Phys.* **2003**, *118*, 5566.

[70] L. F. Chibotaru, L. Ungur, C. Aronica, H. Elmoll, G. Pilet, D. Luneau, *J. Am. Chem. Soc.* **2008**, *130*, 12445.

[71] P. D. Boyd, M. Gerloch, J. H. Harding, R. G. Woolley, *Proc. Roy. Soc. Lond. A.* **1978**, *360*, 161.

[72] M. Gerloch, J. H. Harding, *Proc. Roy. Soc. Lond. A.* **1978**, *360*, 211.

[73] F. K. Larsen, E. J. L. McInnes, H. El Mkami, J. Overgaard, S. Piligkos, G. Rajaraman, E. Rentschler, A. A. Smith, G. M. Smith, V. Boote, M. Jennings, G. A. Timco, R. E. P. Winpenny, *Angew. Chem. Int. Ed.* **2003**, *42*, 101.

[74] R. H. Laye, F. K. Larsen, J. Overgaard, C. A. Muryn, E. J. L. McInnes, E. Rentschler, V. Sanchez, S. J. Teat, H. U. Güdel, O. Waldmann, G. A. Timco, R. E. P. Winpenny, *Chem. Commun.* **2005**, 1125.

[75] E. J. L. McInnes, S. Piligkos, G. A. Timco, R. E. P. Winpenny, *Coord. Chem. Rev.* **2005**, *249*, 2577.

[76] F. K. Larsen, J. Overgaard, S. Parson, E. Rentschler, A. A. Smith, G. A. Timco, R. E. P. Winpenny, *Angew. Chem. Int. Ed.* **2003**, *42*, 5978.

[77] M. Affronte, S. Carretta, G. A. Timco, R. E. P. Winpenny, *Chem. Commun.* **2007**, 1789.

[78] A. Ghirri, A. Candini, M. Evangelisti, M. Affronte, S. Carretta, P. Santini, G. Amoretti, R. S. G. Davies, G. A. Timco, R. E. P. Winpenny, *Phys. Rev. B* **2007**, *76*, 214405.

[79] M. Affronte, A. Ghirri, G. Amoretti, S. Carretta, S. Piligkos, G. A. Timco, R. E. P. Winpenny, *Appl. Phys. Lett.* **2004**, *84*, 3468.

[80] M. Affronte, F. Troiani, A. Ghirri, A. Candini, M. Evangelisti, S. Carretta, P. Santini, G. Amoretti, S. Piligkos, G. A. Timco, R. E. P. Winpenny, *Polyhedron* **2005**, *24*, 2562.

[81] R. E. P. Winpenny, *Angew. Chem. Int. Ed.* **2008**, *47*, 7992.

[82] F. Maier, J. Levy, D. Loss, *Phys. Rev. Lett.* **2003**, *90*, 047901.

[83] F. Maier, J. Levy, D. Loss, *Phys. Rev. B* **2003**, *68*, 134417.

[84] V. Corradini, R. Biagi, U. del Pennino, V. De Renzi, A. Gambardella, M. Affronte, C. A. Muryn, G. A. Timco, R. E. P. Winpenny, *Inorg. Chem.* **2007**, *46*, 4937.

[85] A. Ardavan, O. Rival, J. J. L. Morton, S. J. Blundell, A. M. Tyryshkin, G. A. Timco, R. E. P. Winpenny, *Phys. Rev. Lett.* **2007**, *98*.

[86] M. Affronte, I. Casson, M. Evangelisti, A. Candini, S. Carretta, C. A. Muryn, S. J. Teat, G. A. Timco, W. Wernsdorfer, R. E. P. Winpenny, *Angew. Chem. Int. Ed.* **2005**, *44*, 6496.

[87] G. A. Timco, S. Carretta, F. Troiani, F. Tuna, R. J. Pritchard, C. A. Muryn, E. J. L. McInnes, A. Ghirri, A. Candini, P. Santini, G. Amoretti, M. Affronte, R. E. P. Winpenny, *Nat. Nanotechnol.* **2009**, *4*, 173.

[88] G. A. Timco, E. J. L. McInnes, R. J. Pritchard, F. Tuna, R. E. P. Winpenny, *Angew. Chem. Int. Ed.* **2008**, *47*.

[89] S. Piligkos, E. Bill, D. Collison, E. J. L. McInnes, G. A. Timco, H. Weihe, R. E. P. Winpenny, F. Neese, *J. Am. Chem. Soc.* **2007**, *129*, 760.

[90] F. Troiani, A. Ghirri, M. Affronte, S. Carretta, P. Santini, G. Amoretti, S. Piligkos, G. A. Timco, R. E. P. Winpenny, *Phys. Rev. Lett.* **2005**, *94*, 207208.

[91] S. Piligkos, H. Weihe, E. Bill, F. Neese, H. El Mkami, G. M. Smith, D. Collison, G. Rajaraman, G. A. Timco, R. E. P. Winpenny, E. J. L. McInnes, *Chem. Eur. J.* **2009**, *15*, 3152.

[92] R. Caciuffo, T. Guidi, G. Amoretti, S. Carretta, E. Liviotti, P. Santini, C. Mondelli, G. A. Timco, C. A. Muryn, R. E. P. Winpenny, *Phys. Rev. B* **2005**, *71*, 174407.

[93] S. Carretta, P. Santini, G. Amoretti, T. Guidi, J. R. D. Copley, Y. Qiu, R. Caciuffo, G. A. Timco, R. E. P. Winpenny, *Phys. Rev. Lett.* **2007**, *98*, 167401.

[94] V. Corradini, F. Moro, R. Biagi, U. del Pennino, V. De Renzi, S. Carretta, P. Santini, M. Affronte, J. C. Cezar, G. A. Timco, R. E. P. Winpenny, *Phys. Rev. B* **2008**, *77*, 014402.

[95] F. Palacio, E. Ressouche, J. Schweizer, *"Introduction to Physical Techniques in Molecular Magnetism*, Servicio de Publicaciones de la Universidad de Zaragoza, Zaragoza, **1999**.

[96] A. Cornia, A. G. M. Jansen, M. Affronte, *Phys. Rev. B* **1999**, *60*, 12177.

[97] A. Cornia, M. Affronte, A. G. M. Jansen, D. Gatteschi, A. Caneschi, R. Sessoli, *Chem. Phys. Lett.* **2000**, *322*, 477.

[98] F. Hippert, E. Geissler, J. L. Hodeau, E. Lelievre-Berna, J. R. Regnard, *Neutron and X-ray spectroscopy*, Springer, Heidelberg, **2006**.

[99] S. W. Lovesey, *Theory of neutron scattering from condensed matter Vol. 2*, Clarendon Press, Oxford, **1984**.

[100] S. W. Lovesey, *Theory of neutron scattering from condensed matter Vol. 1*, Clarendon Press, Oxford, **1984**.

[101] G. L. Squires, *Introduction to the theory of thermal neutron scattering*, Cambridge University Press, Cambridge, **1978**.

[102] R. Basler, C. Boskovic, G. Chabousant, H. U. Güdel, M. Murrie, S. Ochsenbein, A. Sieber, *Chem. Phys. Chem.* **2003**, *4*, 910.

[103] T. Unruh, J. Neuhaus, W. Petry, *Nucl. Instrum. Meth. A* **2007**, *580*, 1414.

[104] D. J. Mackey, S. V. Evans, R. F. McMeeking, *J. Chem. Soc., Dalton Trans.* **1978**, 160.

[105] C. J. O'Connor, E. Sinn, T. L. Fariss, B. S. J. Deaver, *J. Phys. Chem.* **1982**, *86*, 2369.

[106] K. O. Joung, C. J. O'Connor, R. L. Carlin, *J. Am. Chem. Soc.* **1977**, *99*, 7387.

[107] R. L. Carlin, C. J. O'Connor, S. N. Bhatia, *J. Am. Chem. Soc.* **1976**, *98*, 685.

[108] L. C. Kuo, M. W. Makinen, *J. Am. Chem. Soc.* **1985**, *107*, 5255

[109] H. Adamsky, *AOMX*, Heinrich-Heine-Universität, http://www.aomx.de/, Düsseldorf, **1996**.

[110] J. Bendix, *LIGFIELD*, University of Copenhagen, Copenhagen.

[111] *Mathematica6*, Wolfram Research, **1988-2008**.

[112] U. Turpeinen, M. Ahlgrén, R. Hämäläinen, *Acta Cryst.* **1982**, *B38*, 1580.

[113] G. Aromí, A. S. Batsanov, P. Christian, M. Helliwell, A. Parkin, S. Parsons, A. A. Smith, G. A. Timco, R. E. P. Winpenny, *Chem. Eur. J.* **2003**, *9*, 5142.

[114] M. Ahlgrén, R. Hämäläinen, U. Turpeinen, *Finn. Chem. Lett* **1983**, 125.

[115] I. D. Brown, K. K. Wu, *Acta Cryst.* **1976**, *B32*, 1957.

[116] J. B. Goodenough, *Magnetism and Chemical Bond*, Interscience Publisher, New York, **1963**.

[117] P. L. Feng, C. C. Beedle, C. Koo, J. Lawrence, S. Hill, D. N. Hendrickson, *Inorg. Chim. Acta* **2008**, *361*, 3465.

[118] J. Liu, S. Datta, E. Bolin, J. Lawrence, C. C. Beedle, E.-C. Yang, P. Goy, D. N. Hendrickson, S. Hill, *unpublished results*.

[119] J. Lawrence, C. C. Beedle, E. C. Yang, J. Ma, S. Hill, D. N. Hendrickson, *Polyhedron* **2007**, *26*, 2299.

[120] S. Maccagnano, A. R., E. Negusse, A. Lussier, M. M. Mola, S. Hill, N. S. Dalal, *Polyhedron* **2001**, *20*, 1441.

[121] H. U. Güdel, A. Furrer, J. K. Kjems, *J. Magnetism Magnetic Mat.* **1986**, *54-57*, 1453.

[122] H. U. Güdel, A. Furrer, W. Bührer, B. Hälg, *Surf. Sci.* **1981**, *106*, 432.

[123] J. T. Haraldsen, T. Barnes, J. L. Musfeldt, *Phys. Rev. B* **2005**, *71*, 064403.

[124] A. Furrer, H. U. Güdel, *J. Magnetism Magnetic Mat.* **1979**, *14*, 256.

[125] R. Basler, G. Chabousant, A. Sieber, H. Andres, M. Murrie, P. Kögerler, H. Bögge, D. C. Crans, E. Krickemeyer, S. Janssen, H. Mutka, A. Müller, H. U. Güdel, *Inorg. Chem.* **2002**, *41*, 5675.

[126] J. M. Bradley, A. J. Thomson, E. J. L. McInnes, R. E. P. Winpenny, G. A. Timco, *Dalton Trans.* **2008**, 3311.

[127] S. Piligkos, *Ph.D. Thesis*, The University of Manchester (Manchester, UK), **2004**.

[128] M. Baker, P. Tregenna-Piggott, H. U. Güdel, T. Guidi, *unpublished results*.

[129] O. Cador, D. Gatteschi, R. Sessoli, A.-L. Barra, G. A. Timco, R. E. P. Winpenny, *J. Magnetism Magnetic Mat.* **2005**, *290-291*, 55.

[130] J. J. Borrás-Almenar, J. M. Clemente-Juan, E. Coronado, B. S. Tsukerblat, *MAGPACK*, juan.j.borras@uv.es; juan.m.clemente@uv.es, Valencia, **2000**.

[131] H. Weihe, *EPR Sim*, weihe@kiku.dk, Copenhagen, **2003**.

[132] A. Bencini, D. Gatteschi, *EPR of Exchange Coupled Systems*, Springer, Heidelberg, **1990**.

[133] A. Caneschi, A. Cornia, S. F. Fabretti, D. Gatteschi, R. Grandi, L. Schenetti, *Chem. Eur. J.* **1996**, *2*, 1379.

[134] J. van Slageren, R. Sessoli, D. Gatteschi, A. A. Smith, M. Helliwell, R. E. P. Winpenny, A. Cornia, A.-L. Barra, A. G. M. Jansen, E. Rentschler, G. A. Timco, *Chem. Eur. J.* **2002**, *8*, 277.

[135] M. Shanmugam, L. P. Engelhardt, F. K. Larsen, M. Luban, E. J. L. McInnes, C. A. Muryn, J. Overgaard, E. Rentschler, G. A. Timco, R. E. P. Winpenny, *Chem. Eur. J.* **2006**, *12*, 8267.

[136] E. I. Tolis, L. P. Engelhardt, P. V. Mason, G. Rajaraman, K. Kindo, M. Luban, A. Matsuo, H. Nojiri, J. Raftery, C. Schröder, G. A. Timco, F. Tuna, W. Wernsdorfer, R. E. P. Winpenny, *Chem. Eur. J.* **2006**, *12*, 8961.

[137] Y. V. Yablokov, V. A. Gaponenko, V. V. Zelentsov, K. M. Suvorova, *Solid State Commun.* **1974**, *14*, 131.

[138] E. C. Sañudo, T. B. Faust, C. A. Muryn, R. G. Prichard, G. A. Timco, R. E. P. Winpenny, *submitted to Inorg. Chem.* **2009**.

[139] *SHELX-PC Package*, Bruker Analytical X-Ray Systems, Madison, WI, **1998**.

[140] *IDA*, Interactive Data Analysis, http://iffwww.iff.kfa-juelich.de/~wuttke/frida2.git/.

[141] *CrysAlisRED*, Xcalibur(TM), Oxford Diffraction, **1995-2008**.

[142] *Mercury*, CCDC, http://www.ccdc.cam.ac.uk/mercury/, Cambridge, **2001-2007**.

[143] *OriginPro8*, OriginLab Corporation, Northampton, **1991-2008**.

[144] B. S. Furniss, A. J. Hannaford, P. W. G. Smith, A. R. Tatchell, *Vogel's Textbook of Practical Organic Chemistry*, 2nd ed., Longman Scientific & Technical, New York, **1989**.

[145] B. R. Judd, *Operator Techniques in Atomic Spectroscopy*, Princeton Univerity Press, Princeton, **1963**.

[146] A. Abragam, B. Bleaney, *Electron paramagnetic resonance of transition ions*, Clarendon Press, Oxford, **1970**.

[147] J. A. Larrabee, S.-A. Chyun, A. S. Volwiler, *Inorg. Chem.* **1008**, *47*, 10499.

[148] E. C. Sañudo, C. A. Muryn, M. A. Helliwell, G. A. Timco, W. Wernsdorfer, R. E. P. Winpenny, *Chem. Commun.* **2007**, 801.

[149] G. A. Timco, A. S. Batsanov, F. K. Larsen, C. A. Muryn, J. Overgaard, S. J. Teat, R. E. P. Winpenny, *Chem. Commun.* **2005**, 3649.

Appendix

Appendix 2.1

***Mathematica* routine to calculate the magnetic properties from the eigenvalues calculated with AOMX (Equations II.4 and II.5)**

The routine is set up for the calculation of the molecular magnetic response of a cobalt(II) dimetallic as a simple *addition* (no exchange) of the single ion magnetic responses per cobalt(II) ion. If different orientations of the molecules in the crystal packing give different responses, the total magnetic properties have to be averaged over those molecules. For the calculation of monometallic cobalt(II) compounds only the sections depending on "`CoI1`" are relevant for the calculation.

Input ASCII files (tables):

Eigenvalues: created in *Origin* for each cobalt(II) ion in each field orientation from AOMX output: 3 files *XYZ* per cobalt atom

Magnetic field / G	E_1	E_2	E_n	E_{12}	$\partial E_1/\partial \vec{H}$	$\partial E_2/\partial \vec{H}$	$\partial E_n/\partial \vec{H}$	$\partial E_{12}/\partial \vec{H}$
0	E_1	E_2	...	E_{12}	$\partial E_1/\partial \vec{H}$	$\partial E_2/\partial \vec{H}$	...	$\partial E_{12}/\partial \vec{H}$
5000	E_1	E_2	...	E_{12}	$\partial E_1/\partial \vec{H}$	$\partial E_2/\partial \vec{H}$	...	$\partial E_{12}/\partial \vec{H}$
...	...	...	...	...	...	...	...	...
70000	E_1	E_2	...	E_{12}	$\partial E_1/\partial \vec{H}$	$\partial E_2/\partial \vec{H}$	...	$\partial E_{12}/\partial \vec{H}$

Experimental data: magnetic properties along principal axes: 4 files *XYZ* and average

Temperature / K	χT / cm3 K mol-1		Magnetic field / G	$M/N\mu_B$ 2 K	$M/N\mu_B$ 4 K
0	χT		0	M	M
0.5	χT		5000	M	M
...	...		...	...	...
300	χT		70000	M	M

Output ASCII files (tables):

Calculated magnetic properties along the principal magnetic axis *XYZ* per individual cobalt(II) ions and dimetallic

T / K	χ_x / cm3 mol-1	χT_x / cm3 K mol-1	χ_y / cm3 mol-1	χT_y / cm3 K mol-1	χ_z / cm3 mol-1	χT_z / cm3 K mol-1	χ_{av} / cm3 mol-1	χT_{av} / cm3 K mol-1

H / G	$M_x/N\mu_B$	$M_y/N\mu_B$	$M_z/N\mu_B$	$M_{av}/N\mu_B$

The *Mathematica* code AOM_Magnetism is available on the accompanying disc.

Appendix 3.1

Synthesis of the deuterated dimetallic 3^D and 4^D

High purity cobalt(II) acetate (99.995%), deuterium oxide (99.9 atom % D), pyridine-d_5 (99.5 atom % D), anhydrous toluene and anhydrous acetonitrile were obtained from Aldrich. The preparation of trimethyl-d_9-acetic acid starting from acetone-d_6 was adapted from standard methods.[144]

$[Co_2(D_2O)((O_2CC(CD_3)_3)_4(HO_2CC(CD_3)_3)_4]$ (3^D)

$Co_2D_{74}O_{17}C_{40}H_4$ RM = 1023.4 g mol^{-1} (1027.4 if only D)

3^D was prepared by a variation of the procedure given in reference.[113] All procedures were performed under a dinitrogen atmosphere.

Cobalt(II) acetate (3.0 g, 16.95 mmol) was added to a solution of trimethyl-d_9-acetic acid (15.0 g, 134.9 mmol) in toluene (25 mL) and the mixture was refluxed while stirring for 1h. Subsequently the solvent was evaporated by distillation to remove the acetic acid as the toluene azeotrope. A new portion of toluene (25 mL) was added at this stage and this procedure was repeated three times. Afterwards the flask was kept at 170 ^{0}C in a slow flow of N_2 for 7 h.

Fresh trimethyl-d_9-acetic acid (10.0 g, 89.9 mmol) was added to the resulting residue (blue fine needles microcrystalline product) and the mixture was refluxed for 0.5 h. Then the flask was cooled to 70 °C, deuterium oxide (0.5 g , 25 mmol) was added and the mixture was stirred for 1 h. Subsequently the solution was diluted with acetonitrile (40 mL). After 15 min the final solution was left undisturbed to cool slowly to RT and kept at RT for 2 days. During this time large pink crystals grew from the blue solution. The sealed flask was placed in a fridge at 4 °C for 4 days for further crystallization of the product. Finally, the crystals (including ones suitable for X-ray crystallography) were filtered, washed with a cold acetonitrile (3 × 5 mL) and dried in a slow flow of N_2.

Yield: 6.4g (73.8 % based on Co).

Elemental analysis: calculated: Co: 11.52, C: 46.94 ; found: Co: 11.59, C: 46.82

X-Ray: monoclinic: $P2_1/n$, a = 11.9857 (3) Å, b = 19.1851 (4) Å, c = 22.7530 (5) Å, $\alpha = 90°$, $\beta = 104.142\ (3)°$ $\gamma = 90°$, V = 5240 (9) Å^3, $Z = 4$

A **3D_Co2Piv.cif** file containing the full crystallographic data is available on the accompanying disc.

$[Co_2(D_2O)((O_2CC(CD_3)_3)_4(HO_2CC(CD_3)_3)_2(NC_5D_5)_2]$ (4^D)

$C_{40}D_{66}Co_2N_2O_{13}H_2$ RM = 969.25 g mol^{-1} (971.25 if only D)

4^D was prepared according to the procedure reported by Winpenny *et al.*[113] for $[Co_2(H_2O)((O_2CC(CH_3)_3)_4(HO_2CC(CH_3)_3)_2(py)_2]$ (**4**) starting from deuterated compound 3^D and by using trimethyl-d_9-acetic acid and pyridine-d_5.

Elemental analysis: calculated for 4^D: Co: 12.16, C: 49.57, N: 2.89; calculated for $4^D \cdot D_2O$ $C_{40}D_{67}Co_2N_2O_{14}H_2$: Co: 11.91, C: 48.56, N: 2.83; found: Co: 11.63, C: 48.27, N: 2.76

X-Ray: monoclinic *C2/c*, a = 24.686(5) Å, b = 19.421(5) Å, c = 9.760(5) Å, β = 96.660(5), V = 4647.63(10) Å^3, Z = 4

A **4D_Co2PivPy.cif** file containing the full crystallographic data is available on the accompanying disc.

Appendix 3.2

Molecular structure, crystal packing and unit cell parameters for 6^b, 7, 8 and 9

$[Co_2(H_2O)(OAcCl)_4(tmen)_2]$ (6^b)[112]

P2/n, a = 10.834(3) Å, b = 8.328(3) Å, c = 18.749(3) Å, β = 105.9(2)°, V = 1626.92 Å^3, Z = 2.

Molecular structure and crystal packing of the previously published isomer of **4**. Both cobalt ions are symmetry equivalent.

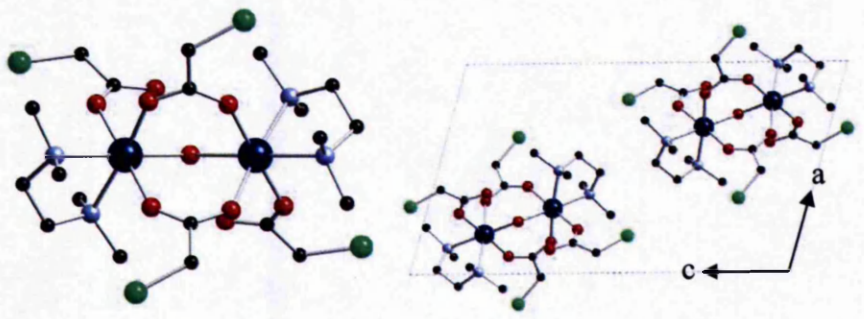

$[Co_2(H_2O)(O_2CCHCl_2)_4(tmen)_2]$ (7)[114]

P-1, a = 9.736(1) Å, b = 11.792(2) Å, c = 16.771(2) Å, α = 78.96(1)°, β = 105.56(1)°, γ= 95.41(1)°, V = 1818.66 Å^3, Z = 2

Molecular structure and crystal packing of **7**:

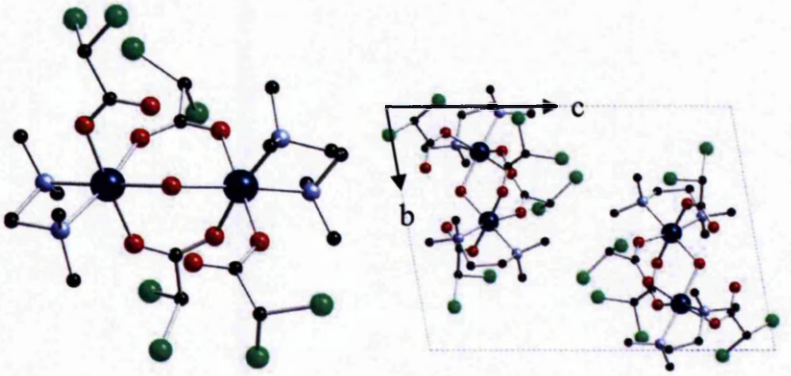

$[Co_2(H_2O)(O_2CC(CH_3)_3)_4(tmen)_2]$ (8)[40]

Reported cell: *P21*/c, a = 11.404(<1) Å, b = 21.870(1) Å, c = 34.735(1) Å, β = 90.12(<1)°, V = 8662.90 Å^3, Z = 8 (full crystallographic data not available on cds)

Found cell: *P21/c*, a = 11.2977(5) Å, b = 21.6976(12) Å, c = 34.4535(18) Å, β = 90° V = 8445.69 Å^3, Z = 8

Molecular structure (asymmetric unit of two molecules) and crystal packing of **8**.

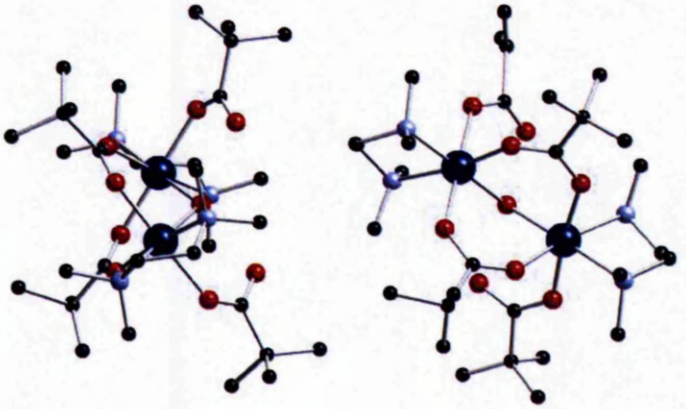

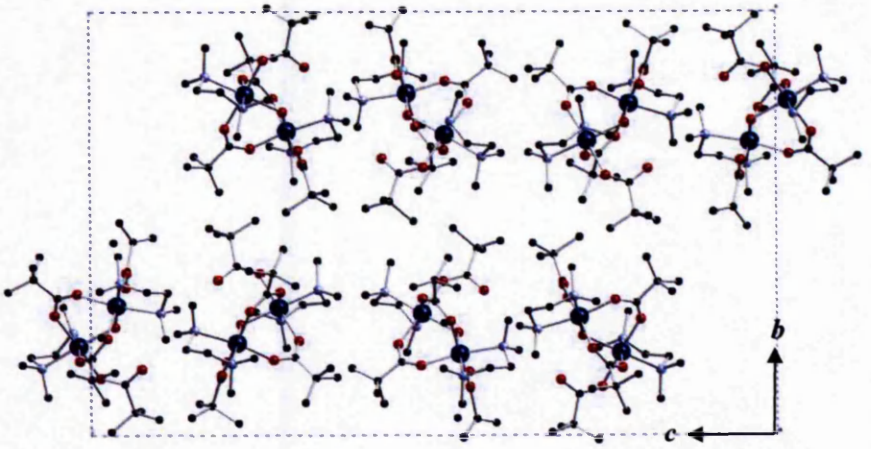

$[Co_2(H_2O)(O_2C(C_6H_5))_4(tmen)_2]$ (9)

P-1, a = 10.7281(3) Å, b = 11.6789(4) Å, c = 17.1733(5) Å, α = 106.092(3)°, β = 91.135(2)° γ = 93.160(2)°, V = 2062.85 Å^3, Z = 2

Molecular structure and crystal packing of **9**:

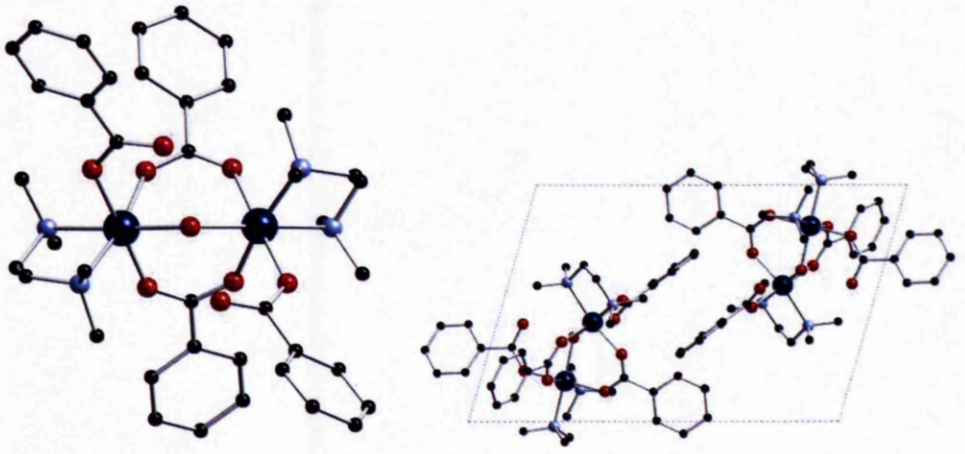

A **9_Co2BenzTmen.cif** file containing the full crystallographic data is available on the accompanying disc.

Appendix 3.3

Temperature dependent susceptibility at 0.1 T and 1 T and field dependent magnetisation at 1.8, 2, 2.2, 3 and 4 K on powder samples of 5, 6, 7, 8 and 9

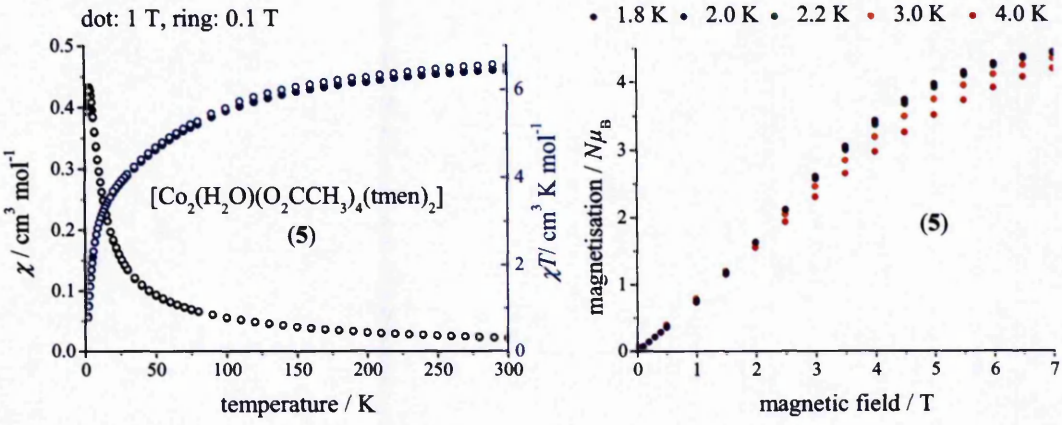

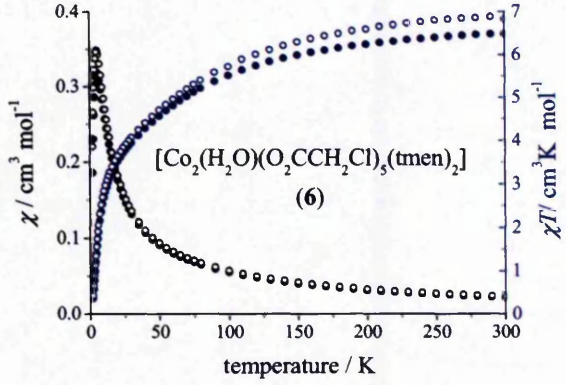

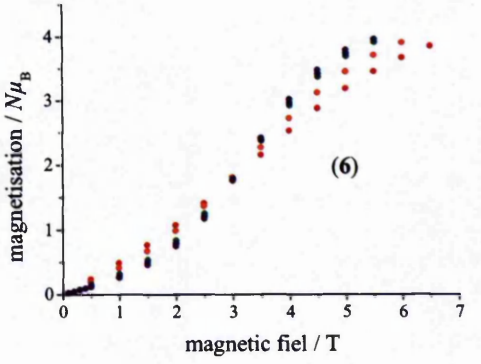

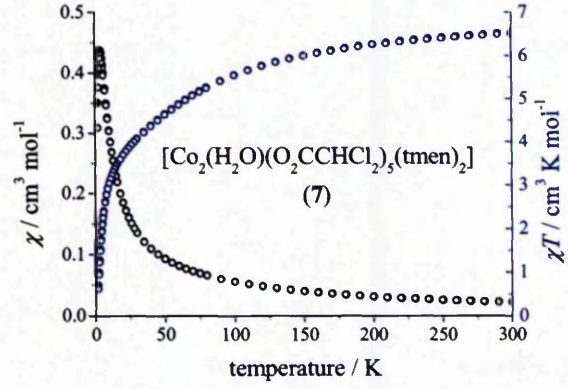

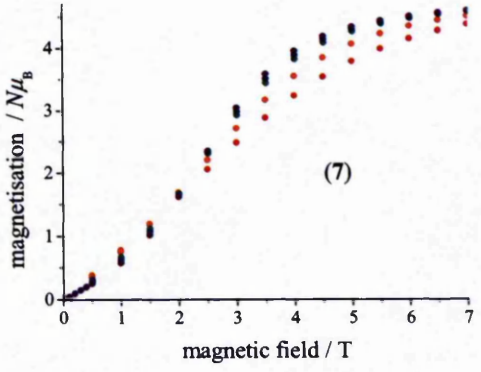

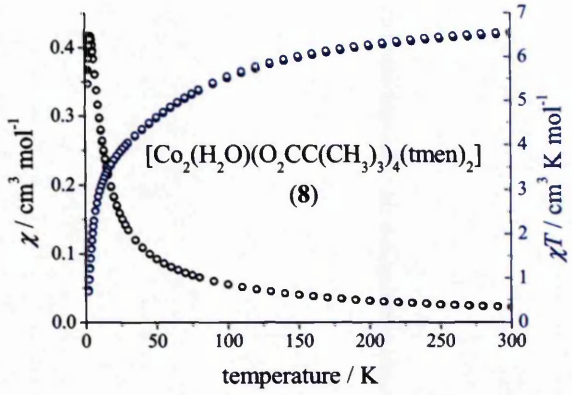

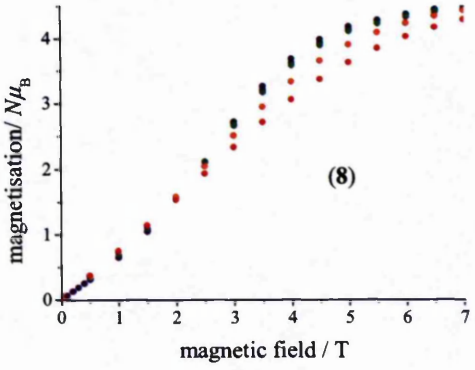

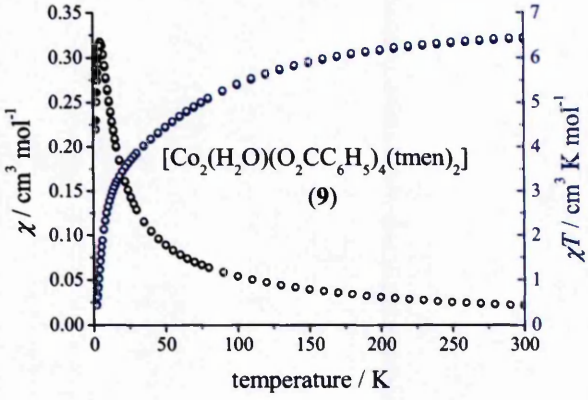

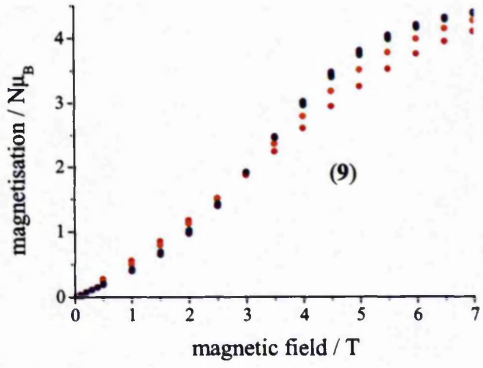

Appendix 3.4

Angular overlap model calculations on 5: Fit to the experimental data and energy diagram for the lowest 6 Kramers doublets per single cobalt(II) ion

Principal average in comparison with the single crystal experiment:

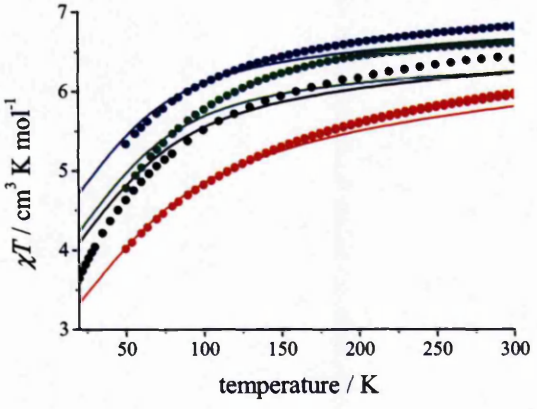

AOM parameters:

Δ_O = 11700 cm^{-1} (MCD of **4**)

e_σ = 4160 cm^{-1} (all)

$e_{\pi x}$ = 300 cm^{-1} (carboxylate)

$e_{\pi y}$ = 500 cm^{-1} (carboxylate)

Racah B = 840 cm^{-1} (MCD of **4**)

Racah C = 3860 cm^{-1} (MCD of **4**)

ξ = 515 cm^{-1} (free ion)

A slightly better agreement is obtained with the same e_π parameters, but a smaller e_σ parameter; however, the ratio of the three AOM parameters was fixed to fit the crystal field splitting obtained experimentally from MCD spectroscopy of **4** (Appendix 3.11).

Contribution of the two independent cobalt(II) ions to the molecular properties along the principal molecular axes:

Molecule 1: dash (contribution doubled), molecule 2: dash-dot (contribution doubled), addition of molecule 1 and 2: solid. (Crystal directions: a = blue, b = green, c = red)

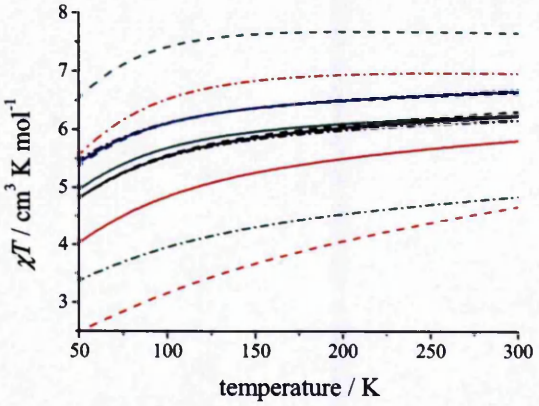

Energy of 6 lowest Kramers doublets (cm^{-1})	
cobalt 1:	cobalt 2:
1390	1381
1248	1269
1077	1035
763	743
159	163
0	0

Zeeman splitting of the lowest Kramers doublets for cobalt 1 (left) and 2 (right):

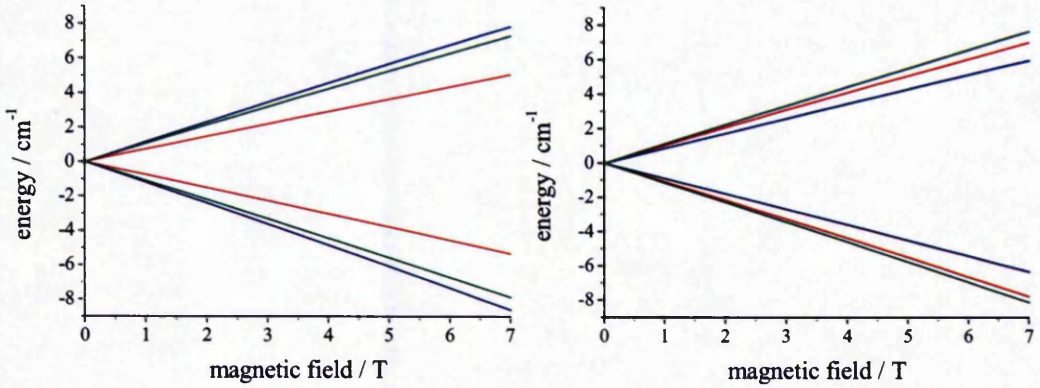

The calculations indicate different "g"-anisotropy for the two single ions, and non-co-linear "**g**"-matrices.

Appendix 3.5

Preliminary *ab-initio* calculations have determined the principal magnetic axes on the single ions in 4.

C_2 symmetry defines the local axis (purple) on the second cobalt(II) ion with respect to the first. Magnetically the resulting two "**g**"-matrices are not co-linear.

Calculations were performed by Professor Liviu Chibotaru and *co*-workers at the University of Leuven / Belgium.

Appendix 3.6

Field dependent magnetisation M_1, M_2 and M_3 of a single crystal sample of 6 at 1.8, 2, 3 and 4 K in the three principal magnetic directions.

The insets show the interpolation of the experimental values to obtain a precise crossing (inflection point) of the four curves.

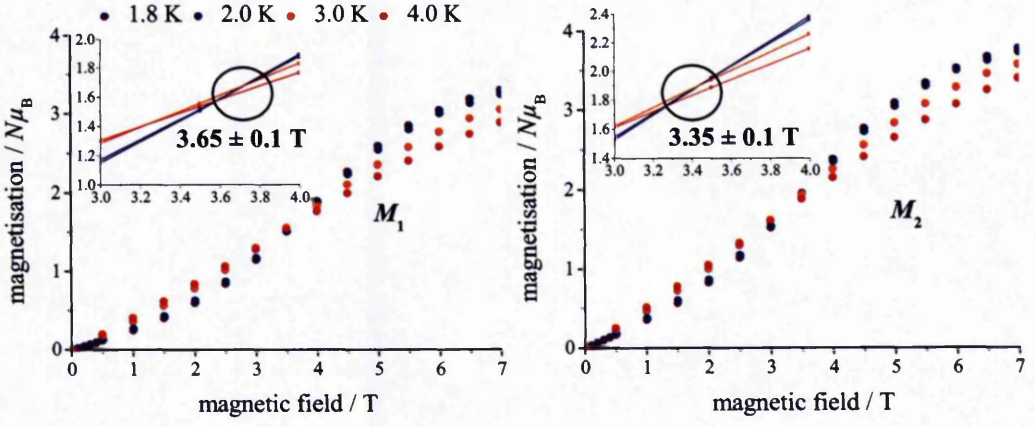

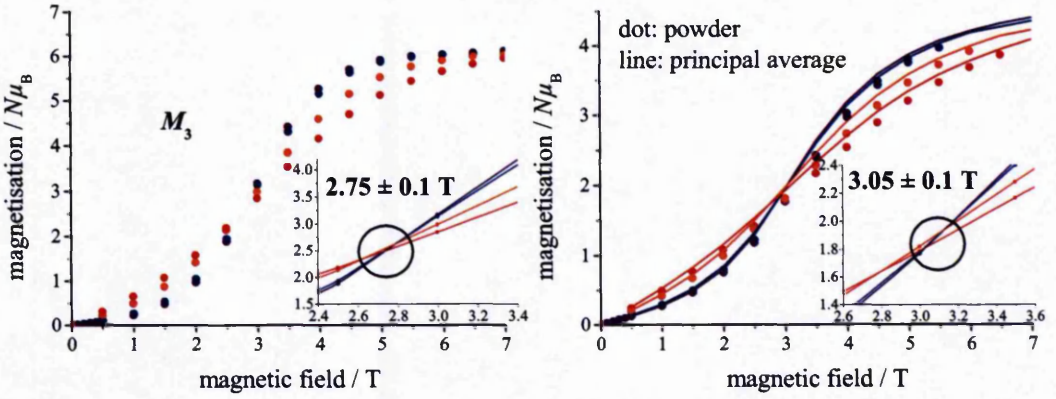

Gaussian variance results 3.25 ± 0.19 T for the principal average.

Appendix 3.7

Normalized EPR spectra of 4 showing the temperature dependence.

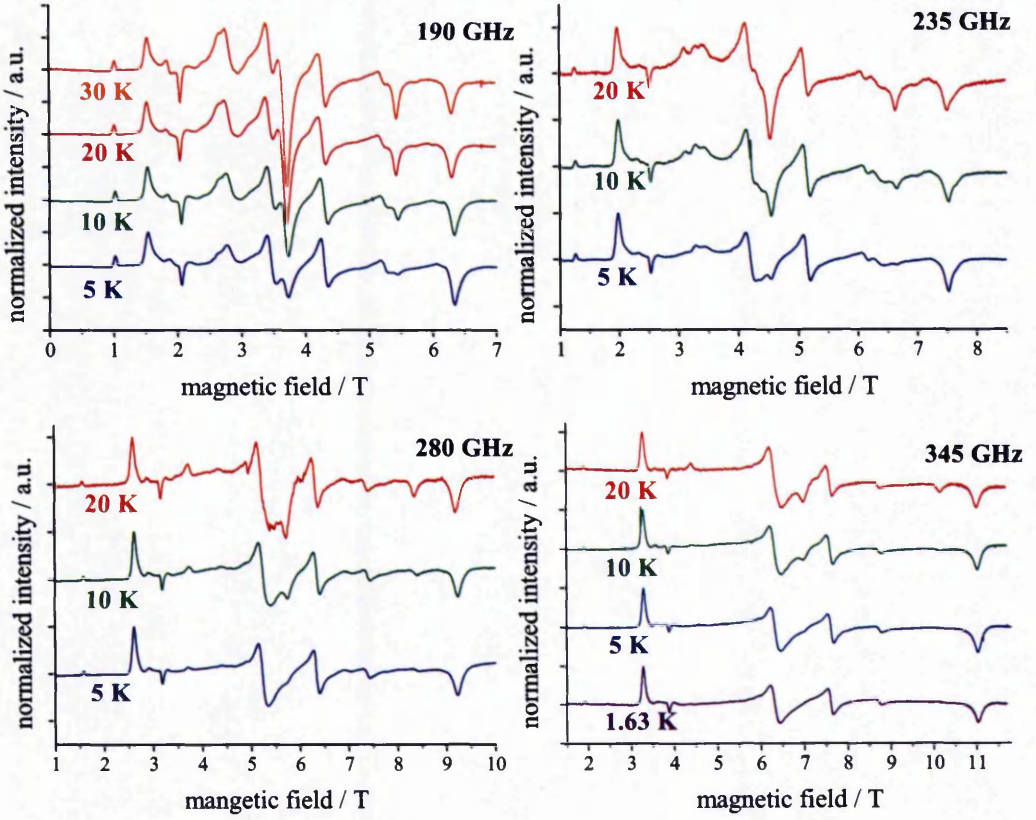

Appendix 3.8

W-band background EPR spectrum at 10 K (manganese signal from the cavity)

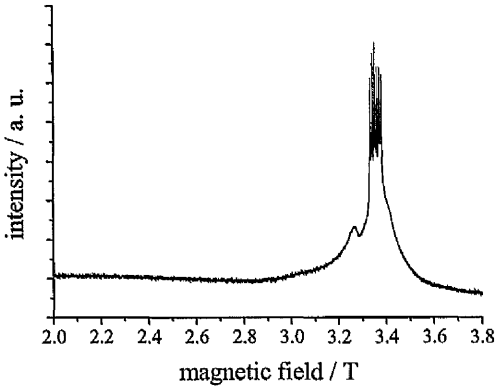

Appendix 3.9

Scattering theory used to calculate the *Q*-dependence of INS transitions in 3^D and 4^D.[99]

The differential neutron scattering for magnetic scattering is given by

$$\frac{d^2\sigma}{d\Omega d\omega} = C\,exp\left(-\frac{E(S)}{k_B T}\right)\sum_{\alpha,\beta}\left(\delta_{\alpha,\beta} - \frac{\vec{Q}_\alpha \vec{Q}_\beta}{\vec{Q}^2}\right)\times \sum_{j,j'} exp\left[i\vec{Q}.(\vec{R}_j - \vec{R}_{j'})\right]$$
$$\times \sum_{M,M'} \langle SM|\hat{S}_j^\alpha|S'M'\rangle\langle S'M'|\hat{S}_j^\alpha|SM\rangle \times \delta\{\hbar\omega + E(S) - E(S')\}$$

where

$$C = \frac{N}{Z}\left(\frac{\gamma e^2}{m_e c^2}\right)^2 \frac{k'}{k} F^2(\vec{Q})\,exp\left[-2W(\vec{Q})\right]$$

N is the total number of dimetallics in the sample, Z the partition function and $\vec{k}$ and $\vec{k}'$ the wave vectors of incoming and scattered neutrons respectively. The scattering vector $\vec{Q}$ is defined as the difference between incoming and scattered neutrons with $\vec{Q} = \vec{k} - \vec{k}'$. $F(\vec{Q})$ is the magnetic form factor, which is conventionally given by numerical approximation of a dipole function.

This is a very crude approximation, because, firstly a dipole approximation is not a good physical description of the interaction between spin-orbit states, and in addition the form factor $F(\vec{Q})$ has a dependence on the orbital angular momentum.

The matrix elements $\langle S'M'|\hat{J}_j^{\alpha}|SM\rangle$ have to be evaluated numerically, using spherical operators, as angular momentum operators are correlated to irreducible tensor operators T of rank 1. The correlation between spin operators and irreducible tensors of rank 1 are given by the following expressions:

$$\hat{T}_j^0 = \hat{S}_j^z \quad \text{and} \quad \hat{T}_j^{\pm 1} = \mp\frac{1}{\sqrt{2}}\left(\hat{S}_j^x \pm i\hat{S}_j^y\right)$$

Use of the Wigner Eckart theorem, allows for the determination of the M dependence of the matrix elements:[145]

$$\langle SM|\hat{T}_j^q|S'M'\rangle = (-1)^{S-M}\begin{pmatrix} S & 1 & S' \\ -M & q & M' \end{pmatrix}\langle S\|\hat{T}_j\|S'\rangle$$

The reduced matrix element $\langle S\|\hat{T}_j\|S'\rangle$ can be expressed as shown below, since the operator $\hat{T}_j$ only operates on the jth part of the coupled system, *i.e.* only operates on one of the two ions in the dimetallic.

$$\langle S_1S_2S\|\hat{T}_1\|S'_1\,S'_2\,S'\rangle = \delta(S_2,S'_2)(-1)^{S_1+S_2+S+1}\times\sqrt{(2S+1)(2S'+1)}\begin{Bmatrix} S & S' & 1 \\ S'_1 & S_1 & S_2 \end{Bmatrix}\langle S_1\|\hat{T}_1\|S'_1\rangle$$

and

$$\langle S_1S_2S\|\hat{T}_2\|S'_1\,S'_2\,S'\rangle = \delta(S_1,S'_1)(-1)^{S_1+S'_2+S+1}\times\sqrt{(2S+1)(2S'+1)}\begin{Bmatrix} S & S' & 1 \\ S'_2 & S_2 & S_1 \end{Bmatrix}\langle S_2\|\hat{T}_2\|S'_2\rangle$$

where

$$\langle S_j\|\hat{T}_j\|S'_j\rangle = \delta(S_j,S'_j)\sqrt{S_j(S_j+1)(2S_j+1)}$$

In both of the above the 3-j and 6-j symbols have been used. These have well defined symmetry properties,[145,146] the result of this is that the selection rules for the transitions are

$$\Delta S = 0,\pm 1 \text{ and } \Delta M = 0, \pm 1$$

Further it can be shown that for $\alpha \neq \beta$ the terms vanish. If we now assume that $S_1 = S_2$, the following equation can be derived.

$$\frac{d^2\sigma}{d\Omega d\omega} = C\,exp\left(-\frac{E(S)}{k_B T}\right)\sum_{\alpha}\left[1-\left(\frac{\vec{Q}_\alpha}{\vec{Q}}\right)^2\right]\frac{2}{3}\left[1+(-1)^{S-S'}\cos(\vec{Q}.\vec{R})\right] \times\left|\left\langle S_1 S_2 S\left\|\hat{T}_1\right\|S'_1 S'_2 S'\right\rangle\right|^2 \delta\{\hbar\omega + E(S) - E(S')\}$$

where $\vec{R} = \vec{R}_1 - \vec{R}_2$.

All experiments were carried out on polycrystalline materials, thus the above expression needs to represent powder average in $\vec{Q}$-space. This yields:

$$\left\langle\frac{d^2\sigma}{d\Omega d\omega}\right\rangle_Q = C\,exp\left(-\frac{E(S)}{k_B T}\right)\frac{4}{3}\left[1+(-1)^{S-S'}\frac{sin\,QR}{QR}\right] \left|\left\langle S_1 S_2 S\left\|\hat{T}_1\right\|S'_1 S'_2 S'\right\rangle\right|^2 \delta\{\hbar\omega + E(S) - E(S')\}$$

Q becomes a scalar, and the term $\left[1+(-1)^{S-S'}\frac{\sin QR}{QR}\right]$ is often referred to as the interference term.

Thus transitions have a Q-dependence that is governed by the inter-ion distance and the spin-state transition.

In an inelastic neutron measurement the structure factor $S(Q, \omega)$ is measured, which is related to the double differential cross section via the following expression.

$$\frac{d^2\sigma}{d\Omega_f dE_f} = N\frac{k_f}{k_i}b^2 S(Q,\omega)$$

Consequently the allowed magnetic transitions for a given model can be predicted on the basis of the selection rules, and on the basis of the Q-dependence the nature of the spin state change can be probed.

Appendix 3.10

Equations for the calculation of the Zeeman splitting in a rhombic triplet[3]

along z:

$$E_1 = -\frac{2}{3}D$$

$$E_2 = \frac{1}{3}D + \sqrt{\left(g_{zz}^2\mu_B^2B^2 + E^2\right)}$$

$$E_3 = \frac{1}{3}D - \sqrt{\left(g_{zz}^2\mu_B^2B^2 + E^2\right)}$$

along x:

$$E_4 = \frac{1}{3}D - E$$

$$E_5 = -\frac{1}{6}D + \frac{1}{2}E + \sqrt{\frac{1}{4}(D+E)^2 + g_{zz}^2\mu_B^2B^2}$$

$$E_6 = -\frac{1}{6}D + \frac{1}{2}E - \sqrt{\frac{1}{4}(D+E)^2 + g_{zz}^2\mu_B^2B^2}$$

along y:

$$E_7 = \frac{1}{3}D + E$$

$$E_8 = -\frac{1}{6}D - \frac{1}{2}E + \sqrt{\frac{1}{4}(D-E)^2 + g_{zz}^2\mu_B^2B^2}$$

$$E_5 = -\frac{1}{6}D - \frac{1}{2}E - \sqrt{\frac{1}{4}(D-E)^2 + g_{zz}^2\mu_B^2B^2}$$

Appendix 3.11

Calculated Q- and W-band transitions in comparison to experimental spectra of compound 4.

Calculation of the Zeeman splitting using the parameters g_{xx} = 3.42, g_{yy} = 6.13, g_{zz} = 2.30, D = 1.2 cm^{-1}, and E = 0.4 cm^{-1} (for equations see Appendix 3.9). The effective singlet level was fixed at 2.4 cm^{-1}.

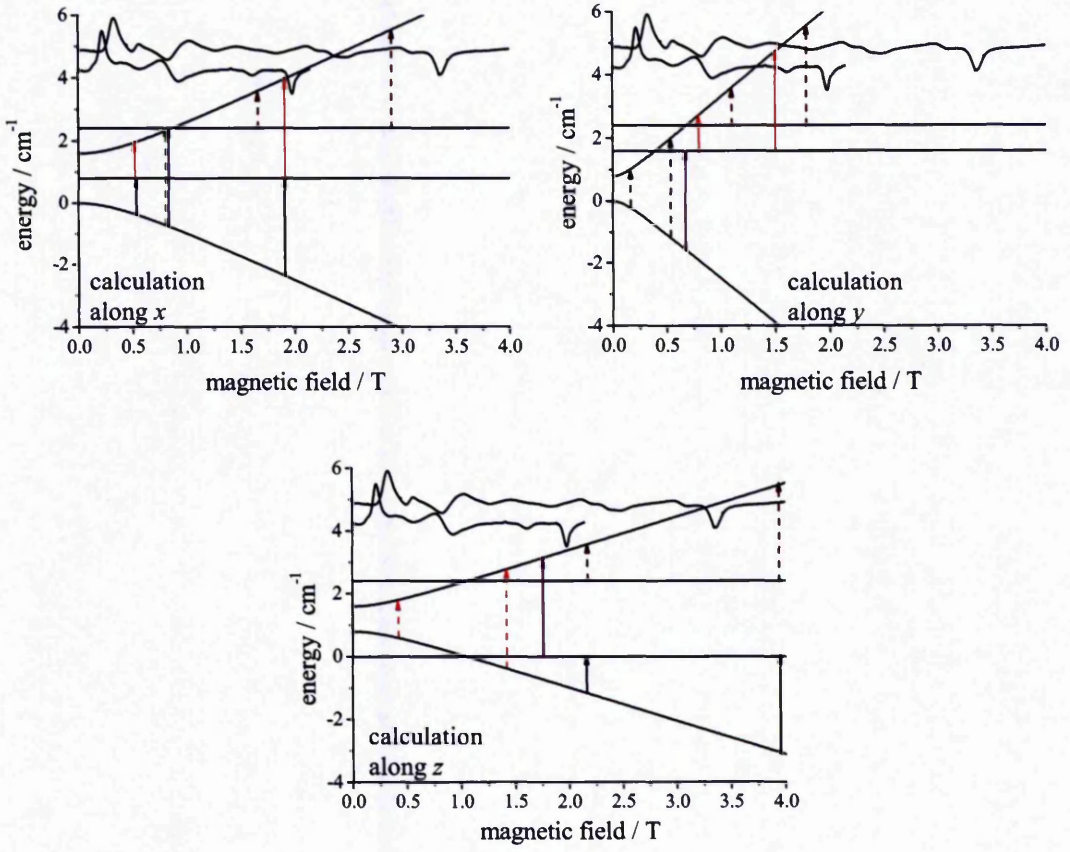

Appendix 3.12

Magnetic circular dichroism spectroscopy of 4

MCD spectra were recorded by Dr. Justin Bradley at the Univerisity of East Anglia / Norwich on samples of **4** mulled in nujol and sandwiched between quartz plates at various fields and temperatures.

Below the room temperature absorption and 1.7 K 5 T MCD spectra across the entire energy range studied is shown. The intensity of the MCD spectrum was converted

into $\Delta\varepsilon$ with ε = extinction coefficient. The calculated $\Delta\varepsilon$ of -3.9 M^{-1} cm^{-1} at 19800 cm^{-1} is in reasonable agreement with reported values for other six coordinated cobalt(II) MCD spectra.[147]

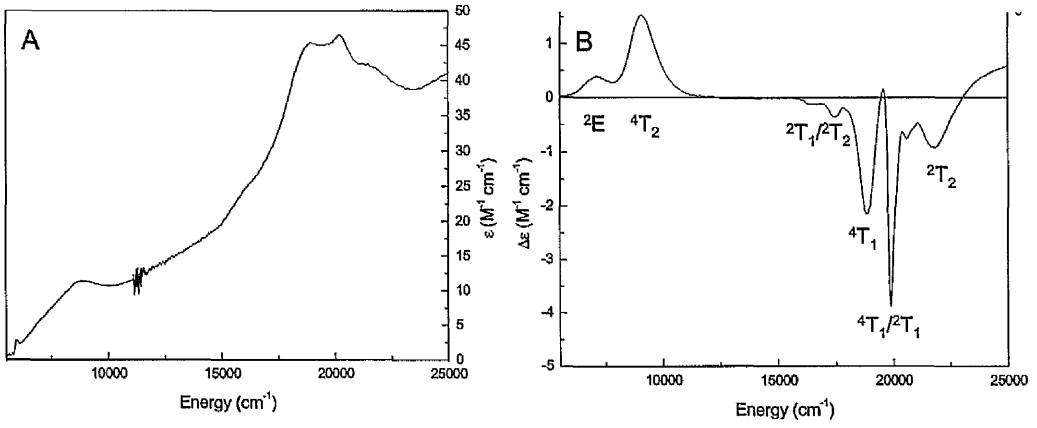

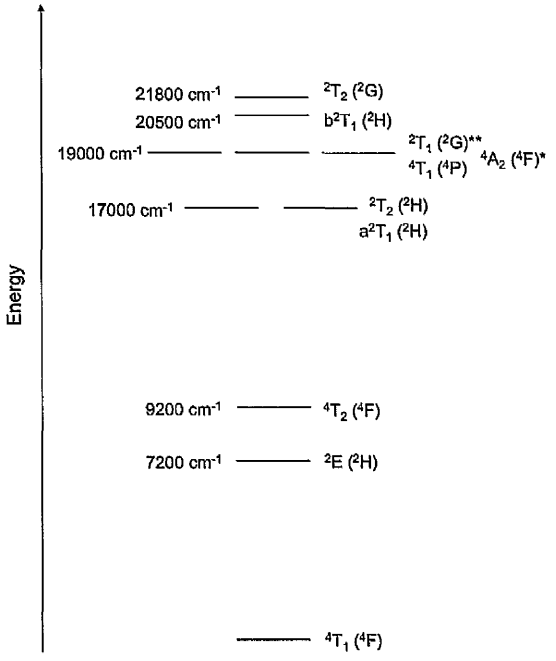

The observed transitions were assigned to a d^7 Tanabe-Sugano diagram[22] and labelled according to the O_h symmetry label of the final state. A Δ_O/B ratio of *ca.* 12.5 produced the most satisfactory fit between the energy of observed MCD transitions and calculated energies of excited states arising from the d^7 configuration. For clarity, the atomic terms from which the excited states originate have been omitted from the assignment in the spectrum, but are outlined in the energy level

scheme depicted above. All energy levels have been calculated from the crystal field parameters Δ_O = 11700 cm^{-1}, B = 840 cm^{-1} and C = 3860 cm^{-1} (with Δ_O = crystal field splitting, B, C = electron repulsion or Racah parameters).

The field dependence of the MCD response at 1.7, 4.2, 10 and 20 K was measured between 0 and 5.0 T in order to determine anisotropy in the magnetic properties. Below is an example of a data set collected on **4** at 1.7 K.

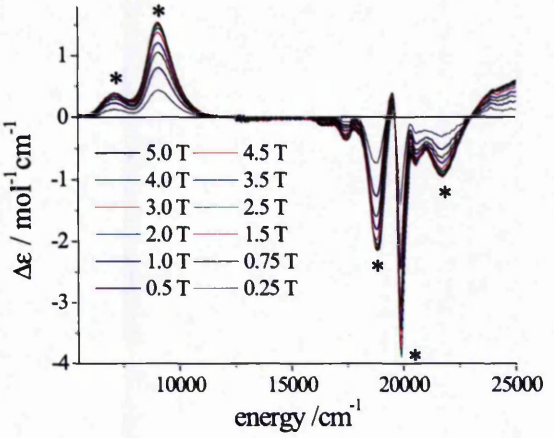

Appendix 4.1

Synthesis of heterometallic chromium rings

All reagents were purchased from Aldrich, except for 2,4-dimethylimidazole, which was obtained from Alfa-Aesar, and used as received. The syntheses of the complexes were carried out in Erlenmeyer Teflon® FEP flasks supplied by Fisher.

$[(CH_3)_2NH_2][Ga_7CoF_8(O_2CC(CH_3)_3)_{16}]$ (Ga_7Co, 12)

$C_{82}CoF_8Ga_7H_{152}NO_{32}$ RM = 2363.1

12 was prepared according to a literature procedure reported in[148] for $[(C_3H_7)_2NH_2][Ga_7CoF_8(O_2CCMe_3)_{16}]$ by using dimethylammonium dimethyl-carbamate instead of propylamine.

Yield: 85%

Elemental analysis: calculated: Ga: 20.65, Co: 2.49, C: 41.67, H: 6.48, N, 0.59, found: Ga: 20.15, Co: 2.39, C: 43.12, H: 6.91, N: 0.55

Mass-spectra ES MS (sample dissolved in toluene, run in MeOH) *m/z*: - 2316 [M – $Me_2NH_2]^-$, + 2385 [M+Na]$^+$, + 2261 [M- $(O_2CCMe_3)]^+$

Crystals suitable for X-ray diffraction studies were obtained by crystallisation of **12** from toluene.

A **12_Ga7Co.cif** file containing the full crystallographic data is available on the accompanying disc.

$[(CH_3)_2NH_2][Ga_7CoF_8(O_2CC(CH_3)_3)_{16}]$ (Cr_7Co, 14)

$C_{82}CoF_8Cr_7H_{152}NO_{32}$ RM = 2239.0

The synthesis, structure and analysis of **14** was reported by Winpenny *et al.*[73]

[2,4-DiMe-ImidH]$[Cr_7NiF_8(O_2CC(CH_3)_3)_{16}]$ (Cr_7Ni, 15)

$C_{85}H_{153}Cr_7F_8N_2NiO_{32}$ RM = 2289.8

$CrF_3 \cdot 4H_2O$ (3.0 g, 17 mmol), 2,4-dimethylimidazole (2,4-DiMeImH) (0.6 g, 6.24 mmol), $2NiCO_3 \cdot 3Ni(OH)_2 \cdot 4H_2O$ (0.7 g, 1.2 mmol) and $(CH_3)_3CCO_2H$ (15.0 g, 147 mmol) were heated while stirring at 140°C for 24 h. The flask was cooled to room temperature and acetone (30 mL) was added and stirred for 12 h. The resulting green precipitate was filtered, washed with acetone and then stirred for at least 1 h at ambient temperature in hexane (250 mL). The reaction mixture was filtered and the filtrate was evaporated under vacuum. The resulting residue was washed with acetone and dried in *vacuo*.

Yield: 2.0 g (37% based on available Cr)

Elemental analysis: calculated: Cr: 15.90, Ni: 2.56, C: 44.59, H: 6.73, N: 1.22, found: Cr: 15.86, Ni: 2.61, C: 44.62, H: 6.74, N: 1.19.

Crystallization of **15** from ethylacetate gave X-ray quality crystals in three days.

Elemental analysis: calculated: Cr: 15.90, Ni: 2.56, C: 44.59, H: 6.73, N: 1.22, found: Cr: 15.46, Ni: 2.61, C: 44.22, H: 6.62, N: 1.10.

A **15_Cr7Ni.cif** file containing the full crystallographic data is available on the accompanying disc.

[2,4-DiMe-ImidH][$Cr_7CoF_8(O_2CC(CH_3)_3)_{16}$] ($Cr_7Co$, 16)

$C_{85}H_{153}Cr_7F_8N_2CoO_{32}$ RM = 2290.0

16 was prepared by an analogous procedure to that for **15** by using $[Co_2(H_2O)(O_2CCMe_3)_4(HO_2CCMe_3)_4]$, instead of $2NiCO_3{\cdot}3Ni(OH)_2{\cdot}4H_2O$.

Yield: 2.6 g (48% based on available Cr)

Elemental analysis: calculated: Cr: 15.89, Co: 2.57, C: 44.58, H: 6.73, N: 1.22, found: Cr: 15.81, Co: 2.70, C: 44.58, H: 6.82, N: 1.21

Crystallization of **16** from ethylacetate gave X-ray quality crystals in three days.

Elemental analysis: calculated Cr: 15.89, Co: 2.57, C: 44.58, H: 6.73, N: 1.22, found: Cr: 16.10, Co: 2.64, C: 44.27, H: 6.45, N: 1.10

A **16_Cr7Co.cif** file containing the full crystallographic data is available on the accompanying disc.

[ImidH]$_2$[$Cr_6Ni_2F_8(O_2CC(CH_3)_3)_{16}$] ($Cr_6Ni_2$, 17)

$C_{86}H_{154}Cr_6F_8N_4Ni_2O_{32}$ RM = 2337.5

17 was first reported as a by-product in the synthesis of $[ImidH]_2[Cr_8NiF_{11}(O_2CCMe_3)_{17}]$.[149] Here a new procedure is presented, which leads to a higher yield of **17** and does not produce the Cr_8Ni ring alongside **17**.

17 was prepared by an analogous procedure to that for **15** by using 1,1′-carbonyldiimidazole (0.7 g, 4.3 mmol), instead of 2,4-dimethylimidazole (2,4-diMeImH).

Yield: 5.6 g (86% based on available Cr).

Elemental analysis: calculated: Cr: 13.35, Ni: 5.02, C: 44.19, H: 6.64, N: 2.40, found: Cr: 13.37, Ni: 4.81, C: 44.89, H: 6.81, N: 2.28.

Crystallization of **17** from ethylacetate gave X-ray quality crystals in two days.

Elemental analysis: calculated: Cr: 13.35, Ni: 5.02, C: 44.19, H: 6.64, N: 2.40, found: Cr: 13.04, Ni: 4.63, C: 43.88, H: 6.66, N: 2.25

A **17_Cr6Ni2.cif** file containing the full crystallographic data is available on the accompanying disc.

$[ImidH]_2[Cr_6Co_2F_8(O_2CC(CH_3)_3)_{16}]$ (Cr_6Co_2, 18)

$C_{86}H_{154}Cr_6F_8N_4Co_2O_{32}$ RM = 2338.0

18 was prepared by an analogous procedure to that for **17** by using $[Co_2(H_2O)(O_2CCMe_3)_4(HO_2CCMe_3)_4]$ instead of $2NiCO_3{\cdot}3Ni(OH)_2{\cdot}4H_2O$.

Yield: 4.0 g (62% based on available Cr).

Elemental analysis: calculated: Cr: 13.34, Co: 5.04, C: 44.18, H: 6.64, N: 2.40, found: Cr: 13.69, Co: 4.73, C: 44.45, H: 7.00, N: 2.26.

Crystallization of **18** from ethylacetate gave X-ray quality crystals in two days.

Elemental analysis: calculated: Cr: 13.34, Co: 5.04, C: 44.18, H: 6.64, N: 2.40, found: Cr: 13.08, Co: 5.06, C: 44.05, H: 6.70, N: 2.28.

A **18_Cr6Co2.cif** file containing the full crystallographic data is available on the accompanying disc.

$[1\text{-}Bz\text{-}ImidH]_2[Cr_7Ni_2F_9(O_2CC(CH_3)_3)_{18}]$ (Cr_7Ni_2, 19)

$C_{110}H_{184}Cr_7F_9N_4Ni_2O_{36}$ RM = 2791.0

19 was prepared by an analogous procedure to that for **15** by using 1-benzyl-imidazole (1-Bz-ImidH) (1.25g, 7.9 mmol), instead of 2,4-dimethylimidazole (2,4-diMeImH).

Yield: 4.3 g (65% based on available Cr).

Elemental analysis: calculated: Cr: 13.04, Ni: 4.21, C: 47.34, H: 6.64, N: 2.01, found: Cr: 12.90, Ni: 4.08, C: 48.65, H: 7.01, N: 1.88

Crystallization of **19** from ethylacetate gave X-ray quality crystals in two days.

Elemental analysis: calculated: Cr: 13.04, Ni: 4.21, C: 47.34, H: 6.64, N: 2.01, found: Cr: 12.75, Ni: 4.05, C: 47.15, H: 6.89, N: 1.86

A **19_Cr7Ni2.cif** file containing the full crystallographic data is available on the accompanying disc.

$[1\text{-}Bz\text{-}ImidH]_2[Cr_7Co_2F_9(O_2CC(CH_3)_3)_{18}]$ (Cr_7Co_2, 20)

$C_{110}H_{184}Cr_7F_9N_4Co_2O_{36}$ RM = 2791.5

20 was prepared by an analogous procedure to that for **19** by using $[Co_2(H_2O)(O_2CCMe_3)_4(HO_2CCMe_3)_4]$ instead of $2NiCO_3{\cdot}3Ni(OH)_2{\cdot}4H_2O$.

Crystallization of **20** from ethylacetate gave X-ray quality crystals in two days. The *Yield*: 0.4 g (6% based on available Cr)

Elemental analysis: calculated: Cr: 13.04, Co: 4.22, C: 47.33, H: 6.64, N: 2.01; found: Cr: 12.40, Co: 5.79, C: 44.47, H: 6.44, N: 1.83

A **20_Cr7Co2.cif** file containing the full crystallographic data is available on the accompanying disc.

Appendix 4.2

Q-band powder EPR spectrum of $[(C_3H_7)_2NH_2][Ga_7CoF_8(O_2CC(CH_3)_3)_{16}]$ at 5 K.

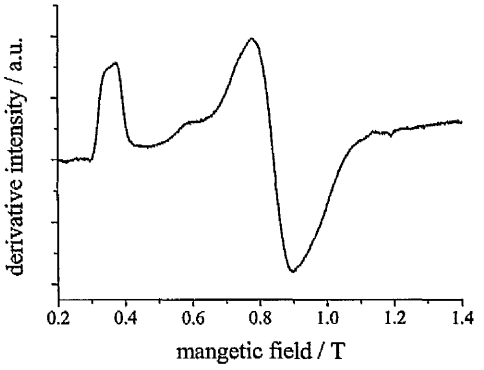

Appendix 4.3

Calculation of total g_{eff}-values for different spin states from the single ion contributions with a vector coupling approach.

The following expressions[132] have been used to calculate the c coefficients and subsequently $\mathbf{g}_S$ (or here isotropic g_S) for the total molecular spin states.

$$\hat{S} = \hat{S}_A + \hat{S}_B$$

$$\mathbf{g}_S = c_1\mathbf{g}_A + c_2\mathbf{g}_B$$

with

$$c_1 = \frac{(1+c)}{2};\ c_2 = \frac{(1-c)}{2}$$

where:

$$c = \frac{S_A(S_A+1) - S_B(S_B+1)}{S(S+1)}$$

$g_{Cr} = 1.96$, $g_{Ni} = 2.23$

Cr_6Ni_2, both nickel ions on the same sub-lattice:

S_A	S_B	S	c_1	c_2	g_S
$^3/_2$	$^3/_2$	3	0.500	0.500	1.960
1	1	2	0.500	0.500	2.230
3	3	6	0.500	0.500	1.960
3	2	5	0.600	0.400	2.068
6	5	**1**	3.500	-2.500	**1.690**
6	5	2	1.500	-0.500	**1.906**

Cr_6Ni_2, nickel ions on different sub-lattices:

S_A	S_B	S	c_1	c_2	g_S
$^3/_2$	$^3/_2$	3	0.500	0.500	1.960
$^3/_2$	1	$^5/_2$	0.600	0.4000	2.068
3	$^5/_2$	$^{11}/_2$	0.545	0.455	2.009
$^{11}/_2$	$^{11}/_2$	**0**	not relevant		
$^{11}/_2$	$^{11}/_2$	**1**	0.500	0.500	**2.009**

Cr_7Ni_2, nickel ions on different sub-lattices, coupling order 1:

S_A	S_B	S	c_1	c_2	g_S
$^3/_2$	$^3/_2$	3	0.500	0.500	1.960
$^3/_2$	1	$^5/_2$	0.600	0.400	2.068
3	3	6	0.500	0.500	1.960
3	$^5/_2$	$^{11}/_2$	0.545	0.455	2.009
6	1	7	0.857	0.143	1.999
$^{11}/_2$	7	$^3/_2$	-2.200	3.200	**1.975**
$^{11}/_2$	7	$^5/_2$	-0.657	1.657	**1.992**

Cr_7Ni_2, nickel ions on different sub-lattices, coupling order 2:

S_A	S_B	S	c_1	c_2	g_S
$^3/_2$	$^3/_2$	3	0.500	0.500	1.960
$^3/_2$	1	$^5/_2$	0.600	0.400	2.068
3	$^5/_2$	$^{11}/_2$	0.545	0.455	2.009
$^{11}/_2$	$^3/_2$	7	0.786	0.214	2.056
$^{11}/_2$	7	$^3/_2$	-2.200	3.200	**2.161**
$^{11}/_2$	7	$^5/_2$	-0.657	1.657	**2.088**

Cr_7Ni_2, both nickel ions on the five ion sub-lattice:

S_A	S_B	S	c_1	c_2	g_S
$^3/_2$	$^3/_2$	3	0.500	0.500	1.960
1	1	2	0.500	0.500	2.230
3	3	6	0.500	0.500	1.960
3	2	5	0.600	0.400	2.068
5	$^3/_2$	$^{13}/_2$	0.769	0.231	2.043
6	$^{13}/_2$	$^1/_2$	-4.000	5.000	**2.375**
6	$^{13}/_2$	$^3/_2$	-0.400	1.400	**2.076**

Cr_7Ni_2, both nickel ions on the four ion sub-lattice:

S_A	S_B	S	c_1	c_2	g_S
$^3/_2$	$^3/_2$	3	0.500	0.500	1.960
1	1	2	0.500	0.500	2.250
3	3	6	0.500	0.500	1.960
3	2	5	0.600	0.400	2.076
6	$^3/_2$	$^{15}/_2$	0.800	0.200	1.960
$^{15}/_2$	5	$^5/_2$	2.429	-1.429	**1.794**
$^{15}/_2$	5	$^7/_2$	1.571	-0.571	**1.894**

Appendix 4.4

Calculation of the magnetic properties of Cr_7Ni_2 (19).

Susceptibility: J = -5.8 cm^{-1} and g_{eff} = 1.98 for isomers A, B, C, D (dash) and a 1:2:1:2 mixture (solid)

Magnetisation: J = -5.8 cm^{-1} and $g_{eff,\ ground\ state}$ = 1.76, $g_{eff,\ excited\ states}$ = 1.98 for isomers A, B, C, D and isomeric mixtures

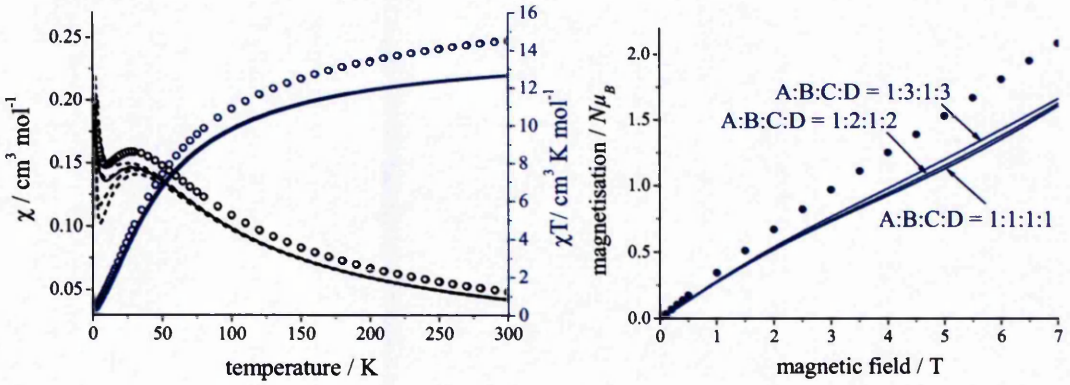

List of publications

Angelika B. Boeer, Eric J. L. McInnes and David Collison, in *Electron Paramagnetic Resonance, Vol. 21* (Ed.: B. C. Gilbert), RSC, Cambridge, **2008**.

Vito Di Noto, Angelika B. Boeer, Sandra Lavina, Christopher A. Muryn, Mathias Bauer, Grigore A. Timco, Giuseppe Pace, Marcio Rancan, Richard E. P. Winpenny, Silvia Gross, *Adv. Funkt. Mater., accepted*, DOI: 10.1002/adfm.200900600

Angelika B. Boeer, David Collison, Christopher A. Muryn, Grigore A. Timco, Floriana Tuna and Richard E. P. Winpenny, *"Linkage Isomerism and Spin Frustration in Heterometallic Rings: Synthesis, Structural Characterisation and Magnetic and EPR Spectroscopic Studies of Cr_7Ni, Cr_6Ni_2 and Cr_7Ni_2 Rings Templated About Imidazolium Cations." submitted to Chem. Eur. J. in 2009*

Several more publications on the work regarding the dimetallics and the cobalt containing heterometallic rings are in preparation.